Baryon Structure Using the Feynman-Hellmann Theorem in Lattice Quantum Chromodynamics

Mischa Batelaan

Supervisors:
James M. Zanotti
Ross D. Young

A thesis submitted towards the degree of Doctor of Philosophy

School of Physics, Chemistry and Earth Sciences
The University of Adelaide

September 1, 2023

Abstract

Baryons such as the proton and neutron make up the large majority of all visible matter in the universe. According to the standard model, the structure of these baryons is defined by the interactions of their constituent parts, the quarks and gluons. The gauge field theory which governs these interactions is called Quantum Chromodynamics (QCD), which has a property that prevents the application of perturbative methods at low energies. Currently, the best first-principles approach to studying the effects of QCD at low energies is Lattice QCD, which relies on a discretisation of spacetime. In this thesis we go through the derivation of the Feynman-Hellmann theorem and its application to lattice QCD, specifically for the calculation of baryon matrix elements. This Feynman-Hellmann method provides us with an alternative approach to conventional lattice QCD techniques.

To study the internal structure of baryons we use the Feynman-Hellmann method to calculate the electromagnetic form factors of the octet baryons at high momentum transfers. In this calculation we take advantage of the improved control of excited states provided by the Feynman-Hellmann method as well as a weighted-averaging approach to provide a robust analysis over a wide range of momenta. The form factor results are then extrapolated to physical quark masses through the use of a flavour breaking expansion. Our results for the electric form factor G_E show good agreement with experimental results, however the results for the magnetic form factor G_M do not agree well, indicating that there could be more systematic effects presently unaccounted for.

The use of an expanded version of the Feynman-Hellmann method which allows for the consideration of quasi-degenerate energy states, allows for the investigation of the transition form factors of hyperons.

These are valuable as they can provide insight into the oscillations between quark flavour permitted by the standard model. We present results for the matrix element of the Σ^- to neutron transition which agree well with a similar calculation using the conventional three-point function method. This is promising as this novel method could provide an independent approach to the determination of the CKM matrix elements.

Declaration

I certify that this work contains no material which has been accepted for the award of any other degree or diploma in my name, in any university or other tertiary institution and, to the best of my knowledge and belief, contains no material previously published or written by another person, except where due reference has been made in the text. In addition, I certify that no part of this work will, in the future, be used in a submission in my name, for any other degree or diploma in any university or other tertiary institution without the prior approval of the University of Adelaide and where applicable, any partner institution responsible for the joint award of this degree. The author acknowledges that copyright of published works contained within the thesis resides with the copyright holder(s) of those works. I give permission for the digital version of my thesis to be made available on the web, via the University's digital research repository, the Library Search and also through web search engines, unless permission has been granted by the University to restrict access for a period of time. I acknowledge the support I have received for my research through the provision of an Australian Government Research Training Program Scholarship.

Mischa Batelaan

Acknowledgements

I would like to thank my supervisors James Zanotti and Ross Young for their help and guidance over the years. They were always happy to discuss any problems I had and helped me stay on the right track with my research. James was always ready to dive into the details of the data analysis and Ross always had a new perspective ready to uncover new questions. Additionally I am thankful to Roger Horsley for his eye for detail which was crucial in getting our research published. The time I was able to spend in Edinburgh working with Roger was also very instructive.

The disruptions and work-from-home time during my PhD allowed me to gain a much greater appreciation for the friendly atmosphere and welcoming community in the office of PhD students. I would especially like to thank Tomas Howson for the many fruitful office discussions throughout the years in honours and our PhD's. The many games of officeball which we played in-between writing sessions or while my code was running were a great motivation to keep me around the office. Sharon and Silvana, for all their help organising conferences and travel over the years, as well as always being there to support the group of graduate students in whichever way possible.

Many thanks to my family; Okke, Lucie, Rebecca, Stella, and Lilly for all the support over the years and the many catch-ups to lift my spirits. Finally, I am very thankful to Meera for supporting me in writing this thesis, she has always been ready to help me through any tough sections and to help me see the path forward. The many walks, hikes and bike-rides we did together provided me with the much-needed energy to finish this project.

Computing Resources

The numerical gauge field configuration used in this thesis were generated using the Berlin Quantum Chromodynamics (BQCD) lattice QCD program [1,2], on the DiRAC Blue

Gene Q and Extreme Scaling (EPCC, Edinburgh, UK) and Data Intensive (Cambridge, UK) services and the GCS supercomputers JUQUEEN and JUWELS (NIC, Jülich, Germany). The simulations in this thesis were undertaken using the resources provided by HLRN (The North-German Supercomputer Alliance), the NCI National Facility in Canberra, Australia, the iVEC facilities at the Pawsey Supercomputing Centre and the Phoenix HPC service at the University of Adelaide. The authors gratefully acknowledge the computing time granted by the Resource Allocation Board and provided on the supercomputer Lise and Emmy at NHR@ZIB and NHR@Göttingen as part of the NHR infrastructure. The calculations for this research were conducted with computing resources under the project hhp00045. The Matrix inversions and the calculation of the correlation functions has been performed using the Chroma software library [3].

Contents

1. Introduction **1**

List of Figures

List of Tables

Chapter 1.

Introduction

Throughout the 20^{th} century there has been a large push to further the understanding of the fundamental building blocks of our universe. The results of this research was the construction of the Standard Model (SM) of particle physics in the 1970's. This model has been incredibly successful at describing the multitude of experimental results over the years, and making predictions for future discoveries. The SM is comprised of a set of matter particles which are acted upon by the force carriers of three fundamental forces, each of which have their own special properties. The electromagnetic force acts on electrically charged particles through photons, the weak force acts on the weak isospin of particles through the Z^0 and $W^{\pm}$ bosons, while the strong force acts on colour-charged particles through the gluons.

The point particles which make up the overwhelming majority of all matter are the quarks and the gluons, these form the constituent parts of both the proton and the neutron, collectively referred to as the nucleons. The theory which describes the interactions between the quarks and gluons is Quantum Chromodynamics (QCD), the rules of these interactions are determined by the SU(3)-colour charge which each of the particles contains.

QCD has a few unique properties which set it apart from other quantum field theories, and which heavily influence how it can be studied. In addition to the quarks themselves, the gluons also carry colour charge which allows them to self-interact. These self-interactions lead to the notable behaviour of the QCD coupling strength decreasing at high energies, this results in the particles being asymptotically free only at high energies and in turn allowing for the application of perturbation theory to this high-energy regime. Another property which stems from the gluon self-interactions is confinement, this is the requirement that any observable particle must always be colour-neutral. A consequence of confinement is that the only way to study the properties of quarks is by considering their bound states, called hadrons.

At low energies, the only first-principles approach to calculations in QCD comes from the Lattice QCD formulation first presented by Wilson [4] in the 1970's. Lattice QCD relies on a discretised formulation of the theory, which can be used to numerically calculate observables. The main challenge of this method lies in the many systematic uncertainties which arise from the discretisation.

Aspects of the internal structure of the nucleons can be described by the distribution of the electric charge and the magnetisation density, two properties which are encoded in the momentum dependence of the electromagnetic form factors of the nucleons. Experiments throughout the 1950's and 60's were able to determine these form factors through the use of the Rosenbluth separation method [5], however more recent results using the polarisation transfer method have produced a discrepancy in the ratio of the electric-to-magnetic form factors of the proton at high momentum transfer (Q^2). This discrepancy has attracted a lot of attention from both experimentalists and theorists as it indicates a potential zero-crossing of the electric form factor at high momenta. The experimental response has seen renewed interest in improving the precision of the form factor measurements at higher Q^2, as well as experiments probing the contributions of two-photon exchange (TPE) processes. Current results from DESY and JLab indicate non-trivial contributions from TPE in various observables at low Q^2, however these seem to be as of yet insufficient to fully explain the discrepancy [6,7]. Since perturbative QCD (pQCD) calculations can provide viable predictions at sufficiently large values of Q^2, there have been efforts in this area as well . Additionally, the Lattice QCD community has shown interest in providing theoretical predictions for the form factors to shed light on the discrepancy as Lattice QCD can theoretically map out the full momentum dependence from zero to the experimental limit and potentially further if the systematic uncertainties can be controlled sufficiently. In this thesis we will show results from a lattice calculation of the nucleon electromagnetic form factors at large Q^2 using a novel approach based on the Feynman-Hellmann method. The aim of the calculation is to provide a viable alternative to the more established three-point function approach which provides the possibility of improved control over excited state contributions.

The standard model is based heavily on the idea of symmetries in nature, however it also contains some approximate symmetries which are very important. One such approximate symmetry is the SU(3)-flavour symmetry, which refers to the approximate degeneracy in mass between the up, down and strange quarks relative to the masses of the three heavier charm, bottom and top quarks. This broken symmetry and the resulting mixing between the different flavours of quarks through the weak force is included in the SM through the unitary Cabibbo-Kobayashi-Maskawa matrix. These matrix elements are parameters of the Standard Model and must obey the unitarity constraints, they are not predicted by the theory but must be determined through a combination of theory and experiment. Since they are universal, once the values of the CKM matrix are determined they can lead to Standard Model predictions of a variety of hadronic decay channels. This has led to many investigations into possible physics beyond the standard model (BSM) through precision determinations of these matrix elements. These calculations rely on experimental results or theoretical calculations of the properties of the hadrons containing the various quark flavours. Lattice QCD is placed in a unique position to investigate this mixing as the quark masses are free parameters for any lattice, this allows for the amount of SU(3)-flavour breaking to be changed and the consequences to be investigated. In this work we will investigate the effects of SU(3)-flavour symmetry breaking by calculating the transition matrix elements of hyperons (baryons containing strange quarks) to nucleons, the approach to these calculations will again use the Feynman-Hellmann theorem.

1.1. Outline

In chapter 2 we will discuss the motivation behind Lattice QCD and present a standard description of the discretised QCD action. This is the method which we use throughout this thesis to perform calculations involving low-energy strong force interactions.

Following this, in chapter 3 we discuss in detail how Lattice QCD can be used to calculate the spectra of hadrons. The main sources of uncertainties in the calculations and how these will be handled are covered here, then we also briefly show an application of these methods to the calculation of the hadron masses on a large set of lattice ensembles. The last section of this chapter covers the standard three-point function approach to the calculation of matrix elements, which will be applied in later chapters.

Chapter 4 covers the Feynman-Hellmann method and its application to the path-integral formalism of Lattice QCD. We derive an expression relating the shift in the energy of the ground state of a lattice correlator to a matrix element in the forward limit. When extending this method to off-forward matrix elements we have to take into account the momentum-spin state degeneracies, we show examples of this for both the temporal and spatial vector currents. These examples allow for the calculation of both the Sachs electromagnetic form factors.

In chapter 5 we investigate the internal structure of the nucleons and other octet baryons by calculating their electromagnetic form factors. To perform this calculation in Lattice QCD we apply the Feynman-Hellmann method as outlined in the previous chapter. We calculate the form factors on a range of lattice ensembles with different quark masses, lattice spacings and volumes, this variation in lattice setups is then used to attempt to extrapolate the form factors to the physical quark masses and continuum limit. Furthermore, this chapter also includes a description of various methods which are used to account for the systematics present in Lattice QCD calculations.

In chapter 6 we investigate the transition matrix elements between Hyperons. To calculate these matrix elements from the Feynman-Hellmann method requires us to develop a new derivation of the theory which allows for quasi-degenerate energy states to be considered. The first part of the chapter outlines this new formulation of the theorem, this approach relies on the the application of the Dyson expansion to the transfer matrix. The usual restriction to energy-degenerate states can be slightly relaxed using this formulation and as a part of the calculation we investigate the higher order effects of the quasi-degeneracy in energies. We apply this method to the calculation of the matrix element for the Σ^- to neutron transition at a range of momentum transfers. Additionally this chapter also shows the results of a comparable calculation using the more established three-point function method, which provides a means for validating and benchmarking the results of the Feynman-Hellmann method.

Chapter 2.

Lattice QCD

Since QCD is a gauge field theory, the natural approach to calculations would be to use perturbation theory similarly to its successfully application in Quantum Electrodynamics (QED). Any such perturbative calculation will depend on the coupling constant of the theory, in QED this is the fine-structure constant $\alpha \approx 1/137$, however due the asymptotic freedom inherent to QCD, its coupling strength decreases as the interaction energy goes up. This QCD coupling can be approximated by

$$\alpha_S(Q^2) \approx \frac{1}{\beta_0 \ln(Q^2/\Lambda^2_{\mathrm{QCD}})}, \tag{2.1}$$

where Λ_{QCD} is a dimensional parameter [8]. This equation shows that the expected behaviour is a decrease in the coupling strength with increasing momentum. At sufficiently high energies this coupling allows for perturbation theory to make predictions of the strong interactions. At low energies however, the large size of the coupling constant means that an infinite number of different interaction diagrams will contribute significantly to any QCD calculation, making perturbation theory impractical. The structure of hadrons at these low energies can be thought of as a complicated mix of quarks and gluons and their interactions rather than just the multiple-quark bound states they behave as at high energies. Figure ?? shows a summary of measurements of the coupling α_S against the energy scale, showing this decrease in the strength of the coupling.

Studying the interactions of the strong force at low energies is very valuable for our understanding of the fundamental particles, to do this requires a non-perturbative approach to QCD calculations. lattice QCD provides a first principles approach to low energy calculations of QCD and was first proposed by Kenneth Wilson in 1974 [4] as a method for studying QCD non-perturbatively. Since then many computational

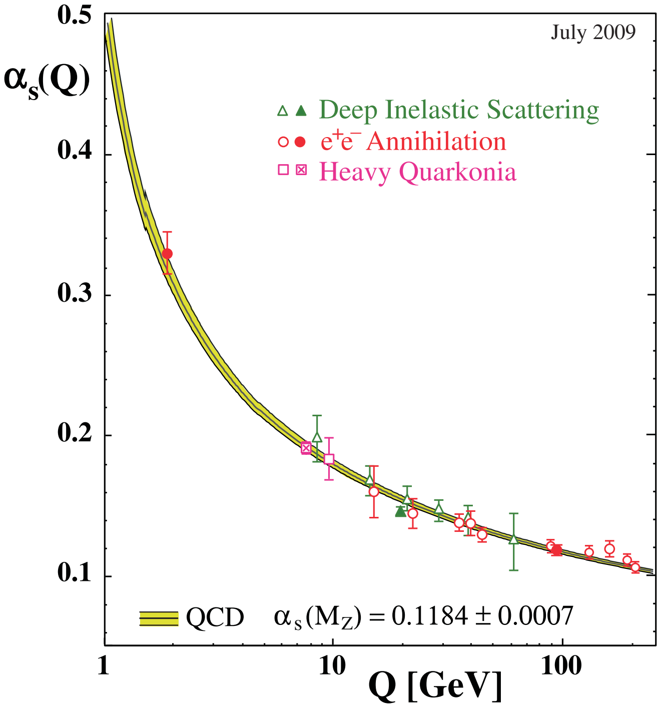

Figure 2.1. Measurements of α_S against the momentum(energy) scale Q in GeV. Figure from [8].

techniques have been developed to improve and extend the capabilities of the method. In this chapter we will lay out the basic construction of lattice QCD as well as the specific methods used in the calculations presented in the following chapters. The explanation in this chapter will mainly follow the texts by Rothe [9] however there are many other good sources which contain more detail [10–13].

2.1. Path Integral Formalism

The path integral formalism for Quantum Field Theories (QFT) was first developed by Feynman [14]. This formalism shows that it is possible to write down observables as integrals over all possible paths weighted by an exponential of the action. The expectation value of some operator $\mathcal{O}$ can be expressed as a path integral over the fermion fields and the gauge fields by

$$\langle \mathcal{O} \rangle = \frac{1}{Z} \int \mathcal{D}[A_\mu, \psi, \bar{\psi}]\, \mathcal{O}\, e^{iS[A_\mu, \psi, \bar{\psi}]}, \tag{2.2}$$

where the partition function Z is defined as the path integral without any operators

$$Z = \int \mathcal{D}[A_\mu, \psi, \bar{\psi}]\, e^{iS[A_\mu,\psi,\bar{\psi}]}. \tag{2.3}$$

The fermionic degrees of freedom here are represented by Grassmann variables. The integral measure contains the product of the integrals of each field over all possible space-time points

$$\mathcal{D}[A_\mu, \psi, \bar{\psi}] = \prod_x d\psi(x) \prod_y d\bar{\psi}(y) \prod_z dA_\mu(z). \tag{2.4}$$

In Minkowski space-time the QCD action can be decomposed into a fermionic and gluonic part

$$\begin{aligned} S_{QCD} &= S_F + S_G \\ &= \sum_{f=1}^{N_f} \int d^4x\, \bar{\psi}(x)(i\gamma^\mu D_\mu - m_f)\psi(x) - \frac{1}{4}\mathrm{Tr} \int d^4x\, F_{\mu\nu}F^{\mu\nu}, \end{aligned} \tag{2.5}$$

where ψ and $\bar{\psi}$ are the quark fields and A_μ are the gauge fields. The fermion action also depends on the gauge fields through the covariant derivative, defined as $D_\mu = \partial_\mu - igA_\mu$. The fermionic part of the action includes a sum over the number of quark flavours in the theory, for full QCD this is 6, however most lattice QCD calculations limit this to the 3 (or 4) lighter quark flavours $u, d, s(, c)$.

2.2. Euclidean Space-time

In the Minkowski space-time formulation of the path integral shown above the exponent containing the action is imaginary. This leads to a sign problem which makes numerical calculations of the path integral impractical. To solve this issue we will use a Wick rotation to transform from Minkowski to Euclidean space-time. The Wick rotation can be considered as an analytic continuation to imaginary time, performed by replacing

$t \to it$. The relation between Minkowski and Euclidean space-time is

$$\begin{aligned} x_E^4 &= i x_M^0, \\ x_E^j &= x_M^j, \\ \partial_4^E &= -i\partial_4^M, \\ \partial_j^E &= \partial_j^M, \end{aligned} \tag{2.6}$$

and the Euclidean space-time the metric is $\delta_{\mu\nu} = \mathrm{diag}(+,+,+,+)$. The Dirac gamma matrices in Minkowski space are related to those in Euclidean space-time by

$$\gamma^4 = \gamma_4 = \gamma_M^0, \qquad \gamma_i = \gamma^i = -i\gamma_M^i. \tag{2.7}$$

Using the above relations we can determine the action in Euclidean space-time

$$\begin{aligned} iS_{QCD}^M &\xrightarrow{\text{Wick}} -\sum_{f=1}^{N_f} \int d^4x\, \bar{\psi}(x)(\gamma^\mu D_\mu + m_f)\psi(x) + \frac{1}{4}\mathrm{Tr} \int d^4x\, F_{\mu\nu}F^{\mu\nu} \\ &= -S_{QCD}^E. \end{aligned} \tag{2.8}$$

The path integral formulation in Euclidean space-time now has a real action in the exponent, which removes the sign problem. From now on we will work in Euclidean space-time and drop the labels.

2.3. Lattice Discretisation

To allow for numerical calculations of observables in lattice QCD, we need to discretise the path integral formalism. The continuous coordinate space will be changed to a discrete lattice of points

$$x_\mu \to a n_\mu, \tag{2.9}$$

where a is the spacing between the points and n^μ is a vector of integers. We will continue to use the discrete 4-vector $x_\mu = a n_\mu$ as a label for the positions on the lattice. The derivative will be replaced by a finite difference between two lattice sites,

$$\partial_\mu \psi(x) \to \frac{1}{2a}\left(\psi(x + a\hat{\mu}) - \psi(x - a\hat{\mu})\right). \tag{2.10}$$

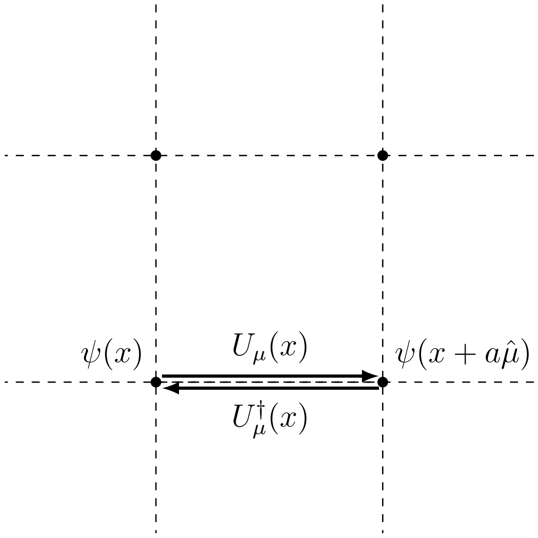

Figure 2.2. The lattice gauge link $U_\mu(x)$ which connects the sites x and $x + a\hat{\mu}$. The Hermitian conjugate of the gauge link connects the same two sites but is oriented in the opposite direction.

Discretising the gauge fields is done by replacing them by gauge links $U_\mu(x)$ which link adjacent sites on the lattice, in this case site x and $x + a\hat{\mu}$ as shown in figure 2.2. These gauge links are defined in terms of the parallel transport operator on the lattice

$$U_\mu(x) \equiv \mathcal{P}\mathrm{exp}\left[ig\int_x^{x+a\hat{\mu}} dz_\mu A_\mu(x)\right], \tag{2.11}$$

where $\mathcal{P}$ is the path-ordering operator. These links are gauge covariant and transform as

$$U_\mu(x) \to U'_\mu(x) = \Omega(x)U_\mu(x)\Omega(x+a\hat{\mu})^\dagger, \tag{2.12}$$

for an element $\Omega(x)$ of SU(3). Taking the Hermitian conjugate of such a gauge link is the same as reversing the direction,

$$U^\dagger_\mu(x) \equiv U_{-\mu}(x+a\hat{\mu}). \tag{2.13}$$

Using these link variables it is possible to define a discretised fermion action

$$S_F[\psi,\bar{\psi},U] = a^4\sum_{x,y}\bar{\psi}(x)M(x,y)\psi(y), \tag{2.14}$$

where the Dirac operator M is defined as

$$M(x,y) = \frac{1}{2a}\sum_{\mu=1}^{4}\gamma_\mu\left(U_\mu(x)\delta_{x+a\hat{\mu},y} - U_{-\mu}(x)\delta_{x-a\hat{\mu},y}\right) + m\delta_{x,y}, \tag{2.15}$$

noting that this formulation of the discretised fermion action is gauge invariant due to the explicit presence of the gauge links. If we check how this action behaves when taking the continuum limit $a \to 0$ we find that the theory suffers from the problem of fermion doublers. These are unphysical fermions which need to be removed for a reliable lattice theory, see eg. [9] for a detailed discussion. The Nielsen-Ninomiya 'no-go' theorem [15,16] shows that this doubling of the fermions in the continuum limit is a direct consequence of discretising the action. The simplest strategy to remove these fermion doublers is to introduce an additional term into the action which gives the doublers infinite mass in the continuum limit and decouples them from the theory. The method which will be used here to counter the doubling is the Wilson Improved action, another commonly used alternative to this method is the staggered-fermion approach [17–19].

2.4. Wilson Improved Action

To solve the problem of doublers, the Wilson improved actions can be constructed [4]. This improvement to the fermion action is defined by

$$S_F^W = -a\frac{r}{2}\sum_x \bar{\psi}(x)\Delta\psi(x), \tag{2.16}$$

where conventionally $r = 1$ and the operator Δ is the discretised covariant Laplacian

$$\Delta\psi(x) = \frac{1}{a^2}\sum_\mu\left[U_\mu(x)\psi(x+a\hat{\mu}) + U_\mu^\dagger(x-a\hat{\mu})\psi(x-a\hat{\mu}) - 2\psi(x)\right]. \tag{2.17}$$

This improvement term modifies the fermion matrix from Eq. (2.15) into

$$\begin{aligned} &M^W(x,y) \\ &\quad= (m+\frac{4}{a})\delta_{x,y} - \frac{1}{2a}\sum_\mu\left[(1-\gamma_\mu)U_\mu(x)\delta_{x+a\hat{\mu},y} - (1+\gamma_\mu)U_\mu^\dagger(x-a\hat{\mu})\delta_{x-a\hat{\mu},y}\right]. \end{aligned} \tag{2.18}$$

Additionally, a reparameterisation of the fermion fields in terms of the *hopping* parameters κ allows the matrix to be rewritten as

$$M^W(x,y) = \delta_{x,y} - \kappa H(x,y), \tag{2.19}$$

where H is the hopping matrix and κ the hopping parameter,

$$H(x,y) = \sum_\mu \left[(1-\gamma_\mu)U_\mu(x)\delta_{x+a\hat{\mu},y} - (1-\gamma_\mu)U_\mu^\dagger(x-a\hat{\mu})\delta_{x-a\hat{\mu},y}\right], \tag{2.20}$$

$$\kappa = \frac{1}{2(am+4)}. \tag{2.21}$$

Now if we consider the continuum limit of this action again the fermion doublers will obtain a contribution to their mass which is proportional to $1/a$, removing them from the theory. There will be one hopping parameter for each quark flavour in the theory, which are used to set the quark masses on the lattice.

Following the ‘no-go’ theorem, removing the fermion doublers in this manner necessarily requires breaking another symmetry, in this case the improved action will break chiral symmetry. This Wilson improved action will approach the continuum limit with corrections occurring at $\mathcal{O}(a)$. There are further improvements which can be made to the fermion action to remove these $\mathcal{O}(a)$ effects, these are outlined in the Symanzik improvement program [20]. In this work we will use the clover-improved fermion action [21], this action includes following additional term

$$S_F^C = c_{SW}a^5 \sum_x \sum_{\mu<\nu} \bar{\psi}(x)\frac{1}{2}\sigma_{\mu\nu}\hat{F}_{\mu\nu}(x)\psi(x), \tag{2.22}$$

where c_{SW} is the Sheikholeslami-Wohlert (clover) parameter, and $\hat{F}_{\mu\nu}(x)$ is a discretised version of the field strength tensor. To construct this discretisation we first define a *plaquette* as the smallest possible loop of link variables on the lattice

$$P_{\mu\nu}(x) = U_\mu(x)U_\nu(x+a\hat{\mu})U_\mu^\dagger(x+\hat{\nu})U_\nu^\dagger(x), \tag{2.23}$$

which is illustrated in figure 2.3. These plaquettes are then used to define the discretised field strength tensor as

$$\hat{F}_{\mu\nu}(x) = \frac{-i}{8a^2}\left(Q_{\mu\nu}(x) - Q_{\nu\mu}(x)\right), \tag{2.24}$$

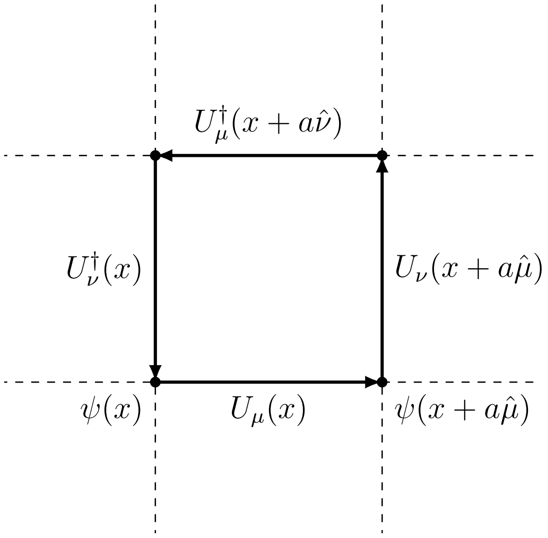

Figure 2.3. The plaquette which consists of the smallest connected loop of gauge links on the lattice.

where we use a sum over the plaquettes in the $\mu-\nu$ plane

$$Q_{\mu\nu}(x) = P_{\mu,\nu}(x) + P_{\nu,-\mu}(x) + P_{-\mu,-\nu}(x) + P_{-\nu,\mu}(x). \tag{2.25}$$

This clover-improved action can remove the $\mathcal{O}(a)$ effects if c_{SW} is tuned correctly, improving accuracy at finite values of a. Additionally this will improve convergence to the continuum limit as extrapolations are possible with respect to a^2.

2.5. Gluon action

The gluon action of QCD contains the field strength tensors, so to define a discretised version of it we will once again use the plaquettes defined in the previous section

$$P_{\mu\nu}(x) = U_\mu(x)U_\nu(x+a\hat{\mu})U^\dagger_\mu(x+\hat{\nu})U^\dagger_\nu(x). \tag{2.26}$$

The trace of any plaquette is gauge invariant (following from Eq. (2.12)) which is important when constructing the action. The Wilson gauge action is defined as the sum over all possible plaquettes on the lattice with each one having only one orientation

$$S_G[U] = \frac{6}{g^2}\sum_x\sum_{\mu<\nu}\mathrm{Re}\left\{\frac{1}{3}\mathrm{Tr}\left[1-P_{\mu\nu}(x)\right]\right\}. \tag{2.27}$$

The first factor is called the inverse coupling and is labelled by $\beta = 6/g^2$. This gluon action will approach the Yang-Mills action up to order $\mathcal{O}(a^2)$ in the continuum limit.

The gauge links can also be combined in shapes other than the square plaquette, these additional shapes can help with the construction of a gluon action which has an improved approach to the continuum limit. Constructing rectangles $R_{\mu\nu}$ and parallelograms $L_{\mu\nu}$ out of gauge links allows us to define the Lüscher-Weisz gluon action [22]

$$S_G^{LW}[U] = \frac{\beta}{3} \sum_{x,\mu<\nu} \left[c_0(1 - P_{\mu\nu}(x)) + c_1(1 - R_{\mu\nu}(x)) + c_2(1 - L_{\mu\nu}(x))\right], \tag{2.28}$$

this new gauge action is improved up to $\mathcal{O}(a^4)$. The coefficients c_i depend on g^2 and have to obey $c_0 + 8c_1 + 8c_2 = 1$, for the tree-level improved action used in this work the coefficients will be fixed to the following values

$$c_0 = \frac{20}{12}, \qquad c_1 = \frac{-1}{12}, \qquad c_2 = 0. \tag{2.29}$$

An alternative set of coefficients which is often used is the Iwasaki gauge action [23].

2.6. Numerical simulations

The discretisation of the QCD action above provides a regularisation of the Euclidean path integral. The path integral however is still defined over a large number of points and considering all gauge field configurations for this would require an impractical amount of computing power. For this reason, lattice QCD simulations rely on Monte Carlo (MC) techniques to estimate the path integral. To see how this works we consider the Euclidean path integral formulation of the expectation value of some operator

$$\langle \mathcal{O} \rangle = \frac{\int \mathcal{D}[U,\psi,\bar{\psi}]\, \mathcal{O}[U,\psi,\bar{\psi}]\, e^{-S[U,\psi,\bar{\psi}]}}{\int \mathcal{D}[U,\psi,\bar{\psi}]\, e^{-S[U,\psi,\bar{\psi}]}}, \tag{2.30}$$

where the operator can be a function of the gauge fields and fermion fields. The fermions in this formulation are represented by the Grassmann variables $\psi(x)$ and $\bar{\psi}(x)$. Splitting the exponential of the action into its fermionic and gluonic parts allows the fermionic part of the path integral to be integrated out

$$
\begin{aligned}
Z &= \int \mathcal{D}U e^{-S_G[U]}\, \mathcal{D}[\psi,\bar{\psi}] e^{-\sum_{x,y}\bar{\psi}(x)M(x,y)\psi(y)} \\
&= \int \mathcal{D}U e^{-S_G[U]}\, \det\left[M\right].
\end{aligned}
\tag{2.31}
$$

This determinant of the fermion matrix M is computationally expensive to calculate, which historically has led to many calculations setting it to be a constant value, which is called the *quenched* approximation. This approximation can be seen as removing all of the sea-quark interactions from the theory, although this is rarely used in modern lattice QCD simulations.

The Dirac operator M for the improved fermion action as described above will be γ_5-Hermitian, making its determinant a real number this means that the determinant will be real

$$
\det[M] = \det[\gamma_5 M^\dagger \gamma_5] = \det[\gamma_5^2]\det[M^\dagger] = \det[M]^*. \tag{2.32}
$$

This allows for the interpretation of $e^{S_G[U]}\det[M]$ as a probability distribution for each of the gauge field configurations U,

$$
\mathcal{P}(U) \propto \det[M] e^{-S_G[U]}. \tag{2.33}
$$

This probability distribution can be used together with importance sampling methods such as the Metropolis algorithm to generate an ensemble of gauge field configurations which can be used to estimate the path integral. This generation of configurations is often the most computationally expensive part of lattice QCD calculations and there is much active research into methods which can bring down this cost [24, 25] . Currently the most common approach involves the use of hybrid monte carlo (HMC) methods [26]. The path integral can now be redefined as an average of the operator evaluated on each of the gauge field configurations in such an ensemble

$$
\langle \mathcal{O} \rangle = \frac{1}{N_{\text{conf}}} \sum_{i=1}^{N_{\text{conf}}} \mathcal{O}(U_i). \tag{2.34}
$$

This method will provide us with an estimate of the path integral, which will improve in its precision with the size of the ensemble of gauge field configurations (N_{conf}) which is used.

Correlation functions

To calculate expectation values of operators constructed from quark fields, we will use Wick's theorem, which describes how quark propagators can be constructed by considering all possible Wick contractions of the quark fields. These quark propagators are defined as the inverse of the fermion matrix linking two points on the lattice

$$\sum_y S(z,y)^{\gamma\alpha}_{ca} M(y,x)^{\alpha\beta}_{ab} = \delta_{x,z}\delta_{c,b}\delta^{\gamma,\beta}, \tag{2.35}$$

where the greek indices (α,β,γ) are the dirac indices, the latin indices (a,b,c) are the colour indices and x,y,z are the lattice coordinates. The quark propagator $S(y,x)$ can be written in terms of the quark fields by considering all possible Wick contractions between them. For the example of two quark fields $\bar{\psi}(x)$ and $\psi(y)$, the propagator is written as

$$S(y,x)^{\gamma\alpha}_{ca} = \wick{\c{\psi}^{\gamma}_{c}(y)\c{\bar{\psi}}^{\alpha}_{a}}(x). \tag{2.36}$$

Where this propagator represents the amplitude of a quark propagating from the lattice site x to y. These Wick contractions remove the dependence on quarks as dynamical fields.

Using the two methods above, the expectation value of an operator can be written as a sum of the Wick-contracted fields on each configuration

$$\begin{aligned}\langle\mathcal{O}\rangle &= \frac{1}{Z}\int \mathcal{D}U \det[M] e^{-S_G[U]}\,\overset{\sqcap}{\mathcal{O}}[U] \\ &= \frac{1}{N_{\text{conf}}}\sum_{i=1}^{N_{\text{conf}}} \overset{\sqcap}{\mathcal{O}}[U_i].\end{aligned} \tag{2.37}$$

Where $\overset{\sqcap}{\mathcal{O}}[U]$ is the set of fully Wick contracted propagators formed from the fields in the operator $\mathcal{O}$.

2.7. Lattice Boundary Conditions

The fermion fields in the path integral formalism are Grassmann variables which means that they are anticommuting. To avoid boundary terms, the fermion fields are given periodic boundary conditions in the spatial dimensions, defined by

$$\psi(\vec{x} + aL\vec{e}_j) = \psi(\vec{x}), \tag{2.38}$$

for $j = 1, 2, 3$ and where L is the spatial extent of the lattice. The temporal boundary conditions meanwhile are set to be anti-periodic. The spatial periodicity makes the fields single-valued, however it can be shown that requiring the observables to be single-valued is sufficient [27, 28]. This allows for a complex phase to be included in the boundary conditions, as long as it is also a symmetry of the action. Introducing this phase into the boundary conditions is referred to as twisted boundary conditions, or partially twisted boundary conditions (pTBC) when this modification is restricted to the valence quarks. Consider redefining the valence quark field as follows

$$\psi_v(x) \equiv e^{i\vec{\theta}\cdot\vec{x}}\tilde{\psi}_v(x), \tag{2.39}$$

where $\tilde{\psi}_v(x)$ obeys the normal periodic boundary conditions. When using a correlation function constructed out of quark fields with these twisted boundary conditions, the momentum of the correlator will be modified by the $\vec{\theta}$ factor

$$\vec{p} = \frac{2\pi}{aL}\left(\vec{n} + \frac{\vec{\theta}}{2\pi}\right). \tag{2.40}$$

There are no restrictions on the values of $\vec{\theta}$, so applying these boundary conditions allows for much finer control over the momentum of the correlation functions than the usual discretised momentum values. This is very advantageous for calculations of form factors where the slope at small values of momentum is of interest [29–32]. The finite-volume effects of using partially twisted boundary conditions have been shown to be exponentially suppressed with the volume [27, 28, 33, 34]. These twisted boundary conditions will be used in the calculations presented in chapter 6.

2.8. Transfer Matrix

We have shown the path integral formalism of QCD, which together with the regularisation provided by the lattice allows for the numerical calculation of observables. In the Euclidean formulation this calculation can be done through the use of Monte Carlo techniques and importance sampling. This path integral formalism can be related to the same system described on a Hilbert space with a Hamiltonian, which in turn allows us to write down the energy spectrum of the observables [10].

In the Hamiltonian formalism, calculating the expectation value of an operator $\mathcal{O}$ involves taking the trace over the complete set of energy eigenstates,

$$\begin{aligned}\langle\mathcal{O}\rangle &= \frac{\mathrm{Tr}\left[e^{-HT}\mathcal{O}\right]}{\mathrm{Tr}\left[e^{-HT}\right]}\\ &= \frac{\sum_n \langle n|e^{-HT}\mathcal{O}|n\rangle}{\sum_n \langle n|e^{-HT}|n\rangle}\\ &= \frac{\sum_n e^{-E_nT}\langle n|\mathcal{O}|n\rangle}{\sum_n e^{-E_nT}}\\ &\xrightarrow{T\to\infty} \langle\Omega|\mathcal{O}|\Omega\rangle\,,\end{aligned} \tag{2.41}$$

where for large time the ground state will dominate the signal, we usually label this the vacuum state Ω.

We consider an operator $\hat{T}_\varphi$ on the full Hilbert space, then consider the trace of this operator over the space

$$\mathrm{Tr}(\hat{T}_\varphi^\beta) = \int d\varphi\,\langle\varphi|\hat{T}_\varphi^\beta|\varphi\rangle\,. \tag{2.42}$$

Now inserting a complete set of states in coordinate space at every timeslice,

$$\mathrm{Tr}(\hat{T}_\varphi^\beta) = \int\prod_x d\varphi(x)\,\langle\varphi_0|\hat{T}_\varphi|\varphi_{\beta-1}\rangle\ldots\langle\varphi_1|\hat{T}_\varphi|\varphi_0\rangle\,. \tag{2.43}$$

The operator $\hat{T}$ is defined by its matrix element,

$$\langle\varphi_{t+1}|\hat{T}|\varphi_t\rangle = e^{L[\varphi_{t+1},\varphi_t]}, \tag{2.44}$$

where $L[\varphi_{t+1},\varphi_t]$ is part of the temporally decomposed action connecting two adjacent timeslices. This decomposition is possible because we are dealing with a local action

$$S[\varphi] = \sum_t L[\phi_{t+1},\phi_t]. \tag{2.45}$$

If the transfer matrix as defined by Eq. (2.44) can be constructed, then it is possible to show it will have the following form [35]

$$\hat{T} = e^{-aH}, \tag{2.46}$$

where H is the Hamiltonian operator which describes the same system as the path integral formulation. This Hamiltonian will differ from the continuum Hamiltonian due to Discretisation effects. The previously mentioned improvements to the lattice action also serve to reduce this discrepancy between the two formalisms.

The existence of this transfer operator and its relation to the Hamiltonian guarantees that the correlation function of any combination of operators has a spectral representation. This is essential for the use of lattice QCD to determine energies and form factors of hadrons. The transfer matrix allows us to describe the Euclidean correlation functions on the lattice in terms of the energies of different states. This method is how lattice QCD makes it possible to calculate the energies of various hadrons. Consider the correlation function of two operators

$$C_\chi(t) \equiv \left\langle \chi(t)\chi^\dagger(0) \right\rangle, \tag{2.47}$$

where $\chi^\dagger(0)$ and $\chi(t)$ are a creation and annihilation operator respectively. Providing the action allows for the existence of a transfer matrix, we can write down this expression in terms of the trace over this transfer matrix,

$$\begin{aligned} C_\chi(t) &= \frac{\mathrm{Tr}\left[\, e^{-H(T-t)}\chi(0)e^{-Ht}\chi^\dagger(0)\right]}{\mathrm{Tr}\, e^{-HT}} \\ &= \frac{\sum_n \langle n|e^{-H(T-t)}\chi(0)e^{-Ht}\chi^\dagger(0)|n\rangle}{\sum_m \langle m|e^{-HT}|m\rangle} \\ &= \frac{\sum_n e^{-E_n(T-t)}\langle n|\chi(0)e^{-Ht}\chi^\dagger(0)|n\rangle}{\sum_m e^{-E_m T}} \\ &= \langle \Omega|\chi(0)e^{-Ht}\chi^\dagger(0)|\Omega\rangle\,. \end{aligned} \tag{2.48}$$

This transfer matrix formalism will be essential for the application of the Feynman-Hellmann method to transition matrix elements presented in chapter 6.

Chapter 3.

Hadronic Observables

3.1. Two-point Correlation Functions

In the previous section we have shown that the lattice formulation of the expectation value of a combination of operators has a spectral decomposition. We will outline the exact expressions for these spectra here, as well as the methods and techniques applied to analyse them. For lattice QCD calculations we will consider a two-point correlation function projected onto some definite momentum state. We start by considering a two-point correlation function constructed out of a creation operator $\bar{\chi}$ and an annihilation operator χ. Using the translational invariance of the operators we can consider the creation operator to be at the origin, while we sum over the spatial coordinates of the annihilation operator to project the correlator onto a definite momentum state,

$$G_H(t,\vec{p}) = \sum_{\vec{x}} e^{-i\vec{p}\cdot\vec{x}} \left\langle \chi_H(t,\vec{x}\,)\bar{\chi}_H(0)\right\rangle , \tag{3.1}$$

we illustrate this two-point function in figure 3.1.

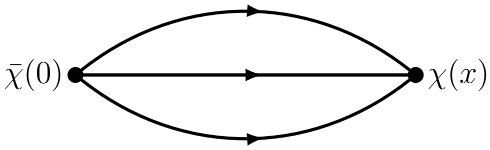

Figure 3.1. A diagram of a baryon two-point function constructed from the creation and annihilation operators $\bar{\chi}(0)$ and $\chi(x)$ respectively.

The two interpolating operators are products of local quark fields, constructed such that they overlap with the ground state of the desired hadron. For example for a baryon these interpolating operators could look like

$$\chi_B(x)^\alpha = \epsilon_{abc}[q(x)]^\alpha_a \left([q(x)]^\beta_b \Gamma^{\beta\gamma} [q(x)]^\gamma_c \right) , \tag{3.2}$$

where the indices a, b, c are colour indices, α, β, γ are Dirac indices and Γ is a γ_4-hermitian matrix. In order to extract the spectrum of this correlator we need to define a set of complete states of the QCD Hamiltonian

$$H \left| X(\vec{p}) \right\rangle = E_X(\vec{p}) \left| X(\vec{p}) \right\rangle . \tag{3.3}$$

We define the complete set of eigenstates of the QCD Hamiltonian as

$$1 = \sum_{X,\vec{k},s} \frac{\Delta^3 k}{(2\pi)^3} \frac{1}{2E_X(\vec{k}\,)} \left| X, \vec{k}, s \right\rangle \left\langle X, \vec{k}, s \right| , \tag{3.4}$$

where $\Delta^3 k$ are the discrete elements of the momentum space and we will neglect the explicit sum over spin indices for simplicity until they become relevant in the example in the next section. We will also use the translational invariance property of the operators defined on the lattice

$$\chi(\vec{x}, t) = e^{\hat{H}t} e^{-i\hat{p}\cdot\vec{x}} \chi(0) e^{-\hat{H}t} e^{i\hat{p}\cdot\vec{x}} . \tag{3.5}$$

By inserting a complete set of states into the correlation function we are able to extract the time-dependence,

$$\begin{aligned} G_H(t, \vec{p}) &= \sum_{X,\vec{k}} \frac{\Delta^3 k}{(2\pi)^3} \sum_{\vec{x}} \frac{e^{-i\vec{p}\cdot\vec{x}}}{2E_X(\vec{k}\,)} \langle \Omega | \chi_H(0) e^{-\hat{H}t} e^{i\hat{p}\cdot\vec{x}} \left| X, \vec{k} \right\rangle \left\langle X, \vec{k} \right| \bar{\chi}_H(0) | \Omega \rangle \\ &= \sum_{X,\vec{k}} \frac{\Delta^3 k}{(2\pi)^3} \sum_{\vec{x}} \frac{e^{-i(\vec{p}-\vec{k}\,)\cdot\vec{x}} e^{-E_X(\vec{k}\,)t}}{2E_X(\vec{k}\,)} \langle \Omega | \chi_H(0) \left| X, \vec{k} \right\rangle \left\langle X, \vec{k} \right| \bar{\chi}_H(0) | \Omega \rangle . \end{aligned} \tag{3.6}$$

We now use $\sum_{\vec{x}} e^{-i(\vec{p}-\vec{k}\,)\cdot\vec{x}} = V\delta_{\vec{p},\vec{k}}$ to project onto a definite momentum state after summing over $\vec{x}$ and $\vec{k}$,

$$G_H(t, \vec{p}) = \sum_X \frac{e^{-E_X(\vec{p})t}}{2E_X(\vec{p})} \langle \Omega | \chi_H(0) \left| X, \vec{p} \right\rangle \left\langle X, \vec{p} \right| \bar{\chi}_H(0) | \Omega \rangle . \tag{3.7}$$

To simplify this expression somewhat we will use the following notation

$$G_H(t,\vec{p}) = \sum_X g^{(2)}_\chi[X;\vec{p}]e^{-E_X(\vec{p})t}, \tag{3.8}$$

where we define

$$g^{(2)}_\chi[X;\vec{p}] = \frac{\langle\Omega|\chi_H(0)\,|X,\vec{p}\rangle\,\langle X,\vec{p}|\,\bar{\chi}_H(0)|\Omega\rangle}{2E_X(\vec{p})}. \tag{3.9}$$

These expressions show that the two-point functions have a time-dependence which is proportional to the sum of the exponentiated energies of all possible states which couple to the operators. Since the states in the sum will have different energies, we expect that at large times, the state with the lowest energy (ground state) will come to dominate the signal

$$G_H(t,\vec{p}) \xrightarrow{t\gg 0} g^{(2)}_\chi[X_0;\vec{p}]e^{-E_{X_0}(\vec{p})t}. \tag{3.10}$$

This holds under the assumption that the temporal size of the lattice is sufficiently large ($T\to\infty$). This spectral expression of the correlation function is the central property which allows lattice calculations to extract the energy of hadronic states.

3.1.1. Nucleon Energy

The interpolating operator used to construct a proton on the lattice is defined as

$$\chi_N(x)_\alpha = \epsilon^{abc}[u(x)]^a_\alpha\left([u(x)]^b_\beta[C\gamma_5]_{\beta\gamma}[d(x)]^c_\gamma\right). \tag{3.11}$$

This operator has a spin degree of freedom and the anti-symmetric tensor ϵ^{abc} makes it antisymmetric in colour. Constructing a two-point function out of these operators will introduce this spin degree of freedom into the overlap factors. Therefore, the overlap of the interpolating operators with the states X can be defined in terms of spinors u and overlap factors Z,

$$\langle\Omega|\chi_\alpha(0)|X(\vec{p},s)\rangle = Z_{\chi,X}(\vec{p})u_\alpha(p,s), \tag{3.12}$$

$$\langle X(\vec{p},s)|\bar{\chi}_\alpha(0)|\Omega\rangle = \bar{Z}_{X,\bar{\chi}}(\vec{p})\bar{u}_\alpha(p,s) = Z^*_{\chi,X}(\vec{p})\bar{u}_\alpha(p,s). \tag{3.13}$$

The convention for our spinors are set by

$$\sum_s u(p,s)\bar{u}(p,s) = \frac{\gamma_\mu p^\mu + M}{2E(\vec{p})}. \tag{3.14}$$

The spin degree of freedom in this expression requires us to include the sum over the spin indices in the complete set of states again

$$G_N^{\alpha\beta}(t,\vec{p}) = \sum_{X,s} \frac{e^{-E_X(\vec{p})t}}{2E_X(\vec{p})} Z_{\chi_N,X}(\vec{p})\bar{Z}_{X,\chi_N^\dagger}(\vec{p})u^\alpha(p,s)\bar{u}^\beta(p,s). \tag{3.15}$$

Now the resulting correlation function has two free Dirac indices, for the calculations in this thesis we are mainly interested in a projection of the two-point function onto some definite spin and parity state. To achieve this we contract the indices with a projection matrix $\Gamma_{\alpha\beta}$,

$$\begin{aligned} G_N(t,\vec{p},\Gamma) &= \sum_{X,s} \frac{e^{-E_X(\vec{p})t}}{2E_X(\vec{p})} |Z_{\chi,X}(\vec{p})|^2 \Gamma_{\beta\alpha} u_\alpha(p,s)\bar{u}_\beta(p,s) \\ &= \sum_X 2\frac{e^{-E_X(\vec{p})t}}{E_X(\vec{p})} |Z_{\chi,X}(\vec{p})|^2 F_2(\Gamma,\vec{p},m), \end{aligned} \tag{3.16}$$

where we have defined the trace over the projection matrix and spinors as

$$F_2(\Gamma,\vec{p},m) = \frac{1}{4}\sum_s \mathrm{Tr}[\Gamma\, u(p,s)\bar{u}(p,s)]. \tag{3.17}$$

The most common projections are the unpolarised and polarised projections,

$$\Gamma_{\text{unpol}} = \frac{1}{2}(\mathbb{1}+\gamma_4), \qquad \Gamma^j_{\text{pol}\pm} = \frac{1}{2}(\mathbb{1}+\gamma_4)\frac{1}{2}(\mathbb{1}\pm i\gamma_5\gamma_j), \tag{3.18}$$

where j is the chosen spin-polarisation axis. As an example, the unpolarised projection of the two-point function of a nucleon at rest, considered in the large Euclidean time limit,

$$G_N(t,\vec{p},\Gamma_{\text{unpol.}}) \xrightarrow{t\gg 0} |Z_N(\vec{p})|^2 \frac{E_N(\vec{p})+M_N}{E_N(\vec{p})} e^{-E_N(\vec{p})t}. \tag{3.19}$$

To visualise the dominant energy scale of the correlation function as a function of time, we can construct the effective energy as

$$E_{\text{eff.}}(t) = \frac{1}{\Delta t} \ln \left[\frac{G(t)}{G(t+\Delta t)} \right] , \tag{3.20}$$

where Δt is often set to unity. For large euclidean times, this will trend towards to the ground state energy of the correlation function

$$E_{\text{eff.}}(t) \xrightarrow{t \gg 0} E_N(\vec{p}) . \tag{3.21}$$

We will use this effective energy as a visual aid in determining the region where the ground state dominates the signal of the correlation function.

3.1.2. Signal to Noise Ratio

For the precise determination of hadronic spectra from lattice QCD, it is necessary to understand the origin of the noise present in the correlation functions and its behaviour as a function of time. We will consider the correlation function of a nucleon as defined in Eq. (3.16) and rewrite it as the gauge average over a combination of operators $C(t)$

$$G_N(t) = \langle C_N(t) \rangle = \sum_{\vec{x}} \Gamma \left\langle \chi_N(\vec{x}, t) \bar{\chi}_N(\vec{0}, 0) \right\rangle . \tag{3.22}$$

The variance of a nucleon two-point function can be expressed as

$$\begin{aligned} N_{\text{calc}} \sigma_N^2(t) \approx & \left\langle C_N(t) C_N^\dagger(t) \right\rangle - \left\langle C_N(t) \right\rangle^2 \\ = & \sum_{\vec{x}, \vec{y}} \Gamma\Gamma \left\langle \chi_N(\vec{x}, t) \bar{\chi}_N(\vec{y}, t) \chi_N(\vec{0}, 0) \bar{\chi}_N(\vec{0}, 0) \right\rangle \\ & \qquad - \sum_{\vec{x}} \Gamma\Gamma \left\langle \chi_N(\vec{x}, t) \bar{\chi}_N(\vec{0}, 0) \right\rangle^2 , \end{aligned} \tag{3.23}$$

where N_{calc} is the number of independent calculations [36]. By evaluating these two expectation values and considering all possible quark contractions it is possible to show their spectral decompositions

$$\left\langle |C_N(t)|^2 \right\rangle \approx Z_{3\pi}^2 e^{-3 m_\pi t} + Z_{N\bar{N}}^2 e^{-2 M_N t} + \ldots \tag{3.24}$$

$$\left\langle C_N(t) \right\rangle^2 \approx Z_N^4 e^{-2 M_N t} + \ldots \tag{3.25}$$

As indicated by the first term in Eq. (3.24), it turns out that the quark fields in the first expectation value can be Wick-contracted to form a three-pion state, which will have a lower energy than the two-nucleon state. This difference in time-dependences in the variance is called Parisi-Lepage scaling [36, 37]. Thus for large time values we expect the variance of the nucleon two-point function to be dominated by the three-pion state

$$\begin{aligned} N_{\text{calc}}\sigma_N^2(t) &\approx Z_{N\bar{N}}^2 e^{-2M_N t} - Z_N^4 e^{-2M_N t} + Z_{3\pi}^2 e^{-3m_\pi t} + \ldots \\ &\xrightarrow{t\gg 0} Z_{3\pi}^2 e^{-3m_\pi t}. \end{aligned} \tag{3.26}$$

Using this variance function we define the numerical Signal-to-Noise (StN) ratio as

$$\mathcal{S}(t) = \frac{\langle C_N(t)\rangle}{\sigma_N(t)} \xrightarrow{t\gg 0} \sqrt{N_{\text{calc}}}\,\frac{Z_N^2}{Z_{3\pi}}\,e^{-(m_N-\frac{3}{2}m_\pi)t}. \tag{3.27}$$

The rate at which this ratio decreases will depend on the gap in energy between the two-nucleon state and the three-pion state which contribute to the variance [38, 39]. It is important to note that this scaling of the StN ratio will only occur at large Euclidean times, at smaller time values the overlap factors Z play an important role in the behaviour of the StN ratio.

In the variance function, the three-meson state which can be constructed from the four nucleon interpolating operators depends on combinations of the quark operators in the two sink operators $\chi_N(\vec{x}, t)$ and $\bar{\chi}_N(\vec{y}, t)$. The overlap of this state will be heavily suppressed when these two operators do not overlap within a volume which is approximately the size of the Compton wavelength of the pion. Since Eq. (3.23) contains independent sums over $\vec{x}$ and $\vec{y}$, this suppression of $Z_{3\pi}$ compared to $Z_{N\bar{N}}$ and Z_N^2 scales with the spatial lattice volume [40]. This suppression will be present for any meson state in the variance function, thus for small time values we expect the variance function to be dominated by the overlap factors of the two-nucleon states. The meson states are only expected to start dominating the variance at large values of time, at which point the Parisi-Lepage scaling from Eq. (3.27) holds. Before this is the case the Singal-to-Noise ratio will have minimal time-dependence and will scale only with N_{calc},

$$\mathcal{S}(t) \propto \sqrt{N_{\text{calc}}}. \tag{3.28}$$

The nucleon correlation function itself will usually become dominated by its ground state long before Parisi-Lepage scaling starts to apply. Depending on the lattice volume it is possible that contributions from 'thermal states' will degrade the signal before Parisi-

Lepage scaling applies, these are states which propagate backwards from the source. The time-region in the correlation function where the ground state is dominant and the StN scaling is relatively time-independent is most useful for the accurate determination of the energy of the nucleon.

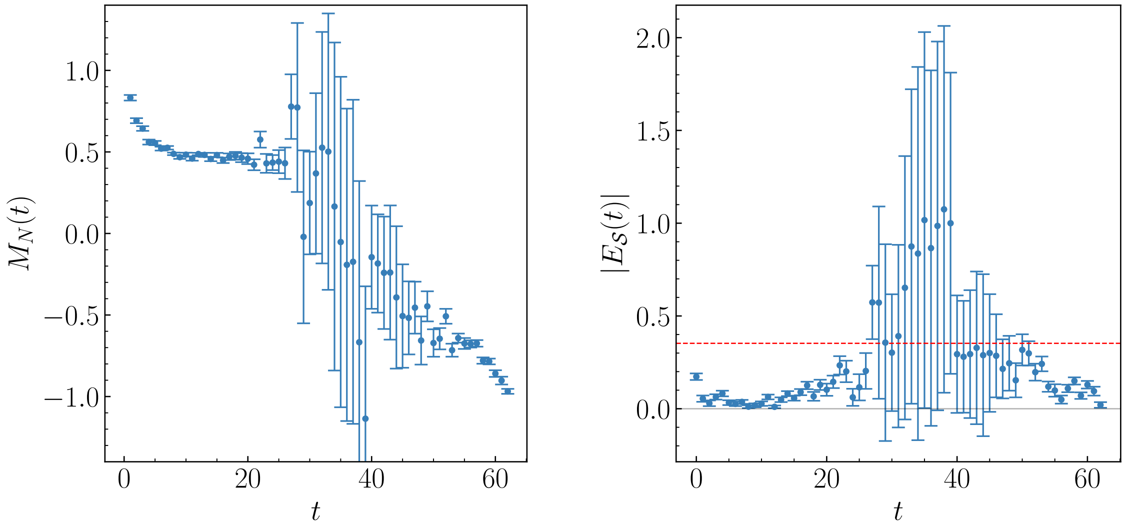

Figure 3.2. The effective energy of a nucleon two-point correlator (left), and the energy scale of the Signal-to-Noise ratio as defined in Eq. (3.29). The red dotted line indicates the expected energy scale for Parisi-Lepage scaling $m_N - \frac{3}{2}m_\pi$.

To illustrate the behaviour of the StN ratio for nucleon correlators we will define the effective energy of the StN ratio,

$$E_{\mathcal{S}}(t) = \ln\left(\frac{\mathcal{S}(t)}{\mathcal{S}(t+1)}\right). \tag{3.29}$$

This function can be interpreted as the energy scale which dominates the StN ratio, at large times we expect this to trend towards the Parisi-Lepage energy scale. Figure 3.2 shows the effective mass of a nucleon correlator on the left as well as the energy scale of the StN ratio on the right. The effective energy in the left hand figure shows a plateau region from timeslice $t = 10$, this indicates that the nucleon ground state dominates the correlation function. From approximately timeslice $t = 26$ we can see that the noise in the correlator increases markedly, indicating that we are in the Parisi-Lepage scaling regime. Looking at the effective StN energy scale in the figure on the right we can confirm this as the red dotted line shows the energy scale associated with Parisi-Lepage scaling and we see that around timeslice $t = 26$, the energy scale starts to agree with the red dotted line. The calculations in this work will focus on making the best use of the signal in the early timeslices before Parisi-Lepage scaling, where the StN ratio is relatively independent of time.

3.1.3. Correlator Analysis

Using the knowledge of the Signal-to-Noise behaviour of nucleon correlation functions, we know that the early time values are particularly valuable for obtaining a clear signal. This is why we will apply analysis techniques which will allow us to make use of as much of the early timeslices as possible. The effective energy as defined in Eq. (3.20) will trend towards a constant value at large times. We identify this with the energy of the ground state coupling to the interpolating operators. Before this asymptotic behaviour however, the correlation function will have significant contributions from excited states with larger energies than the ground state. The left hand figure of 3.2 shows this effective energy and we can see that there is a plateau behaviour around $t = [10, 25]$. A simplified expression of the correlation function spectrum is

$$G(\vec{p}, t, \Gamma) = A_0 e^{-E_0 t} + A_1 e^{-E_1 t} + ..., \tag{3.30}$$

where we define $A_i = g_X^{(2)}[X_i; \vec{p}]$ which contains the overlap factors for the state X_i. A straightforward approach to determine the energy of the ground state is to truncate the above expression after the first term and use it to fit to the correlator in the plateau region. However this method leaves out a significant number of early timeslices in which the Signal-to-Noise ratio is excellent but the ground state is not dominant. To make use of these additional timeslices we will also fit to the correlation function with two terms in the expression in Eq. (3.30).

The effective energy figure does not give any indication of the time window in which the two lowest-energy states are dominant contributions to the signal, this means that there could be a lot of bias through the choice of fit window. To avoid this bias, we use both ansätze to fit to the correlation function over a wide range of fit windows, and then use a weighted averaging procedure to produce one result for the ground state energy. The largest timeslice which can be included in the fit window is relatively straightforward to determine by looking at the effective mass and the Signal-to-Noise ratio of the correlation functions, therefore to vary the fit windows we include a range of different starting points.

3.1.4. Weighted Average of Fits

The weighted averaging shown here uses a modified inverse variance weighting to establish a weight for each fit [41]. The fits which are included in the averaging procedure are from both the fit functions and for variations in the time-window for both. The weight depends on the χ^2 value of the fit and has an inverse dependence on the variance of the fitted energy parameter. The weight corresponding to fit f is defined as

$$\tilde{w}^f = \frac{p_f \left(\delta E_0^f\right)^{-2}}{\sum_{f'=1}^{N} p_{f'} \left(\delta E_0^{f'}\right)^{-2}}, \tag{3.31}$$

where p_f is the p-value of the fit f and δE_0^f is the uncertainty in the ground state energy of fit f. The p-value is defined as

$$p_f = \frac{\Gamma(N_{\text{dof}}/2, \chi_f^2/2)}{\Gamma(N_{\text{dof}}/2)}, \tag{3.32}$$

where $\Gamma(z)$ is the gamma function and $\Gamma(s, x)$ is the upper incomplete gamma function. Using these weights we can calculate the weighted average and the corresponding uncertainties as follows:

$$\bar{E}_0 = \sum_{f=1}^{N} w^f E_0^f, \tag{3.33}$$

$$\delta_{\text{stat}} \bar{E}_0{}^2 = \sum_{f=1}^{N} w^f (\delta E_0^f)^2, \tag{3.34}$$

$$\delta_{\text{sys}} \bar{E}_0{}^2 = \sum_{f=1}^{N} w^f (E_0^f - \bar{E}_0)^2, \tag{3.35}$$

$$\delta \bar{E}_0 = \sqrt{\delta_{\text{stat}} \bar{E}_0{}^2 + \delta_{\text{sys}} \bar{E}_0{}^2}, \tag{3.36}$$

where N is the total number of fits. This method can be applied to multiple fit ansätze as well as variations over the fit window, to minimise the effects of the systematic uncertainties we will not include every fit window.

3.1.5. Baryon Masses

We apply the above analysis methods to the determination of the masses of baryons on a large set of the lattice ensembles generated by the QCDSF-UKQCD-CSSM collaboration, the details of which are shown in Appendix C. The aim of this was to provide an improved determination of the energies which could be applied consistently across multiple lattice sizes and specifications. To visualise the weighted average procedure we show the results of the fits to the nucleon correlation function on a $24^3 \times 48$ lattice in figure 3.3. The figure shows the starting point of the fit window on the x-axis, the ground state energy with uncertainties for each fit on the left y-axis and the weight for each fit on the right y-axis. For all the fits shown here the end-point of the fit window was fixed to $t_{\text{max}} = 24$, after this timeslice, it determined that the noise started to dominate over the signal by looking at the effective mass. The fit results for a range of t_{min} values are included for both of the ansätze, this range was chosen to be as broad as possible without including

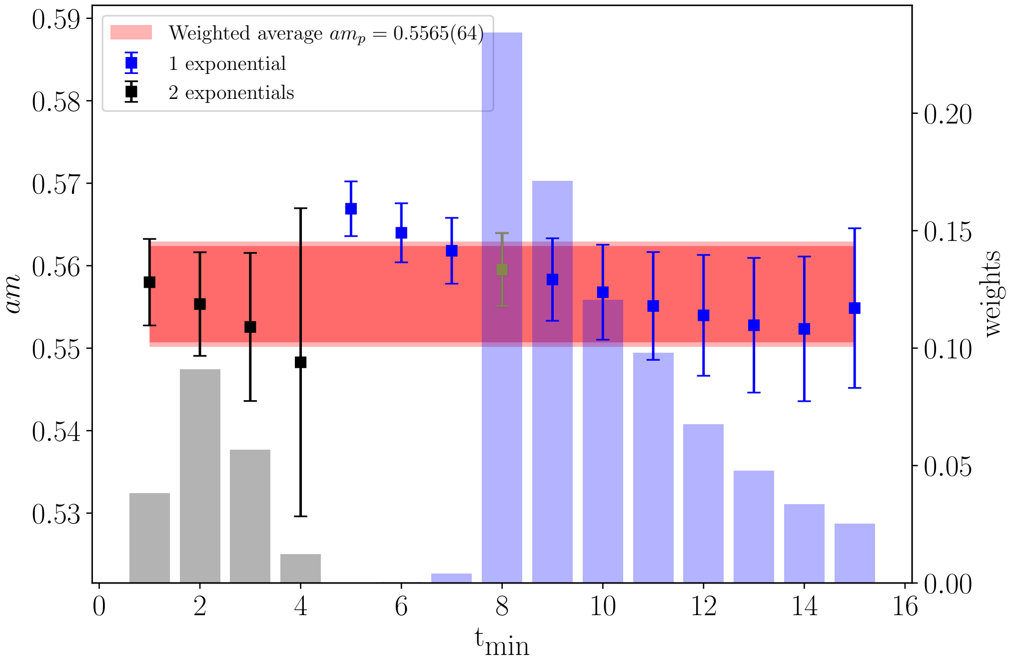

Figure 3.3. On the left-hand axis the mass of the nucleon in lattice units is shown for two different ansätze and a range of $t_{\text{min.}}$ values. The right-hand axis (bar plot) shows the respective weights of each of the fits. The red band shows the weighted average, the inner band shows the statistical uncertainties, the outer band shows the combined statistical and systematic uncertainties. The result shown in green highlights the fit with the highest weighting. The results here are from the $24^3 \times 48$ lattice with $\beta = 5.40$ and $(\kappa_l, \kappa_s) = (0.119820, 0.119820)$.

any 'poor fits'. Fits with very large uncertainties have also been excluded from the figure and the weighted average. The green point indicates that the one-exponential fit starting at $t_{\text{min}} = 8$ has the highest weighting, however some of the fits using the two-exponential ansatz contribute significantly to the average as well. The dark red band in the figure shows the value of the weighted average with statistical uncertainties, while the lighter red band shows the size of the combined uncertainty to the weighted average. The combined uncertainty also includes the systematic uncertainty due to the inclusion of the two ansätze as well as the different fit windows. As expected there is good agreement between the band and the highly-weighted fit results. We also note that there is a difference between the highest weighted one-exponential fit and the highest weighted two-exponential fit. This method allows for a more consistent determination of baryon energies which does not rely on a manual choice of fit window.

The full results of applying this analysis method to the baryon correlation function on all the lattice ensembles are shown in Appendix C, together with the previous determination of the energy using a single 'plateau' fit as comparison.

3.2. Three-point Correlation Functions

A lattice three-point function is defined using two interpolation operators and a current insertion. Starting with the path integral representation of this three-operator expectation value, we can again derive a spectral representation through the existence of a transfer matrix,

$$\begin{aligned} C_{B'\mathcal{O}B}(x,y) &= \langle \chi_{B'}(x)\mathcal{O}(y)\bar{\chi}_B(0)\rangle & (3.37)\\ &= \frac{1}{Z}\int DU\,\det[M]\chi_{B'}(x)\mathcal{O}(y)\bar{\chi}_B(0)\,e^{-S_G[U]}, & (3.38)\end{aligned}$$

where we use the symmetry of the lattice to position the creation operator at the origin. The two interpolating operators χ_B and $\chi_{B'}$ do not necessarily have to be the same as this can also describe transitions between hadrons. If the temporal lattice size is sufficiently large, the transfer matrix will pick out the vacuum state

$$C_{B'\mathcal{O}B}(x,y) = \langle\Omega|\chi_{B'}(x)\mathcal{O}(y)\bar{\chi}_B(0)|\Omega\rangle\,. \tag{3.39}$$

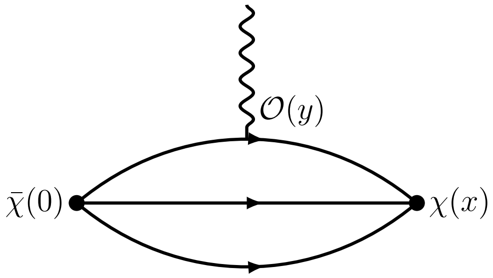

Figure 3.4. A diagram of a three-point function constructed from the creation and annihilation operators $\bar{\chi}(0)$ and $\chi(x)$ respectively and a current insertion $\mathcal{O}(y)$.

The Fourier projected three-point function is then defined as

$$G_{B'\mathcal{O}B}(\vec{p}\,', t; \vec{q}, \tau) = \sum_{\vec{x},\vec{y}} e^{-i\vec{p}\,'\cdot\vec{x}} e^{i\vec{q}\cdot\vec{y}} \langle\Omega|\chi_{B'}(\vec{x},t)\mathcal{O}(\vec{y},\tau)\bar{\chi}_B(\vec{0},0)|\Omega\rangle \,, \tag{3.40}$$

where $\vec{q}$ is the momentum inserted by the current operator. Now inserting two complete sets of states into the expression (with the spinor argument suppressed)

$$\begin{aligned} G_{B'\mathcal{O}B}(\vec{p}\,', t; \vec{q}, \tau) = \sum_{\substack{X,r\\Y,s}} \sum_{\vec{x},\vec{y}} \frac{e^{-i\vec{p}\,'\cdot\vec{x}} e^{i\vec{q}\cdot\vec{y}}}{4E_X E_Y} \langle\Omega|\chi_{B'}(x)|X(p_X)\rangle \\ \langle X(p_X)|\mathcal{O}(y)|Y(p_Y)\rangle \; \langle Y(p_Y)|\bar{\chi}_B(0)|\Omega\rangle \,, \end{aligned} \tag{3.41}$$

and using the translational invariance of the operators allows us to project the momenta through the sum over $\vec{x}$ and $\vec{y}$

$$\begin{aligned} G_{B'\mathcal{O}B}(\vec{p}\,', t; \vec{q}, \tau) &= \sum_{\substack{X,r\\Y,s}} \sum_{\vec{x},\vec{y}} \frac{e^{-i\vec{p}\,'\cdot\vec{x}}}{2E_X} \frac{e^{i\vec{q}\cdot\vec{y}}}{2E_Y} \langle\Omega|\chi_{B'}(0) e^{i\hat{p}\cdot\vec{x}} e^{-\hat{H}t}|X(\vec{p}_X)\rangle \\ &\qquad \langle X(\vec{p}_X)|e^{-i\hat{p}\cdot\vec{y}} e^{\hat{H}\tau} \mathcal{O}(0) e^{i\hat{p}\cdot\vec{y}} e^{-\hat{H}\tau}|Y(\vec{p}_Y)\rangle \; \langle Y(\vec{p}_Y)|\bar{\chi}_B(0)|\Omega\rangle \\ &= \sum_{\substack{X,r\\Y,s}} \sum_{\vec{x},\vec{y}} \frac{e^{-i\vec{x}\cdot(\vec{p}\,'-\vec{p}_X)}}{2E_X} \frac{e^{-i\vec{y}\cdot((\vec{p}_X-\vec{p}_Y)-\vec{q})}}{2E_Y} e^{-E_X(\vec{p}_X)t} e^{-(E_Y(\vec{p}_Y)-E_X(\vec{p}_X))\tau} \\ &\qquad \langle\Omega|\chi_{B'}(0)|X(p_X)\rangle \; \langle X(p_X)|\mathcal{O}(0)|Y(p_Y)\rangle \; \langle Y(p_Y)|\bar{\chi}_B(0)|\Omega\rangle \,. \end{aligned} \tag{3.42}$$

The sum over $\vec{x}$ and $\vec{y}$ combined with the exponentials will now project the momenta as $\vec{p}_X = \vec{p}\,'$ and $\vec{p}_Y = \vec{p}\,' - \vec{q} = \vec{p}$, leading to

$$\begin{aligned} G_{B'\mathcal{O}B}(\vec{p}\,', t; \vec{q}, \tau) = \sum_{\substack{X,r\\Y,s}} \frac{e^{-E_X(\vec{p}\,')(t-\tau)} e^{-E_Y(\vec{p})\tau}}{4E_X E_Y} \\ \langle\Omega|\chi_{B'}(0)|X(\vec{p}\,')\rangle \, \langle X(\vec{p}\,')|\mathcal{O}(0)|Y(\vec{p})\rangle \, \langle Y(\vec{p})|\bar{\chi}_B(0)|\Omega\rangle \,. \end{aligned} \tag{3.43}$$

The time dependence of this expression is now fully contained in the energy exponentials. combining these with the sum over states X and Y will result in only the lowest-energy state remaining for sufficiently large values of τ and $t - \tau$. In this case we label these ground states B and B'

$$\begin{aligned} G_{B'\mathcal{O}B}(\vec{p}\,', t; \vec{q}, \tau) \xrightarrow{t,\tau \gg 0} \sum_{r,s} \frac{e^{-E_{B'}(\vec{p}\,')(t-\tau)} e^{-E_B(\vec{p})\tau}}{4E_{B'}(\vec{p}\,') E_B(\vec{p})} \\ \langle\Omega|\chi_{B'}(0)|B'(\vec{p}\,')\rangle \, \langle B'(\vec{p}\,')|\mathcal{O}(0)|B(\vec{p})\rangle \, \langle B(\vec{p})|\bar{\chi}_B(0)|\Omega\rangle \,. \end{aligned} \tag{3.44}$$

Now we can write the overlap factors in terms of spinors and Z-factors as in Eq. (3.12), while the matrix element of interest can also be decomposed into form factors and spinors. We combine this with a projection of the correlator onto a definite polarisation using the projection matrix Γ,

$$\begin{aligned} G_{B'\mathcal{O}B}(\Gamma, \vec{p}\,', t; \vec{q}, \tau) = \frac{e^{-E_{B'}(\vec{p}\,')(t-\tau)} e^{-E_B(\vec{p})\tau}}{4E_{B'}(\vec{p}\,') E_B(\vec{p})} Z_{B'B'}(\vec{p}\,') \bar{Z}_{B\bar{B}}(\vec{p}) \\ \times \sum_{r,s} \mathrm{Tr} \left\{ \Gamma \, u_{B'}(p', r) \bar{u}_{B'}(p', r) \mathcal{J}(q^2) u_B(p, s) \bar{u}_B(p, s) \right\} , \end{aligned} \tag{3.45}$$

here $\mathcal{J}(q^2)$ is a combination of form factors which describes the operator $\mathcal{O}$. The sum over the spin states can be combined with the spinors in the trace to get the expression

$$\begin{aligned} G_{B'\mathcal{O}B}(\Gamma, \vec{p}\,', t; \vec{q}, \tau) = \sum_{E_{B'}, E_B} \frac{e^{-E_{B'}(\vec{p}\,')(t-\tau)} e^{-E_B(\vec{p})\tau}}{E_{B'}(\vec{p}\,') E_B(\vec{p})} Z_{B'B'}(\vec{p}\,') \bar{Z}_{B\bar{B}}(\vec{p}) \\ \times F_3(\Gamma, \mathcal{J}_{\mathcal{O}}, \vec{p}\,', \vec{q}, m_{B'}, m_B), \end{aligned} \tag{3.46}$$

where we have defined

$$F_3(\Gamma, \mathcal{J}_{\mathcal{O}}, \vec{p}\,', \vec{q}, m_{B'}, m_B) = \frac{1}{4} \sum_{r,s} \mathrm{Tr} \left\{ \Gamma \, u_{B'}(p', r) \bar{u}_{B'}(p', r) \mathcal{J}_{\mathcal{O}}(q^2) u_B(p, s) \bar{u}_B(p, s) \right\} . \tag{3.47}$$

This function will yield different combinations of form factors depending on the current and projection matrix.

3.2.1. Ratio of Correlation Functions

To extract the value of the matrix element, we have to deal with the time-dependence of the three-point function. It is possible to fit the three-point function itself, however this requires determining two separate time-dependences. More commonly a ratio of three-point and two-point functions is constructed such that the time-dependence cancels out in the large time limit. Since the three-point function depends on two Euclidean time distances, we expect this ratio to show the correct value as a plateau when the operator insertion time is approximately halfway between the source and the sink. Consider the three-point function for large Euclidean times $(\tau, t-\tau)$, then the ground state will dominate the signal

$$\begin{aligned} G_{B'\mathcal{O}B}(\vec{p}\,', t; \vec{q}, \tau) \xrightarrow{t,\tau\gg 0} & \frac{e^{-E_{B_0'}(\vec{p}\,')(t-\tau)} e^{-E_{B_0}(\vec{p}\,)\tau}}{E_{B_0'} E_{B_0}} Z_{B'B_0'}(\vec{p}\,') \bar{Z}_{B_0\bar{B}}(\vec{p}\,) \\ & \times F_3(\Gamma, \mathcal{J}_{\mathcal{O}}, \vec{p}\,', \vec{q}, m_{B'}, m_B). \end{aligned} \tag{3.48}$$

We define the ratio of three-point and two-point functions as

$$R(\Gamma, \mathcal{O}; t, \tau; \vec{p}\,', \vec{p}\,) = \frac{G_{B'\mathcal{O}B}(\Gamma; \vec{p}\,', t; \vec{q}, \tau)}{G_{B'}(t, \vec{p}\,')} \sqrt{\frac{G_{B'}(\tau, \vec{p}\,') G_{B'}(t, \vec{p}\,') G_B(t-\tau, \vec{p}\,)}{G_B(\tau, \vec{p}\,) G_B(t, \vec{p}\,) G_{B'}(t-\tau, \vec{p}\,')}}. \tag{3.49}$$

In the simple case of a forward matrix element between two of the same baryons at rest, this ratio reduces

$$\begin{aligned} R(\Gamma, \mathcal{O}; t, \tau; \vec{0}, \vec{0}\,) &= \frac{G_{B\mathcal{O}B}(\Gamma; \vec{0}, t; \vec{0}, \tau)}{G_B(t, \vec{0}\,)} \\ &\xrightarrow{t,\tau\gg 0} \frac{F_3(\Gamma, \mathcal{J}_{\mathcal{O}}, \vec{0}, \vec{0}, m_B, m_B)}{2m_B^2}. \end{aligned} \tag{3.50}$$

In this large Euclidean time limit there will be no more time-dependence, so we expect a plateau region to show up at these times. In practical lattice QCD calculations it is not always feasible to accumulate sufficient statistics to get a clear signal at large enough Euclidean times. Therefore it is useful to explore the contributions to the signal by the excited states. These contributions can be included explicitly in the analysis of the signal to improve the extraction of the matrix elements.

3.3. Error Analysis

Using the Monte Carlo approach to estimating the path integral makes the lattice QCD calculations feasible on modern computers. The expectation value of the operator is defined as the average across all gauge field configurations in the ensemble. To estimate the uncertainty of this evaluation would require the generation of multiple independent ensembles of gauge configurations over which the statistical variation of the observable could be examined. This would increase the computational cost of the calculation. To avoid this additional cost, lattice QCD calculations use resampling methods to determine the uncertainties, such as the bootstrap, or jack-knife methods.

In this work we will be using the bootstrap resampling method for this purpose [42]. To obtain an estimate for the uncertainty of an observable, firstly the observable is calculated on a set of N_{conf} field configurations. From this set of evaluations of the observable, a new set of N_{conf} is sampled with replacement. This resampling with replacement is repeated N_{boot} times, and the average of the observable over the resampled set is saved. If the number of resamples is sufficiently large, the new set of N_{boot} estimates of the observable will then have a normal distribution which is used to determine the uncertainty in the observable. This method produces reliable estimates of the uncertainty only if the initial set of N_{conf} samples is representative of the entire population, which is ensured by the gauge field generation process in lattice QCD.

For an observable $\mathcal{O}$, which has been evaluated on N_{boot} sets of resampled field configurations, the average and the variance are then defined as

$$\overline{\mathcal{O}} \equiv \frac{1}{N_{\text{boot}}} \sum_{i=1}^{N_{\text{boot}}} \mathcal{O}_i \tag{3.51}$$

$$\sigma_{\mathcal{O}}^2 \equiv \frac{1}{N_{\text{boot}}} \sum_{i=1}^{N_{\text{boot}}} \left(\mathcal{O}_i - \overline{\mathcal{O}}\right)^2 . \tag{3.52}$$

In this work we will use $N_{\text{boot}} = 500$ resamplings for all calculations.

Chapter 4.

Feynman-Hellmann Method

The Feynman-Hellmann theorem was first applied in quantum mechanics where it describes a relation between matrix elements and variations in the energy spectrum [43–46]. The theorem states that when a perturbation proportional to λ is made to the Hamiltonian of a system, then the shift in the energy can be related to the matrix element of that perturbation. Taking a Hamiltonan $H = H_0 + \lambda H_\lambda$ which depends on a continuous parameter λ, then the derivative of the energy of its eigenstate ψ with respect to λ can be expressed as

$$\left.\frac{\partial E}{\partial \lambda}\right|_{\lambda=0} = \langle \psi | H_\lambda | \psi \rangle_{\lambda=0} \,. \tag{4.1}$$

This method has been applied to lattice QCD calculation in many forms. It's main strength comes from the fact that the calculation of a hadron spectrum is computationally cheaper than that of matrix elements in lattice QCD. The most straightforward application of this theorem in lattice QCD is for nucleon sigma terms [47–53], as these can be determined from the matrix elements of the scalar currents. These calculations are valuable for the interpretation of dark matter direct detection experiments. In this case the perturbation is taken to be a parameter in the model itself, namely the quark masses. However the perturbation can just as well come from an introduced parameter, this is how the Feynman-Hellmann method has been applied to the calculation of hadronic matrix elements in lattice QCD [54–59].

Other applications in lattice QCD include calculations of the nucleon isovector charges [60, 61], determinations of the gluon component of momentum in the nucleon [62, 63] and quark contributions to the nucleon's spin [54]. Higher order extensions of the Feynman-

Hellmann method have been successfully applied to the calculation of the Compton amplitude and moments of the generalised parton distributions [64–67].

4.1. Path-Integral approach

The Feynman-Hellmann method relates the value of a matrix element to the derivative of the energy. We will consider the effect of a modified QCD action, which we define as $S(\lambda) = S_0 + S_\lambda$. Consider a two-point function defined in the presence of this modified action,

$$C_\lambda(t;\vec{p}) = {}_\lambda\langle \tilde{\chi}(t;\vec{p})\bar{\chi}(0;\vec{0}\,)\rangle_\lambda\,, \tag{4.2}$$

where we define the momentum-projected interpolating operator as

$$\tilde{\chi}(t;\vec{p}\,) = \sum_{\vec{x}} e^{-i\vec{p}\cdot\vec{x}}\chi(t,\vec{x}\,). \tag{4.3}$$

In the path integral formalism the correlation function takes the following form

$$C_\lambda(t;\vec{p}\,) = \frac{1}{\mathcal{Z}_\lambda}\int \mathcal{D}U\,\tilde{\chi}(t;\vec{p}\,)\bar{\chi}(0)e^{-S(\lambda)}, \tag{4.4}$$

where the partition function is

$$\mathcal{Z}_\lambda = \int \mathcal{D}U\,e^{-S(\lambda)}, \tag{4.5}$$

and we use $\mathcal{D}U$ to represent the integrand of all the field operators of the theory.

To consider the application of the Feynman-Hellmann method in lattice QCD we start by taking the partial derivative of the correlation function with respect to the parameter λ, evaluated at $\lambda = 0$,

$$\begin{aligned}\left.\frac{\partial C_\lambda}{\partial\lambda}\right|_{\lambda=0} &= \frac{1}{\mathcal{Z}}\int \mathcal{D}U\,\tilde{\chi}(t;\vec{p}\,)\bar{\chi}(0)e^{-S_0}\frac{1}{\mathcal{Z}}\int \mathcal{D}U\,\frac{\partial S}{\partial\lambda}e^{-S_0} - \frac{1}{\mathcal{Z}}\int \mathcal{D}U\,\tilde{\chi}(t;\vec{p}\,)\bar{\chi}(0)\frac{\partial S}{\partial\lambda}e^{-S_0}\\ &= \langle\tilde{\chi}(t;\vec{p}\,)\bar{\chi}(0)\rangle\left\langle\frac{\partial S}{\partial\lambda}\right\rangle - \left\langle T\left\{\tilde{\chi}(t;\vec{p}\,)\bar{\chi}(0)\frac{\partial S}{\partial\lambda}\right\}\right\rangle,\end{aligned} \tag{4.6}$$

where T indicates the time-ordered product of the operators.

Similarly we can take the derivative of the spectral representation of the two-point function as defined in Eq. (3.8). Noting that both the energy and the overlap factor will now depend on λ, we can write the derivative as

$$\left.\frac{\partial C_\lambda}{\partial \lambda}\right|_{\lambda=0} = \sum_X \left[\left.\frac{\partial g_X^{(2)}[X,\vec{p},\lambda]}{\partial \lambda}\right|_{\lambda=0} - t\,\left.\frac{\partial E_X(\vec{p},\lambda)}{\partial \lambda}\right|_{\lambda=0} g_X^{(2)}[X,\vec{p},0]\right] e^{-E_X(\vec{p},0)t}. \tag{4.7}$$

Here we see that the term which contains the derivative of the energy will be time-enhanced. We will use this to match up terms from the derivative of the path-integral expression.

The modification to the action is defined as an operator projected onto a specific momentum value

$$\begin{aligned} S(\lambda) &= S_0 + \lambda_i \int dt \sum \Delta^3 x\, e^{i\vec{q}_i\cdot\vec{x}}\, j_i(x) \\ &= S_0 + \lambda_i \int dt\, \mathcal{J}_i(t;\vec{q}_i\,), \end{aligned} \tag{4.8}$$

where we define $\mathcal{J}_i(t;\vec{q}\,) = \sum_{\vec{x}} \Delta^3 x\, e^{i\vec{q}_i\cdot\vec{x}}\, j_i(t,\vec{x}\,)$, and we note that we consider only currents with zero vacuum expectation values. The subscript i indicates that we can consider multiple modifications each with their own momentum projection. We consider the theory for continuous time for now as this is sufficient to produce a discrete spectrum on the lattice.

Using this action, the derivative of the correlation function in Eq. (4.6) becomes

$$\left.\frac{\partial C_\lambda}{\partial \lambda}\right|_{\lambda=0} = C(t) \int dt'\, \langle \mathcal{J}(t';\vec{q}\,)\rangle - \int dt'\, \langle T\{\tilde{\chi}(t;\vec{p}\,)\mathcal{J}(t';\vec{q}\,)\bar{\chi}(0)\}\rangle\,. \tag{4.9}$$

The first term here is proportional to the vacuum expectation value of the current operator, which will be zero in most cases. The second term will need to be considered for the various time-orderings. To calculate the contributions from the various time-ordering regions we will rewrite the equation for discretised Euclidean time,

$$\begin{aligned} \int_{-\infty}^{\infty} dt'\, \langle T\{\tilde{\chi}(t;\vec{p}\,)\mathcal{J}(t';\vec{q}\,)\bar{\chi}(0)\}\rangle = &\int_{t}^{\infty} dt'\, \langle \mathcal{J}(t';\vec{q}\,)\tilde{\chi}(t)\bar{\chi}(0)\rangle \\ &+ \int_{0}^{t} dt'\, \langle \tilde{\chi}(t)\mathcal{J}(t';\vec{q}\,)\bar{\chi}(0)\rangle \\ &+ \int_{-\infty}^{0} dt'\, \langle \tilde{\chi}(t)\bar{\chi}(0)\mathcal{J}(t';\vec{q}\,)\rangle\,. \end{aligned} \tag{4.10}$$

The second time-ordering contains the matrix element of interest, where the current is inserted between the two interpolating operators. The other two time-orderings contain three-point functions where the current operator will create or destroy a meson before or after the interpolating operators.

Central Time-ordering

Firstly we consider the time-ordering ($0 < t' < t$) which contains the matrix element of interest. We will start by inserting two complete sets of states into the correlation function

$$\begin{aligned}\int_0^t dt' \, \langle \tilde{\chi}(t;\vec{p})\mathcal{J}(t';\vec{q})\bar{\chi}(0)\rangle = \int_0^t dt' \sum_{\substack{X,\vec{p}_X\\ Y,\vec{p}_Y}} \frac{\Delta^3\vec{p}_X}{(2\pi)^3}\frac{\Delta^3\vec{p}_Y}{(2\pi)^3}\frac{1}{4E_X(\vec{p}_X)E_Y(\vec{p}_Y)} \\ * \, \langle\Omega|\tilde{\chi}(t;\vec{p})\,|X(\vec{p}_X)\rangle\,\langle X(\vec{p}_X)|\,\mathcal{J}(t';\vec{q})\,|Y(\vec{p}_Y)\rangle\,\langle Y(\vec{p}_Y)|\,\bar{\chi}(0)|\Omega\rangle\,.\end{aligned} \tag{4.11}$$

Using the translational invariance of the operators allows us to extract the time dependence

$$\begin{aligned}\int_0^t dt' \sum_{\substack{X,\vec{p}_X\\ Y,\vec{p}_Y}} \sum_{\vec{x},\vec{y}} \frac{\Delta^3\vec{p}_X}{(2\pi)^3}\frac{\Delta^3\vec{p}_Y}{(2\pi)^3}\Delta^3\vec{x}\,\Delta^3\vec{y}\, e^{-i(\vec{p}-\vec{p}_X)\cdot\vec{x}}e^{i(\vec{q}-\vec{p}_X+\vec{p}_Y)\cdot\vec{y}}e^{-E_X(\vec{p}_X)t} \\ * \, \frac{e^{-(E_Y(\vec{p}_Y)-E_X(\vec{p}_X))t'}}{4E_X(\vec{p}_X)E_Y(\vec{p}_Y)}\,\langle\Omega|\chi(0)\,|X(\vec{p}_X)\rangle\,\langle X(\vec{p}_X)|\,j(0)\,|Y(\vec{p}_Y)\rangle\,\langle Y(\vec{p}_Y)|\,\bar{\chi}(0)|\Omega\rangle\,.\end{aligned} \tag{4.12}$$

Summing over the spatial coordinates gives delta functions in momentum which determine the momenta of the states to be $\vec{p}_X = \vec{p}$ and $\vec{p}_Y = \vec{p} - \vec{q} \equiv \vec{p}\,'$

$$\begin{aligned}\int_0^t dt' \sum_{X,Y} \frac{e^{-E_X(\vec{p})t}}{4E_X(\vec{p})E_Y(\vec{p}\,')}e^{-(E_Y(\vec{p}\,')-E_X(\vec{p}))t'}\,\langle\Omega|\chi(0)|X(\vec{p})\rangle \\ * \, \langle X(\vec{p})|j(0)|Y(\vec{p}\,')\rangle\,\langle Y(\vec{p}\,')|\bar{\chi}(0)|\Omega\rangle\,.\end{aligned} \tag{4.13}$$

To solve the integral over t', we will first split the sum over all states into a set of energy-degenerate states and non-degenerate states since the difference in energies in the exponential will vanish for energy-degenerate states. The split integral becomes

$$\int_0^t dt' \Bigg[\sum_{\substack{X,Y\\ E_X=E_Y}} \frac{e^{-E_X(\vec{p})t}}{4E_X^2(\vec{p})} \langle\Omega|\chi(0)|X(\vec{p})\rangle \langle X(\vec{p})|j(0)|Y(\vec{p}\,')\rangle \langle Y(\vec{p}\,')|\bar{\chi}(0)|\Omega\rangle \\ + \sum_{\substack{X,Y\\ E_X\neq E_Y}} \frac{e^{-E_X(\vec{p})t}e^{-(E_Y(\vec{p}\,')-E_X(\vec{p}))t'}}{4E_X(\vec{p})E_Y(\vec{p}\,')} \langle\Omega|\chi(0)|X(\vec{p})\rangle \langle X(\vec{p})|j(0)|Y(\vec{p}\,')\rangle \langle Y(\vec{p}\,')|\bar{\chi}(0)|\Omega\rangle \Bigg]. \tag{4.14}$$

Which, after evaluating the integral, shows that the term with energy-degenerate states will be time-enhanced

$$\sum_{\substack{X,Y\\ E_X=E_Y}} t\,\frac{e^{-E_X(\vec{p})t}}{4E_X^2(\vec{p})} \langle\Omega|\chi(0)|X(\vec{p})\rangle \langle X(\vec{p})|j(0)|Y(\vec{p}\,')\rangle \langle Y(\vec{p}\,')|\bar{\chi}(0)|\Omega\rangle \\ + \sum_{\substack{X,Y\\ E_X\neq E_Y}} \Bigg[\frac{e^{-E_Y(\vec{p}\,')t} - e^{-E_X(\vec{p})t}}{4E_X(\vec{p})E_Y(\vec{p}\,')(E_X(\vec{p}) - E_Y(\vec{p}\,'))} \langle\Omega|\chi(0)|X(\vec{p})\rangle \\ * \langle X(\vec{p})|j(0)|Y(\vec{p}\,')\rangle \langle Y(\vec{p}\,')|\bar{\chi}(0)|\Omega\rangle \Bigg]. \tag{4.15}$$

Other Time-orderings

Now consider the integral over the first time region ($t < t' < \infty$). Inserting two complete sets of states and extracting the time-dependence gives

$$\int_t^\infty dt' \langle \mathcal{J}(t';\vec{q})\tilde{\chi}(t;\vec{p})\bar{\chi}(0)\rangle \\ = \int_t^\infty dt' \sum_{\substack{X,\vec{p}_X\\ Y,\vec{p}_Y}} \frac{1}{4E_XE_Y} \langle\Omega|\mathcal{J}(t';\vec{q})|X(\vec{p}_X)\rangle \langle X(\vec{p}_X)|\chi(t;\vec{p})|Y(\vec{p}_Y)\rangle \langle Y(\vec{p}_Y)|\bar{\chi}(0)|\Omega\rangle \\ = \int_t^\infty dt' \sum_{X,Y} \frac{e^{-E_Xt'}e^{E_Xt}e^{-E_Yt}}{4E_XE_Y} \sum_{\vec{x},\vec{y}} \sum_{\vec{p}_X,\vec{p}_Y} e^{-i\vec{y}\cdot(-\vec{p}_X-\vec{q})}e^{-i\vec{x}\cdot(\vec{p}_Y-\vec{p}_X-\vec{p})} \\ * \langle\Omega|j(0)|X(\vec{p}_X)\rangle \langle X(\vec{p}_X)|\chi(0)|Y(\vec{p}_Y)\rangle \langle Y(\vec{p}_Y)|\bar{\chi}(0)|\Omega\rangle\,. \tag{4.16}$$

Once again we use the spatial and momentum-space sums to determine the momenta to be $\vec{p}_X = -\vec{q}$ and $\vec{p}_Y = \vec{p} - \vec{q} \equiv \vec{p}\,'$,

$$\begin{aligned}\sum_{X,Y}\frac{e^{-(E_Y-E_X)t}}{4E_XE_Y}\sum_{\vec{p}_X,\vec{p}_Y}\delta^{(3)}(\vec{p}_X+\vec{q})\delta^{(3)}(\vec{p}_Y-\vec{p}_X-\vec{q})\int_t^\infty dt' e^{-E_X t'}\\ * \langle\Omega|j(0)|X(\vec{p}_X)\rangle\,\langle X(\vec{p}_X)|\chi(0)|Y(\vec{p}_Y)\rangle\,\langle Y(\vec{p}_Y)|\bar{\chi}(0)|\Omega\rangle\,.\end{aligned} \tag{4.17}$$

Solving the integral gives

$$\begin{aligned}&\int_t^\infty dt'\,\langle\mathcal{J}(t';\vec{q})\chi(t;\vec{p})\bar{\chi}(0)\rangle\\ &\qquad=\sum_{X,Y}\frac{e^{-E_Y(\vec{p}\,')t}}{4E_X^2E_Y}\,\langle\Omega|j(0)|X(-\vec{q})\rangle\,\langle X(-\vec{q})|\chi(0)|Y(\vec{p}\,')\rangle\,\langle Y(\vec{p}\,')|\bar{\chi}(0)|\Omega\rangle\,.\end{aligned} \tag{4.18}$$

The last time-ordering with the integral over $(-\infty < t' < 0)$ gives a similar result

$$\begin{aligned}&\int_{-\infty}^0 dt'\,\langle\chi(t;\vec{p})\bar{\chi}(0)\mathcal{J}(t';\vec{q})\rangle\\ &\qquad=\sum_{X,Y}\frac{e^{-E_Y(\vec{p})t}}{4E_X^2E_Y}\,\langle\Omega|\chi(0)|Y(\vec{p})\rangle\,\langle Y(\vec{p})|\bar{\chi}(0)|X(\vec{q})\rangle\,\langle X(\vec{q})|j(0)|\Omega\rangle\,.\end{aligned} \tag{4.19}$$

Both of these expressions have a similar exponential time dependence and importantly they do not contain the time-enhancement which will be used to extract the matrix element.

4.1.1. Forward Matrix Elements

To show how this method can be used to determine the value of matrix elements we will first consider the forward case where there is no momentum transfer between the states $(\vec{p}\,' = \vec{p})$. The expressions for the derivative of the two-point correlation function in Eq. (4.7) and Eq. (4.9) are equal for all times, allowing us to match the time-enhanced terms in both expressions. We consider both expressions in the large time limit where it can be assumed that the ground state dominates the signal and all other states are exponentially suppressed, we label the ground state N here. We note that for the forward case, the energy degeneracy requirement in Eq. (4.15) reduces to a requirement that the states be identical $X = Y = N$. Combining the time-enhanced terms from Eq. (4.7) and Eq.

(4.15) gives

$$\begin{aligned}\left.\frac{\partial E_N(\vec{p},\lambda)}{\partial\lambda}\right|_{\lambda=0} & \frac{e^{-E_N(\vec{p})t}}{2E_N(\vec{p})}\,\langle\Omega|\chi(0)|N(\vec{p})\rangle\,\langle N(\vec{p})|\bar{\chi}(0)|\Omega\rangle \\ &= \frac{e^{-E_N(\vec{p})t}}{4E_N^2(\vec{p})}\,\langle\Omega|\chi(0)|N(\vec{p})\rangle\,\langle N(\vec{p})|j(0)|N(\vec{p})\rangle\,\langle N(\vec{p})|\bar{\chi}(0)|\Omega\rangle\,,\end{aligned} \tag{4.20}$$

which reduces to

$$\left.\frac{\partial E_N(\vec{p},\lambda)}{\partial\lambda}\right|_{\lambda=0} = \frac{1}{2E_N(\vec{p})}\,\langle N(\vec{p})|j(0)|N(\vec{p})\rangle\,. \tag{4.21}$$

This expression now relates the change in the energy of the state due to the perturbation in the action to the value of the matrix element. The particular interest of this expression for lattice QCD stems from the fact that calculations of the spectrum of states are much simpler than those of matrix elements. This relation then allows for a determination of matrix elements which relies only on the calculation of the spectrum of the perturbed system.

4.1.2. Off-forward Matrix Elements

To extend the Feynman-Hellmann method to the calculation of off-forward matrix elements between two matching baryons, a momentum projection will be added to the modification of the QCD action. We will consider a current insertion which contains both signs of the momentum transfer $\vec{q}$, to retain its Hermitian properties

$$S(\lambda) = S_0 + \lambda\sum_x \Delta^4 x\,(e^{i\vec{q}\cdot\vec{x}} + e^{-i\vec{q}\cdot\vec{x}})j(x), \tag{4.22}$$

where $j(x) = \bar{q}(x)\Gamma q(x)$ and Γ is any Dirac matrix.

To derive an expression relating the energy shift to the matrix element, we will have to deal with the fact that our standard set of states is no longer an eigenstate of the modified Hamiltonian as there will be mixing between the different momentum-spin states with degenerate energies. To be able to take the derivative of the correlator we must first find the states which diagonalise the modified Hamiltonian. The new set of eigenstates are determined by the operator $j(x)$ and how it couples to the momentum and spin states, we will consider both the temporal and the spatial vector currents in this section.

Temporal Vector Current

The temporal vector current $\mathcal{V}_4(x)$ is defined by the fourth gamma matrix between two quark fields of flavour f,

$$\mathcal{V}_4^f(x) = \bar{q}_f(x)\gamma_4 q_f(x). \tag{4.23}$$

For two baryon states which are in the Breit frame with non-zero energy transfer such that $\vec{p}_r = \pm\vec{p}_s$, we write the matrix element of this current as

$$\langle X(\vec{p}_r, \sigma_r)|\mathcal{V}_4^f(0)|X(\vec{p}_s, \sigma_s)\rangle = \begin{bmatrix} 0 & 1 \\ 1 & 0 \end{bmatrix}_{rs} 2M_X\, G_{E,X}^f(Q^2)\, \delta_{\sigma_r\sigma_s}, \tag{4.24}$$

where the matrix is in momentum-space. Diagonalising this matrix gives two eigenvectors (e_j) with corresponding eigenvalues (μ_j)

$$e_+ = \begin{bmatrix} +\frac{1}{\sqrt{2}} \\ +\frac{1}{\sqrt{2}} \end{bmatrix}, \qquad \mu_+ = +2M_X\, G_{E,X}^f(Q^2), \tag{4.25}$$

$$e_- = \begin{bmatrix} +\frac{1}{\sqrt{2}} \\ -\frac{1}{\sqrt{2}} \end{bmatrix}, \qquad \mu_- = -2M_X\, G_{E,X}^f(Q^2). \tag{4.26}$$

Using these eigenvectors we can construct new energy eigenstates

$$|X_+(\vec{p})\rangle = \frac{1}{\sqrt{2}}\big[\,|X(\vec{p})\rangle + |X(-\vec{p})\rangle\,\big], \tag{4.27}$$

$$|X_-(\vec{p})\rangle = \frac{1}{\sqrt{2}}\big[\,|X(\vec{p})\rangle - |X(-\vec{p})\rangle\,\big]. \tag{4.28}$$

These states are combined to form a expression for the identity

$$I = \sum_{X,|\vec{k}|,\sigma} \sum_j \frac{\Delta^3 k}{(2\pi)^3} \frac{|X_j(\vec{k},\sigma)\rangle\, \langle X_j(\vec{k},\sigma)|}{\langle X_j(\vec{k},\sigma)|X_j(\vec{k},\sigma)\rangle}. \tag{4.29}$$

When inserting this complete set of states into the two-point function it is important to note that the nature of the lattice calculation does not allow us to easily choose an arbitrary combination of momentum states at the source, these will be determined by the sink momentum projection and momentum conservation. The sum over all momenta in the correlator will pick out the $X_+(\vec{p})$ combination naturally, thus we will consider the expression using this combination of states,

$$G_\lambda(t;\vec{p},\lambda) = \sum_X \frac{e^{-E_{X_+}(\vec{p})t}}{2E_{X_+}(\vec{p})} \langle\Omega|\chi(0)|X_+(\vec{p})\rangle \; \langle X_+(\vec{p})|\bar{\chi}(0)|\Omega\rangle \,. \tag{4.30}$$

Considering the derivative of this correlator, we can once again match the time-enhanced part to the expression in Eq. (4.15),

$$\begin{aligned}
&\sum_X \frac{\partial E_{X_+}(\vec{p},\lambda)}{\partial\lambda}\bigg|_{\lambda=0} \frac{e^{-E_{X_+}(\vec{p})t}}{2E_{X_+}(\vec{p})} \langle\Omega|\chi(0)|X_+(\vec{p})\rangle \; \langle X_+(\vec{p})|\bar{\chi}(0)|\Omega\rangle \\
&\qquad = \sum_{\substack{X \\ |\vec{p}|=|\vec{p}\,'|}} \frac{e^{-E_{X_+}(\vec{p})t}}{4E^2_{X_+}(\vec{p})} \langle\Omega|\chi(0)|X_+(\vec{p})\rangle \; \langle X_+(\vec{p})|\mathcal{V}^f_4(0)|X_+(\vec{p}\,')\rangle \; \langle X_+(\vec{p}\,')|\bar{\chi}(0)|\Omega\rangle \,.
\end{aligned} \tag{4.31}$$

Taking the large Euclidean time limit for this expression reduces both sides to their ground states and gives us an expression between the matrix element of the baryon and the energy shift

$$\begin{aligned}
\frac{\partial E_{B_+}(\vec{p},\lambda)}{\partial\lambda}\bigg|_{\lambda=0} &= \frac{1}{2E_{B_+}(\vec{p})} \langle B_+(\vec{p})|\mathcal{V}^f_4(0)|B_+(\vec{p}\,')\rangle \\
&= \frac{M_B}{E_{B_+}(\vec{p})} G^f_{E,B}(Q^2).
\end{aligned} \tag{4.32}$$

This relation will only be valid in the Breit frame where $\vec{p}\,' = -\vec{p} = \pm\vec{q}/2$. This limits the accessible lattice momenta for this method, however using the Breit frame will minimise the initial and final momenta $(\vec{p},\vec{p}\,')$ for each value of Q^2. These values of momenta will improve the quality of the signal which is beneficial for calculations of matrix elements at high momenta.

Spatial Vector Current

The spatial vector current is defined as before but with a spatial gamma matrix, for this example we shall choose γ_2,

$$\mathcal{V}^f_2(x) = \bar{q}_f(x)\gamma_2 q_f(x). \tag{4.33}$$

For the spatial vector current to produce a real energy shift we require the current to be imaginary. For the numerical simulations in this thesis however, we will use a real operator which we can show allows us to more easily isolate one of the Hamiltonian eigenstates, allowing for a simpler analysis of the correlators.

We consider the matrix element of this current between two Breit frame momentum-spin states ($|\vec{p}_r| = |\vec{p}_s| \equiv |\vec{p}\,|$),

$$\frac{\langle X(\vec{p}_r,\sigma_r)|\mathcal{V}_2^f(\vec{q})|X(\vec{p}_s,\sigma_s)\rangle}{\langle X(\vec{p})|X(\vec{p})\rangle} = \frac{G^f_{M,X}(Q^2)}{2E_X(\vec{p})}\begin{bmatrix} 0 & 0 & -q_1 & q_3 \\ 0 & 0 & q_3 & q_1 \\ q_1 & -q_3 & 0 & 0 \\ -q_3 & -q_1 & 0 & 0 \end{bmatrix}_{r,\sigma_r,s\sigma_s}, \tag{4.34}$$

where the r and s indices are for momentum space and the σ_r, σ_s indices for spin space. Since this matrix has a non-trivial spin dependence, the diagonalisation will result in four eigenvectors ($e_{j\sigma}$), with two distinct eigenvalues (μ_j)

$$\begin{aligned} e_{++} &= \begin{bmatrix} 1 \\ 0 \\ \frac{iq_1}{\sqrt{q_1^2+q_3^2}} \\ \frac{-iq_3}{\sqrt{q_1^2+q_3^2}} \end{bmatrix}, & e_{-+} &= \begin{bmatrix} 1 \\ 0 \\ \frac{-iq_1}{\sqrt{q_1^2+q_3^2}} \\ \frac{iq_3}{\sqrt{q_1^2+q_3^2}} \end{bmatrix}, \\ e_{+-} &= \begin{bmatrix} 0 \\ 1 \\ \frac{-iq_3}{\sqrt{q_1^2+q_3^2}} \\ \frac{-iq_1}{\sqrt{q_1^2+q_3^2}} \end{bmatrix}, & e_{--} &= \begin{bmatrix} 0 \\ 1 \\ \frac{iq_3}{\sqrt{q_1^2+q_3^2}} \\ \frac{iq_1}{\sqrt{q_1^2+q_3^2}} \end{bmatrix}, \end{aligned} \tag{4.35}$$

$$\mu_{(\pm)} = \pm i\lambda\sqrt{q_1^2+q_3^2}\,\frac{G^f_{M,X}(Q^2)}{2E_B(\vec{p})}, \tag{4.36}$$

where once again the index j spans momentum space and σ spans spin space.

This set of eigenvalues complicates the situation as it becomes difficult to construct a correlation function which couples only to one energy eigenstate and not the other. None of these eigenvalues contain a combination of momentum states as straightforward as for the temporal current. The two-point function constructed with this perturbation will couple to both energy eigenstates, and will not isolate just one energy exponential as for the temporal current. By expanding the transfer matrix for small λ and by writing the matrix element in Eq. (4.34) in terms of the eigenvectors and eigenvalues we get the following expression

$$G_\lambda(\vec{p}_r,t,\Gamma^3_\pm)=\frac{E_B+M_B}{E_B}|Z(\vec{p})|^2\begin{bmatrix}(1\pm\frac{iq_1}{\sqrt{q_1^2+q_3^2}})e^{-E_B^{(+)}(\lambda)t}+(1\mp\frac{iq_1}{\sqrt{q_1^2+q_3^2}})e^{-E_B^{(-)}(\lambda)t}\\(1\mp\frac{iq_1}{\sqrt{q_1^2+q_3^2}})e^{-E_B^{(+)}(\lambda)t}+(1\pm\frac{iq_1}{\sqrt{q_1^2+q_3^2}})e^{-E_B^{(-)}(\lambda)t}\end{bmatrix}_r, \tag{4.37}$$

where

$$E_B^{(\pm)}(\vec{p},\lambda)=E_B(\vec{p})\pm\mu_{(j)}, \tag{4.38}$$

and the correlator is defined as a vector in the momentum space which contains $(+\vec{q}/2,-\vec{q}/2)$ with the index being r. More details on this expansion are included in Appendix B and a more general form of this approach to the Feynman-Hellmann method is derived in chapter 6.

Since the eigenvectors in Eq. (4.36) are imaginary, they can be seen as a phase shift to the terms of correlator in Eq. (4.37), we can expand this phase shift for small values of λt to get an expression for the real shift to the energy,

$$\begin{aligned}e^{-E_B^{(\pm)}(\lambda)t}&=e^{-E_Bt}\left[e^{\mp i\lambda\sqrt{q_1^2+q_3^2}\,\frac{G^f_{M,B}(Q^2)}{2E_B}t}\right]\\&\approx e^{-E_Bt}\left[1\mp i\lambda\,t\sqrt{q_1^2+q_3^2}\,\frac{G^f_{M,B}(Q^2)}{2E_B}+\mathcal{O}(\lambda^2t^2)\right].\end{aligned} \tag{4.39}$$

Inserting this back into (4.37) gives

$$\begin{aligned}G_\lambda(\vec{p}_r,t,\Gamma^3_\pm)&=\frac{E_B+M_B}{E_B}|Z(\vec{p})|^2\begin{bmatrix}e^{-E_Bt}\left(1\mp\lambda\,t\,q_1\frac{G^f_{M,B}(Q^2)}{2E_B}\right)\\e^{-E_Bt}\left(1\pm\lambda\,t\,q_1\frac{G^f_{M,B}(Q^2)}{2E_B}\right)\end{bmatrix}_r\\&=\frac{E_B+M_B}{E_B}|Z(\vec{p})|^2\begin{bmatrix}e^{-\left(E_B(\vec{p})\pm\frac{\lambda q_1}{2E_B}G^f_{M,B}(Q^2)\right)t}\\e^{-\left(E_B(\vec{p})\mp\frac{\lambda q_1}{2E_B}G^f_{M,B}(Q^2)\right)t}\end{bmatrix}_r.\end{aligned} \tag{4.40}$$

This expression is now in the familiar form of a decaying exponential, where we can identify the exponent with the energy of the ground state of the baryon. The shift of this energy compared to the energy of the ground state of the unperturbed correlator allows us to extract the magnetic form factor G_M. Additionally we see that the sign of the energy shift depends on both the projection matrix and the sign of the sink momentum. To summarise, we can write the Feynman-Hellmann relation between the ground state energy of the correlator and the form factor as

$$\left.\frac{\partial E_B(+\vec{p},\lambda,\Gamma^3_\pm)}{\partial\lambda}\right|_{\lambda=0} = \pm\frac{q_1}{2E_B(\vec{p})}\,G^f_{M,B}(Q^2), \tag{4.41}$$

$$\left.\frac{\partial E_B(-\vec{p},\lambda,\Gamma^3_\pm)}{\partial\lambda}\right|_{\lambda=0} = \mp\frac{q_1}{2E_B(\vec{p})}\,G^f_{M,B}(Q^2). \tag{4.42}$$

We can generalise this expression to any spatial vector current γ_i, spin-projection matrix $\Gamma^j_\pm$, and momentum projection $\vec{p}$, satisfying the Breit frame condition $\vec{p} = \pm\vec{q}/2$,

$$\left.\frac{\partial E_B(\vec{p},\Gamma^j_\pm)}{\partial\lambda^f_i}\right|_{\lambda=0} = \pm\frac{\epsilon_{ijk}q_k}{2E_B(\vec{p})}G^f_{M,B}(Q^2). \tag{4.43}$$

Chapter 5.

Electromagnetic Form Factors

5.1. Nucleon Structure

The internal structure of nucleons can be probed experimentally through electron-nucleon scattering processes. The dominant process at low energies in these scattering events is elastic scattering where the particle content before and after the collision is the same and the nucleon remains in the ground state. Early experiments of electron-proton scattering at Stanford University [68] were first able to probe the electric and magnetic charge density of the proton. These densities were described by the electromagnetic form factors which could be extracted from the experimental cross-section. The measurement of these form factors as functions of the momentum transfer Q^2 was first achieved for the proton and then the neutron in the 1950's [69, 70]. These experiments were the first to confirm that the proton had a finite size, providing a measurement of its charge radius at 0.77 fm [71].

Generally, baryon electromagnetic form factors can be described by matrix elements of the electromagnetic current between baryon states, here expressed in Euclidean space,

$$\langle B(p', s')|J_\mu^{\rm em}(q)|B(p,s)\rangle = \bar{u}_B(p', s')\left[\gamma_\mu F_1(Q^2) + \sigma_{\mu\nu}\frac{q_\nu}{2M_B}F_2(Q^2)\right]u_B(p,s), \tag{5.1}$$

where the electromagnetic current is defined as the sum of the quark vector currents weighted by their electric charge:

$$J_\mu^{\rm em} = \frac{2}{3}\bar{u}\gamma_\mu u - \frac{1}{3}\bar{d}\gamma_\mu d - \frac{1}{3}\bar{s}\gamma_\mu s. \tag{5.2}$$

The two form factors $F_1(Q^2)$ and $F_2(Q^2)$ in Eq. (5.1) are often called the Dirac and Pauli form factors [72]. A common alternative basis for the form factors that we will use in this work is the Sachs form factors:

$$G_E(Q^2) \equiv F_1(Q^2) - \frac{Q^2}{4m^2} F_2(Q^2), \tag{5.3}$$

$$G_M(Q^2) \equiv F_1(Q^2) + F_2(Q^2), \tag{5.4}$$

where $G_E(Q^2)$ and $G_M(Q^2)$ are referred to as the electric and magnetic form factors respectively. This basis is commonly used in electron scattering experiments as it allows for the cross section to be expressed as a linear combination of the squares of the form factors, with no cross terms [73]. The Sachs form factors are also useful for providing insights into density distributions within the baryons as they are three-dimensional Fourier tranforms of the charge and magnetisation distributions. These density distributions can be revealed most readily at small values of Q^2 through the definition of a mean-squared radius for each of the distributions. The electric charge radius for the proton can be defined as [74]

$$\left\langle r^2_{E,p} \right\rangle = -6 \frac{dG_{E,p}}{dQ^2}\bigg|_{Q^2=0}. \tag{5.5}$$

A similar definition can be made for the magnetic form factor, however experimental results for this are more difficult to obtain as the contributions from G_M to the cross section are suppressed by a factor of $\tau = \frac{Q^2}{4m^2}$ [74]. In the the forward limit ($Q^2 = 0$) the electric form factor equals the charge of the chosen baryon, while the magnetic form factor equals the baryon magnetic moment.

The interpretation of the form factors in terms of charge densities will only hold in the non-relativistic limit. As we go to larger values of Q^2, the difference in reference frames between the initial and final state results in additional recoil terms in the radii. Restricting the interpretation to the Breit frame, analogous to a boost to the infinite momentum frame, results in a projection of the 3D charge density onto a 2D plane, transverse to the direction of the approaching nucleon. This allows for the form factors to be interpreted in terms of transverse charge and magnetisation densities.

Lattice QCD calculations of the nucleon electromagnetic form factors are useful for guiding and interpreting the experimental results, they can also aid in resolving certain tensions from experiment, such as for the proton radius. From the relation above in equation (5.5) it can be seen that for determinations of the radii of nucleons, lattice

QCD calculations need to focus on the small-Q^2 range. Lattice QCD calculations allow for the determination of the contributions of the individual quarks to the form factors, as well as contributions from connected and disconnected diagrams. Form factors of the hyperons can also be calculated through lattice QCD, these are more difficult to determine through experiments so theoretical predictions from lattice QCD are valuable.

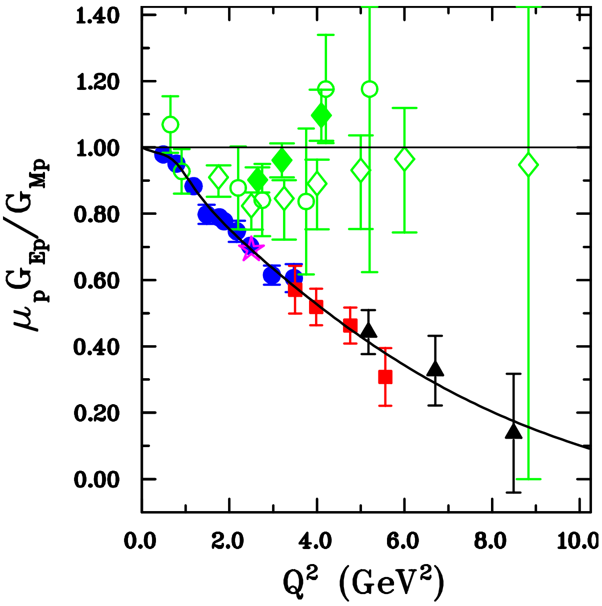

Figure 5.1. Experimental results for the ratio of form factors G_E/G_M against Q^2. The blue, magenta and red points show the results from recoil polarization experiments at JLab [73]. The green points show the Rosenbluth separation data [75]. Figure from [74].

Recent experimental determinations of the nucleon electromagnetic form factors have been obtained at Jefferson Laboratory (JLab) [76]. One aspect of these results which is of interest is the behaviour of the ratio G_E/G_M at large Q^2. The current results seem to indicate that this ratio has a downward trend, deviating from the phenomenological dipole predictions. In figure 5.1 we show the experimental results for this ratio of form factors. Despite the large uncertainties at large values of Q^2, there is an indication that the ratio G_E/G_M decreases and comes close to crossing over zero at large Q^2. This provides a motivation for lattice QCD calculations of the nucleon form factors to probe this large-Q^2 behaviour.

5.2. Feynman-Hellmann Method

The Feynman-Hellmann method relates the shift in energy due to a perturbation in the action to a desired matrix element. To apply this method to the calculation of nucleon electromagnetic form factors we insert the following operator into the lattice QCD action

$$\mathcal{L}(x) \to \mathcal{L}(x) + \lambda_\mu^f \left(e^{i\vec{q}\cdot\vec{x}} + e^{-i\vec{q}\cdot\vec{x}}\right) \bar{q}_f(x)\, \gamma_\mu\, q_f(x), \tag{5.6}$$

where we do not sum over μ and the modifications to each flavour f are considered separately. The two exponentials are included in order to make the operator Hermitian, this will ensure a real energy shift. The Feynman-Hellmann theorem then allows us to extract the matrix element from the linear shift to the energy induced by this modification.

To isolate both the electric and magnetic form factors from the matrix elements we require two different operator insertions. We will use the temporal vector operator γ_4, and the spatial vector operator γ_2. These are two convenient choices as they allow us to directly project onto the electric and magnetic form factors respectively. Since the Feynman-Hellmann method is restricted to the Breit frame we have a smaller set of available Q^2 values than most three-point function calculations, these are listed in table 5.1. The current as defined in Eq. (5.6) includes both signs of the momentum transfer, this means that there are two choices of sink momentum which satisfy the Breit frame kinematics, both of which are included in the simulation as can be seen in the table.

The shifts to the ground state energies due to the temporal vector and spatial vector current are as determined in section 4.1.2 and section 4.1.2 respectively, they take the following form

$$\left.\frac{\partial E_B(\vec{p})}{\partial \lambda_4^f}\right|_{\lambda=0} = \frac{M_B}{E_B(\vec{p})} G_{E,B}^f(Q^2), \tag{5.7}$$

$$\left.\frac{\partial E_B(\vec{p}, \Gamma_\pm^3)}{\partial \lambda_2^f}\right|_{\lambda=0} = \pm\frac{q_1}{2E_B(\vec{p})} G_{M,B}^f(Q^2), \tag{5.8}$$

where the momenta are restricted to the Breit frame condition such that $\vec{p} = \pm\vec{q}/2$.

Table 5.1. The momentum transfer values which are considered here. The choices are restricted to the Breit frame where $\vec{p}\,' = -\vec{p}$. Since the current defined in Eq. (5.6) includes both $\pm\vec{q}$, there are two choices of sink momenta which satisfy Breit frame kinematics, both of which are included in column 3.

β	$\vec{q}(L/2\pi)$	$\vec{p}(L/2\pi)$	Q^2[GeV^2]
5.4	(0,0,0)	(0,0,0)	0.00
	(2,0,0)	±(1,0,0)	0.90
	(2,2,2)	±(1,1,1)	2.69
	(4,2,0)	±(2,1,0)	4.49
	(4,4,0)	±(2,2,0)	7.18
5.5	(0,0,0)	(0,0,0)	0.00
	(2,0,0)	±(1,0,0)	1.10
	(2,2,2)	±(1,1,1)	3.29
	(4,2,0)	±(2,1,0)	5.48
5.65	(0,0,0)	(0,0,0)	0.00
	(2,2,0)	±(1,1,0)	1.15
	(4,2,2)	±(2,1,1)	3.46
	(4,4,2)	±(2,2,1)	5.19
	(6,0,0)	±(3,0,0)	5.19
	(6,4,2)	±(3,2,1)	8.08
5.80	(0,0,0)	(0,0,0)	0.00
	(2,2,0)	±(1,1,0)	1.54
	(4,2,2)	±(2,1,1)	4.63
	(4,4,2)	±(2,2,1)	6.95
	(6,0,0)	±(3,0,0)	6.95
	(6,4,2)	±(3,2,1)	10.80

5.3. Simulation Details

For the calculations in this work we use lattice ensembles with $N_f = 2+1$ flavours of $\mathcal{O}(a)$-improved clover Wilson fermions [77]. We will use four different values for the bare coupling β, with corresponding lattice spacings in the range $a = 0.0588(3)$ fm to $0.0818(9)$ fm. The lattice spacings have been determined through the calculation of singlet quantities in previous works [78–81]. Two different volumes are included with all details of the ensembles listed in table 5.2.

On each of these ensembles we use the Feynman-Hellmann method to calculate the electromagnetic form factors of the octet baryons for a range of Breit frame momenta. The method as described in chapter 4 will be used, with modifications to the QCD action including the momentum transfer, which requires a different action for each value of Q^2. These discrete momenta are chosen such that the corresponding values of Q^2 across ensembles are relatively close together, even as the lattice spacing and volumes change, which will facilitate global fits to the data more easily. The Feynman-Hellmann modifications to the action will include a spatial vector current and a temporal vector current, with the magnitude of the modification set to $\lambda = 10^{-4}$, as this has been shown to produce good results [57].

The calculations presented here will only show results for the connected contributions to the form factors. To apply the Feynman-Hellmann method to the disconnected contributions would require the generation of new gauge ensembles for each new operator and momentum transfer, which would be very computationally expensive. Previous calculations have indicated that the disconnected distributions could be small for large Q^2 [57, 82]. For these reasons we will neglect the disconnected contributions in this work.

Since all the ensembles we use here are in the isospin symmetric limit, the quark contributions to the proton and neutron form factors are related as follows

$$G^u_{E,p} = G^d_{E,n}, \tag{5.9}$$

$$G^d_{E,p} = G^u_{E,n}, \tag{5.10}$$

and similarly for the magnetic form factors. This allows us to construct the neutron form factors from the lattice results calculated for the proton and similar relations apply for the other Baryons in the octet.

5.4. Correlator Analysis

The signal for the matrix elements is contained within the energy shift caused by the modification to the lattice action. To accurately extract this shift from the correlation functions it is beneficial to construct a ratio of the two-point correlators with different momenta, spin and parity projections. These correlators will be calculated on the exact same set of gauge field configurations, therefore the underlying gauge noise in each of

Table 5.2. The ensembles used in the analysis and the number of gauge field configurations used on each. The lattice spacings have been determined in [81].

#	β	$L^3 \times T$	a [fm]	κ_l	κ_s	$N_{\text{conf.}}$
1	5.40	$32^3 \times 64$	0.0818(9)	0.119930	0.119930	1646
2				0.119989	0.119812	664
3				0.120048	0.119695	960
4				0.120084	0.119623	1333
5	5.50	$32^3 \times 64$	0.0740(4)	0.120900	0.120900	1695
6				0.121040	0.120620	1858
7				0.121095	0.120512	1837
8	5.65	$48^3 \times 96$	0.0684(4)	0.122005	0.122005	537
9				0.122078	0.121859	922
10				0.122130	0.121756	531
11	5.80	$48^3 \times 96$	0.0588(3)	0.122810	0.122810	595
12				0.122880	0.122670	561
13				0.122940	0.122551	520

them will be correlated. When taking the ratio of these correlators, the result will have an improved signal strength due to the correlations in the gauge noise.

From Eq. (5.7) we see that to calculate the electric form factor we consider correlators which include the temporal vector current (γ_4) and since the result does not depend on the spin we use the unpolarised spin projection. In the off-forward case, the modification to the action includes two momentum projections; in order to isolate only one of the resulting energy shifts we must take a combination of the two momentum states. As discussed in subsection 4.1.2, the two possible combinations are determined by the eigenvalues of the Hamiltonian. The calculation of these two-point functions only allows us to set the momentum projection for the sink operator, while the source operator will couple to both momentum states due to the modified action. By taking a linear combination of the correlators with the two momentum projections at the sink we are then able to create a correlation function which isolates one of the energy shifts. we define the momentum averaged correlation function

$$\bar{G}(\vec{p}, \lambda, t) = \frac{1}{2}[G(\lambda, +\vec{p}, t) + G(\lambda, -\vec{p}, t)]. \tag{5.11}$$

Additionally, for the temporal vector current, a time-reversal combined with a reversal of the parity projection gives the same result as inverting the sign of λ in the perturbation. We will use this to create a correlator with the opposite energy shift. Combining all the above, we construct a ratio of correlators which can isolate the energy shift for the temporal current

$$R_E(\lambda, \vec{p}, t) = \frac{\bar{G}^+(\lambda, \vec{p}, t)\bar{G}^-(0, \vec{p}, -t)}{\bar{G}^+(0, \vec{p}, t)\bar{G}^-(\lambda, \vec{p}, -t)}, \tag{5.12}$$

where the $\pm$ superscript indicates the parity projection, and the correlators with $\lambda = 0$ are included to improve the cancellation of the gauge field noise.

For the spatial vector current, the spin dependence of the matrix element results in a more complicated set of energy eigenstates. As shown in section 4.1.2, when using a real operator in the Feynman-Hellmann modification, the correlator isolates one energy shift. This energy shift depends on the spin projection as well as the sign of the sink momentum projection. Flipping the sign of both the spin and the momentum projections together will result in the same energy shift being isolated, additionally the time- and parity-reversal does not influence the energy shift. Using this we define two new averaged correlation functions

$$\tilde{G}(\lambda, \pm\vec{p}, t) = \frac{1}{4}[G^+_\uparrow(\lambda, \pm\vec{p}, t) + G^-_\uparrow(\lambda, \pm\vec{p}, -t) + G^+_\downarrow(\lambda, \mp\vec{p}, t) + G^-_\downarrow(\lambda, \mp\vec{p}, -t)], \tag{5.13}$$

where the arrows indicate the spin polarization projection. The ratio for the spatial vector current is then defined as

$$R_M(\lambda, \vec{p}, t) = \frac{\tilde{G}(\lambda, +\vec{p}, t)\tilde{G}(0, -\vec{p}, t)}{\tilde{G}(0, +\vec{p}, t)\tilde{G}(\lambda, -\vec{p}, t)}. \tag{5.14}$$

In the large Euclidean time limit, both of the ratios above will reduce to a simple exponential function, where the exponent contains the odd energy shift

$$R_{E/M}(\lambda, \vec{p}, t) \xrightarrow{t \gg 0} A(\lambda) e^{-2\Delta E(\lambda)_{\mathrm{odd}} t}. \tag{5.15}$$

The odd energy shift is defined as the difference between the energies with a positive λ and negative λ,

$$\Delta E_{\mathrm{odd}} = \frac{1}{2}\left[E(\lambda) - E(-\lambda)\right]. \tag{5.16}$$

The ratios above have the advantage that they will remove the even order contributions in λ. So the leading order term will be $\mathcal{O}(\lambda)$ (the term of interest) with corrections occurring at $\mathcal{O}(\lambda^3)$. We can use the effective energy to get an effective value of this energy shift which can be used to inform the time range in which the ground state is dominant,

$$\Delta E_{\mathrm{Eff}}(t) \equiv \frac{1}{2a} \ln\left[\frac{R_{E/M}(\lambda, t)}{R_{E/M}(\lambda, t+a)}\right]. \tag{5.17}$$

We expect this effective energy to show a constant plateau for sufficiently large times. In figure 5.2 we show this effective energy for the ratio $R_{E,p}$ where the Feynman-Hellmann modification has been applied to the u-quark in the proton, on ensemble #5. The two plots show the same effective energies, the shaded regions show the results of two different fits which we will explain in more detail later.

In our analysis we will apply these correlator ratios to calculate matrix elements up to large momentum transfers where we observe a degradation in the signal to noise ratio of the correlation functions. In order to constrain the shift in the energy of the ground state we will use a combination of two ansätze to fit the above ratios. The first ansatz relies on the ground state becoming dominant at sufficiently large Euclidean time, but before the signal is lost to noise. In this case each correlator in the ratios can be described by a simple exponential function and the overall ratio reduces to an exponential of the energy shift

$$R(\vec{p}, t) = A e^{-2\Delta E t}. \tag{5.18}$$

This ansatz has been used successfully in [57], where the calculations were done on ensemble #5 in table 5.2.

The second ansatz takes into account the contributions from excited states explicitly. Since the modified action will also shift the energy of the excited states in the spectrum as well as the overlap factors of both states, we have to include these as parameters. Using the unperturbed correlation function we are able to accurately determine the values of the overlap factors and the unperturbed energies of both states

$$G^{\mathrm{2pt}}(\vec{p}, t) = A_0 e^{-E_0 t} + A_1 e^{-E_1 t}. \tag{5.19}$$

Then using these determined values as inputs into the ansatz in Eq. (5.20) allows us to get a better determination of the energy shift at early time-slices,

$$R(\vec{p},t) = \frac{(A_0+\Delta A_0)e^{-(E_0+\Delta E_0)t} + (A_1+\Delta A_1)e^{-(E_1+\Delta E_1)t}}{(A_0-\Delta A_0)e^{-(E_0-\Delta E_0)t} + (A_1-\Delta A_1)e^{-(E_1-\Delta E_1)t}}. \tag{5.20}$$

The form factor calculations presented here span a large range of momentum transfers ($Q^2 = 0-11\,\mathrm{GeV}^2$). Over this range the contributions from excited states to the two-point correlators can change significantly. To extract the ground state reliably across this range, we need to find an optimal fit window for both ansätze. Since this process of choosing a fit window can influence the results significantly, we apply a weighted average method. This method will reduce the reliance on researcher choice of fit window and allow the two fit functions to complement each other. Figure 5.2 shows the effective energy of the ratio in Eq. (5.12) with the results from both ansätze overlaid as bands. The dark line covers the timeslices which are included in the fit while the light shaded region is drawn to show the large-time value of the fits.

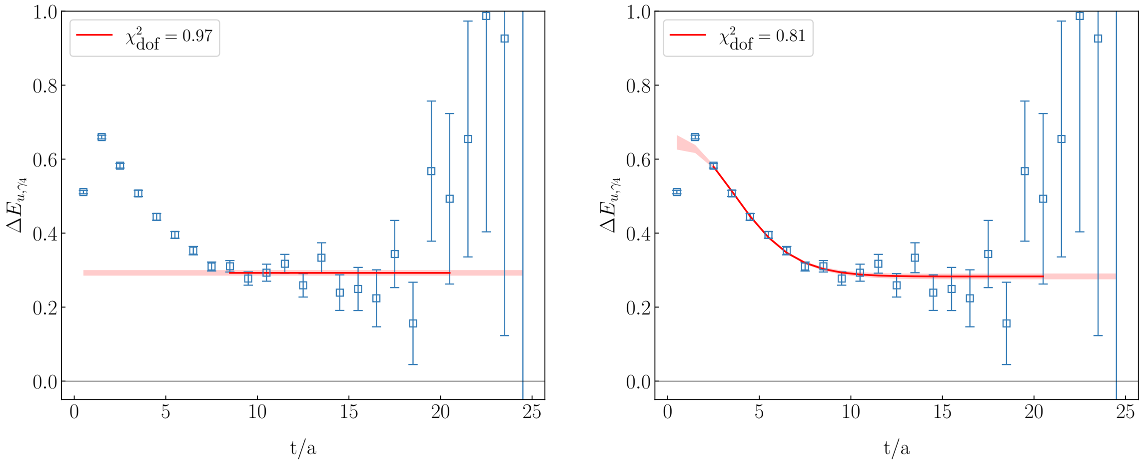

Figure 5.2. The effective energy of the ratio of correlators for the γ_4 operator inserted on the up-quark in the proton. The results are for momenta $\vec{q} = \pm(2,0,0)$ and $\vec{p} = \pm(1,0,0)$ calculated on ensemble #5. The effective energy of the one-exponential fit and the two-exponential fit to the ratio are also shown with their respective χ^2_{dof} values. The dark line covers the timeslices which are included in the fit while the light shaded region is drawn to show the large-time value of the fits.

5.4.1. Weighted Average

We use the same weighted average method here as was shown in subsection 3.1.3. The weighted average is calculated for results from both ansätze to the ratio (Eq. (5.18), (5.20)) and for variations over the fitting time window. The weight corresponding to fit f is defined as

$$\tilde{w}^f = \frac{p_f \left(\delta E_0^f\right)^{-2}}{\sum_{f'=1}^{N} p_{f'} \left(\delta E_0^{f'}\right)^{-2}}. \tag{5.21}$$

The subset of suitable fit windows is chosen by looking at the effective energy of each correlator (e.g. Figure 5.2), these fit windows are then averaged for both fit functions to produce the final fit parameters. Figure 5.3 shows an example of this weighted average for a selection of different fits. The upper figure shows fit results for a low momentum transfer ($\vec{q} = \frac{2\pi}{L}(2,0,0)$), the blue bars show the weights for the two-exponential fit results while the black bars show the weights for the one-exponential fit results. It can be seen that the results for the energy shift span quite a large range which introduces the possibility of large effects from the researcher choice of fitting window. The weighted average, shown in the red band removes this effect by including the result from each of the fits as well as their quality. The lighter shaded red band shows the total uncertainty, including the systematic uncertainty which comes from the inclusion of the large number of fits. The lower figure shows the result for a high momentum transfer ($\vec{q} = \frac{2\pi}{L}(4,2,2)$), in this case the number of viable fit ranges is smaller due to the increased noise in the correlator at high momentum. Here we see that the one-exponential fit results are weighted more heavily, with smaller contributions from the two-exponential fit results. Both plots are for the temporal current insertion on the u-quark on ensemble $\#5$ in table 5.2.

5.5. Three-point Function Method Comparison

Three-point correlation functions are the most direct way to calculate form factors in lattice QCD, this method has been studied extensively and many techniques have been developed to improve the analysis of these functions. The main difficulty facing calculations of lattice three-point functions is the decreasing signal-to-noise ratio at large Euclidean times and the associated computational costs. Since the calculation of

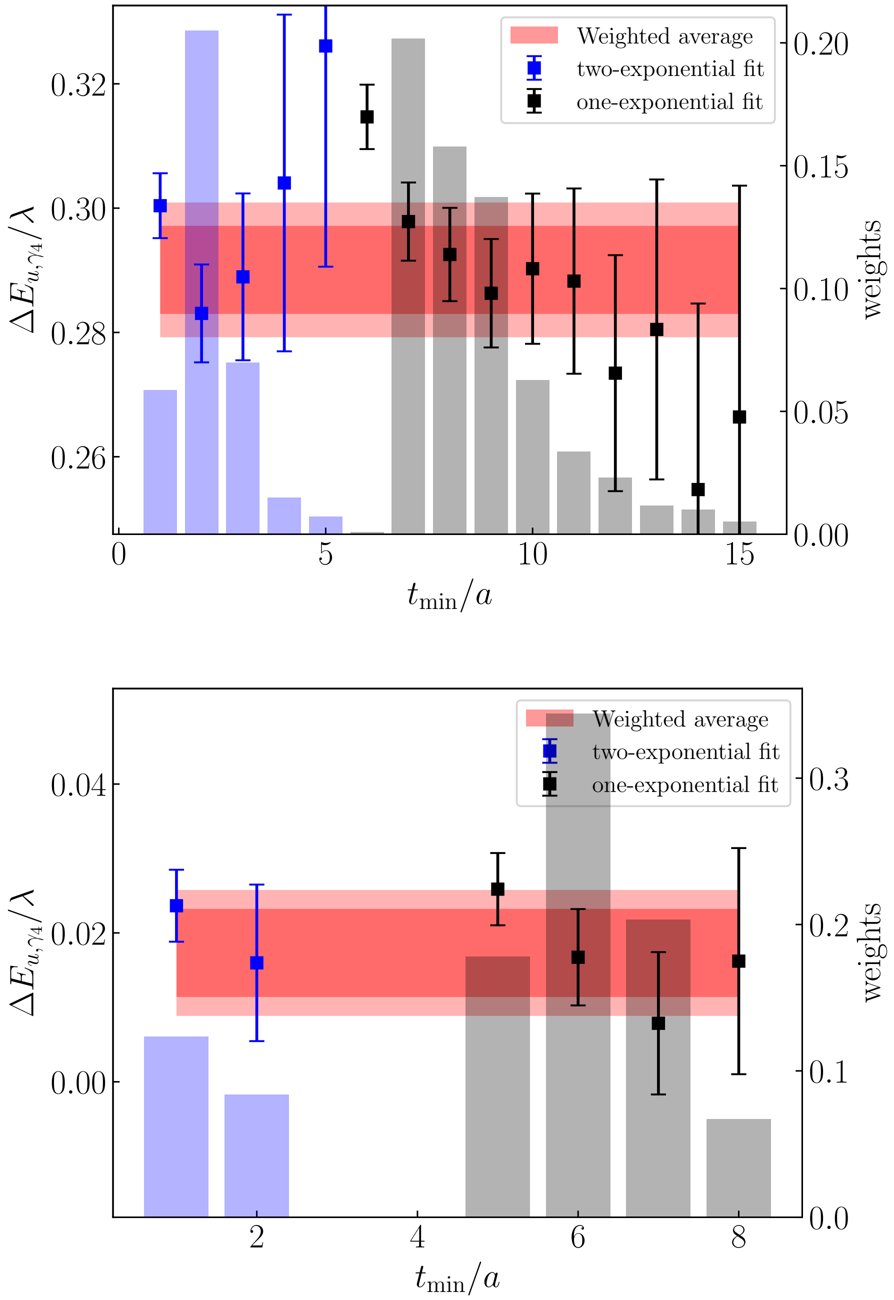

Figure 5.3. The energy shift extracted from the fit to the ratio with the two-exponential function (blue points) and the one-exponential function (black points). The bar graph shows the weight of each fit result for the value of $t_{\min}$ where the blue bars correspond to the two-exponential fit and the black bars to the one-exponential fit. The red band is the weighted average value, where the inner band shows the statistical uncertainty and the outer band shows the total uncertainty, this includes the statistical uncertainty and the systematic uncertainty from the spread between the included fit results. The upper plot shows the energy shift for the lattice momentum of $\vec{q} = \pm(2,0,0)2\pi/L$, the lower plot shows the energy shift for the lattice momentum of $\vec{q} = \pm(4,2,2)2\pi/L$, both results are from ensemble #5.

three-point functions requires fixing either the operator insertion time or the sink time before the final matrix inversions, it is costly to include many time combinations. Some of the often used techniques to deal with this are multi-state fits [83–85], the summation method [86–88] and Generalised Eigenvalue Problems [89, 90], amongst others.

To compare the validity and effectiveness of the Feynman-Hellmann method we will perform a comparison with the more established three-point function approach. We calculate the same two nucleon electromagnetic form factors on ensemble # 5 using three-point functions. This calculation is performed by using a sequential source inversion through the sink. This method fixes the sink momentum in order to calculate the final propagator from the sequential source. Since our comparison will be most useful if it involves the exact same initial and final momentum states, we will perform four different sequential source inversions where we set the sink momentum to match up with the Breit frame conditions used in the Feynman-Hellmann calculation. This construction also gives us access to a range of non-Breit frame momenta at no additional cost. To account for the contributions of excited states to the signal, we also include three different source-sink time separations ($t = 0.74,\ 0.96,\ 1.18\,\mathrm{fm}$). For each source-sink separation the three-point correlation functions were calculated on 999 gauge configurations. Combining the lattice results from all three source-sink separations allows us to perform a two-exponential fit which explicitly includes the excited state contributions.

We construct the ratio as defined in Eq. (3.49) for each of the three source-sink time separations. We will use the same two currents as were used in the Feynman-Hellmann calculation (although we have access to all currents at no extra cost). Since we are considering Breit frame kinematics, we can construct the ratios with the chosen projection matrices such that they give the Sachs form factors

$$R(\Gamma_{\mathrm{unpol}}, \gamma_4; t, \tau; -\frac{\vec{q}}{2}, \frac{\vec{q}}{2}) \xrightarrow{\tau, t-\tau \gg 0} \frac{E(\vec{q}/2)}{m} G_E(Q^2), \tag{5.22}$$

$$R(\Gamma^3_{\pm}, \gamma_2; t, \tau; -\frac{\vec{q}}{2}, \frac{\vec{q}}{2}) \xrightarrow{\tau, t-\tau \gg 0} \frac{2E(\vec{q}/2)}{q_1} G_M(Q^2), \tag{5.23}$$

where τ is the time-separation between the source and the current insertion time and $t - \tau$ is the time-separation between the current insertion time and the sink.

We expect these ratios to show a constant plateau for sufficiently large separations between the source, current insertion and the sink. In figure 5.4 we show the ratio for all three source-sink separations. It can be seen that for the largest source-sink separation there is potentially a constant plateau, however the trend with increasing source-sink separation suggests that contributions from excited states are still present in the signal.

This indicates that the source-sink separation is not sufficiently large enough to suppress all of the excited state contributions. To improve the determination of the ground state signal we will explicitly take the excited states into account in our ansatz by using a two-exponential fit. Here we take the two lowest terms in the infinite sum over states, the second exponential will not necessarily contain just the first excited state, it will contain a mix of the first few excited states. Since we consider the three-point functions for the Breit frame kinematics, the initial and final nucleon states will have the same momenta, simplifying the analysis. The ansätze we use are as follows,

$$G_{\text{fit}}(t,\vec{p}) = A_0 e^{-E_0(\vec{p})t} + A_1 e^{-E_1(\vec{p})t} \tag{5.24}$$

$$\begin{aligned} R(t,\tau;\vec{p}\,',\vec{p}) = &\sum_{i,j=0}^{1} \sqrt{A_i(\vec{p})A_j(\vec{p}\,')}\, B_{ij}\, e^{-E_i(\vec{p})\tau} e^{-E_j(\vec{p}\,')(t-\tau)} \\ &* \frac{1}{G_{\text{fit}}(t,\vec{p}\,')}\sqrt{\frac{G_{\text{fit}}(\tau,\vec{p}\,')G_{\text{fit}}(t,\vec{p}\,')G_{\text{fit}}(t-\tau,\vec{p})}{G_{\text{fit}}(\tau,\vec{p})G_{\text{fit}}(t,\vec{p})G_{\text{fit}}(t-\tau,\vec{p}\,')}}. \end{aligned} \tag{5.25}$$

We first fit to the two-point functions at the source and sink momenta, then we fit to the ratio by using Eq. (5.25). In this fit to the ratio we use the evaluated fit functions of the two-point functions as well as their energies, there are then four fit parameters remaining in this function, B_{ij}. The ground state matrix element we are interested in is contained in B_{00}.

In figure 5.4 we show the effective electric and magnetic form factors for the u quark in the proton. We show both the results from the 3-point function calculation and the Feynman-Hellmann calculation. The results are for the form factor at the lowest non-zero momentum $\vec{q} = \frac{2\pi}{L}(2,0,0)$. The three-point function results are plotted as a function of the operator insertion time τ, while the Feynman-Hellmann results are plotted as a function of the sink time t. These figures highlight the additional time-slices which are available in the Feynman-Hellmann analysis, facilitating improved control over excited state contributions.

There are some qualitative differences between the two methods which should be mentioned. When using the three-point functions, the sink momentum is fixed but the operator insertion and the associated momentum can be changed for no additional cost. This makes it relatively cheap to gather results for a large number of momentum transfers, for this comparison we include only the results from the matching Breit frame momenta

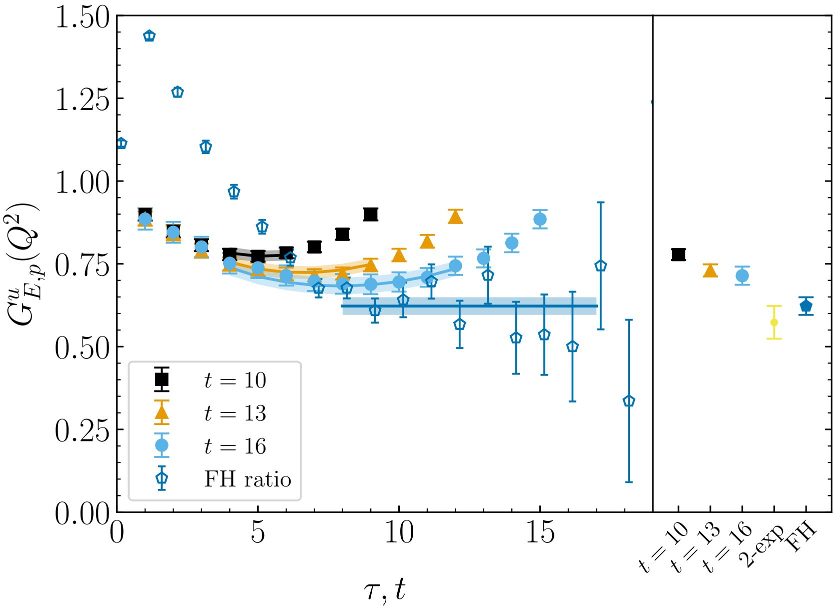

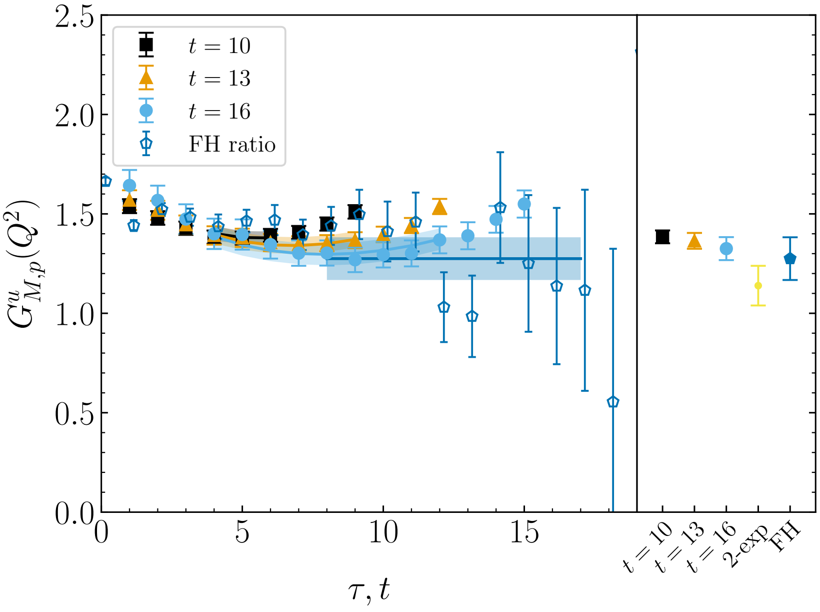

Figure 5.4. The effective electric (upper) and magnetic (lower) form factor of the u quark in the proton. The squares, triangles and circles are the results from the 3-point function calculation for source-sink separations of $t = 10, 13, 16$ timeslices respectively. The pentagons show the results of the Feynman-Hellmann calculation of the same form factor. The right hand side shows the results of fitting the 3-point ratios with simple plateaus, a combined two-exponential fit (yellow circles) and the weighted average result from Feynman-Hellmann method. Both form factors shown are at the lowest non-zero momentum transfer $\vec{q} = \frac{2\pi}{L}(2,0,0)$ on ensemble #5.

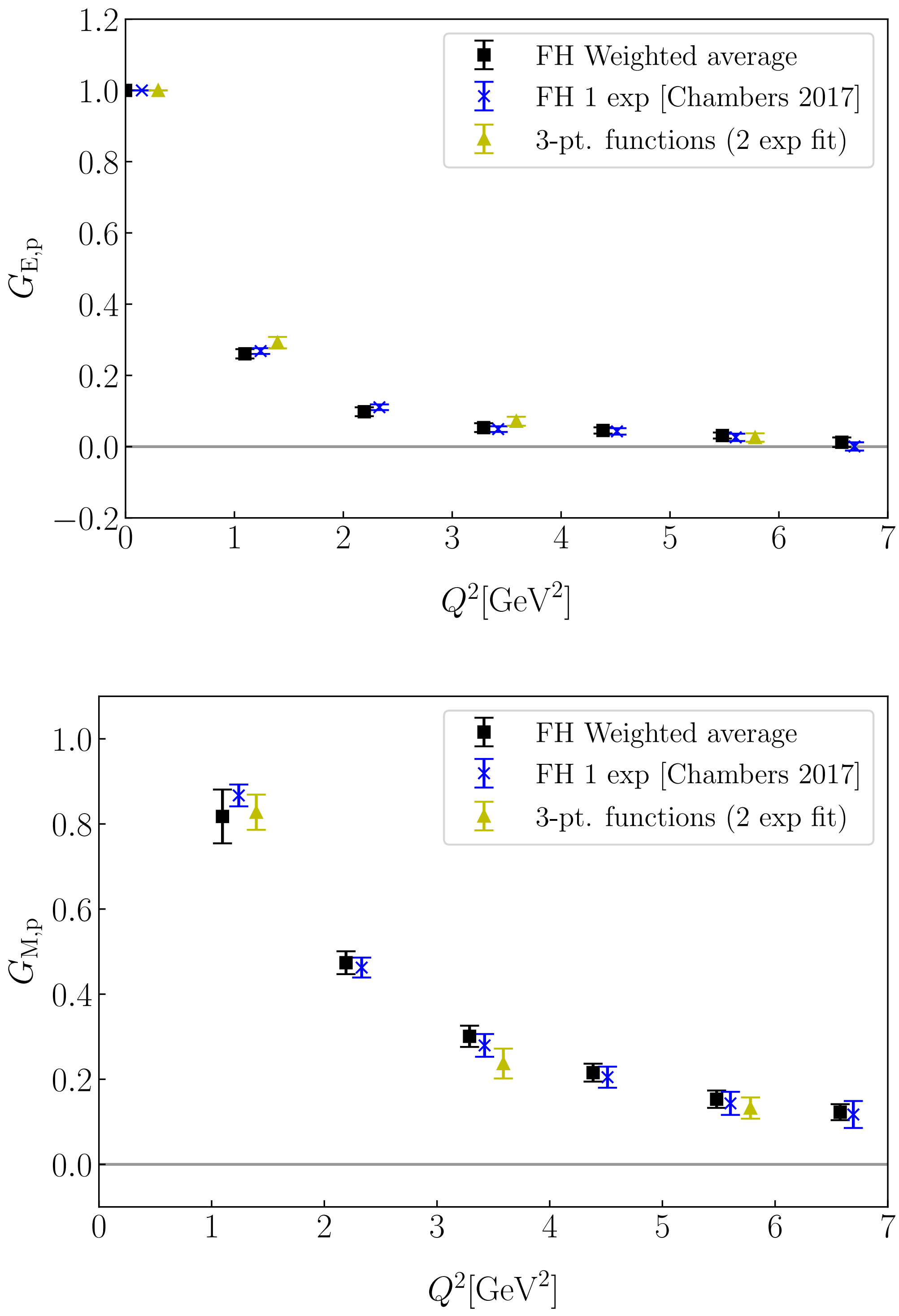

Figure 5.5. The electric (upper) and magnetic (lower) form factors of the proton versus momentum transfer Q^2. Results are shown from the two-exponential fit to the 3-point function ratios (triangles), the one-exponential fits to the Feynman-Hellmann results from [57] (crosses) and the Feynman-Hellmann results using the weighted-average analysis (squares).

however. The Feynman-Hellmann method does not require the source-sink separation to be fixed which gives it access to a large range of source-sink separations, which aids in the determination of the excited state contributions. The three-point functions require a new set of simulations for each source-sink separation on the other hand.

In figure 5.5 we show the electric and magnetic form factors for both the Feynman-Hellmann method as calculated in [57] as well as the re-analysis of the same data using the weighted average method outlined above and the results from the three-point function calculation. It can be seen that the results from both methods are compatible within uncertainties, and there is minimal change in the size of the uncertainties between the two methods.

5.6. Systematics

5.6.1. Orientation of the Spatial Current

The magnetic form factor can be calculated by the Feynman-Hellmann method through the use of any spatial vector current, in the above results we have used the γ_2 current. Since the form factor depends only on Q^2, it should be independent of which spatial current and momentum configuration is used to calculate it. It is useful to investigate whether the results from this method stay consistent under a change of spatial vector current. To isolate only the effects of the lattice symmetry we will consider a Feynman-Hellmann calculation in which we use the current $-\gamma_3$ and combine this with the $\Gamma_\pm^2$ projection matrix. By using the Feynman-Hellmann relation in Eq. (4.43) we see that this should produce the same shift to the energy up to the effects of the lattice symmetry. We do this calculation on ensemble #1 from table 5.2. Figure 5.6 shows this comparison between γ_2 and $-\gamma_3$ for a momentum transfer of $\vec{q} = \frac{2\pi}{L}(2, 2, 2)$, we show the effective energy shift together with the results of fitting the correlators over the same time windows. The effective energies in the figure agree up to statistics, as do the fit results, which indicates that any dependence on the direction of the spatial vector current is minimal.

5.6.2. Momentum Discretisation Effects

The electromagnetic form factors should in principle only depend upon the value of Q^2, however in the case of discretised momenta such as on the lattice there could be

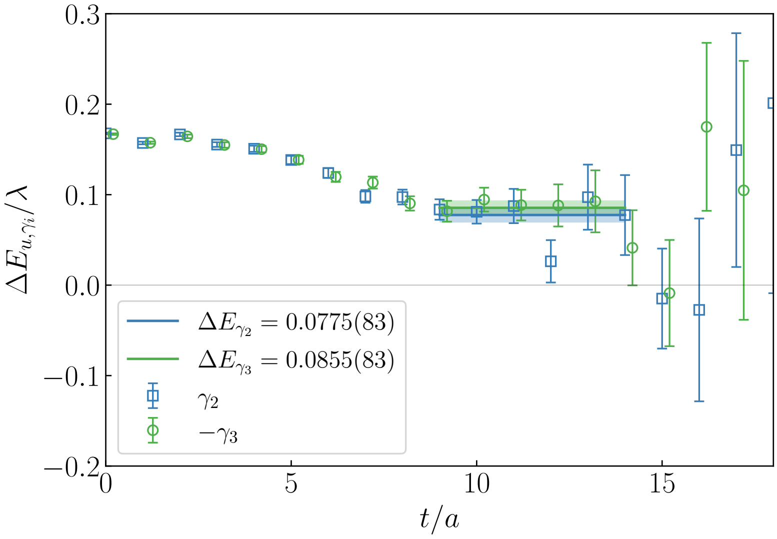

Figure 5.6. The effective energy of the ratio in equation (5.14), together with a fit to the ratio which extracts a value for ΔE. We show this for two different spatial currents γ_2 and γ_3. The current insertion here includes a momentum transfer of $\vec{q} = \frac{2\pi}{L}(2, 2, 2)$

additional momentum dependences. The usual symmetries which are present in momenta for the continuum will not transfer directly to lattice QCD. The effect of this difference in symmetries on the Q^2 dependence of the form factors is especially important for simulations using the Feynman-Hellmann method as these use a small subset of all possible momentum configurations.

To investigate these momentum discretisation effects we will consider two different momentum transfer values which have the same value of Q^2. The two chosen momenta are $\vec{q} = \frac{2\pi}{L}(4, 4, 2)$ and $\vec{q} = \frac{2\pi}{L}(6, 0, 0)$, we will limit this test to one ensemble only (#8 in table 5.2). In the continuum we would expect both momenta to produce the same form factors, however on the lattice we expect some differences between the two results. In figure 5.7 we show the effective energy of the energy shift produced by the γ_4 operator with these two momenta for both the u-quark and the d-quark. From the fit results in the right hand panel of each figure we can see that the energy shifts agree statistically.

For the γ_2 operator insertion we expect the energy shifts to show a significantly discrepancy as they depend on the first element of the momentum transfer as well as the form factor as was shown in Eq. (5.8). To compare these results we will therefore divide out the first element of the momentum transfer for each energy shift. In figure

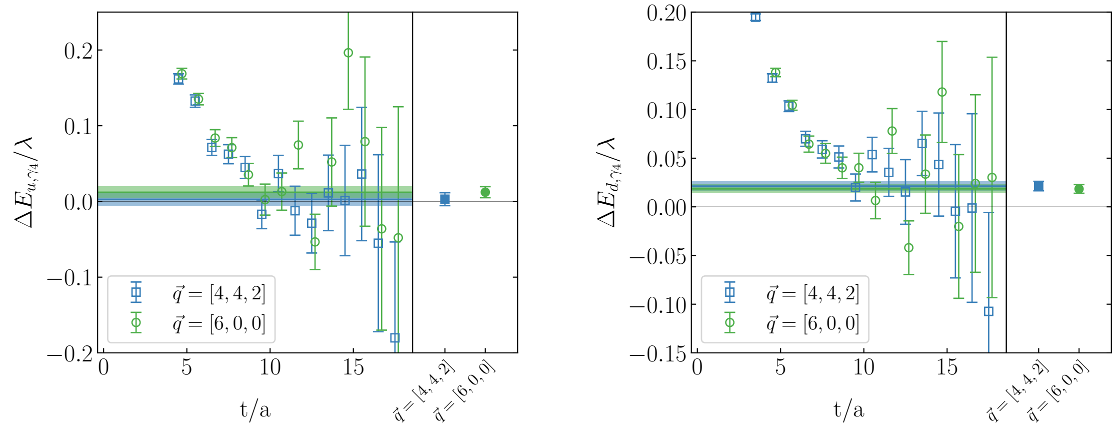

Figure 5.7. The effective energy shift for the γ_4 operator inserted on the u-quark (left) and the d-quark (right) for two momentum transfers with the same value of Q^2. The bands show the result of our fitting procedure and they correspond to the points in the right hand panel of each figure.

5.8 we show the effective energy of the energy shift now produced by the γ_2 operator for both momenta. once again we see statistical agreement with slight difference between the two momenta. These two tests are a good indication that we are not dealing with large momentum discretisation effects, however to produce higher precision results it will be necessary to do a more thorough investigation into these effects over multiple lattice ensembles.

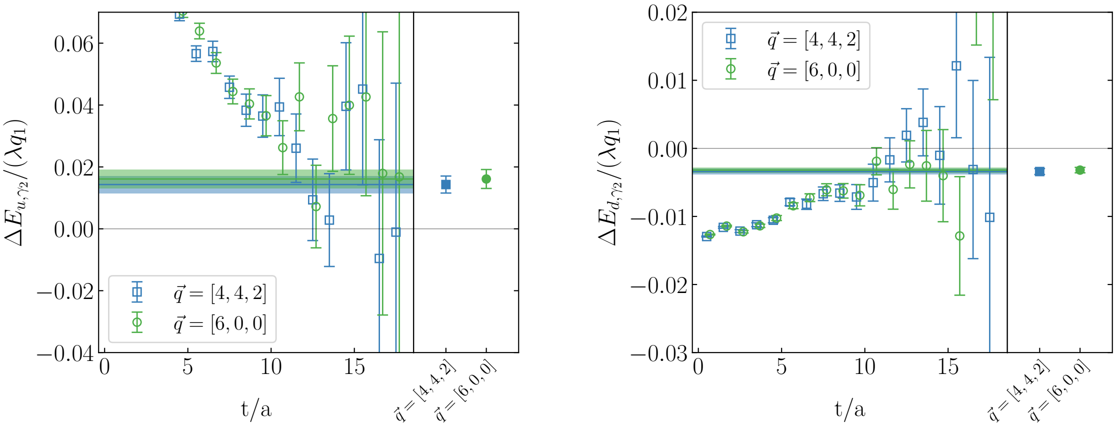

Figure 5.8. The effective energy shift for the γ_2 operator inserted on the u-quark (left) and the d-quark (right) for two momentum transfers with the same value of Q^2. The bands show the result of our fitting procedure and they correspond to the points in the right hand panel of each figure.

5.6.3. Lambda dependence

For the Feynman-Hellmann method to be applicable, the perturbation to the action needs to produce a shift in the ground state energy which is predominantly linear in λ. When the magnitude of the perturbation is too large, the higher orders in λ will start to dominate which will contaminate the signal. However the perturbation still needs to be sufficiently large such that the signal will not be lost in the noise. To ascertain that our calculation remains in the linear regime and that we are able to extract a signal from the lattice results, we perform the calculation for two values of λ $(-10^{-4}, 10^{-3})$ at the largest momentum transfer value. The results of this comparison on ensemble #8 are shown in figure 5.9, where we show the behaviour of the energy shift for both the spatial and temporal currents. From the figure we can see that the relation between the energy shifts is still predominately linear. For the simulations on all other ensembles we use the value of $\lambda = -10^{-4}$ to determine the form factors.

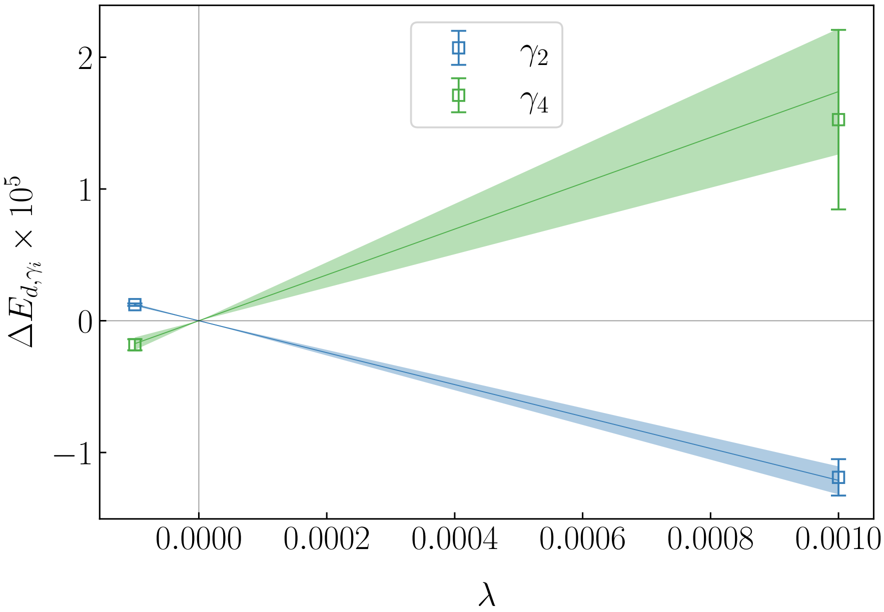

Figure 5.9. The shift in the ground state energy due to the perturbations in the action, plotted against the magnitude of the perturbation λ. The energy shifts shown here are for the larges momentum transfer considered on ensemble #8 in table 5.2, $\vec{q} = \frac{2\pi}{L}(6, 4, 2)$. We are able to show the linearity of the energy shift by calculating the two-point functions at two different values of λ $(-10^{-4}, 10^{-3})$ and using the zero intercept.

Table 5.3. The baryons and mesons labelled by their index and their corresponding currents. Here γ is any arbitrary Dirac matrix [91].

Index	Baryon (B)	Meson (F)	Current (J^F)
1	n	K^0	$\bar{d}\gamma d$
2	p	K^+	$\bar{u}\gamma s$
3	Σ^-	π^-	$\bar{d}\gamma u$
4	Σ^0	π^0	$\frac{1}{\sqrt{2}}(\bar{u}\gamma u - \bar{d}\gamma d)$
5	Λ^0	η	$\frac{1}{\sqrt{6}}(\bar{u}\gamma u + \bar{d}\gamma d - 2\bar{s}\gamma s)$
6	Σ^+	π^+	$\bar{u}\gamma d$
7	Ξ^-	K^-	$\bar{s}\gamma u$
8	Ξ^0	$\bar{K}^0$	$\bar{s}\gamma d$
0		η'	$\frac{1}{\sqrt{3}}(\bar{u}\gamma u + \bar{d}\gamma d + \bar{s}\gamma s)$

5.7. Flavour-Breaking Expansion

After calculating the form factors for all light- and strange-quark combinations on each of the lattice ensembles listed in table 5.2 we wish to investigate their dependence on the quark masses. This quark mass dependence will allow for the extrapolation of the form factors to their values at the physical quark mass through the use of a flavour breaking expansion, outlined in detail in [79, 91]. This expansion relies on the fact that across the ensembles we have used the average quark mass is kept constant at its physical value

$$\bar{m} \equiv \frac{1}{3}\left(m_u + m_d + m_s\right). \tag{5.26}$$

All of the ensembles have $N_f = 2+1$ flavours of quarks, where the up- and down-quark masses have been made degenerate ($m_u = m_d \equiv m_l$). This allows us to consider the quark mass dependence of each ensemble in terms of a single parameter, the deviation from the $SU(3)$ symmetric point

$$\delta m_l \equiv m_l - \bar{m}. \tag{5.27}$$

Using the notation listed in table 5.3, we write the matrix element of a current J^{F_j} between two baryons B_i and B_k as

$$\langle B_i | J^{F_j} | B_k \rangle \equiv A_{\bar{B}_i F_j B_k}, \tag{5.28}$$

where the indices i, j, k correspond to any of the indices in table 5.3. In this notation, 1 to 8 corresponds to the octet hadrons and non-singlet currents and 0 corresponds to the singlet current. For our calculations presented in this chapter we do not consider transition matrix elements so we are restricted to $i = k$.

The expansion in terms of δm_l was derived in [81] using SU(3) group theory, by defining multiple D_i and F_i quantities in terms of the matrix elements of the octet baryons it is possible to extrapolate to the physical point. For the expansion we will calculate three D_i values and F_i values from the form factors of the various baryons. These quantities are defined in such a way that they will have the same value at the $SU(3)$ symmetric point. The dependence of these quantities with respect to δm_l can then be used to extrapolate to the physical quark masses. The D_i values are defined as

$$\begin{aligned} D_1 &\equiv -(A_{\bar{N}\eta N} + A_{\bar{\Xi}\pi\Xi}) = 2d - 2r_1\delta m_l, \\ D_2 &\equiv A_{\bar{\Sigma}\eta\Sigma} = 2d + (r_1 + 2\sqrt{3}r_3)\delta m_l, \\ D_4 &\equiv \frac{1}{\sqrt{3}}(A_{\bar{N}\pi N} - A_{\bar{\Xi}\pi\Xi}) = 2d - \frac{4}{\sqrt{3}}r_3\delta m_l, \end{aligned} \tag{5.29}$$

and for F_i

$$\begin{aligned} F_1 &\equiv \frac{1}{\sqrt{3}}(A_{\bar{N}\eta N} - A_{\bar{\Xi}\eta\Xi}) = 2f - \frac{2}{\sqrt{3}}s_2\delta m_l, \\ F_2 &\equiv (A_{\bar{N}\pi N} - A_{\bar{\Xi}\pi\Xi}) = 2f + 4s_1\delta m_l, \\ F_3 &\equiv A_{\bar{\Sigma}\pi\Sigma} = 2f + (-2s_1 + \sqrt{3}s_2)\delta m_l. \end{aligned} \tag{5.30}$$

The mesons and their corresponding currents are listed in table 5.3. As an example, this means that for the case of $A_{\bar{N}\pi N}$ we have the following

$$\begin{aligned} A_{\bar{N}\pi N} &= \langle N|J^{\pi}|N\rangle \\ &= \frac{1}{\sqrt{2}}\langle N|(\bar{u}\gamma u - \bar{d}\gamma d)|N\rangle \\ &= \frac{1}{\sqrt{2}}\left(\langle N|\bar{u}\gamma u|N\rangle - \langle N|\bar{d}\gamma d|N\rangle\right). \end{aligned} \tag{5.31}$$

The D_i and F_i quantities can be combined into an 'average D' and 'average F' for which the δm_l dependence cancels and there is only a residual δm_l^2 dependence

$$X_D \equiv \frac{1}{6}(D_1 + 2D_2 + 3D_4) = 2d + \mathcal{O}(\delta m_l^2), \tag{5.32}$$

and for F_i,

$$X_F \equiv \frac{1}{6}(3F_1 + F_2 + 2F_3) = 2f + \mathcal{O}(\delta m_l^2). \tag{5.33}$$

These will be used to normalise the D_i and F_i quantities. The expressions in Eq. (5.29) and (5.30) also show the parameterisation in terms of two slope parameters each for both D_i and F_i, while X_D and X_F constrain the values of d and f up to order $\mathcal{O}(\delta m_l^2)$.

5.7.1. X_D and X_F values

Firstly looking at the values of X_D and X_F tells us whether there are still δm_l^2 effects present. This flavour breaking expansion is defined such that it is valid at any Q^2. In figure 5.10 we show the values of X_D and X_F for both G_E and G_M against δm_l at $Q^2 = 1.1\,\mathrm{GeV}^2$ for the ensembles #5-7. We expect the values at each Q^2 to be constant up to $\mathcal{O}(\delta m_l^2)$. Additionally, in figure 5.11 we show the same values at $Q^2 = 5.48\,\mathrm{GeV}^2$, the highest momentum transfer used on this ensemble, while the statistics are worse for the higher momentum transfer, the fit still shows a relatively constant behaviour.

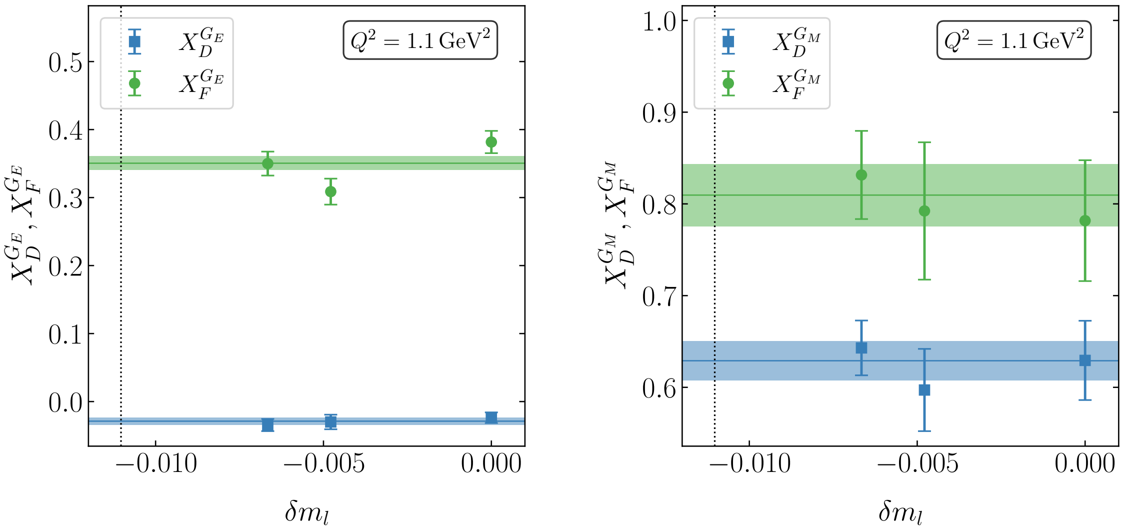

Figure 5.10. The values of X_D and X_F plotted against Q^2, for the three ensembles at $\beta = 5.50$, (5-7 in table 5.2) for G_E (left) and G_M (right) at $Q^2 = 1.1\,\mathrm{GeV}^2$.

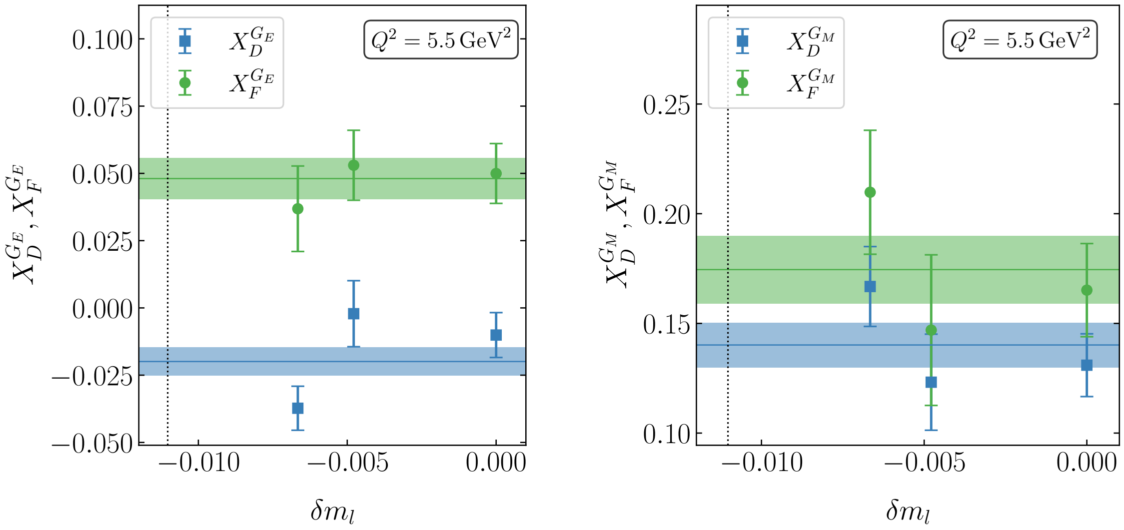

Figure 5.11. The values of X_D and X_F plotted against Q^2, for the three ensembles at $\beta = 5.50$, (5-7 in table 5.2) for G_E (left) and G_M (right) at $Q^2 = 5.48\,\mathrm{GeV}^2$.

5.7.2. Fanplots

For the electric form factor, $X_D^{G_E}$ will vanish for $Q^2 = 0$ and be very small for any non-zero Q^2. To avoid divisions by zero we will use X_F to normalise the fan plots of D_i for G_E, and for consistency we will do the same for G_M. Using the coefficients outlined in equation (5.29) and (5.30) we fit to the $\tilde{D}_i$ and $\tilde{F}_i$ quantities, where we have defined $\tilde{D}_i = D_i/X_F$ and $\tilde{F}_i = F_i/X_F$.

Figure 5.12 shows the resulting fan plot for the electric form factor for both $\tilde{D}_i$ and $\tilde{F}_i$ at the lowest non-zero momentum transfer. The characteristic branching out of the quantities as δm_l deviates from zero can be seen. The vertical dotted line in the figure represents the physical quark masses which have been taken from [81]. We modify the linear functions defined in equations (5.29)-(5.30) to include the normalisation by X_D and then use them to fit to $\tilde{D}_i$ and $\tilde{F}_i$, these fits are shown as the bands in the figure. In the left hand plot we can see that for $\delta m_l = 0$, the three D_i agree and have small uncertainties, while at non-zero δm_l they branch out due to $SU(3)$-symmetry breaking. In the left hand figure we divide F_i by X_F, which is exactly equal to one when δm_l, this improves the constraints on the fit parameters. Taking the value of the fit functions at the physical point as shown by the dotted line in the figure we can determine the values of the D_i and F_i at the physical point. This in turn will allow us to reconstruct the full form factors at the physical point.

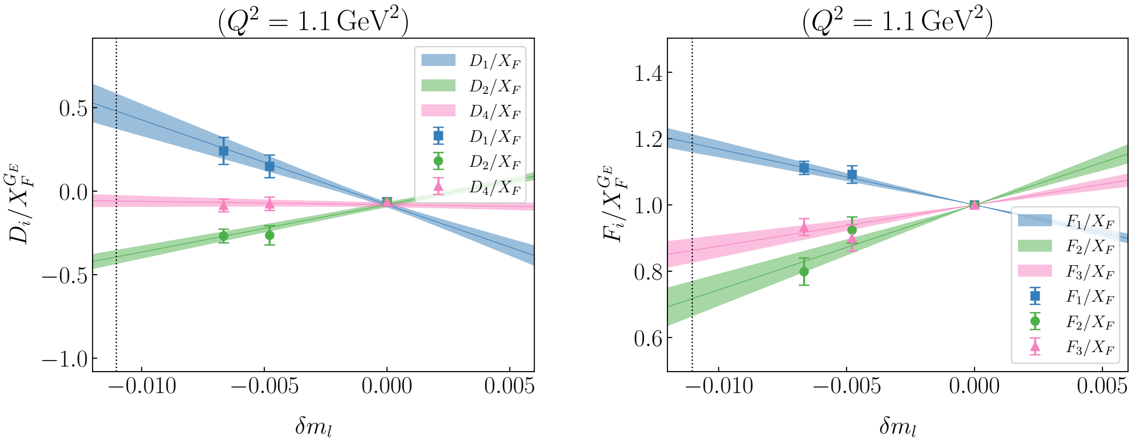

Figure 5.12. The D_i and F_i quantities for the electric form factor G_E at $Q^2 = 1.1$ GeV^2 plotted against δm_l for the three ensembles at $\beta = 5.50$, (5-7 in table 5.2). The dotted line represents the physical point. This is from the flavour diagonal form factors of the N, Ξ and Σ baryons.

5.8. Lattice Spacing and Volume Dependence

The flavour breaking expansion as outlined above takes into account only the variation of the quark masses along a specified trajectory. To further understand the systematics present in our calculations we need to account for additional factors of the lattice calculation. To do this we will extend the flavour breaking expansion to include terms involving the lattice spacing, the lattice volume and the quark mass of each ensemble. Such an expansion will only work if we are able to include form factor results at the same Q^2 value across these different ensembles. Since the momentum on each lattice is dependent on the spacing and volume, we currently do not have matching Q^2 values across the ensembles as can be seen in figure 5.13, where we show the value of Q^2 plotted against the lattice spacing a. The Q^2 values in this figure are valid for all baryons on those ensembles as a feature of the Feynman-Hellmann method is that the momentum transfer always satisfies the Breit frame condition.

5.8.1. Momenta Grouping

To allow an investigation of the effects of lattice spacing (and different δm_l values) on the form factors, we will shift the form factors on different ensembles to a common set of nearby momenta. The black lines in figure 5.13 show the values of these shifted momenta,

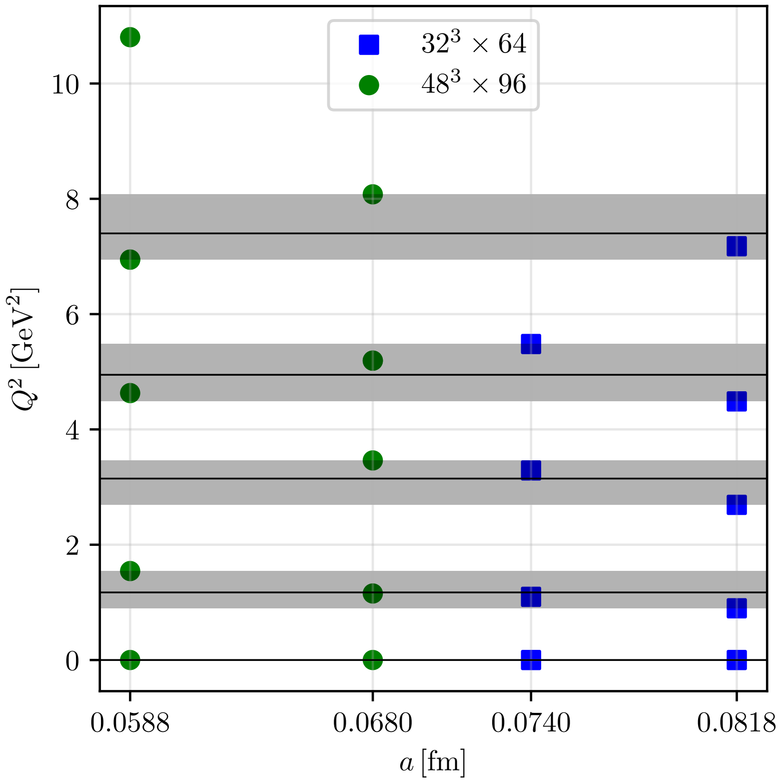

Figure 5.13. The momenta with black lines which show the average momenta of values which lie close together. The bands show the range of the values which we will scale to the black line.

Table 5.4. The five values of Q^2 which were chosen such that we can shift the form factor results on separate ensembles to them.

Q^2[GeV^2]
0
1.17
3.13
4.93
7.37

while the grey bands show the spread of the points in each grouping of momentum, the black lines are set by the average of the Q^2 values in each grouping. Table 5.4 shows these five values of Q^2. The Q^2 dependence of the form factors is most commonly parameterised by a dipole form factor [74, 92]. Other parameterisations have been observed to describe the form factors better, such as the z-expansion [93, 94], however since we have a small number of points and the dipole form is relatively simple we will use this form. Importantly, we will only use this dipole form to shift the form factors to the common Q^2 values. The dipole is defined by

$$G_D = \frac{a_D}{\left(1 + \frac{Q^2}{\Lambda^2}\right)^2}, \tag{5.34}$$

where for the parameterisation of the experimental results of the nucleon form factors, $\Lambda^2 = 0.71\,\mathrm{GeV}^2$ [92]. For our results Λ is kept as a free parameter, while for G_E, a_D is fixed to either 2 or 1 for the doubly represented and singly represented quarks respectively. For the fits to the magnetic form factor G_M, a_D is kept as a free parameter.

After fitting each of the quark contributions to both of the form factors we use these fits to shift the results to the common values of Q^2 using the following equation

$$G(Q^2_{\text{avg.}}) = G(Q^2_{\text{sim.}}) + \left(G^{\text{fit}}(Q^2_{\text{avg.}}) - G^{\text{fit}}(Q^2_{\text{sim.}})\right). \tag{5.35}$$

This shift is done by using the fit function from each bootstrap and using that to shift the data point for that bootstrap. In figure 5.14 we show an example of the fit of the dipole function to the up-quark contribution to the proton electric form factor ($G^u_{E,p}$). Also shown are the shifted form factor values which line up well with the bands.

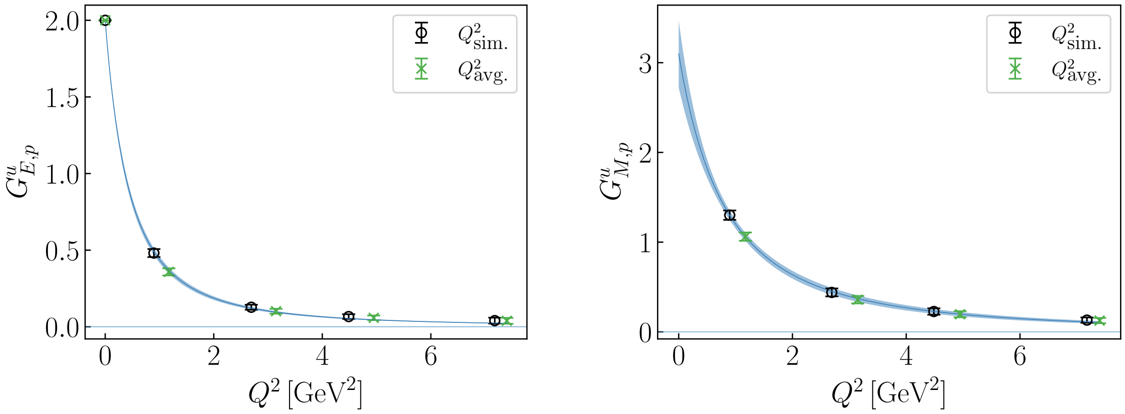

Figure 5.14. The dipole fit to the up-quark contribution to the electric (left) and magnetic (right) form factor of the proton. The simulation results are the black circles, the dipole fit is the blue band and the shifted results are the green crosses. Results are from ensemble #1 in table 5.2.

5.9. Global Fits

The previously shown flavour breaking expansion was defined in terms of δm_l. In order to combine results at different lattice spacings, we will use a dimension-less combination of observable pseudoscalar meson masses to quantify the amount of SU(3)-flavour symmetry breaking on each ensemble. To do this we will use the pion and kaon masses on each of the ensembles, redefining δm_l as

$$\delta m_l \to \frac{m_\pi^2 - X_\pi^2}{X_\pi^2}, \qquad X_\pi^2 = \frac{2m_K^2 + m_\pi^2}{3}. \tag{5.36}$$

Now we can express the flavour breaking expansion in terms of this dimensionless variable.

To account for the effects of the finite lattice spacing and lattice volume we will introduce new parameters into the expressions for both $X_{D/F}$ and D_i, F_i. To fit the singlet quantities X_D and X_F, we will use the following ansatz [79]

$$X_{D,F} = X_{D,F}^* \left(1 + c_1 \frac{1}{3}[f_L(m_\pi) + 2f_L(m_K)]\right) + c_2^{(n)} a^n + c_3 \delta m_l^2, \tag{5.37}$$

where the first term encodes the finite size effect, the function $f_L(m)$ is motivated by chiral perturbation theory [79, 95, 96], it is defined as

$$f_L(m) = (am)^2 \frac{e^{-mL}}{X_N L}, \tag{5.38}$$

and

$$X_N = \frac{m_N + m_\Sigma + m_\Xi}{3}, \tag{5.39}$$

is the average of the octet baryon masses. The index n is taken to be either 1 or 2, as it is possible that the dependence on a^2 is more dominant than that on a. We also note that the parameterisation of the lattice spacing here is only approximate as it does not take into account the differences in lattice geometry of the different $\vec{q}$ values. The ansatz for the singlet quantities in equation (5.37) now has three additional fit parameters $(c_1, c_2^{(n)}, c_3)$. The relative size of each of these additional parameters is not well known so in order to find the minimal set of parameters required to describe the results we will consider ansätze with all combinations of these parameters.

Table 5.5. The lattice ensembles restated with the lattice spacing, $m_\pi L$, the pion mass and the kaon mass for each ensemble. The numbering is that same as in table 5.2.

#	a [fm]	$m_\pi L$	m_π [MeV]	m_K [MeV]	X_N [MeV]
1	0.0818(9)	5.44	410	410	1125
2		4.84	365	424	1129
3		4.25	320	440	1097
4		3.85	290	450	1101
5	0.0740(4)	5.59	466	466	1239
6		4.32	360	505	1203
7		3.72	310	526	1187
8	0.0684(4)	6.86	412	412	1113
9		5.94	357	441	1151
10		5.04	303	457	1118
11	0.0588(3)	6.11	427	427	1192
12		5.12	358	456	1182
13		4.02	281	477	1180

We modify the ansätze for the D_i and F_i quantities with correction terms proportional to a and δm_l^2. For the D fan, $\tilde{D}_i = D_i / X_F$,

$$\tilde{D}_1 = \frac{X_D}{X_F} - 2(\tilde{r}_1 + \tilde{b}_1^{(n)} a^n)\delta m_l + \tilde{d}_1 \delta m_l^2, \tag{5.40}$$

$$\tilde{D}_2 = \frac{X_D}{X_F} + ((\tilde{r}_1 + \tilde{b}_1^{(n)} a^n) + 2\sqrt{3}(\tilde{r}_3 + \tilde{b}_3^{(n)} a^n))\delta m_l + \tilde{d}_2 \delta m_l^2, \tag{5.41}$$

$$\tilde{D}_4 = \frac{X_D}{X_F} - \frac{4}{\sqrt{3}}(\tilde{r}_3 + \tilde{b}_3^{(n)} a^n)\delta m_l + \tilde{d}_4 \delta m_l^2. \tag{5.42}$$

Similarly for $\tilde{F}_i = F_i / X_F$,

$$\tilde{F}_1 = 1 - \frac{2}{\sqrt{3}}(\tilde{s}_2 + \tilde{e}_2^{(n)} a^n)\delta m_l + \tilde{f}_1 \delta m_l^2, \tag{5.43}$$

$$\tilde{F}_2 = 1 + 4(\tilde{s}_1 + \tilde{e}_1^{(n)} a^n)\delta m_l + \tilde{f}_2 \delta m_l^2, \tag{5.44}$$

$$\tilde{F}_3 = 1 + (-2(\tilde{s}_1 + \tilde{e}_1^{(n)} a^n) + \sqrt{3}(\tilde{s}_2 + \tilde{e}_2^{(n)} a^n))\delta m_l + \tilde{f}_3 \delta m_l^2. \tag{5.45}$$

Once again we will also consider the above ansätze with the a terms replaced with a^2. The parameters of our lattice ensembles which we require for these correction terms are listed in the table 5.5.

Table 5.6. The fit results for the first non-zero momentum transfer value $Q^2 = 1.17\text{GeV}^2$. The values given for X_D, X_F, $G_{E,p}$ and $G_{M,p}$ are all determined from taking the fit functions to the limit where $a \to 0$, $m_\pi L \to \infty$ and $m_\pi, m_K \to$ physical masses.

Fit	$X_D^{G_E}$	χ^2_{dof}	$X_F^{G_E}$	χ^2_{dof}	$G_{E,p}$	χ^2_{dof} D_i	χ^2_{dof} F_i
δm_l	-0.0287(26)	0.14	0.2889(50)	3.42	0.1452(88)	0.29	0.94
$a, \delta m_l$	-0.030(30)	0.15	0.383(55)	3.45	0.31(15)	0.29	0.90
$a^2, \delta m_l$	-0.029(15)	0.15	0.341(28)	3.40	0.227(65)	0.29	0.88
δm_l^2	-0.037(17)	0.13	0.320(34)	3.66	0.160(50)	0.27	1.05
a, δm_l^2	-0.038(35)	0.14	0.420(66)	3.69	0.35(19)	0.27	1.02
a^2, δm_l^2	-0.037(23)	0.14	0.376(45)	3.64	0.26(10)	0.26	0.99
a, δm_l^2, $m_\pi L$	-0.038(35)	0.16	0.436(84)	3.96	0.37(20)	0.27	1.02
a^2, δm_l^2, $m_\pi L$	-0.037(23)	0.16	0.377(45)	3.90	0.26(10)	0.26	0.99

Fit	$X_D^{G_M}$	χ^2_{dof}	$X_F^{G_M}$	χ^2_{dof}	$G_{M,p}$	χ^2_{dof} D_i	χ^2_{dof} F_i
δm_l	0.5962(72)	1.76	0.783(11)	1.14	0.718(23)	0.43	0.77
$a, \delta m_l$	0.619(84)	1.91	0.68(13)	1.19	0.46(21)	0.33	0.80
$a^2, \delta m_l$	0.617(44)	1.90	0.741(68)	1.21	0.58(12)	0.33	0.80
δm_l^2	0.580(53)	1.91	0.724(83)	1.19	0.59(12)	0.36	0.68
a, δm_l^2	0.604(95)	2.09	0.63(15)	1.25	0.39(22)	0.27	0.69
a^2, δm_l^2	0.600(66)	2.08	0.69(11)	1.27	0.49(16)	0.27	0.68
a, δm_l^2, $m_\pi L$	0.62(11)	2.29	0.66(18)	1.38	0.41(23)	0.27	0.69
a^2, δm_l^2, $m_\pi L$	0.605(67)	2.23	0.70(11)	1.34	0.50(16)	0.27	0.68

5.9.1. Fitting X_D and X_F

In table 5.6 we list the results of the fits at one Q^2 with all the different ansätze described above. The table lists the χ^2 per degree of freedom, as well as the extrapolated values of X_D and X_F in the limit $a \to 0$, $m_\pi L \to \infty$ and $m_\pi, m_K \to$ physical masses. The results are listed for a range of combinations of correction terms to the fit functions. The fit results for the additional momentum transfer values can be found in Appendix E.

From table 5.6 we can see that the first fit which only uses the δm_l dependent terms is able to constrain the values of X_D and X_F much better than any other with no visible decrease in fit quality. Any fit which includes the lattice spacing or the lattice volume has a reduced ability to constrain these values, this then also results in a much increased uncertainty on the form factor extrapolation. We conclude from this that with the current set of ensembles we are unable to sufficiently constrain the lattice spacing and lattice volume effects. The values shown for X_D and X_F in the table are determined by taking the ansatz in (5.37) at the limit where $a \to 0$, $m_\pi L \to \infty$ and $m_\pi, m_K \to$ physical masses.

In figures 5.15, 5.16 we show the results of the third and the eighth ansatz from table 5.6. To be able to compare the simulation results with the fit results, we shift them to the limit where $a \to 0$, $m_\pi L \to \infty$ and $m_\pi, m_K \to$ physical masses by using the fit results in a similar way as Eq. (5.35). All of the simulation results are relatively far removed from the continuum limit $a \to 0$, which means that the fit results are not very well constrained in this region. It can also be noted that while there is a spread in the values of X_D and X_F, there is no clear indication of any strong a- or a^2-dependence.

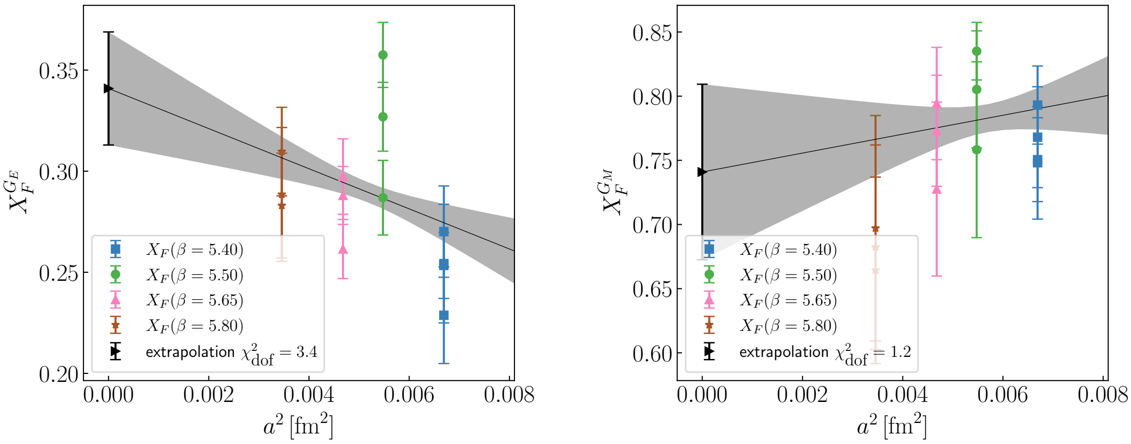

Figure 5.15. LH panel: $X_F^{G_E}$ against a^2, RH panel: $X_F^{G_M}$. The grey band is a fit using the correction term a^2 in the ansatz (third fit in table 5.6). The results are for the momentum transfer $Q^2 = 1.17\,\text{GeV}^2$.

5.9.2. Fan Plots

The results of fitting $\tilde{D}_i$ and $\tilde{F}_i$ with different variations of the ansätze shown in equation (5.40) and (5.43) are shown in table 5.6. In figures 5.17 and 5.18 we show the results of two of these fits. To present the fit function and simulation results in a clear manner we have used the fit values to shift the results to a common lattice spacing of $a = 0.07\,\text{fm}$. We have chosen a non-zero value of the lattice spacing for this comparison as shifting the results to the continuum limit reduces the clarity due to X_D and X_F being relatively unconstrained using these fits. Figure 5.17 shows that the values of D_i and F_i cluster well

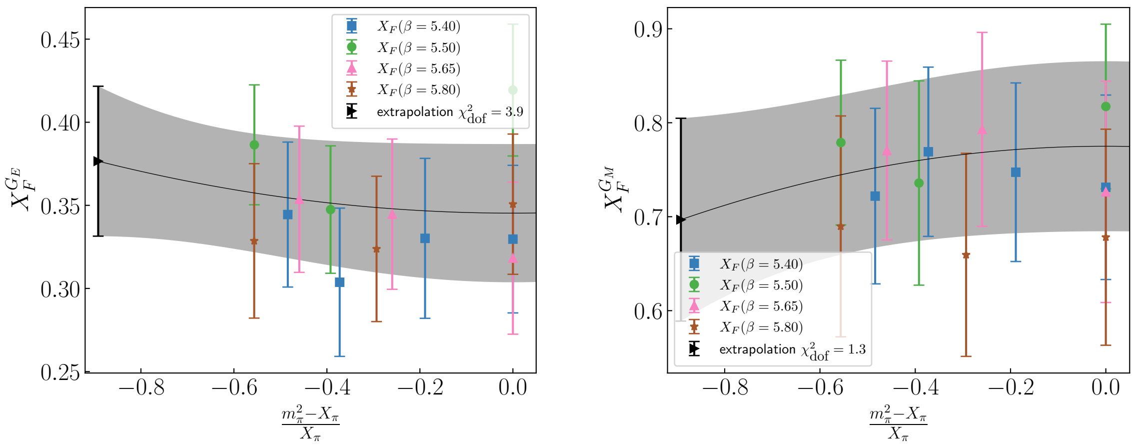

Figure 5.16. LH panel: $X_F^{G_E}$ against δm_l, RH panel: $X_F^{G_M}$. The grey band is a fit using the correction terms a^2, δm_l^2, $m_\pi L$ in the ansatz (eighth fit in table 5.6). The results are for the momentum transfer $Q^2 = 1.17\,\text{GeV}^2$. The simulation results here are shifted to the limit $a \to 0$, $m_\pi L \to \infty$ and $m_\pi, m_K \to$ physical masses using the fit results.

together and the chosen ansatz fits the points very well. The same can be said for the extrapolation shown in figure 5.18 which looks very similar apart from some increased uncertainties on the points. However as we concluded earlier due to the poor constraints on the lattice spacing and volume dependence of X_D and X_F, once the fan plots are shifted to $a = 0$, the noise on all of the points blows up. The fan plots for the magnetic form factor as well as the higher momentum transfers can be found in Appendix E.

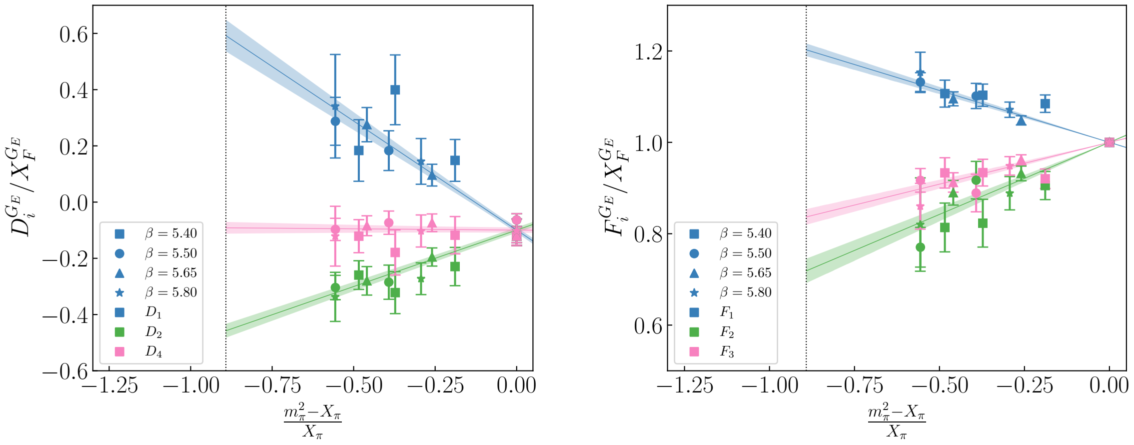

Figure 5.17. The D-fan (left) and F-fan (right) with fit ansätze using only the δm_l dependence (first fit in table 5.6).

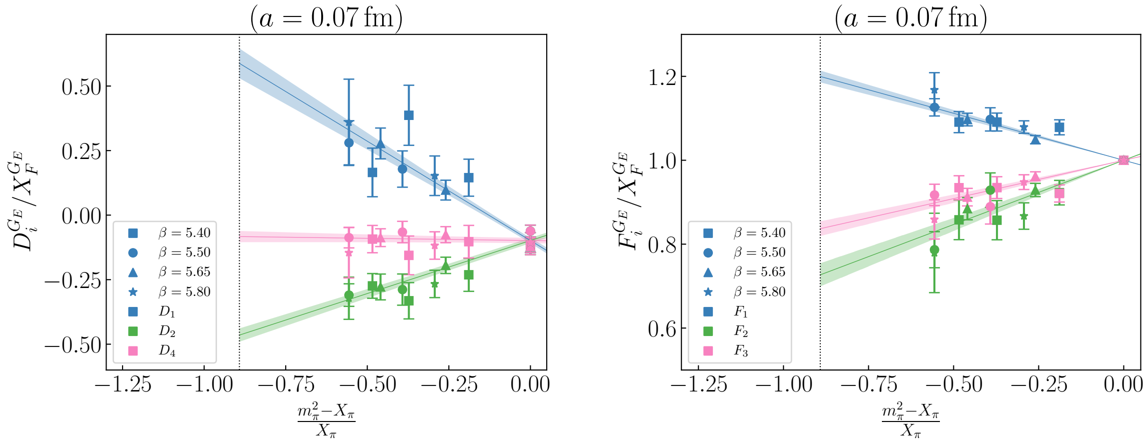

Figure 5.18. LH-panel: the D-fan with fits including the terms: $\delta m_l, a^2$ (third fit in table 5.6). RH-panel: the F-fan with fits using the same fit functions The simulation data here have been shifted to the lattice spacing of $a = 0.07\,\mathrm{fm}$.

5.10. Reconstructed Form Factors at the Physical Point

After extrapolating the parameterisations of the D- and F-fans we can use these to reconstruct the form factors in the physical limit. To do this we will multiply the fan plot parameters by the parameterisation of X_F using the same set of correction parameters

$$r_i = (\tilde{r}_i + \tilde{b}_i a)X_F, \tag{5.46}$$

$$s_i = (\tilde{s}_i + \tilde{e}_i a)X_F, \tag{5.47}$$

$$d_i = \tilde{d}_i X_F, \tag{5.48}$$

$$f_i = \tilde{f}_i X_F. \tag{5.49}$$

We also take $d = X_D/2$ and $f = X_F/2$. Now we use the currents as defined in [91] in the following combinations

$$\bar{u}\gamma u = \frac{1}{\sqrt{3}}J^{\eta'} + \frac{1}{\sqrt{2}}J^{\pi^0} + \frac{1}{\sqrt{6}}J^{\eta}, \tag{5.50}$$

$$\bar{d}\gamma d = \frac{1}{\sqrt{3}}J^{\eta'} - \frac{1}{\sqrt{2}}J^{\pi^0} + \frac{1}{\sqrt{6}}J^{\eta}, \tag{5.51}$$

$$\bar{s}\gamma s = \frac{1}{\sqrt{3}}J^{\eta'} - \sqrt{\frac{2}{3}}J^{\eta}. \tag{5.52}$$

Our calculation is restricted to the connected contributions to the form factors, this gives us some constraints on the flavour-diagonal matrix elements. There are no connected contributions for $\langle p|\bar{s}\gamma s|p\rangle$, $\langle \Sigma^+|\bar{d}\gamma d|\Sigma^+\rangle$ or $\langle \Xi^0|\bar{d}\gamma d|\Xi^0\rangle$. This constraint gives the following relations

$$A_{\bar{N}\eta' N} = \sqrt{2}A_{\bar{N}\eta N}, \tag{5.53}$$

$$A_{\bar{\Sigma}\eta'\Sigma} = \sqrt{6}A_{\bar{\Sigma}\pi\Sigma} - \sqrt{2}A_{\bar{\Sigma}\eta\Sigma}, \tag{5.54}$$

$$A_{\bar{\Xi}\eta'\Xi} = \sqrt{6}A_{\bar{\Xi}\pi\Xi} - \sqrt{2}A_{\bar{\Xi}\eta\Xi}. \tag{5.55}$$

The quark contributions to the proton form factors are therefore

$$\langle p|\bar{u}\gamma u|p\rangle = \frac{1}{\sqrt{3}}A_{\bar{N}\eta' N} + \frac{1}{\sqrt{2}}A_{\bar{N}\pi N} + \frac{1}{\sqrt{6}}A_{\bar{N}\eta N} \tag{5.56}$$

$$= \sqrt{\frac{3}{2}}A_{\bar{N}\eta N} + \frac{1}{\sqrt{2}}A_{\bar{N}\pi N}. \tag{5.57}$$

This can be constructed from a linear combination of D_1, D_4, F_1, F_2. Solving the linear equations gives

$$\langle p|\bar{u}\gamma u|p\rangle = -\frac{\sqrt{3}}{2\sqrt{2}}D_1 + \frac{\sqrt{3}}{2\sqrt{2}}D_4 + \frac{3}{2\sqrt{2}}F_1 + \frac{1}{2\sqrt{2}}F_2. \tag{5.58}$$

For our analysis we require this expression in terms of the expansion parameters. The same method gives the other connected quark contributions to the baryon form factors,

$$\langle p|\bar{u}\gamma u|p\rangle = 2\sqrt{2}f + \left(\sqrt{\frac{3}{2}}r_1 - \sqrt{2}r_3 + \sqrt{2}s_1 - \sqrt{\frac{3}{2}}s_2\right)\delta m_l \tag{5.59}$$

$$+ \left(-\frac{\sqrt{3}}{2\sqrt{2}}d_1 + \frac{\sqrt{3}}{2\sqrt{2}}d_4 + \frac{3}{2\sqrt{2}}f_1 + \frac{1}{2\sqrt{2}}f_2\right)\delta m_l^2, \tag{5.60}$$

$$\langle p|\bar{d}\gamma d|p\rangle = \sqrt{2}(f - \sqrt{3}d) + \left(\sqrt{\frac{3}{2}}r_1 + \sqrt{2}r_3 - \sqrt{2}s_1 - \sqrt{\frac{3}{2}}s_2\right)\delta m_l \tag{5.61}$$

$$+ \left(-\frac{\sqrt{3}}{2\sqrt{2}}d_1 - \frac{\sqrt{3}}{2\sqrt{2}}d_4 + \frac{3}{2\sqrt{2}}f_1 - \frac{1}{2\sqrt{2}}f_2\right)\delta m_l^2, \tag{5.62}$$

$$\left\langle \Sigma^+ \middle| \bar{u}\gamma u \middle| \Sigma^+ \right\rangle = 2\sqrt{2} f + \left(-2\sqrt{2} s_1 + \sqrt{6} s_2\right) \delta m_l \tag{5.63}$$

$$+ \left(\sqrt{2} f_3\right) \delta m_l^2, \tag{5.64}$$

$$\left\langle \Sigma^+ \middle| \bar{s}\gamma s \middle| \Sigma^+ \right\rangle = \sqrt{2}(f - \sqrt{3}d) + \left(-\sqrt{\frac{3}{2}} r_1 - 3\sqrt{2} r_3 - \sqrt{2} s_1 + \sqrt{\frac{3}{2}} s_2\right) \delta m_l \tag{5.65}$$

$$+ \left(\frac{1}{\sqrt{2}} f_3 - \sqrt{\frac{3}{2}} d_2\right) \delta m_l^2, \tag{5.66}$$

$$\left\langle \Xi^0 \middle| \bar{u}\gamma u \middle| \Xi^0 \right\rangle = \sqrt{2}(f - \sqrt{3}d) + \left(2\sqrt{2} r_3 + 2\sqrt{2} s_1\right) \delta m_l \tag{5.67}$$

$$+ \left(-\sqrt{\frac{3}{2}} d_4 + \frac{1}{\sqrt{2}} f_2\right) \delta m_l^2, \tag{5.68}$$

$$\left\langle \Xi^0 \middle| \bar{s}\gamma s \middle| \Xi^0 \right\rangle = 2\sqrt{2} f + \left(-\sqrt{\frac{3}{2}} r_1 + \sqrt{2} r_3 + \sqrt{2} s_1 - \sqrt{\frac{3}{2}} s_2\right) \delta m_l \tag{5.69}$$

$$+ \left(\frac{\sqrt{3}}{2\sqrt{2}} d_1 - \frac{\sqrt{3}}{2\sqrt{2}} d_4 + \frac{3}{2\sqrt{2}} f_1 + \frac{1}{2\sqrt{2}} f_2\right) \delta m_l^2. \tag{5.70}$$

To construct the form factors from the parameters we combine them with the values of X_D and X_F in the limit $a \to 0$, $m_\pi L \to \infty$ and $m_\pi, m_K \to$ physical masses. This will give the individual quark contributions to the form factors which can then be combined to produce the connected electromagnetic form factors of the baryons.

5.10.1. Connected Nucleon Form Factors

Using the methods in the previous section we can combine the quark contributions together with their respective electric charges (Eq. (5.2)) to produce the connected contributions to the nucleon form factors. Figure 5.19 shows the electric and magnetic form factors for the proton, showing only the results from the extrapolation with the δm_l term. The yellow dotted lines in the figures show a parameterisation of experimental data from [92]. The electric form factor shows great agreement with the data over the entire range of momentum transfers. The uncertainties on the electric form factor are also reasonably small for all but the highest momentum transfer, although we do note that many of the lattice systematics are not included in this extrapolation to the physical point. Including the other lattice ensemble variables in the extrapolation results in much larger uncertainties which are left out here as they are not very informative. The magnetic form factor results show a large discrepancy with the experimental data over the entire range of momentum transfers. The points all have similar uncertainties to the electric form factor, however we must conclude that there is some systematic uncertainty which has not been accounted for here. This could either come from some aspect of the analysis or due to our limited ability to constrain the flavour breaking expansion.

Figure 5.20 shows the electric and magnetic form factors for the neutron, again compared to a parameterisation of experimental data [92]. Since these results are related to the proton form factors through the isospin symmetry it is natural that they exhibit similar properties. The electric form factor of the neutron also shows very good agreement with the data as well as small uncertainties. The magnetic form factor shows the same discrepancy as for the proton although it is slightly smaller here.

5.10.2. Isovector Form Factors

The results from this calculation did not include the disconnected contributions to the form factors. These are expected to be small at large momenta, but nonetheless they limit our results. Isovector combinations of the form factors are very useful in this regard, because for the nucleon these quantities contain only the connected contributions. The disconnected contributions will cancel out when taking the difference. In figure 5.21 we show the isovector electric and magnetic form factors, as well as the parameterisation of experimental results [92]. The electric form factor once again shows very good agreement with the experimental results. The magnetic form factor shows less agreement which should warrant further study as this indicates that the issue does not lie with missing disconnected contributions.

For the electric form factor, the isovector combination has an interesting feature which can be seen from parameterisations of the experimental results. This is the point around $Q^2 = 4.5\,\mathrm{GeV}^2$ where the proton and neutron form factors cross over and the isovector form factor crosses zero. In figure 5.22 we show the isovector combination for the electric form factor, the lattice results shown are those from the global fit using only δm_l. The uncertainties for the isovector combination cross over zero, however the central values seem to agree well with the parameterisation of the experimental results.

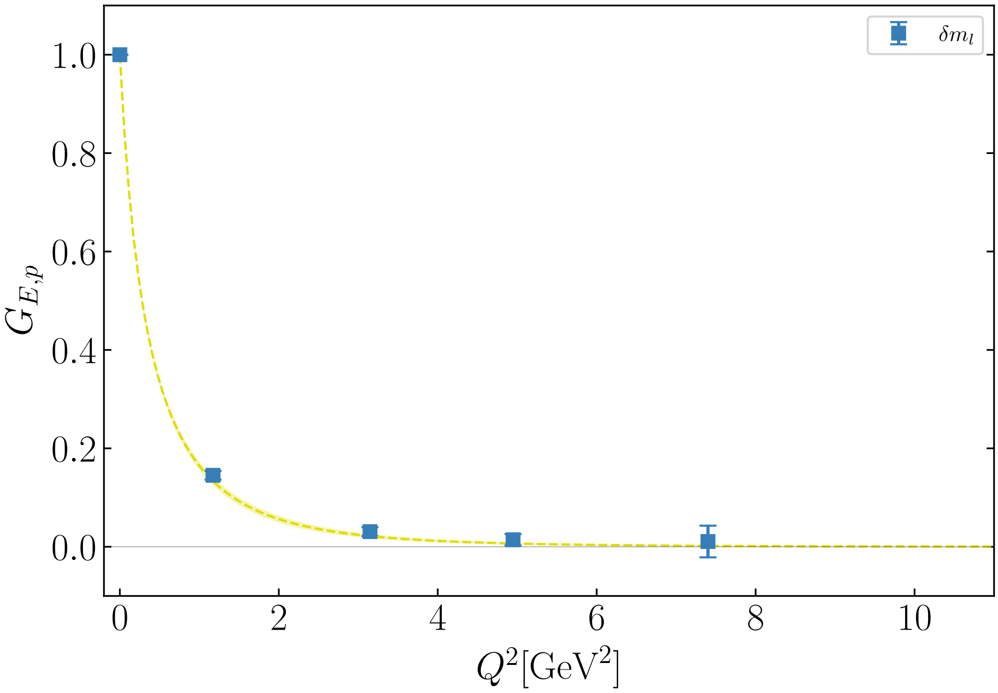

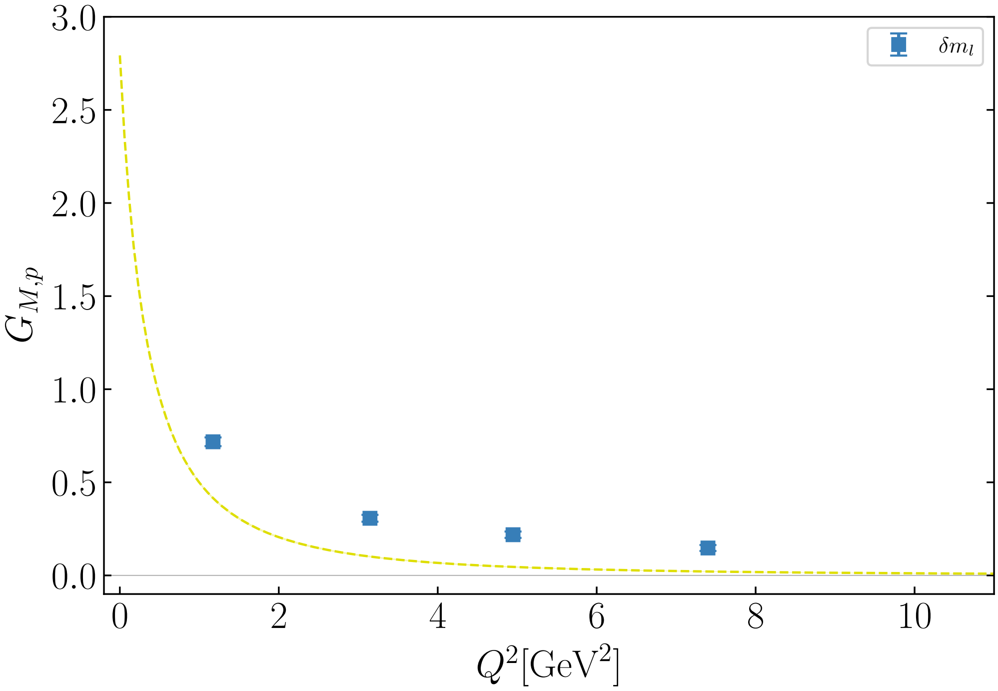

Figure 5.19. The Extrapolated values for $G_{E,p}$ and $G_{M,p}$. Showing the results from extrapolating the lattice data to the physical parameters using only the first fit listed in table 5.6. The dotted line shows the parameterisation of experimental data [76, 92]. The points are offset slightly for clarity.

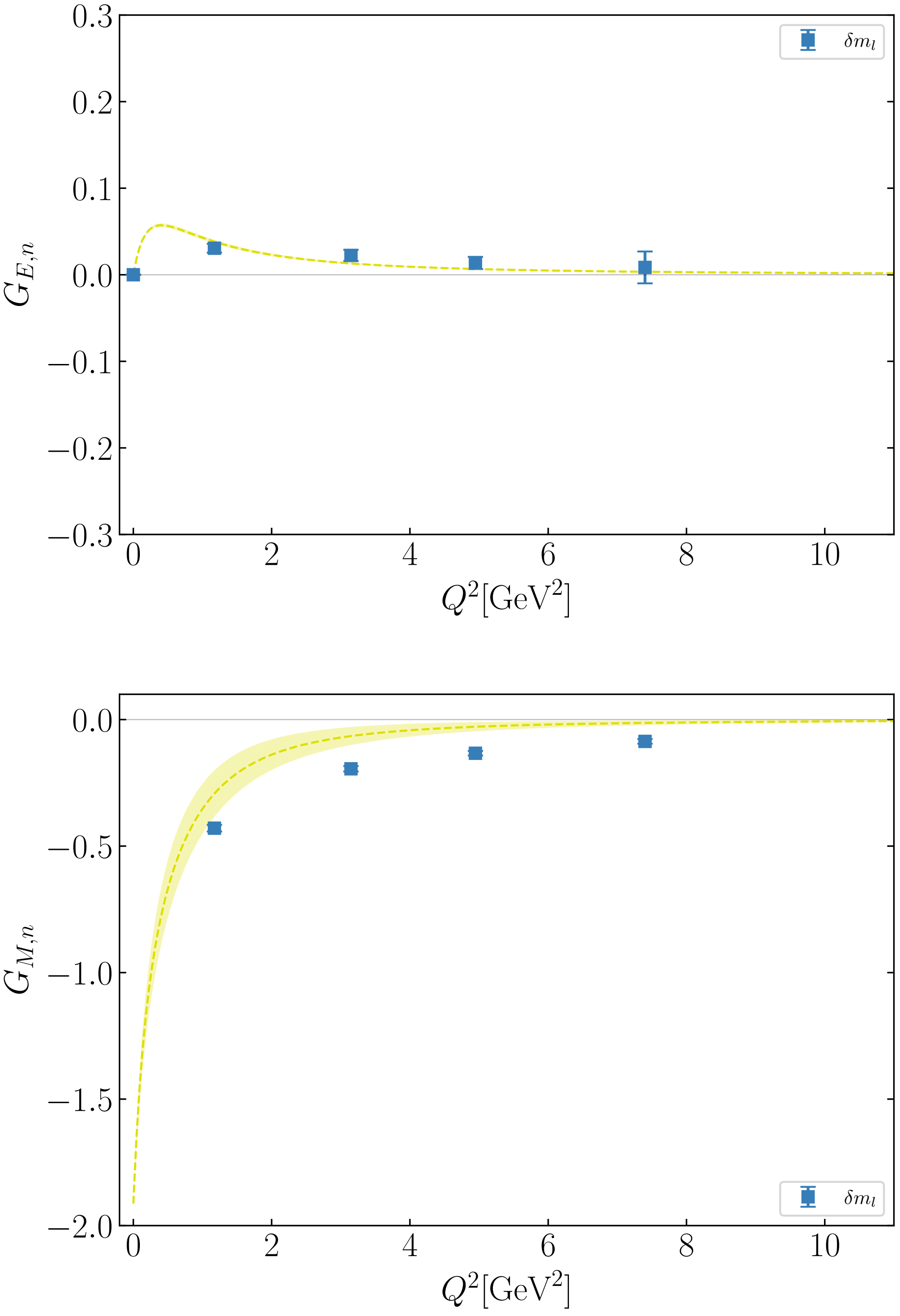

Figure 5.20. The Extrapolated values for $G_{E,n}$ and $G_{M,n}$. Showing the results from extrapolating the lattice data to the physical parameters using only the first fit listed in table 5.6. The dotted line shows the parameterisation of experimental data [76, 92].

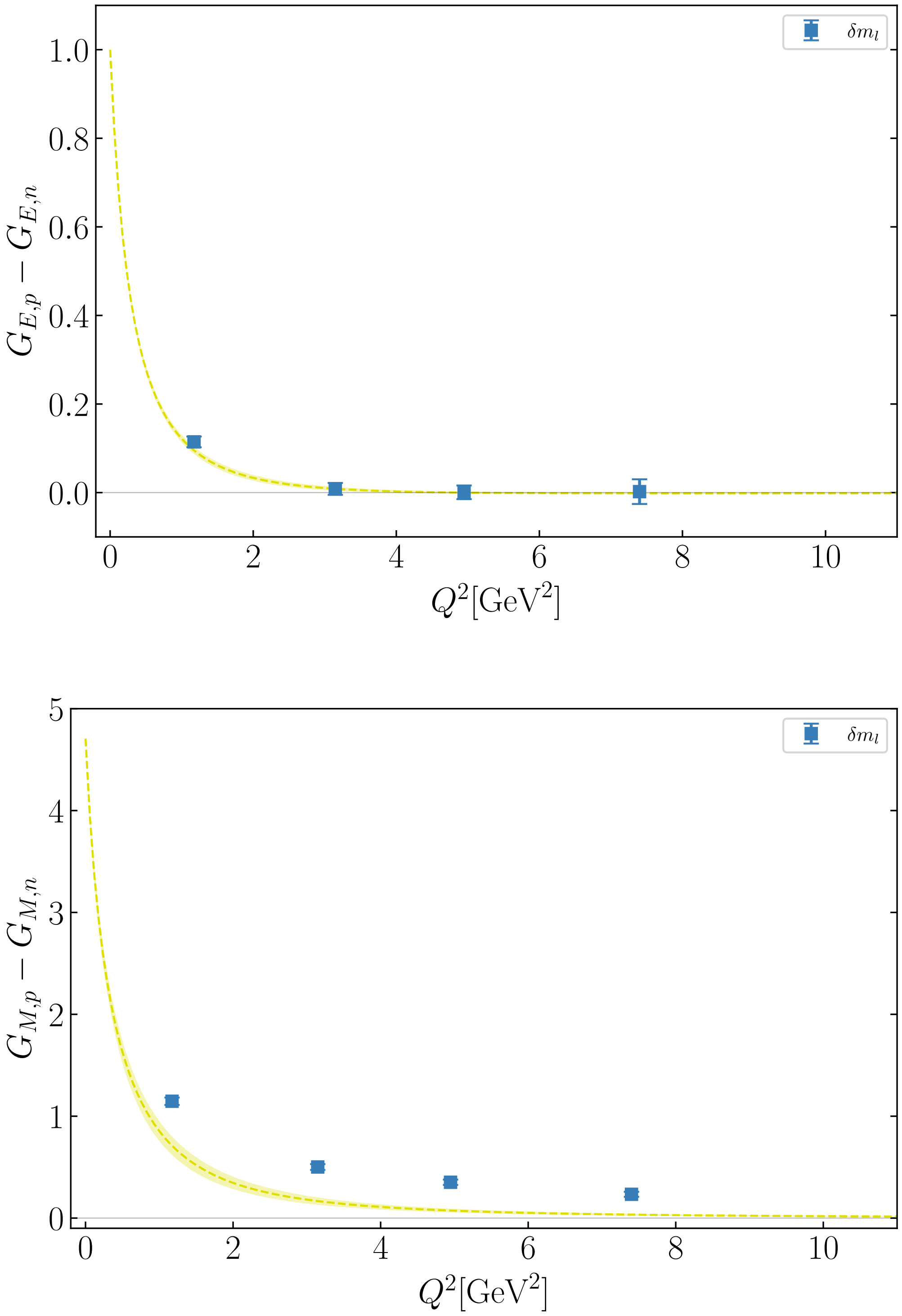

Figure 5.21. The Extrapolated values for the isovector form factors G_E and G_M. Showing the results from extrapolating the lattice data to the physical parameters using only the first fit listed in table 5.6. The dotted line shows the parameterisation of experimental data [76, 92]. The points are offset slightly for clarity.

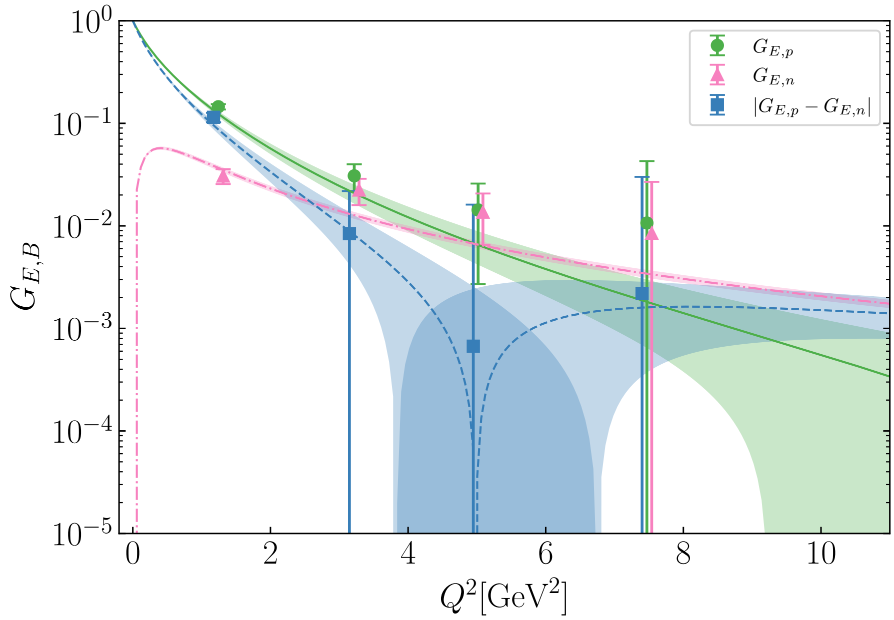

Figure 5.22. The isovector electric form factor as well as the proton and neutron electric form factors, shown on a logarithmic scale. This highlights the point around $Q^2 = 4.5\,\mathrm{GeV}^2$ where the form factors cross over and the isovector combination has a crosses zero. The lattice results shown here are from using the first global fit in table 5.6. The bands are from the Kelly parameterisation.

5.10.3. Ratio of the Electric and Magnetic Form Factors

Using the extrapolated values of the form factors we can now also consider the ratio of the electric and magnetic form factors. We can compare the the lattice results to experimental values for this ratio of form factors for the proton from Jefferson Lab [73, 97, 98]. Since the extrapolations with additional parameters were unable to constrain the form factors sufficiently, we consider only the leading order (δm_l) fit results from table 5.6. In figure 5.23 we show these results together with the experimental data. As noted before there is a large discrepancy between our results for the magnetic form factor which produces a similar discrepancy in the ratio of the form factors which can be seen in the figure. We must conclude that there is still some unknown systematic present in our calculations of the magnetic form factor or in the extrapolation of this form factor to the physical masses which is causing the large discrepancy. We do note that our results show the same downwards trend as seen in the experimental results, however it is as yet impossible to tell whether there is a zero crossing present without additional statistics at the high momentum transfers.

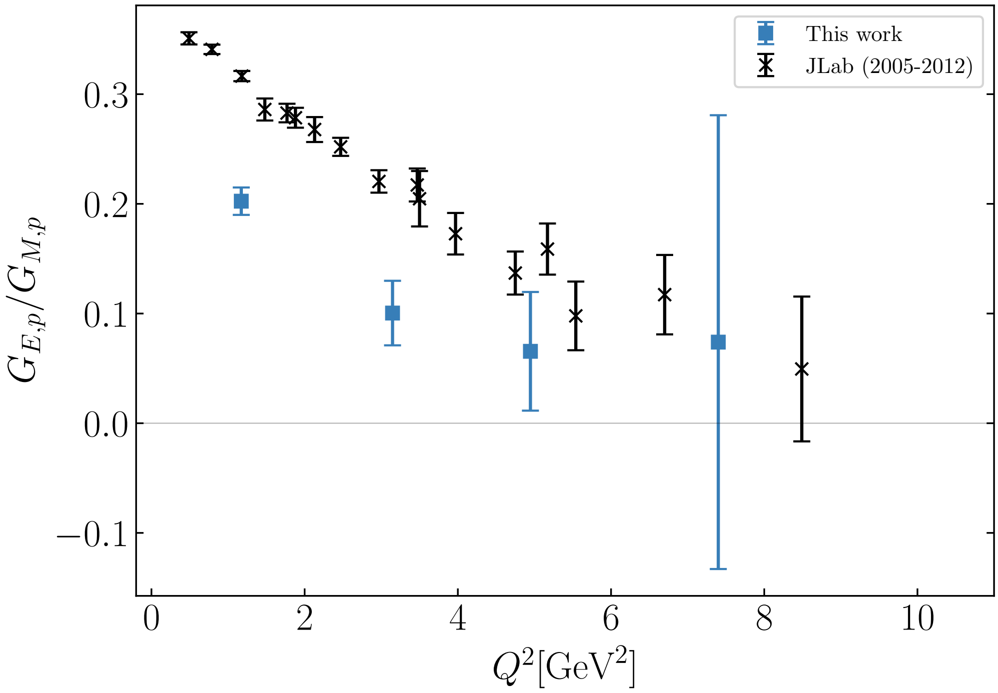

Figure 5.23. The Extrapolated values for G_E/G_M for the proton. Showing the results from extrapolating the lattice data to the physical parameters using the δm_l fit listed in table 5.6.

5.10.4. Baryon Form Factors

The flavour breaking expansion allows us to reconstruct the form factors for the nucleons as well as for the Σ baryons and Ξ baryons. We compare the doubly represented and singly represented quark contributions to G_E and G_M for these baryons in figures 5.24 and 5.25 respectively. Here we have chosen to show the results from the first global fit in table 5.6 (δm_l).

This grouping into singly and doubly represented quark contributions is useful as it allows for investigations of the environmental effects on the form factors. The difference between the $G^u_{E,p}$ and G^u_{E,Σ^+} form factors must be due to the difference in mass of the spectator quark, in this case the d-quark and s-quark. The upper plot in figure 5.24 shows these form factors and we can see that the heavier spectator quark results in an enhanced form factor. This is confirmed by comparing $G^d_{E,p}$ and $G^u_{E,\Xi}$ in the lower plot of the same figure, here again the heavier spectator quark results in an enhanced form factor. On the other hand the spectator quarks in $G^d_{E,p}$ and G^s_{E,Σ^+} are identical, thus their difference can be attributed to the difference in mass of the active quarks (d and s). Figure 5.24 shows that a heavier active quark also results in an enhanced form factor, while the comparison between $G^u_{E,p}$ and $G^s_{E,\Xi}$ confirms this relation for the doubly represented quarks.

These insights can give us some intuition as to the difference in the charge distribution between the baryons. The charge radius depends on the slope of the form factors at $Q^2 = 0$, such that a steeper slope indicates a broader charge distribution and vice versa. Using this, our results indicate that a heavier spectator quark produces a narrower charge distribution. For the active quark a larger mass also results in a narrower distribution. The magnetic form factors in figure 5.25 show the same relation at the smallest value of Q^2, however we note that for larger momenta the order of the form factors is inverted for the doubly represented quarks. We should note that this simulation was not aimed at small values of Q^2 and as such we do not show any explicit values for the charge/magnetisation distributions.

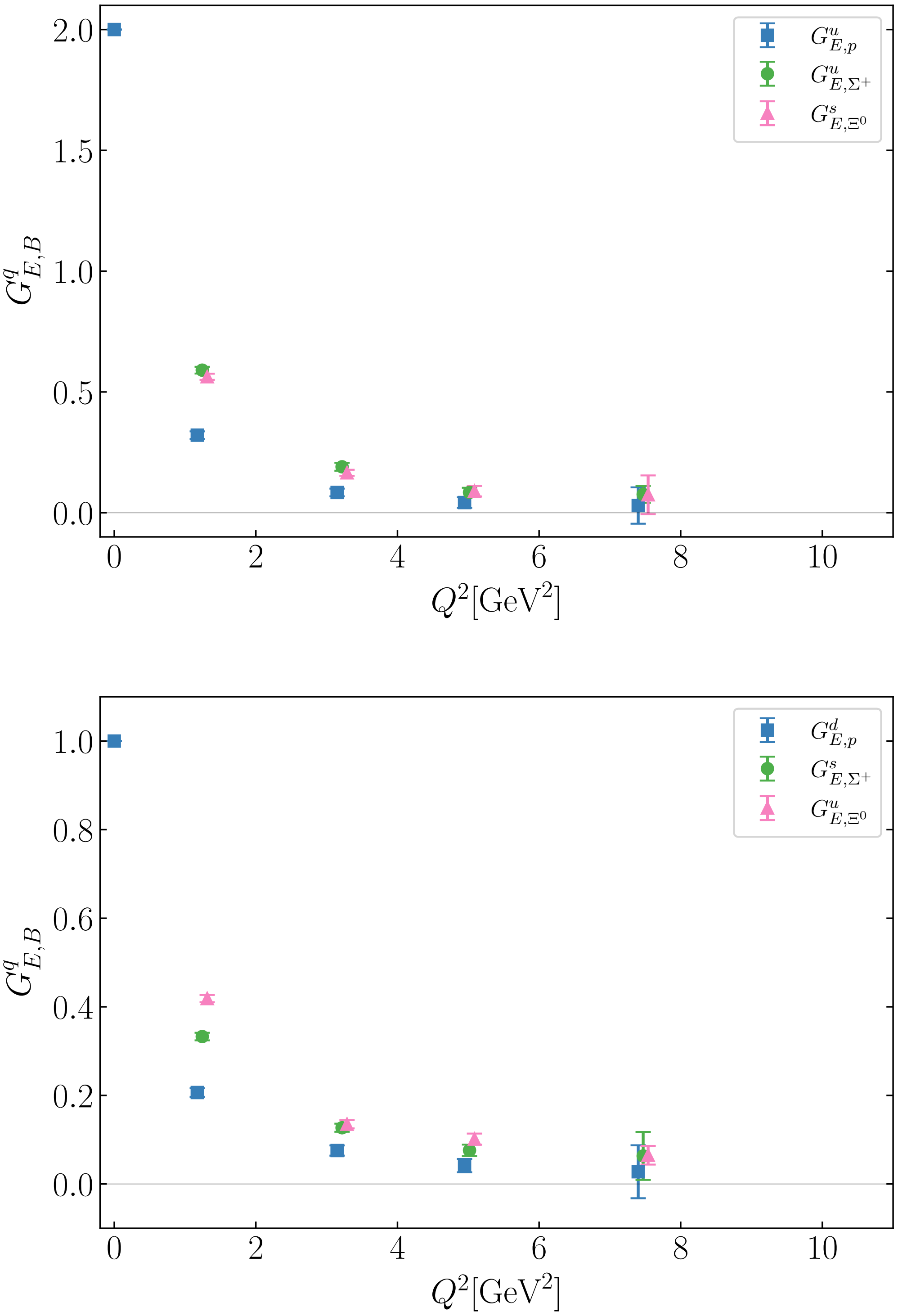

Figure 5.24. The extrapolated values of the quark contributions to the electric form factor (G_E) of each of the baryons. The upper plot shows the doubly represented quark contributions and the lower plot shows the singly represented quark contributions. The points are offset slightly for clarity.

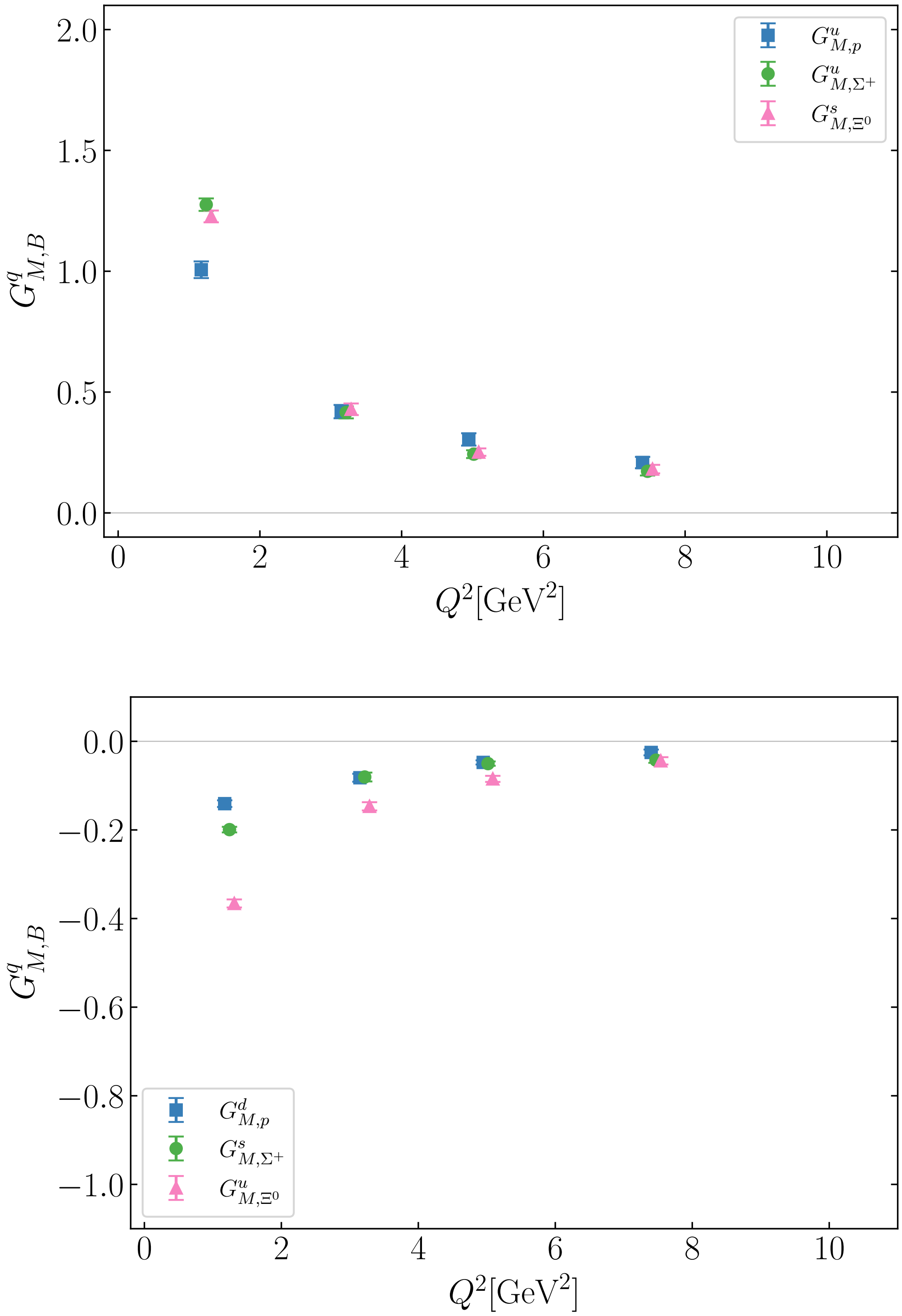

Figure 5.25. The extrapolated values of the quark contributions to the magnetic form factor (G_M) of each of the baryons. The upper plot shows the doubly represented quark contributions and the lower plot shows the singly represented quark contributions. The points are offset slightly for clarity.

Chapter 6.

Transition Matrix Elements

6.1. Weak Interactions and the CKM Matrix

Weak Interactions

In the standard model, the strong force is known to conserve flavour at all times, however the weak force allows flavour mixing interactions. This mixing is encoded in the Cabibbo-Kobayashi-Maskawa (CKM) matrix which was constructed as an extension of the Cabibbo model to the three generations of quarks [99, 100]. The CKM matrix describes the transitions between ‘up’-type quarks and ‘down’-type quarks of the three quark generations. Each element represents the probability amplitude of a quark changing flavour through a weak interaction. The elements of the 3 × 3 matrix are defined as

$$V_{\mathrm{CKM}} = \begin{pmatrix} V_{ud} & V_{us} & V_{ub} \\ V_{cd} & V_{cs} & V_{cb} \\ V_{td} & V_{ts} & V_{tb} \end{pmatrix} . \tag{6.1}$$

The standard model puts a constraint on this matrix, by requiring it to be a unitary matrix. If the CKM matrix were found to be non-unitary then this would be an indication of new physics beyond the standard model.

The unitarity constraint on the first row of the matrix can be written as

$$|V_{ud}|^2 + |V_{us}|^2 + |V_{ub}|^2 = 1, \tag{6.2}$$

where the current determinations of the magnitudes of the elements in the first row are [101]

$$|V_{ud}| = 0.97373(31), \qquad |V_{us}| = 0.2243(8), \qquad |V_{ub}| = 0.00382(20). \tag{6.3}$$

The magnitude of $|V_{ub}|$ is sufficiently small that it does not contribute significantly to the unitarity constraint, leaving the most room for improvement in the determination of the second element $|V_{us}|$. This element encodes the probability of a u-quark changing into an s-quark through the weak interaction. This can happen in various processes such as (semi-)leptonic kaon or hyperon decays.

The majority of efforts to constrain the V_{us} element have been focused on neutral kaon decays $K_L^0 \to \pi e \nu$ as well as several charged kaon decays [101, 102]. These decays allow for the extraction of the product $|V_{us} f_+(0)|$, which includes the CKM matrix element and the form factor at $q^2 = 0$. These experimental measurements can then be combined with lattice QCD calculations of the form factor $f_+(0)$ to produce results for V_{us} [103].

Hyperon Semi-leptonic Decays

Hyperons are a class of baryons containing at least one strange quarks but no heavier quarks. As an alternative to kaon decays, the $|V_{us}|$ element can also be constrained by hyperon semi-leptonic decays which satisfy $|\Delta S| = 1$.

In figure 6.1 we show a diagram of an example of a $|\Delta S| = 1$ semi-leptonic decay of the Σ^- to a neutron and a lepton-antineutrino pair. Consider the general semi-leptonic decay of a hyperon $B \to B' \, l \, \bar{\nu}_l$. We can write down the matrix element in terms of a hadronic component and a leptonic component

$$\mathcal{M} = \frac{G_S}{\sqrt{2}} \bar{u}_{B'} (\mathcal{O}_\alpha^V + \mathcal{O}_\alpha^A) u_B \; \bar{u}_e \gamma^\alpha (1 + \gamma_5) v_\nu, \tag{6.4}$$

where G_S contains the Fermi coupling constant G_F and the relevant Cabibbo mixing angle, e.g. $G_S = G_F V_{us}$ for $|\Delta S| = 1$ transitions and $G_S = G_F V_{ud}$ for $\Delta S = 0$ transitions. The matrix elements of the hadronic vector current and axial-vector current are defined

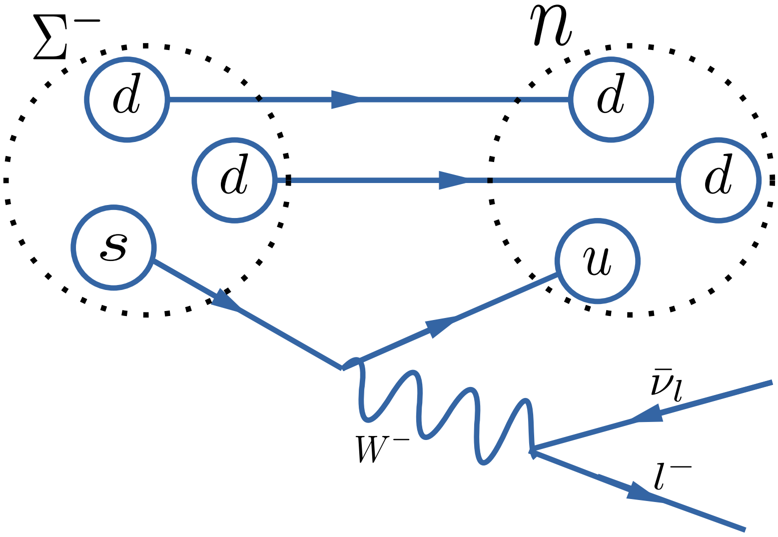

Figure 6.1. A diagram showing the semi-leptonic decay $\Sigma^- \to n\, l^-\, \bar{\nu}_l$ where a Σ^- decays into a neutron and a lepton-antineutrino pair. This transition is mediated by the weak force, which allows for the change in quark flavour from s to u.

(in Euclidean space) as

$$\mathcal{O}^V_\alpha = \gamma_\alpha f_1(Q^2) + \sigma_{\alpha\beta} q^\beta \frac{f_2(Q^2)}{M_B + M_{B'}} + q_\alpha \frac{f_3(Q^2)}{M_B + M_{B'}}, \tag{6.5}$$

$$\mathcal{O}^A_\alpha = \gamma_\alpha \gamma_5 g_1(Q^2) + \sigma_{\alpha\beta} \gamma_5 q^\beta \frac{g_2(Q^2)}{M_B + M_{B'}} + q_\alpha \gamma_5 \frac{g_3(Q^2)}{M_B + M_{B'}}. \tag{6.6}$$

The vector current is described by three form factors, the vector f_1, the weak magnetism f_2 and the induced scalar form factor f_3. The axial current is also described by three form factors, the axial vector g_1, the weak electricity g_2 and the induced pseudo-scalar form factor g_3. At zero momentum transfer $Q^2 = 0$ the first two form factors of each current are called the vector coupling and the axial-vector coupling, $g_V = f_1(0)$ and $g_A = g_1(0)$, respectively.

Additionally we define the scalar form factor $f_0(q^2)$ as the combination of the vector and induced scalar form factor

$$f_0(q^2) \equiv f_1(q^2) + \frac{q^2}{M_B^2 - M_{B'}^2} f_3(q^2), \tag{6.7}$$

which is often more convenient for the lattice QCD calculation.

In Weinberg's classification, both f_3 and g_2 are second class form factors [104]. These form factors are equal to zero when the initial and final states are the same baryon, as well as in the exact flavour-SU(3) limit.

Experimental results for the $\Sigma^- \to n e^- \bar{\nu}_e$ decay have resulted in the determinations of some ratios of these form factors. The ratio of the axial coupling over the vector coupling has been determined as $g_A/g_V = 0.340(17)$ and the ratio of the weak magnetism form factor over the vector form factor as $f_2(0)/f_1(0) = 0.97(14)$ [101, 105, 106].

Just as for the kaon decays, the product $|V_{us} f_1(0)|$ can be extracted from $|\Delta S| = 1$ hyperon semi-leptonic decay experiments [106]. For these experimental results the common assumption is made that $g_2 = 0$. The latest determination of $|V_{us}|$ from hyperon decays has produced the result $|V_{us}| = 0.2250(27)$ [107].

In the exact flavour-SU(3) limit, the value of the vector form factor $f_1(0)$ is set by the Clebsch-Gordon coefficients [107]. The Ademollo-Gatto theorem requires the corrections to $f_1(0)$ to only start at second order in the flavour-SU(3) breaking [108, 109]. Therefore a precise determination of the SU(3) breaking effects on $f_1(0)$ is required to be able to constrain $|V_{us}|$ using semi-leptonic hyperon decays.

Phenomenological determinations of the SU(3) breaking contributions to $f_1(0)$ have so far not been able to produce sufficient precision on the magnitude or the sign of the correction [110]. There is a demand for model independent calculations of these SU(3) breaking effects.

Recent lattice QCD calculations have shown a negative sign for the SU(3) breaking correction to $f_1(0)$ [31, 111–115]. The standard procedure for lattice QCD determinations of the form factor f_1 at $q^2 = 0$ has been to first determine $f_0(q^2_{\mathrm{max}})$, where $q^2_{\mathrm{max}} = (M_\Sigma - M_N)^2$, then the momentum dependence of $f_0(q^2)$ is calculated, which can then be used with an e.g. dipole ansatz to scale the value of $f_0(q^2_{\mathrm{max}})$ to $f_0(0) = f_1(0)$. The calculated value of $f_1(0)$ then needs to be extrapolated to physical pion masses to produce a reliable result.

In this chapter we will present a calculation of $f_0(q^2_{\mathrm{max}})$ from the $\Sigma^- \to n l^- \bar{\nu}_l$ transition, using a novel approach to the lattice QCD calculation based on the Feynman-Hellmann method, this is similar to the approach suggested in [56]. Additionally we will also calculate the momentum dependence of the vector matrix element. Since determining the momentum dependence of $f_0(q^2)$ requires simulations with at least two vector currents it is not included here, as we will only use one vector current. To verify the results of this new method we calculate the same quantities using the standard three-point function methods and present a comparison between the two methods. The work in this chapter also appears in [116], which has been accepted for publication by Physical Review D.

6.2. Transfer Matrix and Feynman-Hellmann

As in chapter 4, we will use the Feynman-Hellmann theorem in this calculation, we will hover present a different derivation of the method using the Dyson expansion of the transfer matrix. To start we consider a system which is determined by a Hamiltonian with a modification, $\hat{H}_\lambda(\vec{q}\,)$ and a possible momentum transfer $\vec{q}$

$$\hat{H}_\lambda(\vec{q}\,) = \hat{H}_0 - \sum_\alpha \lambda_\alpha \hat{\tilde{\mathcal{O}}}_\alpha(\vec{q}\,). \tag{6.8}$$

The sum over the index α allows for multiple modification operators $\mathcal{O}_\alpha$ with different magnitudes λ_α, however here we will just be considering a single modification.

This Hamiltonian can now be used to define lattice correlation functions. Consider a two-point correlation function of two baryon operators, where the creation operator is defined at a single space-time location and the annihilation operator is defined in momentum space

$$C_\lambda(t;\vec{q},\vec{p}\,') = \left\langle \hat{\tilde{B}}(t;\vec{p}\,')\hat{\bar{B}}(0,\vec{0}\,)\right\rangle_\lambda, \tag{6.9}$$

here the annihilation operator is defined as

$$\hat{\tilde{B}}(t;\vec{p}\,') = \int_{\vec{x}} e^{-i\vec{p}\cdot\vec{x}}\hat{B}(t,\vec{x}\,). \tag{6.10}$$

As shown in chapter 2, we can rewrite this correlation function in terms of the transfer matrix of the system (which depends on the modified Hamiltonian)

$$C_\lambda(t;\vec{q},\vec{p}\,') = \frac{\mathrm{Tr}[\hat{S}_\lambda(\vec{q}\,)^T\hat{\tilde{B}}(t;\vec{p}\,')\hat{\bar{B}}(0,\vec{0}\,)]}{\mathrm{Tr}[\hat{S}_\lambda(\vec{q}\,)^T]}, \tag{6.11}$$

where $\hat{S}_\lambda(\vec{q}\,)$ is the transfer matrix of the system. The transfer matrix is related to the Hamiltonian of the system as follows

$$\hat{S}_\lambda(\vec{q}\,) = e^{-\hat{H}_\lambda(\vec{q}\,)}. \tag{6.12}$$

The temporal length of the lattice is defined by T. If this length is taken to be sufficiently large relative to the operator insertion time, then the vacuum state will dominate the trace. Translational invariance of the operators allows them to be written as $B(t;\vec{p}\,') = S_\lambda^{-t} B(0;\vec{p}\,') S_\lambda^t$. Using this gives the following expression for the correlation function

$$\begin{aligned} C_\lambda(t;\vec{q},\vec{p}\,) &= \frac{\sum_n \langle n| e^{\hat{H}_\lambda(\vec{q}\,)(T-t)} \hat{\bar{B}}(0;\vec{p}\,') e^{\hat{H}_\lambda(\vec{q}\,)t} \hat{\bar{B}}(0,\vec{0}\,)|n\rangle}{\sum_m \langle m| e^{\hat{H}_\lambda(\vec{q}\,)T} |m\rangle} \\ &\xrightarrow{T-t \gg 0} {}_\lambda\langle \Omega | \hat{\bar{B}}(0;\vec{p}\,') S_\lambda^t \hat{\bar{B}}(0,\vec{0}\,)|\Omega\rangle_\lambda \,. \end{aligned} \tag{6.13}$$

Inserting a complete set of states we get an expression for the two-point function where the transfer matrix uses the modified Hamiltonian,

$$\begin{aligned} & C_{\lambda B' B}(t;\vec{p},\vec{q}) \\ & \quad = \sum_{X(\vec{p}_X)} \sum_{Y(\vec{p}_Y)} {}_\lambda\langle 0 | \hat{\bar{B}}'(\vec{p}\,') | X(\vec{p}_X)\rangle \; \langle X(\vec{p}_X)| \hat{S}_\lambda(\vec{q}\,)^t | Y(\vec{p}_Y)\rangle \; \langle Y(\vec{p}_Y)| \hat{\bar{B}}(\vec{0}\,)|0\rangle_\lambda \,. \end{aligned} \tag{6.14}$$

The sum over the complete set of states here can be broken up into states which are in the set of quasi-degenerate energy states and states outside this set

$$\sum_{X(\vec{p}_X)} |X(\vec{p}_X)\rangle \, \langle X(\vec{p}_X)| \equiv \sum_r^{d_s} |B_r(\vec{p}_r)\rangle \, \langle B_r(\vec{p}_r)| + \sum_{X(\vec{p}_X) \notin S} |X(\vec{p}_X)\rangle \, \langle X(\vec{p}_X)| = \hat{1}, \tag{6.15}$$

where we define the set S of quasi-degenerate energy states by their energies such that for the d_S elements of the set, their energies satisfy

$$E_{B_r}(\vec{p}_r) = \bar{E} + \epsilon_r, \qquad r = 1, ..., d_S. \tag{6.16}$$

6.3. Dyson Expansion

We write the transfer matrix with the perturbed Hamiltonian as

$$\hat{S}_\lambda(\vec{q}) = e^{-(\hat{H}_0 - \lambda\hat{\mathcal{O}}(\vec{q}))}. \tag{6.17}$$

This expression can be expanded by an approach similar to the Dyson expansion, using the following identity,

$$e^{t(\hat{A}+\hat{B})} = e^{t\hat{A}} + \int_0^t dt' e^{(t-t')\hat{A}}\hat{B}e^{t'(\hat{A}+\hat{B})}. \tag{6.18}$$

This expression can be iterated if we consider the operator $\hat{B}$ to be small. We apply this expansion to the transfer matrix for small values of λ

$$\begin{aligned} \hat{S}(\vec{q})^t &= e^{-(\hat{H}_0 - \lambda\hat{\mathcal{O}}(\vec{q}))t} \\ &= e^{-\hat{H}_0 t} + \lambda\int_0^t dt' e^{-\hat{H}_0(t-t')}\hat{\mathcal{O}}(\vec{q})e^{-\hat{H}_0 t'} \\ &\qquad + \lambda^2\int_0^t dt'\int_0^{t'} dt'' e^{-\hat{H}_0(t-t')}\hat{\mathcal{O}}(\vec{q})e^{-\hat{H}_0(t'-t'')}\hat{\mathcal{O}}(\vec{q})e^{-\hat{H}_0 t''} \\ &\qquad + \mathcal{O}(\lambda^3). \end{aligned} \tag{6.19}$$

Pulling out the first exponential and truncate the expansion at $\mathcal{O}(\lambda^2)$ gives

$$e^{-(\hat{H}_0 - \lambda\hat{\mathcal{O}}(\vec{q}))t} = e^{-\hat{H}_0 t}\left(1 + \lambda\int_0^t dt' e^{\hat{H}_0 t'}\hat{\mathcal{O}}(\vec{q})e^{-\hat{H}_0 t'} + \mathcal{O}(\lambda^2 t^2)\right). \tag{6.20}$$

Now we insert this expansion into Eq. (6.14) and consider the central matrix element for all the possible combinations in the sum over the complete set of states. Firstly we consider the case where both X and Y are elements of the set S. The matrix element then takes the following form

$$\begin{aligned} &\langle B_r|e^{-(\hat{H}_0 - \lambda\hat{\mathcal{O}})t}|B_s\rangle \\ &\quad = \langle B_r|e^{-\hat{H}_0 t}\left(1 + \lambda\int_0^t dt' e^{\hat{H}_0 t'}\hat{\mathcal{O}}e^{-\hat{H}_0 t'} + \mathcal{O}(\lambda^2 t^2)\right)|B_s\rangle && (6.21) \\ &\quad = e^{-E_{B_r}t}\delta_{rs} + \lambda e^{-E_{B_r}t}\int_0^t dt' e^{-(E_{B_s}-E_{B_r})t'}\langle B_r|\hat{\mathcal{O}}|B_s\rangle + \mathcal{O}(\lambda^2 t^2), && (6.22) \end{aligned}$$

using $\langle B_r | B_s \rangle = \delta_{rs}$. The integral over t' can be evaluated

$$\begin{aligned} & e^{-E_{B_r} t} \int_0^t dt' e^{-(E_{B_s}-E_{B_r})t'} \\ & \quad = e^{-(E_{B_r}+E_{B_s})t/2} \frac{e^{-(E_{B_r}-E_{B_s})t/2} - e^{(E_{B_r}-E_{B_s})t/2}}{E_{B_s}-E_{B_r}}. \end{aligned} \tag{6.23}$$

Since the states in the set S have quasi-degenerate energies, we can expand the energies for small deviations around the average energy. Using the fact that we defined the average energy of the set as $\bar{E}$ and each state in S has an energy defined as $E_{B_r} = \bar{E} + \epsilon_r$, then

$$\begin{aligned} & e^{-E_{B_r} t} \int_0^t dt' e^{-(E_{B_s}-E_{B_r})t'} \\ & \quad = e^{-\bar{E}t} \frac{\left[1-(\epsilon_r-\epsilon_s)\frac{t}{2}\right] - \left[1+(\epsilon_r-\epsilon_s)\frac{t}{2}\right] + \mathcal{O}\left(\epsilon^3 t^3\right)}{\epsilon_s-\epsilon_r} && (6.24) \\ & \quad = e^{-\bar{E}t} \left(t + \mathcal{O}\left(\epsilon^2 t^3\right)\right), && (6.25) \end{aligned}$$

where we note that the second order in the expansion cancels out in the difference. Inserting this back into equation (6.22)

$$\langle B_r | e^{-(\hat{H}_0 - \lambda \hat{O})t} | B_s \rangle = e^{-E_{B_r} t} \delta_{rs} + \lambda \langle B_r | \hat{O} | B_s \rangle e^{-\bar{E}t} \left(t + \mathcal{O}(\epsilon^2 t^3)\right) + \mathcal{O}(\lambda^2 t^2). \tag{6.26}$$

The same expansion for small values of ϵ can be applied to the first term

$$\begin{aligned} & \langle B_r | e^{-(\hat{H}_0 - \lambda \hat{O})t} | B_s \rangle \\ & \quad = e^{-\bar{E}t} \left[\delta_{rs} + t\left(-\epsilon_r \delta_{rs} + \lambda \langle B_r | \hat{O} | B_s \rangle\right) + \mathcal{O}(\lambda t \epsilon^2 t^2) + \mathcal{O}(\epsilon^2 t^2)\right] + \mathcal{O}(\lambda^2 t^2). \end{aligned} \tag{6.27}$$

To get to this point we have relied on two expansions, in λt and in ϵt. We will consider only the lowest orders in either expansion and denote any second order contributions from each expansion or a combination of them as $\mathcal{O}(2)$. The expression for the matrix element now reads

$$\langle B_r | e^{-(\hat{H}_0 - \lambda \hat{O})t} | B_s \rangle = e^{-\bar{E}t} \left[\delta_{rs} + t\left(-\epsilon_r \delta_{rs} + \lambda \langle B_r | \hat{O} | B_s \rangle\right) + \mathcal{O}(2)\right]. \tag{6.28}$$

6.3.1. Cross Terms

We have so far only considered the terms for which both states in the matrix elements are contained within the set S. We will consider the cross terms now

$$\begin{aligned}&\langle B_r|e^{-(\hat{H}_0-\lambda\hat{\mathcal{O}})t}|X\rangle\\&\quad=e^{-E_{B_r}t}\langle B_r|Y\rangle+\lambda e^{-E_{B_r}t}\int_0^t dt' e^{-(E_Y-E_{B_r})t'}\langle B_r|\hat{\mathcal{O}}|Y\rangle+\mathcal{O}(\lambda^2t^2).\end{aligned}\tag{6.29}$$

The inner product in the first term equals zero and the integral in the second term can be split up

$$\begin{aligned}&\langle B_r|e^{-(\hat{H}_0-\lambda\hat{\mathcal{O}})t}|X\rangle\\&\quad=\lambda\frac{e^{-E_{B_r}t}}{E_Y-E_{B_r}}\langle B_r|\hat{\mathcal{O}}|Y\rangle-\lambda\frac{e^{-E_Yt}}{E_Y-E_{B_r}}\langle B_r|\hat{\mathcal{O}}|Y\rangle+\mathcal{O}(\lambda^2t^2).\end{aligned}\tag{6.30}$$

We can expand the energy of the B_r state again in terms of the deviation from the average energy $\bar{E}$,

$$\langle B_r|e^{-(\hat{H}_0-\lambda\hat{\mathcal{O}})t}|X\rangle=\lambda e^{-\bar{E}t}\frac{1-\epsilon_rt+(\epsilon_rt)^2}{E_Y-E_{B_r}}\langle B_r|\hat{\mathcal{O}}|Y\rangle+\mathcal{O}(2)+\text{damped terms}.\tag{6.31}$$

We now define the more damped terms as any term that includes e^{-E_Yt} for $Y\notin S$, which will decay exponentially faster than $e^{-\bar{E}t}$,

$$\langle B_r|e^{-(\hat{H}_0-\lambda\hat{\mathcal{O}})t}|X\rangle=\lambda e^{-\bar{E}t}\frac{\langle B_r|\hat{\mathcal{O}}|Y\rangle}{E_Y-E_{B_r}}+\mathcal{O}(2)+\text{damped terms}.\tag{6.32}$$

Similarly for the other cross term,

$$\langle X|e^{-(\hat{H}_0-\lambda\hat{\mathcal{O}})t}|B_s\rangle=\lambda e^{-\bar{E}t}\frac{\langle X|\hat{\mathcal{O}}|B_s\rangle}{E_X-E_{B_s}}+\mathcal{O}(2)+\text{damped terms}.\tag{6.33}$$

The last set of terms in the sum over states is fully made up of damped terms

$$\langle X|e^{-(\hat{H}_0-\lambda\hat{\mathcal{O}})t}|Y\rangle=\text{damped terms}.\tag{6.34}$$

We now redefine the states in the presence of the perturbation as follows

$$|B_s(\vec{p}_s)\rangle_\lambda=|B_s(\vec{p}_s)\rangle+\lambda\sum_{E_Y\gg\bar{E}}|Y(\vec{p}_Y)\rangle\frac{\langle Y(\vec{p}_Y)|\hat{\mathcal{O}}|B_s(\vec{p}_s)\rangle}{E_Y-E_{B_s}}.\tag{6.35}$$

Using the above we can now express the two-point function from Eq. (6.14) such that the sum over all states is reduced to only go over the set S,

$$C_{\lambda BB'}(t) = \sum_{rs} {}_{\lambda}\langle 0|\hat{\bar{B}}'(\vec{p}\,')|B_r(\vec{p}_r)\rangle_{\lambda}\ \langle B_r|e^{-(\hat{H}_0-\lambda\hat{\mathcal{O}})t}|B_s\rangle\ {}_{\lambda}\langle B_s(\vec{p}_s)|\hat{\bar{B}}(\vec{0}\,)|0\rangle_{\lambda}\,. \tag{6.36}$$

At this point we can use Eq. (6.36) to determine the matrix element by extracting the term linear in time from the correlation function. However it is also possible to consider this correlation function as a Generalised Eigenvalue Problem (GEVP), doing this allows us to get a better determination of the matrix element.

6.3.2. Systematics

In order to satisfy the assumptions we have made here we require that the parameters in our expansion remain small. Additionally, since we disregard the damped terms, we also require that $t \gg 0$ to make sure these terms are sufficiently suppressed. This means $\mathcal{O}(2)$ contains $\mathcal{O}(\epsilon^2 t^2)$,$\mathcal{O}(\lambda^2 t^2)$ and $\mathcal{O}(\epsilon t \lambda t)$. To satisfy the validity of these expansions we require the following

$$0 \ll t \ll \frac{1}{\lambda}, \qquad\qquad 0 \ll t \ll \frac{1}{\max|E_{B_r} - E_{B_s}|}. \tag{6.37}$$

6.4. Generalised Eigenvalue Problem

The matrix element between the two states B_r and B_s in Eq. (6.36) can be expanded as we have shown in equation (6.28). We will define the linear-in-time part of this equation as the matrix D_{rs}

$$\langle B_r|e^{-(\hat{H}_0-\lambda\hat{\mathcal{O}})t}|B_s\rangle = e^{-\bar{E}t}\left(\delta_{rs} + tD_{rs}\right), \tag{6.38}$$

with

$$D_{rs} = -\epsilon_r\delta_{rs} + \lambda\,\langle B_r|\hat{\mathcal{O}}|B_s\rangle\,. \tag{6.39}$$

The matrix D_{rs} is a $d_S \times d_S$ Hermitian matrix, which can be diagonalised. Doing so, we let $\mu^{(i)}$ be the real eigenvalues and $e_r^{(i)}$ the orthonormal eigenvectors of this matrix (for

$i = 1, ..., d_S$). The eigenvectors will produce the identity when summed together,

$$\sum_{i=1}^{d_S} e_r^{(i)} e_s^{(i)*} = \delta_{rs}. \tag{6.40}$$

The matrix D_{rs} can then be written as a sum over the eigenvalues and eigenvectors

$$D_{rs} = \sum_{i=1}^{d_S} \mu^{(i)} e_r^{(i)} e_s^{(i)*}. \tag{6.41}$$

Now we can replace D_{rs} in Eq. (6.36) by the sum over the diagonalised components

$$\langle B_r | e^{-(\hat{H}_0 - \lambda \hat{O})t} | B_s \rangle = \sum_{i=1}^{d_S} e_r^{(i)} \left[1 + \mu^{(i)} t \right] e_s^{(i)*} \; e^{-\bar{E}t}. \tag{6.42}$$

The eigenvalues $\mu^{(i)}$ are expected to be small as they depend on the size of both ϵ and λ. Using this, we re-exponentiate the factor between the eigenvalues in Eq. (6.42),

$$\langle B_r | e^{-(\hat{H}_0 - \lambda \hat{O})t} | B_s \rangle = \sum_{i=1}^{d_S} e_r^{(i)} e_s^{(i)*} \; e^{-E_\lambda^{(i)} t}, \tag{6.43}$$

where we define the energy in the exponent as

$$E_\lambda^{(i)} = \bar{E} - \mu^{(i)}. \tag{6.44}$$

6.4.1. Correlation Function

Using the methods outlined above allows us to rewrite the original correlation function in terms of the eigen-values and -vectors of D_{rs},

$$C_{\lambda B' B}(t) = \sum_{i=1}^{d_S} A_{\lambda B' B}^{(i)} e^{-E_\lambda^{(i)} t}, \tag{6.45}$$

where we have defined the amplitudes as containing the overlap factors together with the eigenvectors

$$A_{\lambda B' B}^{(i)} = \sum_{r=1}^{d_S} Z_r^{B'} e_r^{(i)} \sum_{s=1}^{d_S} \bar{Z}_s^{B} e_s^{(i)*}, \tag{6.46}$$

with the overlap factors here being defined as

$$Z_r^{B'} = {}_{\lambda}\langle 0|\hat{\tilde{B}}'(\vec{p}\,')|B_r(\vec{p}_r)\rangle_{\lambda}\,, \tag{6.47}$$

$$\bar{Z}_s^{B} = {}_{\lambda}\langle B_s(\vec{p}_s)|\hat{\bar{B}}(\vec{0}\,)|0\rangle_{\lambda}\,. \tag{6.48}$$

Now we have a relation between the matrix element and the energy of the diagonalised correlation matrix. Determining the energies $E_{\lambda}^{(i)}$ from the perturbed two-point correlation functions now follows the same method as a Generalised Eigenvalue Problem (GEVP) which will diagonalise the time dependence of $C_{\lambda B'B}(t)$.

6.5. Quasi-Degenerate Baryon States

We will now apply the Feynman-Hellmann method to the calculation of the transition matrix element between two baryon states with quasi-degenerate energies.

6.5.1. $\Sigma \to N$ Transition

We will now consider the transition between a Σ baryon and a neutron. We would like the energies of the two baryons to be as degenerate as possible, to minimise contaminations from other energy states. To achieve this, we will use partially twisted boundary conditions for the neutron which will give it very specific momentum values which we use to tune the energies to be close together. We will consider these two states to be our set of quasi-degenerate baryons, defining them as

$$|B_1(\vec{p}_1)\rangle = |\Sigma(\vec{p}\,)\rangle, \qquad\qquad |B_1(\vec{p}_2)\rangle = |N(\vec{p}+\vec{q}\,)\rangle\,. \tag{6.49}$$

Where $E_N(\vec{p}+\vec{q}\,) \approx E_{\Sigma}(\vec{p}\,)$, we define the average energy such that both states are a small deviation away from it $E_N(\vec{p}+\vec{q}\,) = \bar{E} \pm \epsilon$ and $E_{\Sigma}(\vec{p}\,) = \bar{E} \mp \epsilon$. Any other states present in the system will have energies well above these two energies. In figure 6.2 we show the energies of the Σ and neutron plotted against their momentum. As shown, when the neutron is given a specific momentum θ, its energy will equal the mass of the Σ baryon.

In this setup we have two quasi-degenerate states in the set S, meaning that the matrix D_{rs} will be a 2×2 matrix with two eigenvalues and eigenvectors which we will

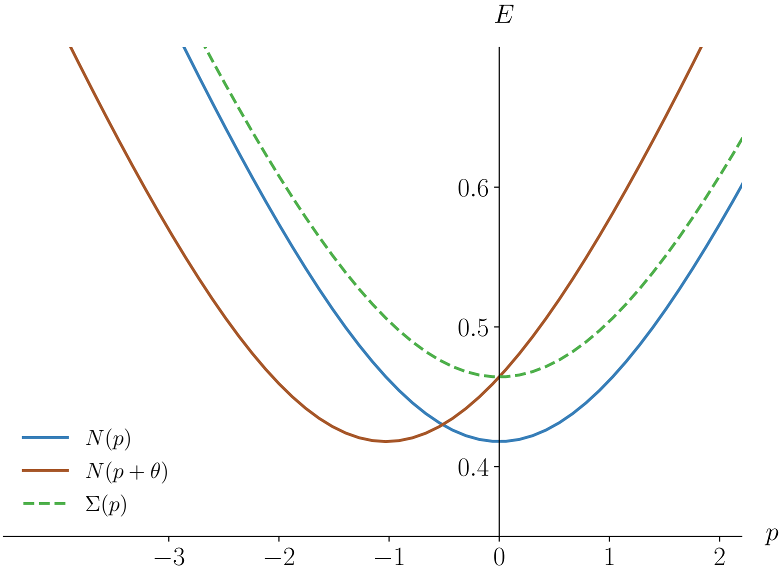

Figure 6.2. A sketch of the energy of the neutron and Σ states plotted against the momentum p. The red line shows the energy of the neutron when it has an additional momentum θ. The additional momentum θ from the twisted boundary conditions allows for the quasi-degeneracy of the energies $E_N(\theta) = E_\Sigma(0)$ as can be seen at $p = 0$.

label by ±. To satisfy momentum conservation between the states, we express the matrix elements between the two baryons as

$$\langle B_r(\vec{p}_r)|\hat{\hat{\mathcal{O}}}(\vec{q})|B_s(\vec{p}_s)\rangle = \begin{pmatrix} 0 & a^* \\ a & 0 \end{pmatrix}_{rs}, \tag{6.50}$$

where

$$a = \langle B_2(\vec{p}_2)|\hat{\mathcal{O}}(\vec{0})|B_1(\vec{p}_1)\rangle\,. \tag{6.51}$$

Now to get these matrix elements we need to determine the eigenvalues of the matrix D_{rs} in Eq. (6.39). We do this by applying the quadratic equation

$$\mu^{(\pm)} = -\frac{1}{2}(\epsilon_1 + \epsilon_2) \pm \frac{1}{2}\sqrt{(\epsilon_1 - \epsilon_2)^2 + 4\lambda^2|a|^2}, \tag{6.52}$$

this gives the modified energies

$$E_\lambda^{(\pm)} = \bar{E} - \mu^{(\pm)} = \frac{1}{2}(E_1 + E_2) \mp \Delta E_\lambda. \tag{6.53}$$

Since we only consider a set of two states here, the eigenvalues must be related by $\mu^{(+)} = -\mu^{(-)} = \Delta E_\lambda$. A more convenient form is to express the matrix element in terms of the difference between the energies from the two eigenstates,

$$\Delta E_\lambda = E_\lambda^{(-)} - E_\lambda^{(+)} = \sqrt{(E_2 - E_1)^2 + 4\lambda^2|a|^2}. \tag{6.54}$$

We can also obtain an expression for the eigenvectors from this

$$e_r^{(\pm)} = N^{(\pm)} \begin{pmatrix} \lambda|a| \\ \kappa_\pm \frac{1}{|a|} a \end{pmatrix}_r , \tag{6.55}$$

where $\kappa_\pm = \frac{1}{2}(E_1 - E_2) \pm \frac{1}{2}\Delta E_\lambda$ and $N^{(\pm)}$ are the normalisations chosen such that the eigenvectors are orthonormal. We can now use Eq. (6.54) to determine the value of the matrix element at various momentum transfers $\vec{q}$. Since the difference in the energies between the two states in our system $(E_2 - E_1)$ is also present under the square root in this relation, we expect to get a better determination when this difference is minimised.

6.6. Lattice Calculation of the Transition Matrix Element

To perform this lattice QCD calculation we are required to calculate 2-point correlation functions with a modified action. Since we are considering the transition between a Σ^- baryon and a neutron, the operator we insert into the action will introduce a mixing between the u-quark and the s-quark. This mixing requires that new elements be added to the fermion matrix,

$$S = S_g + \int_x \begin{pmatrix} \bar{u}, & \bar{s} \end{pmatrix} \begin{pmatrix} D_u & -\lambda\mathcal{T} \\ -\lambda\mathcal{T}' & D_s \end{pmatrix} \begin{pmatrix} u \\ s \end{pmatrix} + \int_x \bar{d}\, D_d\, d. \tag{6.56}$$

We note that we have split the fermionic part of the action from the gluon action (S_g) and the operator we insert is defined by

$$\mathcal{T}(x, y; \vec{q}) = \Gamma\, e^{i\vec{q}\cdot\vec{x}} \delta_{x,y}, \tag{6.57}$$

where Γ is any combination of γ-matrices. The requirement of γ_5-hermiticity gives $\mathcal{T}' = \gamma_5 \mathcal{T}^\dagger \gamma_5$. Using this action we then define the (u, s)-flavour fermion matrix as

$$\mathcal{M} = \begin{pmatrix} D_u & -\lambda \mathcal{T} \\ -\lambda \gamma_5 \mathcal{T}^\dagger \gamma_5 & D_s \end{pmatrix}, \tag{6.58}$$

where we leave out the Dirac and colour matrices, but each element is a matrix in Dirac-, colour- and coordinate space.

6.6.1. Expansion of the Green's Functions

The correlation function will be constructed out of the elements of the inverse of the matrix in Eq. (6.58). Taking the inverse gives the following matrix,

$$\begin{aligned} &\mathcal{M}^{-1} \\ &= \begin{pmatrix} (D_u - \lambda^2 \mathcal{T} D_s^{-1} \gamma_5 T^\dagger \gamma_5)^{-1} & \lambda D_u^{-1} \mathcal{T} (D_s - \lambda^2 \gamma_5 \mathcal{T}^\dagger \gamma_5 D_u^{-1} \mathcal{T})^{-1} \\ \lambda D_s^{-1} \gamma_5 \mathcal{T}^\dagger \gamma_5 (D_u - \lambda^2 \mathcal{T} D_s^{-1} \gamma_5 T^\dagger \gamma_5)^{-1} & (D_s - \lambda^2 \gamma_5 \mathcal{T}^\dagger \gamma_5 D_u^{-1} \mathcal{T})^{-1} \end{pmatrix}. \end{aligned} \tag{6.59}$$

We identify the Green's functions as the elements of the inverted fermion matrix

$$\begin{pmatrix} G_{uu} & G_{us} \\ G_{su} & G_{ss} \end{pmatrix} = \begin{pmatrix} (\mathcal{M}^{-1})_{uu} & (\mathcal{M}^{-1})_{us} \\ (\mathcal{M}^{-1})_{su} & (\mathcal{M}^{-1})_{ss} \end{pmatrix}. \tag{6.60}$$

The Green's functions for these correlators are defined as

$$\begin{aligned} G^{(uu)} &= (1 - \lambda^2 D_u^{-1} \mathcal{T} D_s^{-1} \gamma_5 \mathcal{T}^\dagger \gamma_5)^{-1} D_u^{-1} \\ G^{(ss)} &= (1 - \lambda^2 D_s^{-1} \gamma_5 \mathcal{T}^\dagger \gamma_5 D_u^{-1} \mathcal{T}^\dagger)^{-1} D_s^{-1} \\ G^{(us)} &= \lambda D_u^{-1} \mathcal{T} G^{(ss)} \\ G^{(su)} &= \lambda D_s^{-1} \gamma_5 \mathcal{T}^\dagger \gamma_5 G^{(uu)}. \end{aligned} \tag{6.61}$$

This shows that the off-diagonal elements can be written in terms of the diagonal elements. Additionally, these expressions contain nested matrix inversions, this is possible to calculate but it would be computationally expensive. To simplify the calculation, we will expand the elements of this matrix for small values of λ, which is appropriate as our calculation relies on λ being small. We also note that the expansion parameter here is λ^2 which will reduce the higher order contributions. This expansion leads to the following iterative equations for the Green's functions

$$\begin{aligned} G^{(uu)}_{2n+2} &= D_u^{-1} + \lambda^2 D_u^{-1}\mathcal{T}D_s^{-1}\gamma_5\mathcal{T}^\dagger\gamma_5 G^{(uu)}_{2n}, \\ G^{(ss)}_{2n+2} &= D_s^{-1} + \lambda^2 D_s^{-1}\gamma_5\mathcal{T}^\dagger\gamma_5 D_u^{-1}\mathcal{T}G^{(ss)}_{2n}, \\ G^{(us)}_{2n+1} &= \lambda D_u^{-1}\mathcal{T}G^{(ss)}_{2n}, \\ G^{(su)}_{2n+1} &= \lambda D_s^{-1}\gamma_5\mathcal{T}^\dagger\gamma_5 G^{(uu)}_{2n}, \end{aligned} \tag{6.62}$$

for integer values of $n = 0, 1, 2, ...$ We define the lowest order Green's functions as $G_0^{(uu)} = D_u^{-1}$ and $G_0^{(ss)} = D_s^{-1}$. These equations will approach the true form of the Green's functions for $n \to \infty$. We note that all of the odd orders in λ will contribute to the off-diagonal Green's functions while the even orders contribute to the diagonal elements. This expansion also allows for the value of λ to be set after performing the inversions, allowing us to freely choose it without additional computational costs.

The leading order results for each of the Green's functions are

$$\begin{aligned} G^{(uu)} &= D_u^{-1} + \mathcal{O}(\lambda^2), \\ G^{(ss)} &= D_s^{-1} + \mathcal{O}(\lambda^2), \\ G^{(us)} &= \lambda D_u^{-1}\mathcal{T}D_s^{-1} + \mathcal{O}(\lambda^3), \\ G^{(su)} &= \lambda D_s^{-1}\gamma_5\mathcal{T}^\dagger\gamma_5 D_u^{-1} + \mathcal{O}(\lambda^3). \end{aligned} \tag{6.63}$$

In these calculation we will use $\delta_{\vec{x},\vec{0}}\,\delta_{t,0}$ as the initial source for the Green's functions. Consider the leading order off-diagonal Green's function $G_1^{(us)}$, now with the Dirac, colour and coordinate indices explicit, as well the full expression for $\mathcal{T}$ from Eq. (6.57)

$$[G_1^{(us)}(x,0)]^{\alpha\delta}_{ad} = \lambda e^{-i\vec{q}\cdot\vec{z}}\,[D_u^{-1}(x,y)]^{\alpha\beta}_{ab}\,[\Gamma]^{\beta\gamma}\,\delta_{yz}\,\delta_{bc}\,[D_s^{-1}(z,0)]^{\gamma\delta}_{cd}, \tag{6.64}$$

where we use the Einstein convention of summing over repeated indices. If we explicitly write out the coordinate-space sum over y and z, we get the expression

$$[G_1^{(us)}(\vec{x},t;\vec{0},0)]_{ad}^{\alpha\delta} = \lambda \sum_{\vec{y}} e^{-i\vec{q}\cdot\vec{y}} \sum_{t_y} [D_u^{-1}(\vec{x},t;\vec{y},t_y)]_{ab}^{\alpha\beta} \, [\Gamma]^{\beta\gamma} \, [D_s^{-1}(\vec{y},t_y;\vec{0},0)]_{bd}^{\gamma\delta}. \tag{6.65}$$

From this expression we can see that the off-diagonal Green's function can be calculated in a similar manner to a lattice three-point function with a sequential source inversion through the operator, with a sum over the operator insertion time t_y. Similarly, the higher order contributions to the diagonal and off-diagonal Green's function are calculated by constructing sequential sources from the preceding order and summing over time, noting that the quark flavour changes after each sequential source.

Using these Green's functions we can now construct a 2×2 matrix of correlation functions

$$C_{\lambda rs}(t;\vec{q}) = \begin{pmatrix} C_{\lambda NN}(t;\vec{q}) & C_{\lambda N\Sigma}(t;\vec{q}) \\ C_{\lambda \Sigma N}(t;\vec{q}) & C_{\lambda \Sigma\Sigma}(t;\vec{q}) \end{pmatrix}, \tag{6.66}$$

where we define the correlators as follows

$$\begin{aligned} C_{\lambda NN}(t) = \sum_{\vec{x}} & e^{-i(\vec{p}+\vec{q})\cdot\vec{x}} \epsilon_{abc}\epsilon_{a',b',c'} \\ & \langle \mathrm{tr}_D[\Gamma[G^{(dd)}(x,0)]^{aa'}] \mathrm{tr}_D[[\tilde{G}^{(uu)}(x,0)]^{bb'}[G^{(dd)}(x,0)]^{cc'}] \\ & \quad + \mathrm{tr}_D[\Gamma[G^{dd}(x,0)]^{aa'}[\tilde{G}^{(uu)}(x,0)]^{bb'}[G^{(dd)}(x,0)]^{cc'}]\rangle, \end{aligned} \tag{6.67}$$

where the tilde modifies the correlator by $\tilde{G} = (C\gamma_5 G\gamma_5)^{T_D}$ and Γ is the spin projection matrix. The other correlators defined similarly, these are listed in Appendix F.

By using the iterative expressions in (6.62) it is possible to construct the correlation functions up to any order in λ (with associated computational costs). As the multiplication with lambda is done after all of the fermion matrix inversions, each order in the expansion can be calculated by adding a sequential source to the previous order

By using these expressions we can incrementally construct the correlation functions for any value of λ, as the multiplication with λ is done after all of the fermion matrix inversions. We expect there to be a sweet spot where the magnitude of lambda is sufficiently large to give a clear signal but not so large that the energy shift is outside the linear regime[1]. To get a good idea of how well the expansion holds for a range of λ values we will construct the correlation functions for values of λ up to 0.05 and consider the energy shift for each order in the expansion up to and including $\mathcal{O}(\lambda^4)$.

6.6.2. Calculation Kinematics

We will now apply the Feynman-Hellmann method to the calculation of the $\Sigma \to N$ transition. To achieve this we introduce the temporal component of the vector current γ_4 into the flavour off-diagonal elements of the action, allowing mixing between the u- and s-quark to occur. This means that the modification to the action will take the form of

$$\mathcal{T}(x, y; \vec{q}) = e^{-i\vec{q}\cdot\vec{x}}\, \delta_{xy}\, \gamma_4. \tag{6.68}$$

The modified fermion matrix produced by this action can then be approximated by constructing the sequential sources as outlined above.

As outlined in Eq. (6.49), the set of quasi-degenerate states will consist of $|\Sigma(\vec{p})\rangle$ and $|N(\vec{p}+\vec{q})\rangle$. We shall consider the case where the Σ is stationary ($\vec{p}=\vec{0}$), meaning that the Euclidean momentum transfer is given by

$$q = \left(i(M_\Sigma - E_N(\vec{q})), \vec{q}\right), \quad \text{and} \quad Q^2 = -\left(M_\Sigma - E_N(\vec{q})\right)^2 + \vec{q}^{\,2}. \tag{6.69}$$

The vector matrix element for a transition between two different baryons can be parameterised by three form factors, if we average over the spin index this gives

$$\begin{aligned}
&\langle N(\vec{q}\,', +)|\bar{u}\gamma_4 s|\Sigma(\vec{0}, +)\rangle_{\text{rel}} \\
&\quad = \sqrt{2M_\Sigma(E_N(\vec{q}) + M_N)} \\
&\qquad \left(f_1^{\Sigma N}(Q^2) + \frac{E_N(\vec{q}) - M_N}{M_N + M_\Sigma} f_2^{\Sigma N}(Q^2) + \frac{E_N(\vec{q}) - M_\Sigma}{M_N + M_\Sigma} f_3^{\Sigma N}(Q^2) \right),
\end{aligned} \tag{6.70}$$

where we have used the relativistic normalisation.

To calculate the necessary correlators on the lattice, we start with a two-point correlator for the nucleon and one for Σ. Then we construct a sequential source from this correlator using the operator defined above (Eq. (6.68)), while summing over the operator time. We do this iteratively until we have reached the correlator at $\mathcal{O}(\lambda^4)$. We

---

[1] Eq. (6.54) is not strictly linear in λ, we refer to the regime where the λ^2 term is the dominant contribution under the square root.

save the intermediate steps and contract them with other quark correlators to get a baryon spectrum for each of the four orders in lambda to check for convergence. The difference between the perturbed energies extracted from the GEVP will contain the relevant matrix element

$$\Delta E_\lambda = \sqrt{\left(E_N(\vec{q}) - M_\Sigma\right)^2 + 4\lambda^2 \left| \frac{\langle N(\vec{q},+)|\bar{u}\gamma_4 s|\Sigma(\vec{0},+)\rangle_{\text{rel}}}{\sqrt{(2E_N(\vec{q}))(2M_\Sigma)}} \right|^2} . \tag{6.71}$$

6.6.3. Partially Twisted Boundary Conditions

To be able to test the limits of our theory for quasi-degenerate baryons, we apply partially twisted boundary conditions. We do this by modifying the boundary conditions of the valence quarks by including a phase shift, which then contributes to the momentum of the quark. Applying these boundary conditions to the valence quarks is sufficient to achieve the desired energy [27,28]. The use of these partially twisted boundary conditions introduces new finite volume corrections, however these have been demonstrated to be exponentially small in the volume, and are usually neglected [32,117]. For our chosen kinematics, the neutron has a lower energy than the Σ, so we modify the boundary conditions of one of the valence quarks of the neutron to adjust its momentum. For our chosen kinematics, we introduce the twisted boundary conditions for the u-quark in the neutron, adding a twist in the y-direction. This will shift the momentum of the neutron such that its energy is closer to the mass of the Σ. The momentum of the Σ and neutron will be defined as

$$\vec{p} = \vec{0}, \qquad \vec{q} = \left(0, \frac{\theta_2}{L}, 0\right) . \tag{6.72}$$

In table 6.1 we show the various values of the twist parameter we use in this calculation. For run #5 we are able to get the energies of the neutron and Σ to be almost degenerate, while for run #2 we aimed to set the neutron energy such that the four-momentum transfer between the two states is close to zero ($Q^2 = 0$). The other momentum values are included to attempt to map out the momentum dependence of the matrix element. The column for $(M_\Sigma - M_N)$ in table 6.1 is computed from the ratio of the two-point correlators for those baryons.

Table 6.1. The chosen twist values in the y-direction and the corresponding values of $\vec{q}^{\,2}$ and the energy gap between the Σ and N.

run #	θ_2/π	$\vec{q}^{\,2}$	E_N	$M_\Sigma - E_N$	Q^2 [GeV^2]
1	0.0	0.0	0.424(11)	0.0366(33)	-0.0095
2	0.448	0.0019	0.429(10)	0.0351(35)	0.0050
3	1	0.0096	0.437(10)	0.0301(42)	0.0621
4	1.6	0.0247	0.450(12)	0.0182(57)	0.1730
5	2.06	0.0408	0.462(12)	0.0030(69)	0.2900
6	2.25	0.0488	0.469(13)	-0.0037(78)	0.3468

6.6.4. Generalised Eigenvalue Problem

The Generalised Eigenvalue Problem (GEVP) is commonly used in lattice QCD calculations to separate the ground state from excited states through the use of operators with different couplings to these states. This is often done through different amounts of smearing [118–121] or different parity projections [90]. Here we will use the GEVP to diagonalise the matrix in Eq. (6.66).

We apply the GEVP to the 2×2 correlator matrix $C_{\lambda rs}(t; \vec{0}, \vec{q})$ at a chosen time-slice t_0 and time-step Δt_0, since there will be two eigenvectors and eigenvalues we label these with ±. The GEVP is expressed as

$$C_\lambda^{-1}(t_0) C_\lambda(t_0 + \Delta t_0) u^{(i)}(t_0, \Delta t_0) = c^{(i)}(t_0, \Delta t_0) u^{(i)}(t_0, \Delta t_0), \tag{6.73}$$

$$v^{(i)}(t_0, \Delta t_0) C_\lambda(t_0 + \Delta t_0) C_\lambda^{-1}(t_0) = c^{(i)}(t_0, \Delta t_0) v^{(i)}(t_0, \Delta t_0), \qquad i = \pm \tag{6.74}$$

where $v^{(i)}$ are the left handed eigenvectors and $u^{(i)}$ are the right handed eigenvectors; $c^{(i)}$ are the eigenvalues for $i = \pm$. Solving the GEVP will give the two eigenvectors which can be combined with the correlator matrix to construct two new states. These two states are defined by the following matrix multiplication of the eigenvectors and the correlator matrix,

$$C_\lambda^{(i)}(t) = v_r^{(i)} [C_\lambda(t)]_{rs} u_s^{(i)}, \tag{6.75}$$

again for $i = \pm$. These two correlators represent the two eigenstates of the perturbed system. The eigenvectors of the correlator matrix are related to the eigenvectors of the matrix D_{rs} by

$$v_r^{(i)} = \frac{N^{(i)}}{Z_r} e_r^{(i)}, \quad \text{and} \quad u_r^{(i)} = \frac{\bar{N}^{(i)}}{\bar{Z}_s} e_s^{(i)}, \tag{6.76}$$

where $N^{(i)}$ and $\bar{N}^{(i)}$ are normalisation constants.

The transition matrix element will be contained in the energy difference between the two correlators $C_\lambda^{(-)}$ and $C_\lambda^{(+)}$. To extract this energy splitting we construct the ratio of the correlators

$$R_\lambda(t;\vec{q}) = \frac{C_\lambda^{(+)}(t;\vec{q})}{C_\lambda^{(-)}(t;\vec{q})}. \tag{6.77}$$

In the large Euclidean time limit, this ratio will behave like a one-exponential function which will show up in the effective energy as a plateau region. We use this effective energy to pick out a suitable plateau region and fit a one-exponential function to the ratio,

$$R_\lambda(t;\vec{q}) \xrightarrow{t \gg 0} \frac{A_{\lambda,0}^{(+)} e^{-E_{\lambda,0}^{(+)} t}}{A_{\lambda,0}^{(-)} e^{-E_{\lambda,0}^{(-)} t}} = B_\lambda e^{-\Delta E_\lambda t}, \tag{6.78}$$

where $\Delta E_\lambda = E_{\lambda,0}^{(+)} - E_{\lambda,0}^{(-)}$ is the energy splitting defined in equation (6.71). We can fit to this ratio with the ansatz in Eq. (6.78) to extract the energy shift ΔE_λ for a range of λ values. Once we have extracted this energy shift for a range of λ values, we can fit to it and extract a value for the matrix element by using Eq. (6.71).

6.7. Results

6.7.1. Two-point Correlators

In figure 6.3 we show the values of the correlators defined in Eq. (6.62) on a logarithmic scale. The left hand figure shows the correlators which start with a nucleon propagator and then have sequential sources appended to this i.e. $n = 0, 1, 2$ in Eq. (6.62). The right hand figure shows the correlators which start with a Σ propagator, both figures are shown for all the orders up to $\mathcal{O}(\lambda^4)$ at $\lambda = 0.025$. In the lower subplot we show the magnitude of the highest order correction for both the flavour diagonal and flavour off-diagonal correlators. The flavour off-diagonal contribution at $\mathcal{O}(\lambda^3)$ still contributes at this value of λ, while the $\mathcal{O}(\lambda^4)$ does not produce any significant correction.

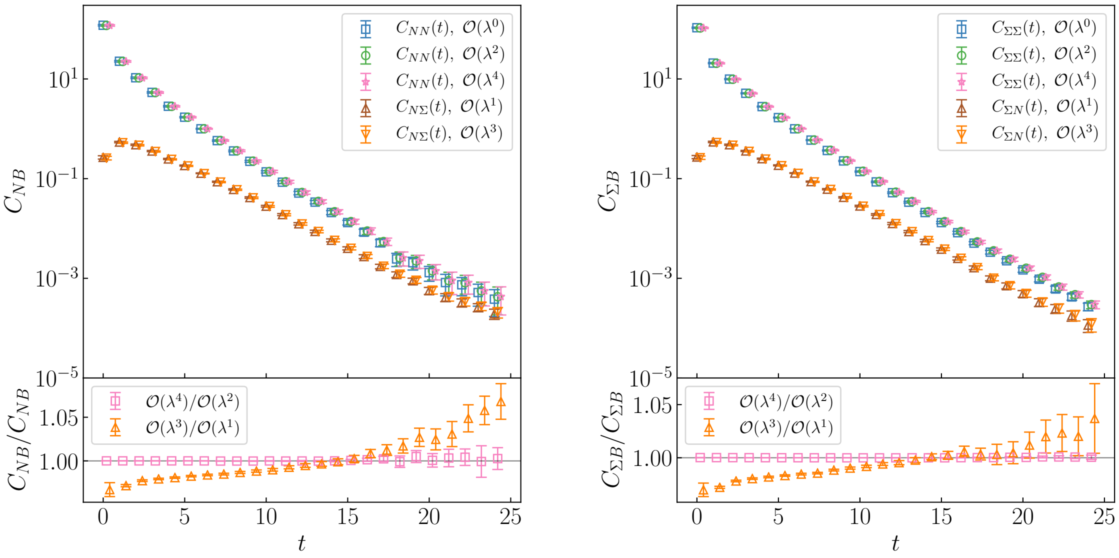

Figure 6.3. LH panel: The value of the two-point functions $C_{NN}(t)$ and $C_{N\Sigma}(t)$ versus t for $\lambda = 0.025$ at $\mathcal{O}(\lambda), \mathcal{O}(\lambda^2), \mathcal{O}(\lambda^3), \mathcal{O}(\lambda^4)$ for run #5. RH panel: similarly for the two-point functions $C_{\Sigma N}(t)$ and $C_{\Sigma\Sigma}(t)$. The lower subplot shows the magnitude of the change due to the highest order correction for both the flavour diagonal and off-diagonal correlators. The points are slightly offset for visibility

In figure 6.4 we show the effective value of the energy shift, this is determined by taking the effective energy of the ratio defined in Eq. (6.78)

$$(\Delta E_\lambda)_{\text{eff}} = -\ln\left(\frac{R_\lambda(t+1)}{R_\lambda(t)}\right). \tag{6.79}$$

The effective energy shift is shown once again for the correlators at $\mathcal{O}(\lambda^1)$, $\mathcal{O}(\lambda^2)$, $\mathcal{O}(\lambda^3)$ and $\mathcal{O}(\lambda^4)$. The left hand panel shows the results for $\lambda = 0.025$, which shows very minimal differences between the different orders in λ. The right hand panel is for $\lambda = 0.05$, here the two lowest order results clearly start to deviate from the higher order results, the results at $\mathcal{O}(\lambda^3)$ and $\mathcal{O}(\lambda^4)$ are still in agreement however. Since the approximation is truncated at a finite order of λ, it is important to be careful in pushing λ to large values as can be seen from these figures.

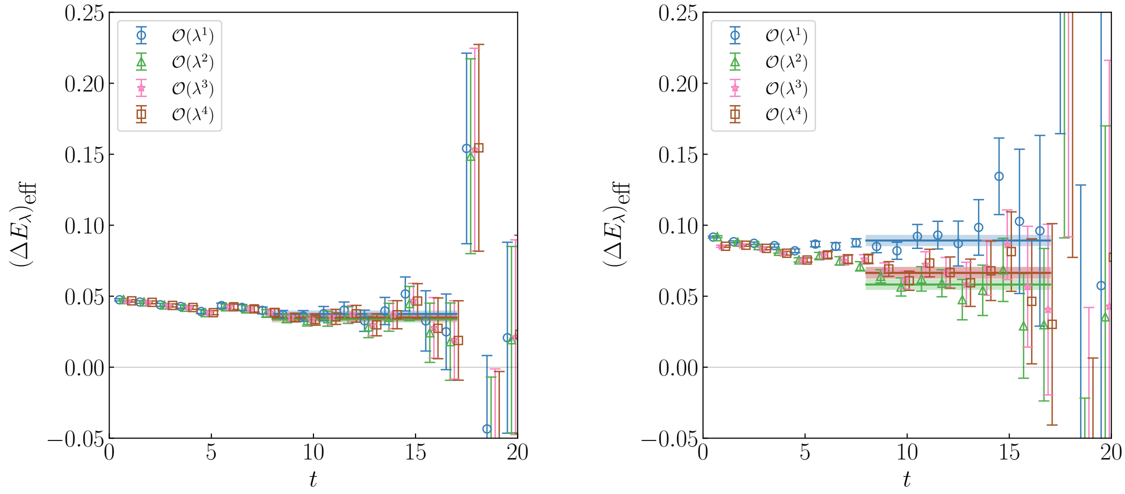

Figure 6.4. LH panel: ΔE_λ versus t for $\lambda = 0.025$ at $\mathcal{O}(\lambda), \mathcal{O}(\lambda^2), \mathcal{O}(\lambda^3), \mathcal{O}(\lambda^4)$ for run #5. RH panel: similarly for $\lambda = 0.05$. The points are slightly offset for visibility

6.7.2. Tests

GEVP Parameters

We need to check that the parameters used in the GEVP are appropriate and give reliable results. This becomes more of an issue as the energies of the two states come closer together. We will use a set of criteria to determine an optimal set of parameters introduced by [122].

- The correlation functions should have a good statistical signal over the range spanned by t_0 and Δt_0.
- The estimate of the energy difference from the eigenvalue $c^{(i)}$ should be close to the final estimate of the energy difference from the projected correlators.

The energies can be estimated from the eigenvalues $c^{(i)}$ by using $E(c^{(i)}) = -\left(\ln c^{(i)}\right)/\Delta t_0$, while by the projected correlators we refer to the correlators constructed by multiplying the correlator matrix with the eigenvectors. Since we are interested in the energy

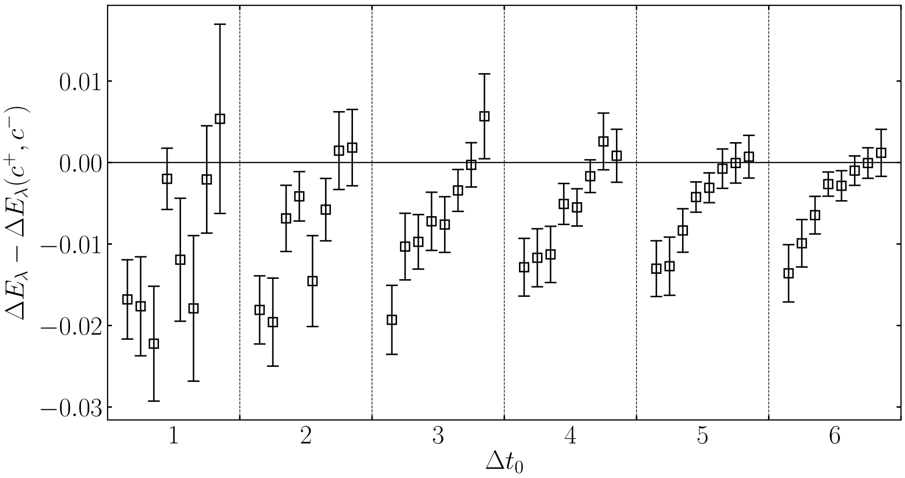

Figure 6.5. The difference between two estimates of the ΔE, one calculated from the eigenvalues of the GEVP and the other from a fit to the ratio of correlators in Eq. (6.78). The difference is shown as a function of both t_0 and Δt_0. For each value of Δt_0 it is shown for the values $t_0 = 1-8$, where the dashed lines separate the values of Δt_0. These results are from run #5. The uncertainties are reduced for $\Delta t_0 \geq 4$ and they start agreeing with zero for $t_0 \geq 6$.

difference between the two states, we will consider

$$\begin{aligned} \Delta E(c^+, c^-) &= (\ln c^{(+)} - \ln c^{(-)})/\Delta t_0 \\ &= \frac{\ln\big(c^{(+)}/c^{(-)}\big)}{\Delta t_0}. \end{aligned} \tag{6.80}$$

This will then be compared to the energy shift from fitting to the ratio of correlators as described in Eq. (6.78). Figure 6.5 shows the difference between these two estimates of the energies for run #5. For $\Delta t_0 \geq 4$ the uncertainty in the difference is reduced and for $t_0 \geq 6$ the difference starts to agree with zero. Therefore we will choose $t_0 = 6, \Delta t_0 = 4$ as the parameters for the GEVP in runs #4, #5 and #6. For the first three runs the difference between the energies of the neutron and Σ^- is large enough that the GEVP gives consistent results for smaller parameters and so we choose $t_0 = 4, \Delta t_0 = 2$ for those runs.

Eigenvectors and state mixing

The eigenvectors from the GEVP contain information about the mixing between the two baryons. The amount of mixing will be dependent on the size of λ as well as the difference

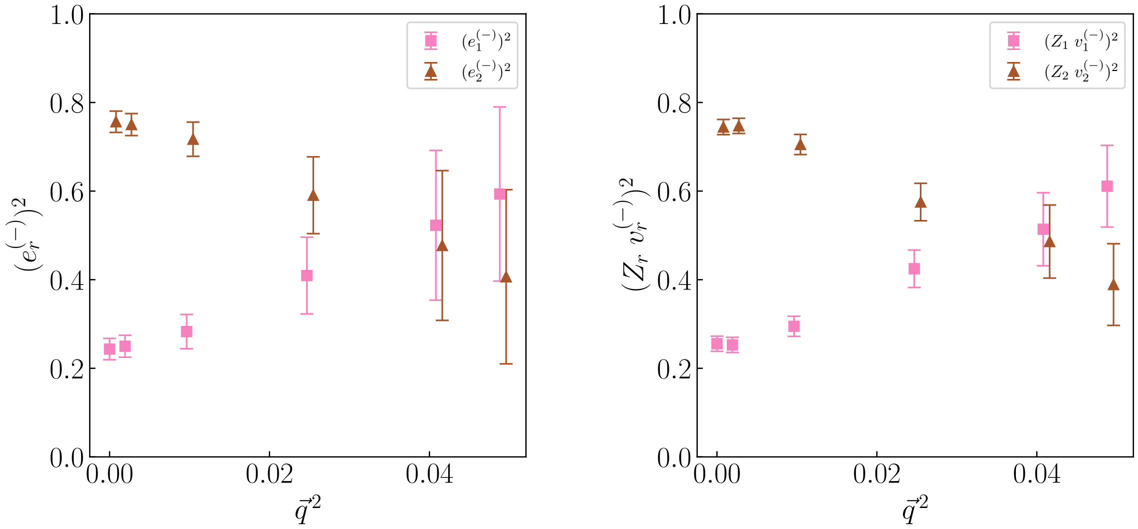

Figure 6.6. LH panel: the squared elements of the right-orthogonal eigenvector. This eigenvector is constructed from the value of the matrix element and the energy shifts through Eq. (6.55). RH panel: the eigenvector from from solving the GEVP, multiplied by the overlap factors Z_r. These two determinations of the eigenvectors should be equal as shown by equation (6.76). All eigenvectors are shown for $\lambda = 0.025$.

in energy between the two baryons. We expect there to be the most amount of mixing when the baryons are degenerate in energy and less mixing at momenta removed from this degeneracy. Figure 6.6 shows the squares of the elements of each of the eigenvectors for λ=0.025.

The left hand figure shows the eigenvectors constructed by using Eq. (6.55), using the value of the matrix element and the energies of the baryons. The right hand figure shows the eigenvectors as determined by solving the GEVP, multiplied by the appropriate overlap factor Z_r. These eigenvectors should be equal as was shown in Eq. (6.76). The squares of the eigenvalues show how much mixing is occurring due to the perturbation to the action, values close to 0.5 mean that the states are strongly mixed, while values closer to 0 and 1 imply minimal mixing of the states. We can see that for this value of λ, some mixing is occurring at all momenta, but it is maximised around $\vec{q}^2 \approx 0.03$, when the squares of the eigenvector values are around 0.5 and the energies are close to being degenerate.

6.7.3. Energy Shifts

In figure 6.7 we show the energy shift as a function of λ for each of the four orders in the expansion of the correlator. Since we can choose the value of λ freely after all of the propagators have been calculated, we show these results here as bands. The left hand figure displays the energy shifts for run #1, which shows that the lower orders in the approximation start to deviate from the expected linear behaviour at values of λ around $\lambda \approx 0.015 - 0.025$.

The right hand panel shows the energy shift for run #5, which is the run where the two states are the most degenerate in energy. It can be seen that in this case the expansion in λ holds up better as the two highest orders agree up to $\lambda \approx 0.05$. We note that the value of ΔE_λ is negative at small values of λ, in contrast to the theoretical description which predicts a purely positive energy shift. This is due to the ordering of the states being difficult to determine for small λ when the energies are near degenerate.

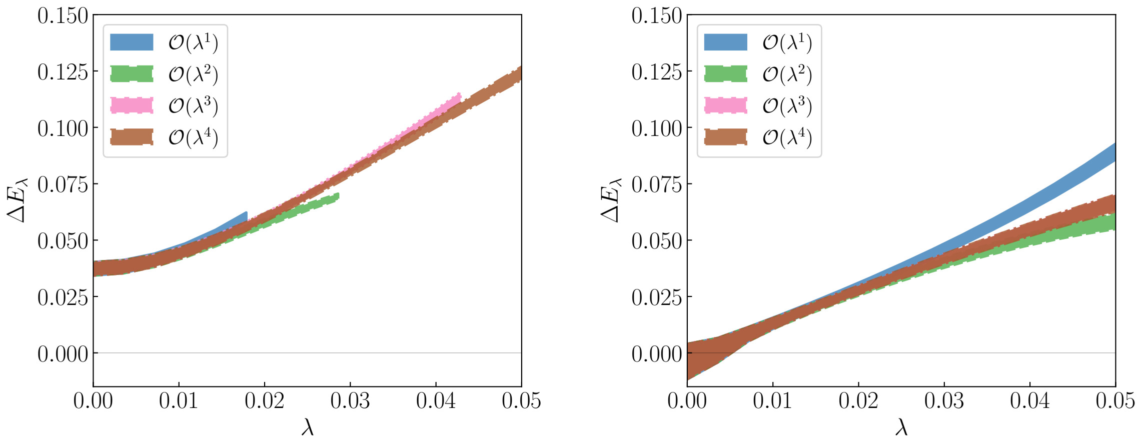

Figure 6.7. LH panel: $\Delta E_{\lambda \Sigma N}$ versus λ at $\mathcal{O}(\lambda), \mathcal{O}(\lambda^2), \mathcal{O}(\lambda^3), \mathcal{O}(\lambda^4)$ for run #1. RH panel: similarly for run #5. The bands only show the energy shifts which have been determined from a fit with $\chi^2_{\text{dof}} < 1.5$. Once λ becomes large enough that the ansatz does not produce a high quality fit, we cut off the band.

To extract a value for the matrix element we consider the results from the $\mathcal{O}(\lambda^4)$ correlator. To avoid issues with the negative energy shift we fit to the square of the energy shift, using the square of Eq. (6.71) as an ansatz

$$(\Delta E_\lambda)^2 = (E_N(\vec{q}) - M_\Sigma)^2 + 4\lambda^2 \left| \frac{\langle N(\vec{q},+)|\bar{u}\gamma_4 s|\Sigma(\vec{0},+)\rangle_{\mathrm{rel}}}{\sqrt{(2E_N(\vec{q}))(2M_\Sigma)}} \right|^2 . \tag{6.81}$$

Here the energies of the neutron and the Σ, as well as their energy difference are known quantities which we have determined by fitting to the unperturbed two-point correlation functions.

Since the energy shift is calculated from the same set of correlation functions multiplied together with different powers of λ, they are very strongly correlated. This correlation prevents the application of a conventional χ^2 goodness-of-fit test for a fit to the λ-dependence. To determine the quality of our fit we therefore investigate the region in λ where our derivation holds up well.

6.7.4. Fitting the λ-dependence

The method described here relies on the assumption that both baryons are quasi-degenerate in energy as well as assumptions on the size of the expansion parameter λ. To determine whether or not these assumptions hold, we look at the slope of the energy shift. In the limit of the energy degeneracy we expect that for sufficiently large values of λ the energy shift will show a linear behaviour.

To get an estimate of the matrix element in this quasi-degenerate limit, we can consider the ratio in Eq. (6.77) at two successive values of λ. This will take advantage of the cancellation of correlations between the ratios

$$\frac{R_{\lambda+\delta\lambda}(t)}{R_\lambda(t)} \overset{t\gg 0}{\propto} e^{-(\Delta E_{\lambda+\delta\lambda} - \Delta E_\lambda)t} . \tag{6.82}$$

Using this we can define an effective value for the matrix element by taking the effective energy of the double ratio

$$\begin{aligned} \langle \mathrm{ME} \rangle_{\mathrm{eff}}(t,\lambda) &= -\frac{1}{2\delta\lambda} \ln\left(\frac{R_{\lambda+\delta\lambda}(t+1)}{R_\lambda(t+1)} \frac{R_\lambda(t)}{R_{\lambda+\delta\lambda}(t)} \right), \\ &\xrightarrow{\substack{E_N(\vec{q})-M_\Sigma\to 0 \\ 0\ll t\ll \frac{1}{\lambda}}} \langle \mathrm{ME} \rangle , \end{aligned} \tag{6.83}$$

where we define $\langle \mathrm{ME} \rangle$ as the normalised value of the matrix element in Eq. (6.81).

In figure 6.8 we show this effective matrix element against time for the $\mathcal{O}(\lambda^4)$ results. The fits to this produce a good result and they show a good plateau region where the contributions from the ground state energy dominate.

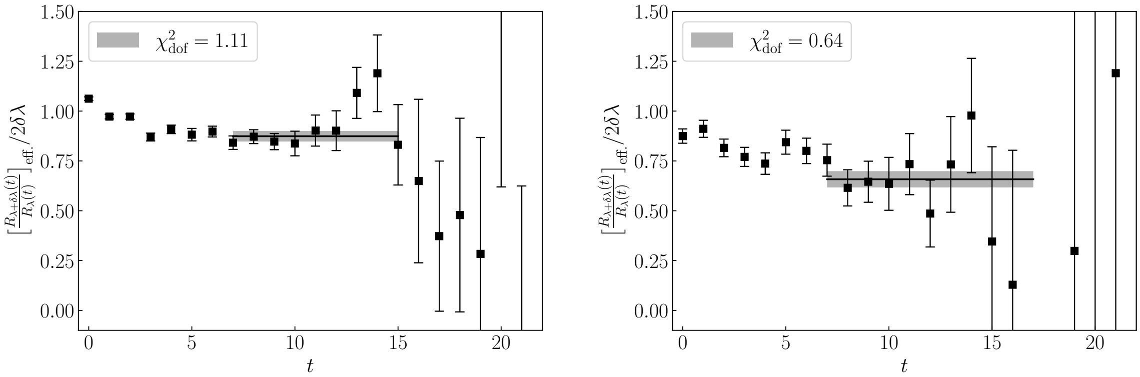

Figure 6.8. The effective energy of the double ratio of equation (6.82) versus time, showing the fit the to the slope of the λ-dependence of ΔE_λ at $\mathcal{O}(\lambda^3)$ and $\mathcal{O}(\lambda^4)$ for run #1 (LH) and run #5 (RH). For the first run, the ratio is taken at $\lambda = 0.01429$, while for the run #5 it is taken at $\lambda = 0.02143$.

In figure 6.9 we show effective matrix element as a function of λ for both $\mathcal{O}(\lambda^3)$ and $\mathcal{O}(\lambda^4)$ results. Additionally we show the value of the matrix element extracted from solving Eq. (6.81) at each value of λ. The black circles in these figures correspond with the matrix element at the value of λ used in figure 6.8. It can be seen that for the first three runs the disagreement between the two orders starts around $\lambda \approx 0.02$. For the runs #4–#6 the two highest orders start to deviate from each other around $\lambda \approx 0.03$.

These figures give us a good indication of how well our method holds up over a range of λ values. The upper limit of usable λ values is set by the agreement between $\mathcal{O}(\lambda^3)$ and $\mathcal{O}(\lambda^4)$. On the lower end of λ, the GEVP produces large uncertainties in the energy shift for runs #4–#6, which we will avoid. From these figures we determine that the range of optimal values is approximately $0 < \lambda < 0.015$ for runs #1–#3 and $0.015 < \lambda < 0.03$ for runs #4–#6.

As a last comparison we insert the extracted value for the matrix element into Eq (6.82) and compare this to the absolute value of the energy shift as a function of λ. This comparison in shown in figure 6.10 for the order $\mathcal{O}(\lambda^4)$ results of all six runs. For runs #5 and #6 there is some discrepancy at small values of λ as the energy shift was negative for certain bootstrap resamplings. The fit result however does agree well in the central region of λ which we are considering.

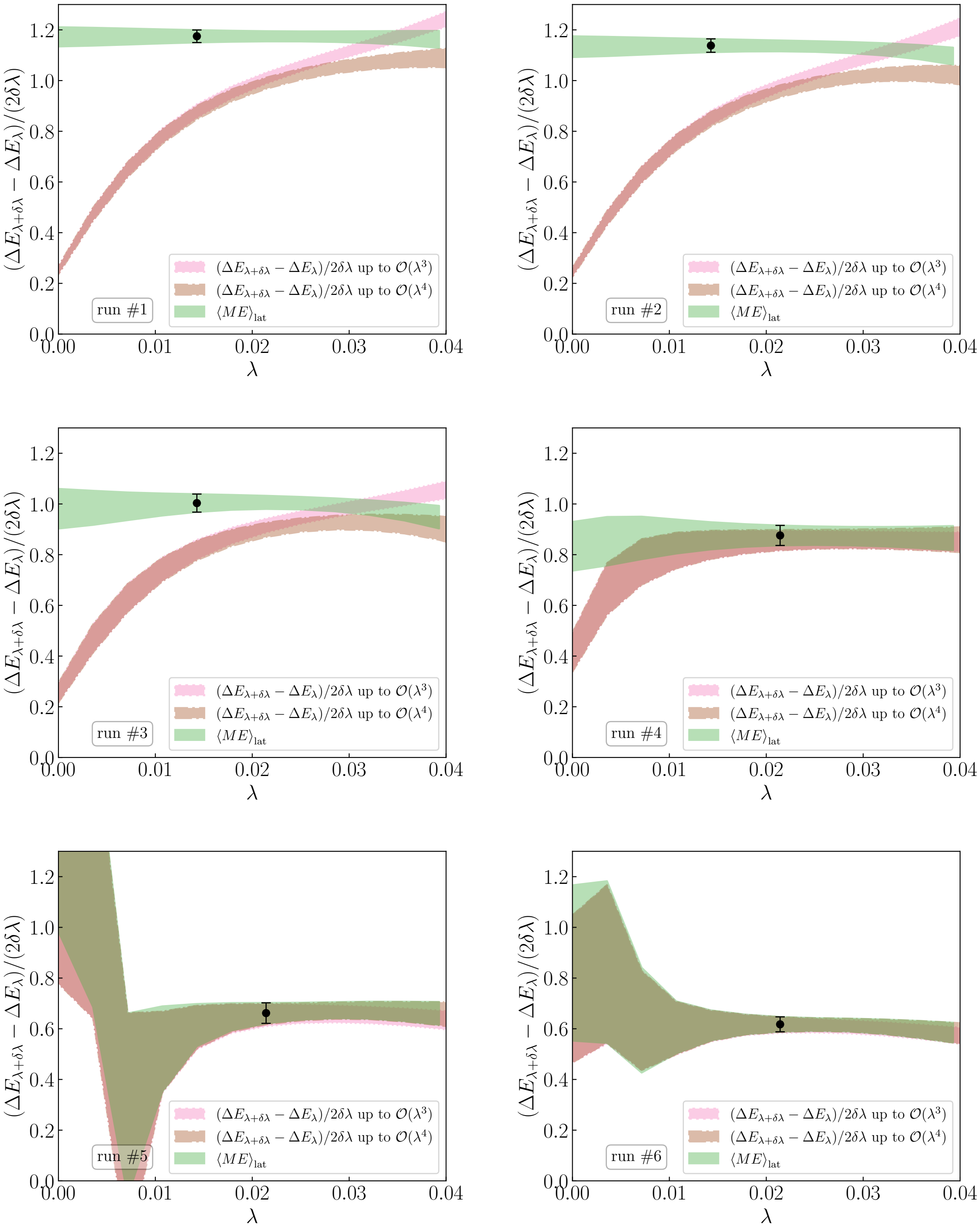

Figure 6.9. The slope of $|\Delta E_{\lambda}|$ versus λ for at $\mathcal{O}(\lambda^3)$ and $\mathcal{O}(\lambda^4)$ for all runs. The bands show the matrix element produced by taking the slope between two successive values of λ, while the black point indicates the value of λ we have chosen to keep consistent between runs.

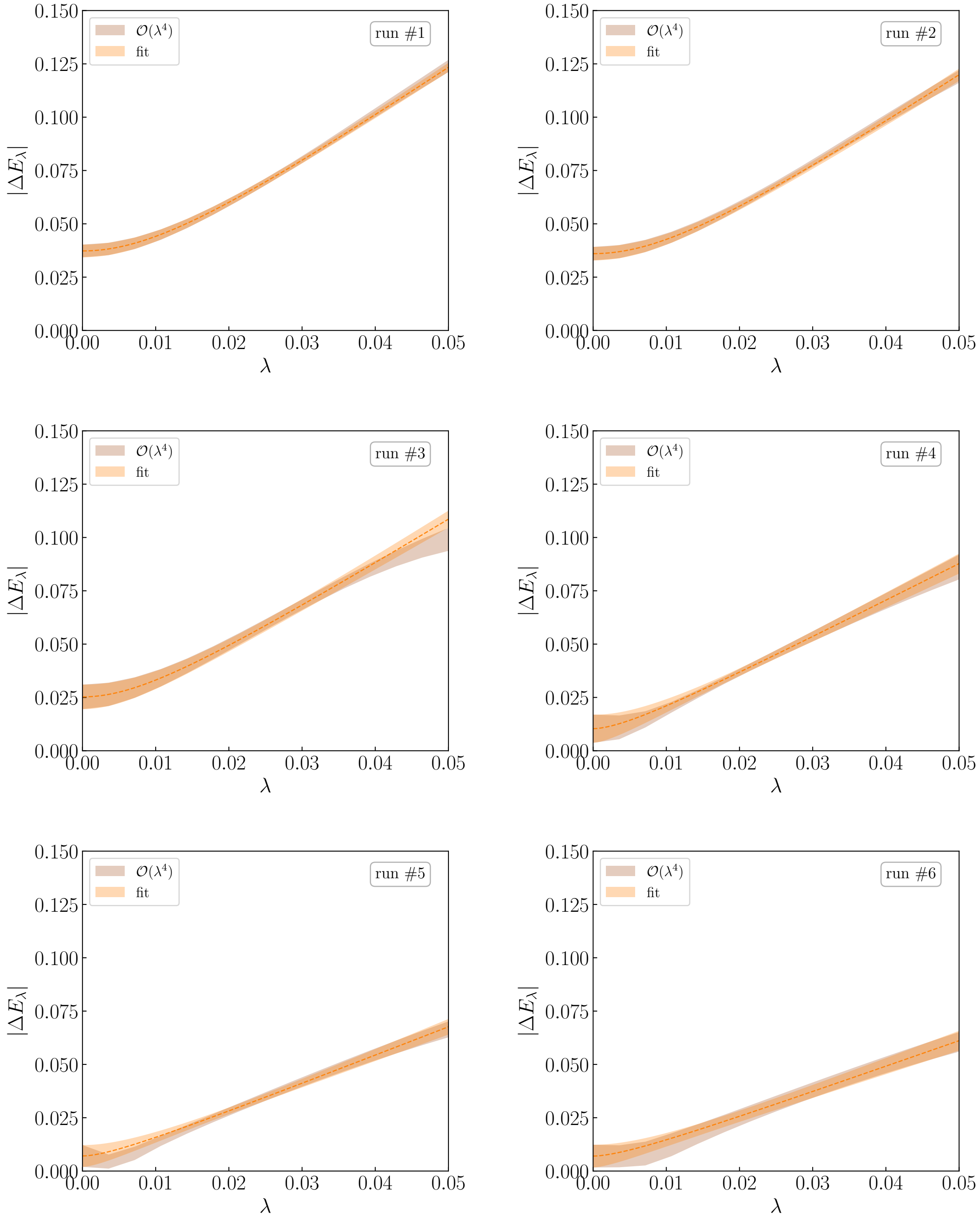

Figure 6.10. $|\Delta E_\lambda|$ versus λ for at $\mathcal{O}(\lambda^4)$ for all runs. The fit results are overlaid over the lattice results.

6.7.5. Expansion Parameters

To double check the validity of our chosen windows in time as well as λ, we can compare them to the requirements laid out in the previous section. Recall that the requirements outlined earlier were

$$0 \ll t \ll \frac{1}{\lambda}, \qquad 0 \ll t \ll \frac{1}{\max|E_{B_r} - E_{B_s}|}. \tag{6.84}$$

In this calculation, the largest values for each of the expansion parameters which we considered are

$$\begin{aligned} t_{\text{fit}} &= 8 - 16, && (6.85)\\ \frac{1}{\lambda_{\max}} &= \frac{1}{0.03} \approx 33, && (6.86)\\ \frac{1}{\max|E_{B_r} - E_{B_s}|} &= \frac{1}{0.0366} \approx 27. && (6.87) \end{aligned}$$

For runs #4–#6, the energy shift will be much smaller than the above, improving the expansion in $\mathcal{O}(\epsilon t)$. The magnitude of λ will remain consistent between the runs however.

6.7.6. Avoided Level Crossing

This calculation relies on introducing a mixing parameter between two quark flavours and determining the resulting energy shift. This shift in energy will have avoided level crossing behaviour as in perturbation theory. In figure 6.11 we show the energies of the neutron and Σ^- baryons plotted against the momentum of the neutron, for each of the runs. The left hand figure shows the unperturbed energies, while the right hand figure shows the energies after applying the GEVP to the correlator matrix. The right hand figure shows the distinctive avoided level crossing behaviour in the energies.

6.8. Three-point Function Calculation

To assess the qualities of the Feynman-Hellmann calculation we construct a similar calculation using three-point functions and compare the results of both methods. To make the comparison as informative as possible we will use the same number of lattice configurations for each run.

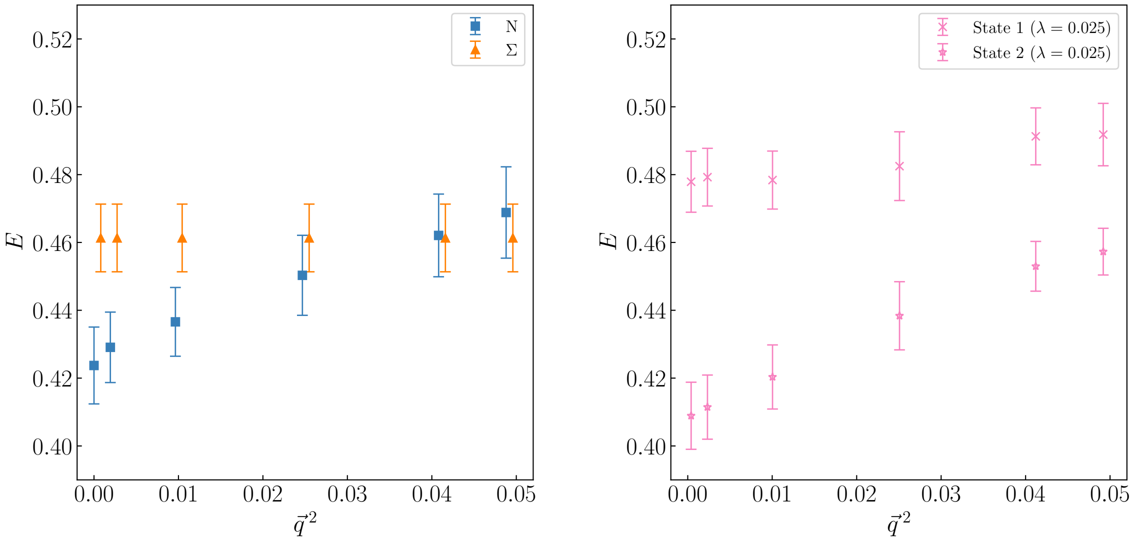

Figure 6.11. The energy of the neutron and Σ^- baryons plotted against the momentum of the neutron. The left hand panel shows the unperturbed energies of the neutron and Σ. The right hand figure shows the energies of the two states ($C_\lambda^{(-)}$, $C_\lambda^{(+)}$) which are produced by the GEVP, where the size of the perturbation is $\lambda = 0.025$.

The three-point function calculation will be constructed using a sequential source inversion through the sink, this means that the source-sink time-separation is fixed and the operator insertion time can be varied after the propagators are calculated. To get an estimate of the contribution from excited states in this calculation we simulate with three different source-sink separations ($t_{\text{sink}} = 0.74, 0.96, 1.18$ fm). The sequential source through the sink method also requires fixing the momentum at the sink. We choose to keep the sink at zero momentum allowing the initial momentum to change.

6.8.1. Lattice Three-point Functions

As shown in previous sections the lattice three-point function has a spectral decomposition. Here we consider the case of a $n \to \Sigma^-$ transition where the Σ^- is at rest,

$$\begin{aligned} G^{N\Sigma}(\Gamma_{\text{proj}}, \Gamma_{\mathcal{O}}; \vec{0}, \vec{p}; t, \tau) = \sum_{i,j} \frac{e^{-E_N^i(\vec{p})\tau} e^{-M_\Sigma^j(t-\tau)}}{M_\Sigma^j E_N^i(\vec{p})} Z_{\chi,\Sigma}^j(\vec{0}\,) \tilde{Z}_{N,\chi}^i(\vec{p}\,) \\ * F_3(\Gamma_{\text{proj}}, \Gamma_{\mathcal{O}}; \vec{0}\,, \vec{p}\,; M_\Sigma^j, M_N^i), \end{aligned} \tag{6.88}$$

and F_3 is defined in Eq. (3.47). The vertex function of the vector current $\mathcal{V}_\mu$ between two different baryons can be parameterised by three form factors

$$\begin{aligned}\langle \Sigma(\vec{p}\,',r')|\mathcal{V}_\mu(\vec{q})|N(\vec{p},r)\rangle = \bar{u}_\Sigma(\vec{p}\,',r')\Big[\gamma_\mu f_1^{N\Sigma}(Q^2) + \sigma_{\mu\nu}\frac{q_\nu}{M_N+M_\Sigma} f_2^{N\Sigma}(Q^2) \\ + i\frac{q_\mu}{M_N+M_\Sigma} f_3^{N\Sigma}(Q^2)\Big] u_N(\vec{p},r),\end{aligned} \tag{6.89}$$

where $q = p' - p$. We will consider this three-point function for the case where the Σ baryon at the sink is fixed at zero momentum $\vec{p}\,' = \vec{0}$ and only the initial neutron can have non-zero momentum. Using the two-point and three-point functions we can construct a ratio which will remove any time dependence in the limit where both time intervals are sufficiently large $(\tau, t-\tau \gg 0)$

$$\begin{aligned}R(\Gamma_{\text{Proj}},\mathcal{O};t,\tau;\vec{0}\,,\vec{p}\,) = \frac{G^{N\Sigma}(\Gamma_{\text{Proj}};\mathcal{O};t,\tau;\vec{0}\,,\vec{p}\,)}{G^{\Sigma}(t,\vec{0}\,)} \\ \sqrt{\frac{G^{\Sigma}(\tau,\vec{0}\,)G^{\Sigma}(t,\vec{0}\,)G^{N}(t-\tau,\vec{p}\,)}{G^{N}(\tau,\vec{p}\,)G^{N}(t,\vec{p}\,)G^{\Sigma}(t-\tau,\vec{0}\,)}},\end{aligned} \tag{6.90}$$

where all the two-point functions are projected onto the unpolarised, positive parity state. Consider the temporal vector current $\mathcal{V}_4$ and the unpolarised projector for the kinematics above, then in the large Euclidean time limit, this ratio will reduce to the matrix element with some kinematic factors

$$R(\Gamma_{\text{unpol}},\mathcal{V}_4;t,\tau;\vec{0}\,,\vec{p}\,) \xrightarrow{\tau,t-\tau\gg 0} \frac{F_3(\Gamma_{\text{unpol}},\Gamma_{\mathcal{V}_4};\vec{0}\,,\vec{p}\,)}{M_\Sigma\sqrt{2E_N(\vec{p}\,)(E_N(\vec{p}\,)+M_N)}} \tag{6.91}$$

$$= \frac{1}{2\sqrt{E_N(\vec{p}\,)M_\Sigma}}\,\langle N(\vec{p}\,,+)|\bar{u}\gamma_4 s|\Sigma(\vec{0},+)\rangle_{\text{rel}}\,. \tag{6.92}$$

We will once again consider a two-exponential function as the ansatz for fitting the ratio. The ansätze with two exponentials for both the two-point functions and the ratio are

$$G^{\Sigma}_{\text{fit}}(t,\vec{p}) = \sum_{i=0}^{1} A_i^{\Sigma} e^{-E_i^{\Sigma} t}, \qquad G^{N}_{\text{fit}}(t,\vec{p}) = \sum_{i=0}^{1} A_i^{N} e^{-E_i^{N} t}, \tag{6.93}$$

$$\begin{aligned} R(t,\tau;\vec{0},\vec{p}) &= \sum_{i,j=0}^{1} \sqrt{A_i^{\Sigma} A_j^{N}}\; B_{ij}\; e^{-E_i^{\Sigma} t} e^{-(E_j^{N}-E_i^{\Sigma})\tau} \\ &\quad * \frac{1}{G^{\Sigma}_{\text{fit}}(t,\vec{0})} \sqrt{\frac{G^{\Sigma}_{\text{fit}}(\tau,\vec{0}) G^{\Sigma}_{\text{fit}}(t,\vec{0}) G^{N}_{\text{fit}}(t-\tau,\vec{p})}{G^{N}_{\text{fit}}(\tau,\vec{p}) G^{N}_{\text{fit}}(t,\vec{p}) G^{\Sigma}_{\text{fit}}(t-\tau,\vec{0})}}, \end{aligned} \tag{6.94}$$

where we fit the two-point functions first to determine the amplitudes (A_i) and the energies (E_i) and then use these parameters in the fit to the ratio where the parameters B_{ij} are determined. For this calculation we are only interested in the matrix element between the ground states which is contained within B_{00}. The fit to the ratio is performed using the data from all three source-sink separations simultaneously.

6.8.2. Double ratio

To improve the signal of the ratios we also perform the three-point function calculation of the reverse transition $\Sigma^- \to n$. For this calculation we once again keep the sink momentum fixed at zero. Since this is now the neutron momentum, the discretised lattice momenta will result in slightly different Q^2 values. For $\vec{q}^{\,2} = 0$ we have access to the three-point functions for both transitions, these can be combined to form a 'double ratio' which has been shown to produce a more symmetric signal [30]. This ratio uses both transition three-point functions together with the two-point functions to cancel out the time-dependence in the large Euclidean time limit

$$\begin{aligned} R_2(\Gamma_{\text{unpol}},\Gamma_{\mathcal{V}_4};t,\tau;\vec{0},\vec{0}) &= \sqrt{\frac{G^{N\Sigma}(t,\tau;\vec{0},\vec{0}) G^{\Sigma N}(t,\tau;\vec{0},\vec{0})}{G^{\Sigma}(t,\vec{0}) G^{N}(t,\vec{0})}} \\ &\xrightarrow{\tau,\, t-\tau \gg 0} \frac{F_3(\Gamma_{\text{unpol}},\Gamma_{\mathcal{V}_4};\vec{0},\vec{0})}{2M_{\Sigma}M_N} \\ &= \frac{1}{2\sqrt{M_N M_{\Sigma}}} \langle N(\vec{0},+)|\bar{u}\gamma_4 s|\Sigma(\vec{0},+)\rangle_{\text{rel}}\,. \end{aligned} \tag{6.95}$$

In this ratio the time dependence due to the current insertion is canceled off by the two three-point functions, which should result in a better cancellation than the previous ratio where this cancellation was achieved by dividing by two-point functions. . To apply the

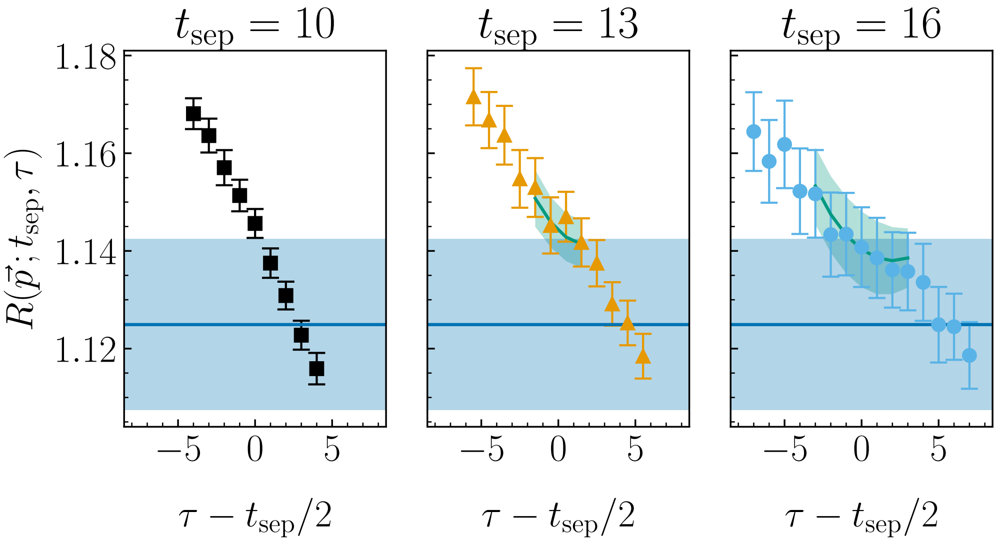

Figure 6.12. The ratio of the three-point function and multiple two-point functions for the operator $\mathcal{V}_4$ at zero momentum $\vec{p} = \vec{0}$ with the unpolarised projector. The green bands show the result of the fit to the ratio while the blue band shows the extracted value of the matrix element $\langle \Sigma(\vec{0}) | \mathcal{V}_4 | N(\vec{0}) \rangle$

two-exponential fitting method to this ratio we construct a similar ansatz to Eq. (6.93) containing two three-point functions with common parameters B_{ij}.

6.8.3. Results

Figure 6.12 shows the ratio in Eq. (6.90) for the three different source-sink separations at $\vec{p} = \vec{0}$. For all three ratios the results do not show a plateau behaviour, this is most readily explained by the difference in excited state contributions from the source and sink operators. In figure 6.13 we show the double ratio from Eq. (6.95) again for $\vec{p} = \vec{0}$. This time the ratios do exhibit a plateau behaviour for the larger source-sink separations and as expected the double ratio produces a more symmetric signal by including both transition directions.

Figures 6.12 and 6.13 also show the results of the two-exponential fit overlaid on the ratio in the blue band. Noting the change in the scale of the y-axis, the double ratio clearly produces a much better signal. We apply the fitting method described above to all the vector operators for both the unpolarised and polarised projector, using the

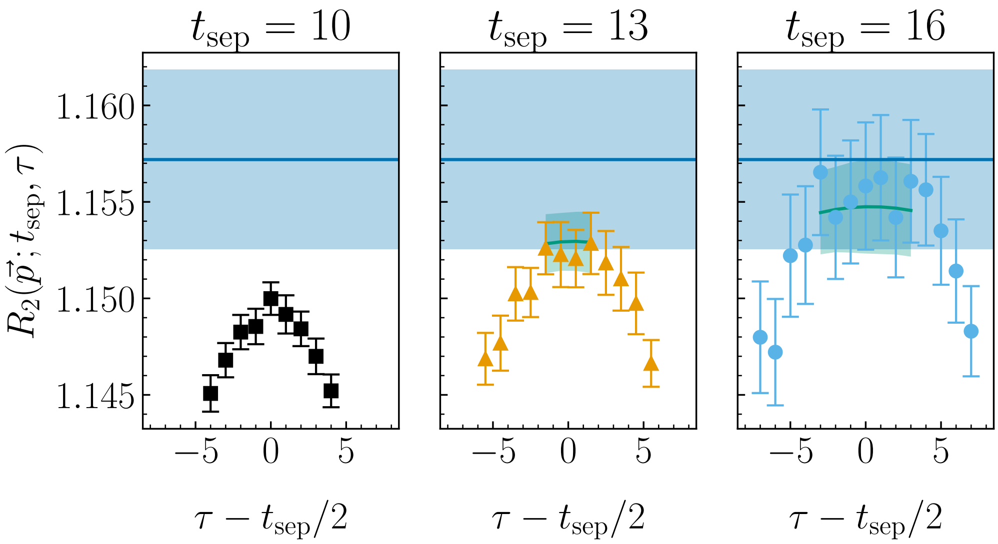

Figure 6.13. The double ratio from equation (6.95), shown for the three source-sink separations. The blue band shows the result of the fit with the two-exponential ansätze in Eq. (6.93).

results from these fits allows us to solve the system of linear equations and get a value for each of the three form factors.

6.8.4. Results Comparison

In order to consider the relative qualities of the Feynman-Hellmann and three-point function method, we will compare two values of the matrix element from the two methods. These points are at $Q^2 = 0.29\,\text{GeV}^2$ for the FH method and $Q^2 = 0.27\,\text{GeV}^2$ for the three-point function method. For the comparison we will show the effective value of the matrix element as a function of time for both methods. For the three-point function method, this means we show the ratios for each of the source-sink time separations, while for the Feynman-Hellmann method we show the value of effective matrix element as defined in Eq. (6.83). At the chosen values for Q^2 the energy difference between the Σ and neutron is relatively small ($M_\Sigma - E_N = 0.0030(69)$) as can be seen from table 6.1. This means that the effective matrix element from the Feynman-Hellmann method will have minimal corrections due to the quasi-degeneracy at this Q^2 value.

In figure 6.14 we show the effective FH result together with the ratios from three-point function calculation (multiplied with the appropriate kinematic factors). There is good

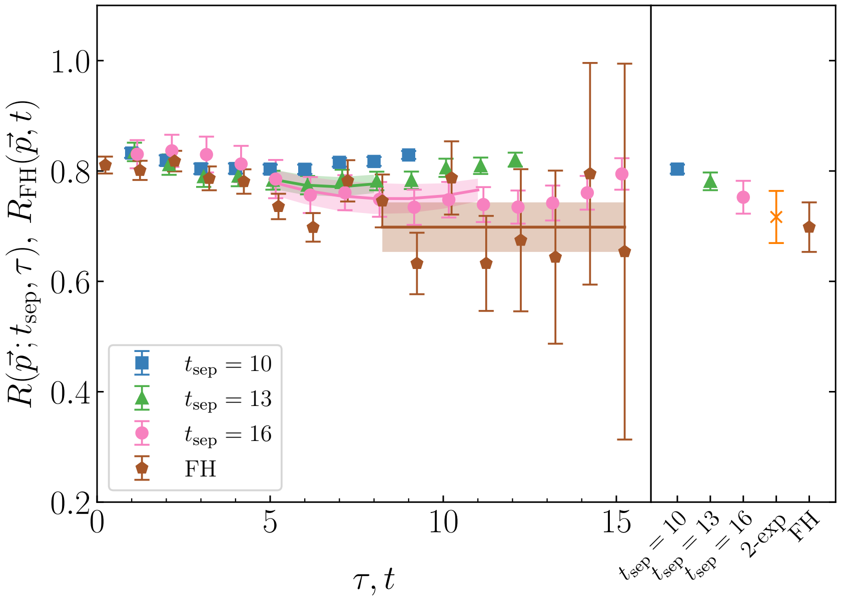

Figure 6.14. A comparison between the values of the matrix element from Feynman-Hellmann and the three-point function calculation at $Q^2 \approx 0.28\,\text{GeV}^2$. The left hand panel shows the effective value of the matrix element as a function of operator insertion time (τ) for the three-point function and as a function of sink time (t) for the Feynman-Hellmann method. The bands show the fit results, while the right hand panel shows these fit results in more detail, the orange cross shows the result of the two-exponential fit to all three-point function results.

agreement between the two results as can be seen in the right hand panel of this figure. Qualitatively we can say that while the Feynman-Hellmann results are noisier at large times, access to these large times gives us a clearer indication of the control over the excited state contributions, which is more difficult to estimate from the three-point function results.

Figure 6.15 shows the values of the matrix element against Q^2 from this calculation as well as those from the Feynman-Hellmann approach. both results have been renormalised using renormalisation constant $Z_V = 0.863(4)$ from [91]. The agreement between both methods is very good as can be seen. The three-point function method produces smaller uncertainties at $Q^2_{\rm min}$ ($= q^2_{\rm max}$), due to the double ratio, otherwise the uncertainties for both methods are comparable in size. In table 6.2 we show the results for the renormalised matrix element from both the Feynman-Hellmann method and the three-point method. The Feynman-Hellmann approach presented here has shown good agreement

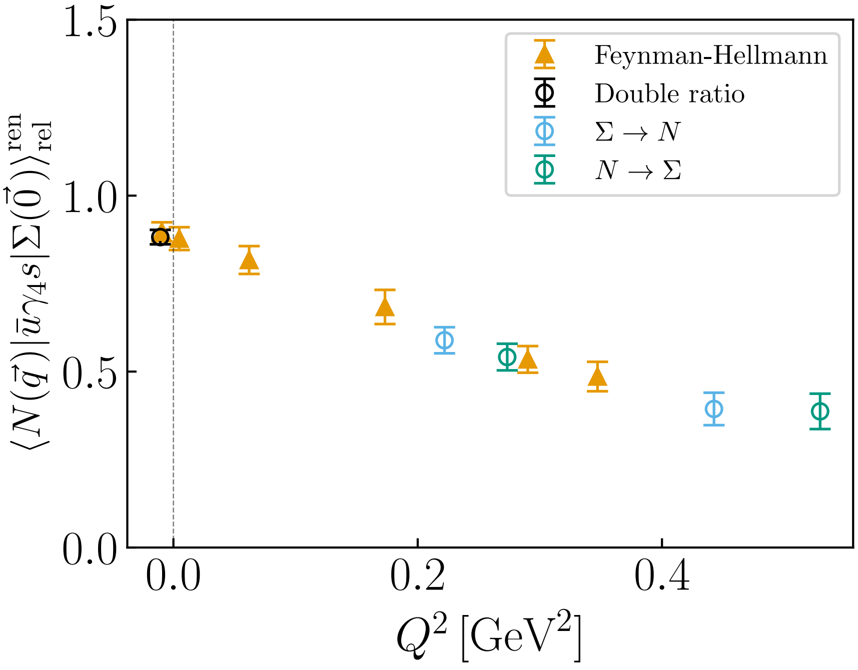

Figure 6.15. Results for $\langle N(\vec{q})|\bar{u}\gamma_4 s|\Sigma(\vec{0})\rangle^{\mathrm{ren}}_{\mathrm{rel}}$ versus Q^2. The triangles show the results from the Feynman-Hellmann method while the circles show the various three-point function results.

with the established three-point function approach. This is encouraging for extending this calculation to produce a full estimate of $f_1(0)$.

This calculation only used one component of the vector current, which gives access to the scalar form factor $f_0(q^2)$ at Q^2_{min}, but not its full momentum dependence as that requires simulations with at least two vector currents. To calculate the momentum dependence would require doing the calculation for an additional component of the vector current. Doing this additional calculation would allow for the extrapolation of the scalar form factor to $Q^2 = 0$ which determines $f_1(0)$. Beyond that, the calculation can be performed on a range of ensembles with different pion masses, which would allow for the extrapolation of $f_1(0)$ to the physical quark masses. Providing that the method holds up across a range of lattice ensembles, it could be used to produce a new determination of the CKM matrix element $|V_{us}|$.

This specific Feynman-Hellmann approach has the advantage that the perturbed quark propagators are fully calculated before they are combined with the λ parameter

Table 6.2. The renormalised matrix element $\langle N(\vec{q},+)|u\gamma_4 s|\Sigma(\vec{0},+)\rangle^{\text{ren}}_{\text{rel}}$ against Q^2 in GeV^2 for the six runs. We also give five additional Q^2 results: a-e using the conventional 3-point correlation function approach.

run #	Q^2 [GeV^2]	$\langle N(\vec{q},+)\|u\gamma_4 s\|\Sigma(\vec{0},+)\rangle^{\text{ren}}_{\text{rel}}$
1	-0.0095	0.897(27)
2	0.0048	0.878(32)
3	0.062	0.817(40)
4	0.17	0.684(49)
5	0.29	0.535(38)
6	0.35	0.486(42)
a	-0.011	0.882(21)
b	0.22	0.589(37)
c	0.27	0.541(38)
d	0.44	0.394(46)
e	0.53	0.387(50)

and contracted to form baryon correlators. This allows the propagators to be reused at little extra cost to construct other hadron correlation functions which can be used for other hyperon transitions, such as $\Lambda \to p$, $\Xi \to \Sigma$, $K \to \pi$, etc. Since the masses of these hadrons are different, the form factors would be determined at different values of Q^2.

Chapter 7.

Conclusion & Outlook

The scope of lattice QCD calculations have been progressing at a fast pace in recent years with improvements in computing capabilities and the development of new algorithms. Further, we are seeing more and more simulations being performed at the physical quark masses, extending the predictive power of lattice QCD. There are however still many limitations to current simulations which would benefit from improvements in the analysis methods. Many of the current limitations to lattice QCD simulations stem from our lack of understanding of systematic uncertainties. To improve our understanding of these uncertainties it is valuable to consider multiple methods for calculating the same observables, especially when these methods contain different systematic uncertainties.

A large part of the uncertainty in the calculation of hadron spectra on the lattice can be traced to the contributions from excited states. As our understanding of these excited states improves the need for advanced analysis tools has increased as well. In this thesis we have focused on model averaging as a method for handling the excited state contributions reliably across a large range of momenta. This weighted averaging across multiple time windows and ansätze has shown to produce robust results for extracting the spectrum of nucleons across a wide range of lattice ensembles, the results of which were presented in chapter 3.

The Feynman-Hellmann method as applied to the calculation of electromagnetic form factors relies heavily on the accurate determination of energies of the hadrons and small shifts in these energies. To determine the momentum dependence of the form factors it is of great importance that these energy shifts are extracted consistently from correlators with a large range of momentum projections. In this work we have shown that the weighted averaging method is a useful addition to the analysis tool set which removes some of the biases due to the choice of fit window and which allows for the inclusion of a systematic uncertainty which encapsulates the variability between the fit windows. In chapter 5 we have shown the results of simulations making use of these tools to calculate the nucleon electromagnetic form factors on a range of lattice ensembles. The form factors shown in this chapter are compared to results from a three-point function calculation and we show that there is agreement between the two methods. We argue that the Feynman-Hellmann method together with the analysis tools allows for better control over the contributions from excited states. We repeat the calculation on a large set of lattice ensembles and apply a flavour-breaking expansion to attempt an extrapolation of the form factors to the physical quark masses. The extrapolation results in a set of nucleon form factors which can be compared to experimental data. For the electric form factor we are able to show good agreement with the data, however for the magnetic form factor there is a large discrepancy. This discrepancy is likely due to the inability of our simulation results to fully constrain the form factor dependence on many of the lattice systematics. These results show a promising path for the Feynman-Hellmann method to be used as an alternative method for calculating the nucleon electromagnetic form factors at high momentum. The use of a larger set of lattice ensembles or quark masses closer to the physical ones will be necessary to provide truly competitive predictions of the form factors.

In chapter 6 we have extended the derivation of the Feynman-Hellmann method to include quasi-degenerate energy states, which allowed for an expolarative calculation of hyperon transition matrix elements. This extension relies on the energy difference between the two unperturbed states being relatively small, as such we chose the $\Sigma^- \to n$ transition with the nucleon at non-zero momentum. The results in the chapter show that the Feynman-Hellmann method is able to produce results of comparable precision to the three-point function method on this lattice ensemble. As for the previous results, the analysis of the Feynman-Hellmann method here is simpler due to there being only one set of exponentially decaying excited states present in the correlator. These simulation are a first step towards developing an alternative approach for the determination of the hyperon transition form factors. Further calculations will be necessary in order to test the applicability of this method once the mass-splitting between the hyperons increases at lower quark masses, and to study the effects of other lattice systematics on the results. This is a promising result however, and it opens the door to many other calculations, the simplest extensions being the calculation of meson transition matrix elements and simulations with a spatial vector current to allow for the determination of individual form factors.

Appendix A.

Conventions

A.1. Metric and Dirac Matrices

A.1.1. Euclidean Spacetime

The Euclidean spacetime metric is defined by

$$\delta_{\mu\nu} \equiv \begin{bmatrix} 1 & 0 & 0 & 0 \\ 0 & 1 & 0 & 0 \\ 0 & 0 & 1 & 0 \\ 0 & 0 & 0 & 1 \end{bmatrix}. \tag{A.1}$$

The rotation to Euclideon space is set by the following transformation

$$\gamma_M^\mu \equiv (\gamma_M^0, \gamma_M^i) \xrightarrow{\text{Wick}} \gamma_\mu \equiv (\gamma_i, \gamma_4) - (-i\gamma_M^i, \gamma_M^0), \tag{A.2}$$

this gives the relationship for the Dirac matrices in Euclidean space,

$$\{\gamma_\mu, \gamma_\nu\} = 2\delta_{\mu\nu}\mathbb{I}. \tag{A.3}$$

The fifth Dirac matrix is defined as

$$\gamma_5 \equiv \gamma_1\gamma_2\gamma_3\gamma_4 = -\gamma_M^5, \tag{A.4}$$

and the antisymmetric tensor is defined as

$$\sigma_{\mu\nu} \equiv \frac{i}{2}[\gamma_\mu, \gamma_\nu], \tag{A.5}$$

which relates to Minkowski spacetime by

$$\sigma_{4i} = -i\sigma_M^{0i}, \tag{A.6}$$
$$\sigma_{ij} = -\sigma_M^{ij}. \tag{A.7}$$

We use the following Dirac basis,

$$\gamma_4 = \begin{bmatrix} \mathbb{I} & 0 \\ 0 & -\mathbb{I} \end{bmatrix}, \qquad \gamma_i = \begin{bmatrix} 0 & -i\sigma_i \\ i\sigma_i & 0 \end{bmatrix}, \qquad \gamma_5 = \begin{bmatrix} 0 & -\mathbb{I} \\ -\mathbb{I} & 0 \end{bmatrix}, \tag{A.8}$$

where σ_i are the Pauli matrices and all the matrices are Hermitian. The Pauli matrices are

$$\sigma^1 = \begin{bmatrix} 0 & 1 \\ 1 & 0 \end{bmatrix}, \qquad \sigma^2 = \begin{bmatrix} 0 & -i \\ i & 0 \end{bmatrix}, \qquad \sigma^3 = \begin{bmatrix} 1 & 0 \\ 0 & -1 \end{bmatrix}. \tag{A.9}$$

A.2. Projection Matrices

Paritye and spin projectors for the spin-half baryons are defined as

$$\Gamma_{P\pm} = \frac{1}{2}(\mathbb{I} \pm \gamma_4), \tag{A.10}$$
$$\Gamma_{S\pm}^j = \frac{1}{2}(\mathbb{I} \pm i\gamma_5\gamma_j), \tag{A.11}$$

where $\hat{e}_j$ is the chosen spin-polarisation axis, which is chosen to be e_3 for the work in this thesis. The combinations of these projectors which are used in the analysis of baryon correlators are

$$\Gamma_{\text{unpol}} \equiv \Gamma_{P+}\left(\Gamma_{S+} + \Gamma_{S-}\right) = \frac{1}{2}(\mathbb{I} + \gamma_4), \tag{A.12}$$
$$\Gamma_{\text{pol}}^j \equiv \Gamma_{P+}\left(\Gamma_{S+} - \Gamma_{S-}\right) = \frac{i}{2}(\mathbb{I} + \gamma_4)\gamma_5\gamma_j, \tag{A.13}$$
$$\Gamma_\pm^j \equiv \Gamma_{P+}\Gamma_{S\pm} = \frac{1}{2}(\mathbb{I} + \gamma_4)\frac{1}{2}(\mathbb{I} \pm i\gamma_5\gamma_j) = \frac{1}{2}(\Gamma_{\text{unpol}} \pm \Gamma_{\text{pol}}). \tag{A.14}$$

Appendix B.

Feynman-Hellman Method for the Spatial Vector Current

Consider the perturbed two-point correlator

$$G_\lambda(\vec{p}, t, \Gamma) = \Gamma_{\alpha\beta} \; {}_\lambda\langle \tilde{\chi}_\alpha(\vec{p}, t) \bar{\chi}_\beta(0) \rangle_\lambda \tag{B.1}$$

Inserting two complete sets of states

$$\begin{aligned} G_\lambda(\vec{p}, t, \Gamma) = \Gamma_{\alpha\beta} \sum_{\substack{X, \vec{k}_X \\ \sigma_X}} \sum_{\substack{Y, \vec{k}_Y \\ \sigma_Y}} \frac{\Delta^3 k_X}{(2\pi)^3} \frac{\Delta^3 k_Y}{(2\pi)^3} \frac{1}{(2E_X)(2E_Y)} \langle \Omega | \tilde{\chi}_\alpha(\vec{p}, 0) | X(\vec{p}_X, \sigma_X) \rangle \\ * \langle X(\vec{p}_X, \sigma_X) | e^{-\hat{H}_\lambda t} | Y(\vec{p}_Y, \sigma_Y) \rangle \; \langle Y(\vec{p}_Y, \sigma_Y) | \bar{\chi}_\beta(0) | \Omega \rangle \end{aligned} \tag{B.2}$$

Using the Dyson expansion we can expand the matrix element in the previous equation, we will consider this for the set of states which are degenerate in energy, such that the only free variables are the sign of the momentum and the spin,

$$\frac{\langle B(\vec{p}_r, \sigma_r) | e^{-\hat{H}_\lambda t} | B(\vec{p}_s, \sigma_s) \rangle}{2E(\vec{p})} \tag{B.3}$$

$$= \frac{1}{2E_B(\vec{p})} \langle B(\vec{p}_r, \sigma_r) | e^{-\hat{H}_0 t} (1 - \lambda \int_0^t dt' e^{\hat{H}_0 t'} \tilde{\mathcal{V}}_2(\vec{q}) e^{-\hat{H}_0 t'}) | B(\vec{p}_s, \sigma_s) \rangle \tag{B.4}$$

$$= e^{E_B(\vec{p})t} \left[\delta_{\sigma_r \sigma_s} \delta_{rs} - \frac{t\lambda}{2E_B(\vec{p})} \langle B(\vec{p}_r, \sigma_r) | \tilde{\mathcal{V}}_2(\vec{q}) | B(\vec{p}_s, \sigma_s) \rangle \right]. \tag{B.5}$$

From above we know the matrix element of the spatial vector current between two Breit frame states, we use this with a slight modification to the eigenvalues to include the additional terms of the above expression,

$$\frac{t\lambda}{2E_B(\vec{p})}\langle B(\vec{p}_r,\sigma_r)|\tilde{\mathcal{V}}_2(\vec{q})|B(\vec{p}_s,\sigma_s)\rangle = \sum_{j,\sigma} e^{(j\sigma)}_{\sigma_r r}\, e^{(j\sigma)*}_{\sigma_s s}\,\mu^{(j)}\,t, \tag{B.6}$$

where

$$\mu^{(\pm)} = \pm i\lambda\sqrt{q_1^2+q_3^2}\,\frac{G^f_{M,X}(Q^2)}{2E_B(\vec{p})}. \tag{B.7}$$

The eigenvectors and eigenvalues can be used to rewrite the expression in Eq. B.5 as

$$\begin{aligned}\frac{\langle B(\vec{p}_r,\sigma_r)|e^{-\hat{H}_\lambda t}|B(\vec{p}_s,\sigma_s)\rangle}{\langle B(\vec{p})|B(\vec{p})\rangle} &= \sum_{j,\sigma} e^{(j\sigma)}_{\sigma_r r}\left[1-t\mu^{(j)}\right] e^{(j\sigma)*}_{\sigma_s s}\, e^{E_B(\vec{p})t} && \text{(B.8)}\\ &= \sum_{j,\sigma} e^{(j\sigma)}_{\sigma_r r}\, e^{(j\sigma)*}_{\sigma_s s}\, e^{E_B^{(j)}(\vec{p},\lambda)t}, && \text{(B.9)}\end{aligned}$$

where

$$E_B^{(\pm)}(\vec{p},\lambda) = E_B(\vec{p}) \pm \mu^{(j)} \tag{B.10}$$

The next step is to evaluate the expression for the two-point correlator in Eq. B.2 using these new eigenvectors and the polarised projection matrix

$$\begin{aligned}G_\lambda(\vec{p}_r,t,\Gamma^3_\pm) &= \frac{E_B+M_B}{2E_B}|Z(\vec{p})|^2\sum_j e^{E_B^{(j)}(\vec{p},\lambda)t}\sum_{\sigma_r,\sigma_s,s}(1\pm\sigma_r)\delta_{\sigma_r\sigma_s}\sum_\sigma e^{(j\sigma)}_{\sigma_r r}\, e^{(j\sigma)*}_{\sigma_s s} && \text{(B.11)}\\ &= \frac{E_B+M_B}{E_B}|Z(\vec{p})|^2\sum_{j,s} e^{E_B^{(j)}(\vec{p},\lambda)t}\begin{bmatrix} 1 & \mp(j)\frac{iq_1}{\sqrt{q_1^2+q_3^2}}\\ \pm(j)\frac{iq_1}{\sqrt{q_1^2+q_3^2}} & 1\end{bmatrix}_{rs} && \text{(B.12)}\\ &= \frac{E_B+M_B}{E_B}|Z(\vec{p})|^2\begin{bmatrix}(1\pm\frac{iq_1}{\sqrt{q_1^2+q_3^2}})e^{E_B^{(+)}(\lambda)t}+(1\mp\frac{iq_1}{\sqrt{q_1^2+q_3^2}})e^{E_B^{(-)}(\lambda)t}\\ (1\mp\frac{iq_1}{\sqrt{q_1^2+q_3^2}})e^{E_B^{(+)}(\lambda)t}+(1\pm\frac{iq_1}{\sqrt{q_1^2+q_3^2}})e^{E_B^{(-)}(\lambda)t}\end{bmatrix}_r && \text{(B.13)}\end{aligned}$$

This expression is now in the same form as Eq. 4.37.

Appendix C.

Baryon masses

β	$L^3 \times T$	(κ_l, κ_s)	(κ_1, κ_2)	$am_{\text{1-exp}}$	$am_{\text{w.avg}}$
5.4	$24^3 \times 48$	$(0.119820, 0.119820)$	$(0.119820, 0.119820)$	0.5626(34)	0.5565(64)
		$(0.119860, 0.119860)$	$(0.119860, 0.119860)$	0.5159(65)	0.5115(93)
		$(0.119895, 0.119895)$	$(0.119895, 0.119895)$	0.5061(60)	0.5051(76)
		$(0.119930, 0.119930)$	$(0.119930, 0.119930)$	0.4815(55)	0.4819(56)
		$(0.120000, 0.120000)$	$(0.120000, 0.120000)$	0.4709(90)	0.4692(98)
		$(0.120048, 0.119695)$	$(0.120048, 0.119695)$	0.4941(63)	0.4945(61)
			$(0.120048, 0.120048)$	0.460(12)	0.4623(96)
			$(0.119695, 0.120048)$	0.5127(44)	0.5122(46)
			$(0.119695, 0.119695)$	0.5466(34)	0.5395(39)
	$32^3 \times 64$	$(0.119930, 0.119930)$	$(0.119930, 0.119930)$	0.4671(27)	0.4664(37)
		$(0.119989, 0.119812)$	$(0.119989, 0.119812)$	0.4541(42)	0.4523(50)
			$(0.119989, 0.119989)$	0.4723(35)	0.4709(44)
			$(0.119812, 0.119989)$	0.4821(29)	0.4809(37)
			$(0.119812, 0.119812)$	0.4984(26)	0.4946(32)
		$(0.120048, 0.119695)$	$(0.120048, 0.119695)$	0.4691(42)	0.4606(65)
			$(0.120048, 0.120048)$	0.4264(59)	0.4142(94)
			$(0.119695, 0.120048)$	0.4919(30)	0.4893(39)
			$(0.119695, 0.119695)$	0.5245(25)	0.5155(38)
		$(0.120084, 0.119623)$	$(0.120084, 0.119623)$	0.4644(49)	0.4644(72)
			$(0.120084, 0.120084)$	0.4098(98)	0.414(17)
			$(0.119623, 0.120084)$	0.4916(29)	0.4905(43)
			$(0.119623, 0.119623)$	0.5329(23)	0.5292(34)

β	$L^3 \times T$	(κ_l, κ_s)	(κ_1, κ_2)	$am_{\text{1-exp}}$	$am_{\text{w.avg}}$
5.5	$32^3 \times 64$	$(0.120900, 0.120900)$	$(0.120900, 0.120900)$	0.4690(40)	0.4646(43)
		$(0.120920, 0.120920)$	$(0.120920, 0.120920)$	0.4440(70)	0.4431(73)
		$(0.120950, 0.120950)$	$(0.120950, 0.120950)$	0.4348(77)	0.4333(97)
		$(0.120990, 0.120990)$	$(0.120990, 0.120990)$	0.4107(89)	0.4097(78)
		$(0.121021, 0.121021)$	$(0.121021, 0.121021)$	0.385(12)	0.380(11)
		$(0.121040, 0.120620)$	$(0.121040, 0.120620)$	0.4642(42)	0.4622(81)
			$(0.121040, 0.121040)$	0.4179(70)	0.411(12)
			$(0.120620, 0.121040)$	0.4833(25)	0.4805(52)
			$(0.120620, 0.120620)$	0.0	0.4991(27)
		$(0.121040, 0.120770)$	$(0.121040, 0.120770)$	0.4490(59)	0.4370(68)
			$(0.121040, 0.121040)$	0.4236(83)	0.4043(79)
			$(0.120770, 0.121040)$	0.4600(50)	0.4451(67)
			$(0.120770, 0.120770)$	0.4769(30)	0.4745(48)
		$(0.121050, 0.120661)$	$(0.121050, 0.120661)$	0.4502(63)	0.4493(59)
			$(0.121050, 0.121050)$	0.3923(92)	0.3963(90)
			$(0.120661, 0.121050)$	0.4727(39)	0.4700(55)
			$(0.120661, 0.120661)$	0.5108(30)	0.5101(30)
		$(0.121095, 0.120512)$	$(0.121095, 0.120512)$	0.4641(49)	0.4673(93)
			$(0.121095, 0.121095)$	0.397(11)	0.400(14)
			$(0.120512, 0.121095)$	0.470(10)	0.468(10)
			$(0.120512, 0.120512)$	0.0	0.5216(30)
		$(0.121099, 0.120653)$	$(0.121099, 0.120653)$	0.4312(99)	0.430(12)
			$(0.121099, 0.121099)$	0.379(16)	0.380(21)
			$(0.120653, 0.121099)$	0.4581(57)	0.4561(69)
			$(0.120653, 0.120653)$	0.4984(36)	0.4950(51)
		$(0.121145, 0.120413)$	$(0.121145, 0.120413)$	0.4739(42)	0.4715(58)
			$(0.121145, 0.121145)$	0.395(11)	0.3959(84)
			$(0.120413, 0.121145)$	0.5073(21)	0.5063(28)
			$(0.120413, 0.120413)$	0.5670(14)	0.5658(16)
	$48^3 \times 96$	$(0.121166, 0.120371)$	$(0.121166, 0.120371)$	0.4680(66)	0.4666(62)
			$(0.121166, 0.121166)$	0.3859(66)	0.3851(83)
			$(0.120371, 0.121166)$	0.5074(26)	0.5040(44)
			$(0.120371, 0.120371)$	0.5730(26)	0.5669(32)

β	$L^3 \times T$	(κ_l, κ_s)	(κ_1, κ_2)	$am_{\text{1-exp}}$	$am_{\text{w.avg}}$
5.65	$32^3 \times 64$	$(0.121975, 0.121975)$	$(0.121975, 0.121975)$	0.4222(30)	0.4160(52)
		$(0.122005, 0.122005)$	$(0.122005, 0.122005)$	0.4129(34)	0.4030(71)
		$(0.122030, 0.122030)$	$(0.122030, 0.122030)$	0.3933(76)	0.3922(99)
		$(0.122050, 0.122050)$	$(0.122050, 0.122050)$	0.3817(60)	0.3772(69)
		$(0.122078, 0.121859)$	$(0.122078, 0.121859)$	0.4063(30)	0.4019(60)
			$(0.122078, 0.122078)$	0.3825(39)	0.3807(78)
			$(0.121859, 0.122078)$	0.4190(25)	0.4172(44)
			$(0.121859, 0.121859)$	0.4396(21)	0.4378(36)
		$(0.122130, 0.121756)$	$(0.122130, 0.121756)$	0.4162(39)	0.4156(52)
			$(0.122130, 0.122130)$	0.3801(71)	0.3807(83)
			$(0.121756, 0.122130)$	0.4307(28)	0.4286(42)
			$(0.121756, 0.121756)$	0.4620(20)	0.4592(32)
	$48^3 \times 96$	$(0.122005, 0.122005)$	$(0.122005, 0.122005)$	0.3858(48)	0.3860(44)
		$(0.122078, 0.121859)$	$(0.122078, 0.121859)$	0.4047(24)	0.4039(30)
			$(0.122078, 0.122078)$	0.3810(27)	0.3801(33)
			$(0.121859, 0.122078)$	0.4149(19)	0.4136(24)
			$(0.121859, 0.121859)$	0.4360(17)	0.4343(24)
		$(0.122130, 0.121756)$	$(0.122130, 0.121756)$	0.3976(31)	0.3976(54)
			$(0.122130, 0.122130)$	0.3527(39)	0.3488(68)
			$(0.121756, 0.122130)$	0.4194(24)	0.4165(36)
			$(0.121756, 0.121756)$	0.4548(20)	0.4515(31)
		$(0.122167, 0.121682)$	$(0.122167, 0.121682)$	0.4003(36)	0.3929(68)
			$(0.122167, 0.122167)$	0.3427(53)	0.3345(98)
			$(0.121682, 0.122167)$	0.4227(31)	0.4226(45)
			$(0.121682, 0.121682)$	0.4652(23)	0.4646(34)
	$64^3 \times 96$	$(0.122227, 0.121563)$	$(0.122227, 0.121563)$	0.3769(58)	0.3782(36)
			$(0.122227, 0.122227)$	0.3272(89)	0.325(14)
			$(0.121563, 0.122227)$	0.4240(35)	0.4149(28)
			$(0.121563, 0.121563)$	0.480(15)	0.4744(23)

β	$L^3 \times T$	(κ_l, κ_s)	(κ_1, κ_2)	$am_{\text{1-exp}}$	$am_{\text{w.avg}}$
5.80	$48^3 \times 96$	(0.122760, 0.122760)	(0.122760, 0.122760)	0.3782(18)	0.3766(28)
		(0.122810, 0.122810)	(0.122810, 0.122810)	0.3557(24)	0.3552(27)
		(0.122870, 0.122870)	(0.122870, 0.122870)	0.3152(65)	0.3136(73)
		(0.122880, 0.122670)	(0.122880, 0.122670)	0.3588(19)	0.3570(28)
			(0.122880, 0.122880)	0.3353(24)	0.3336(36)
			(0.122670, 0.122880)	0.3688(16)	0.3663(24)
			(0.122670, 0.122670)	0.3894(14)	0.3872(19)
		(0.122920, 0.122920)	(0.122920, 0.122920)	0.3156(59)	0.316(13)
		(0.122940, 0.122551)	(0.122940, 0.122551)	0.3614(23)	0.3597(32)
			(0.122940, 0.122940)	0.3190(33)	0.3178(43)
			(0.122551, 0.122940)	0.3798(15)	0.3772(21)
			(0.122551, 0.122551)	0.4149(12)	0.4118(18)

β	$L^3 \times T$	(κ_l, κ_s)	(κ_1, κ_2)	$am_{\text{1-exp}}$	$am_{\text{w.avg}}$
5.95	$48^3 \times 96$	(0.123411, 0.123411)	(0.123411, 0.123411)	0.3344(20)	0.3334(25)
		(0.123411, 0.123558)	(0.123411, 0.123558)	0.3057(18)	0.3046(24)
			(0.123411, 0.123411)	0.3210(15)	0.3198(20)
			(0.123558, 0.123411)	0.2969(26)	0.2957(33)
			(0.123558, 0.123558)	0.2782(34)	0.2773(45)
		(0.123460, 0.123460)	(0.123460, 0.123460)	0.3082(30)	0.3071(41)
		(0.123510, 0.123510)	(0.123510, 0.123510)	0.2938(30)	0.2927(36)
		(0.123523, 0.123334)	(0.123523, 0.123334)	0.3076(32)	0.3041(60)
			(0.123523, 0.123523)	0.2831(40)	0.2788(78)
			(0.123334, 0.123523)	0.3184(24)	0.3157(43)
			(0.123334, 0.123334)	0.3395(20)	0.3373(34)

Appendix D.

Additional X_D and X_F plots

D.1. $\beta = 5.40$ ensembles

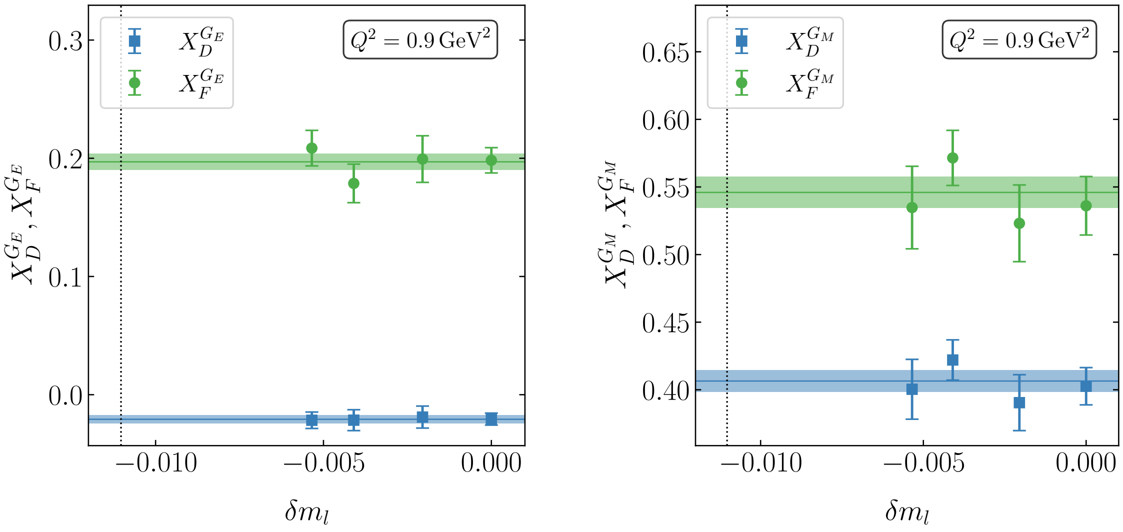

Figure D.1. The values of X_D and X_F plotted against Q^2, for the three ensembles at $\beta = 5.40$, (1-4 in table 5.2) for G_E (left) and G_M (right) at $\mathrm{Q}^2 = 0.9\,\mathrm{GeV}^2$.

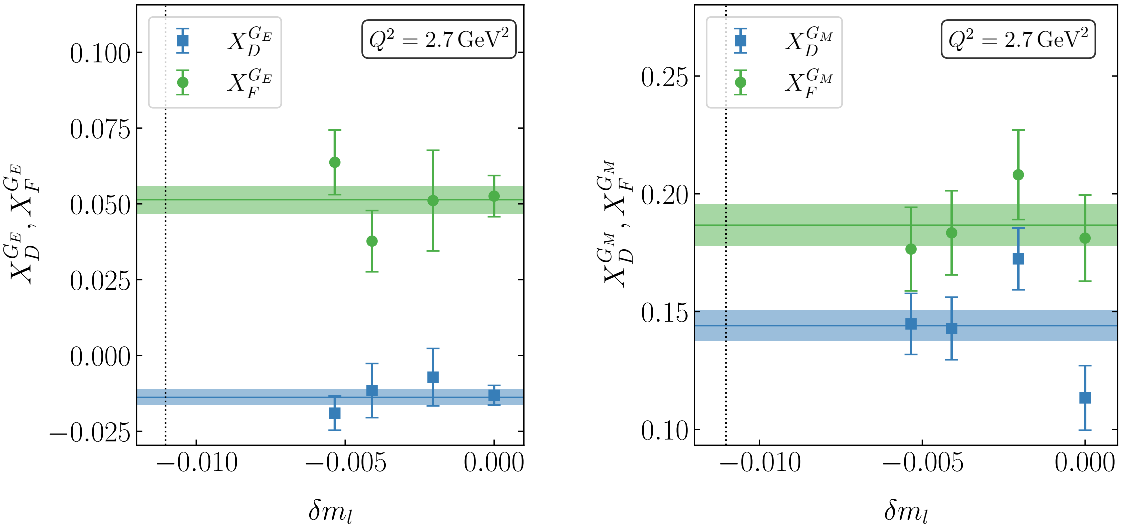

Figure D.2. The values of X_D and X_F plotted against Q^2, for the three ensembles at $\beta = 5.40$, (1-4 in table 5.2) for G_E (left) and G_M (right) at $\mathrm{Q}^2 = 2.7\,\mathrm{GeV}^2$.

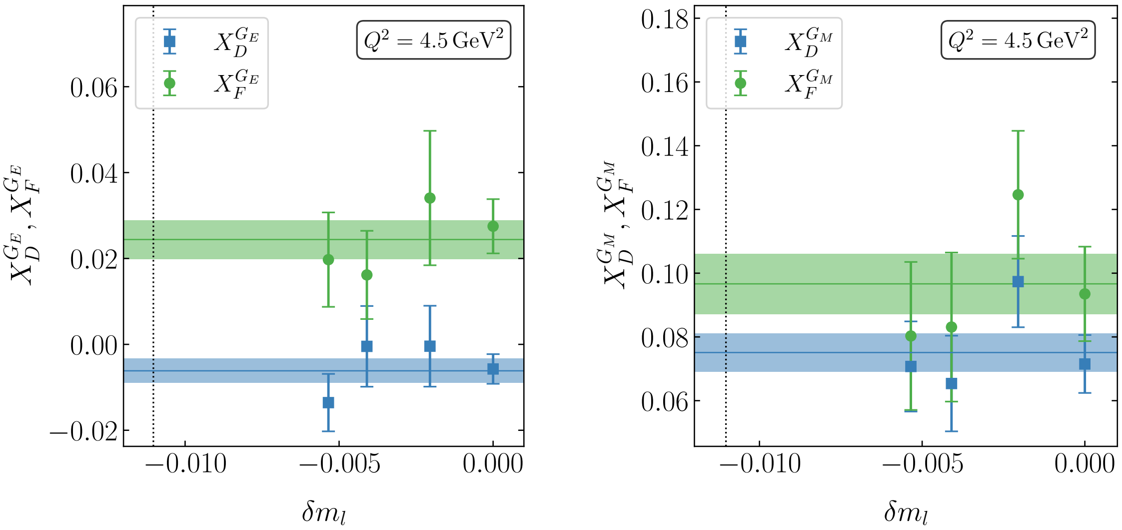

Figure D.3. The values of X_D and X_F plotted against Q^2, for the three ensembles at $\beta = 5.40$, (1-4 in table 5.2) for G_E (left) and G_M (right) at $\mathrm{Q}^2 = 4.5\,\mathrm{GeV}^2$.

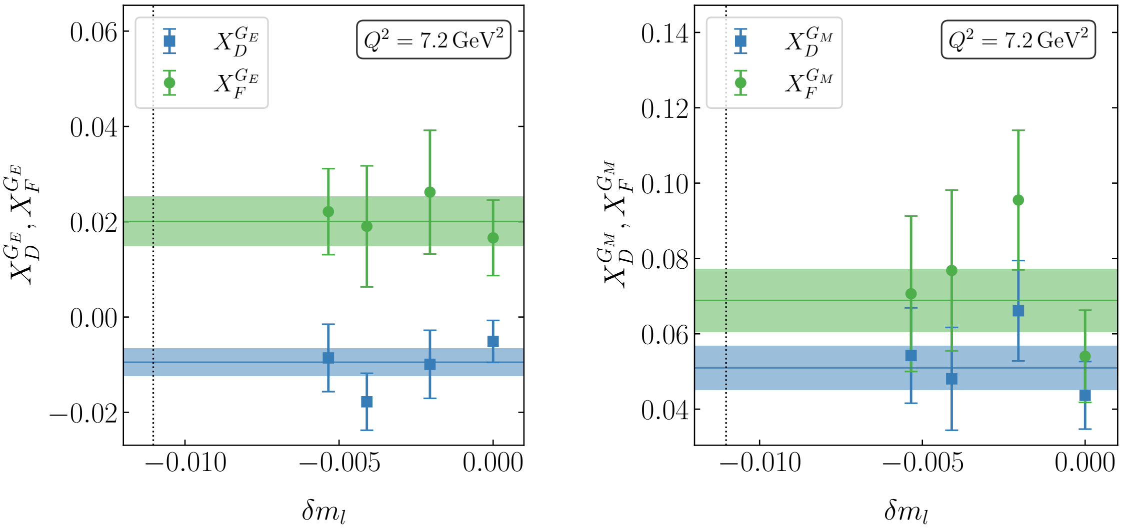

Figure D.4. The values of X_D and X_F plotted against Q^2, for the three ensembles at $\beta = 5.40$, (1-4 in table 5.2) for G_E (left) and G_M (right) at $Q^2 = 7.2\,\mathrm{GeV}^2$.

D.2. $\beta = 5.50$ ensembles

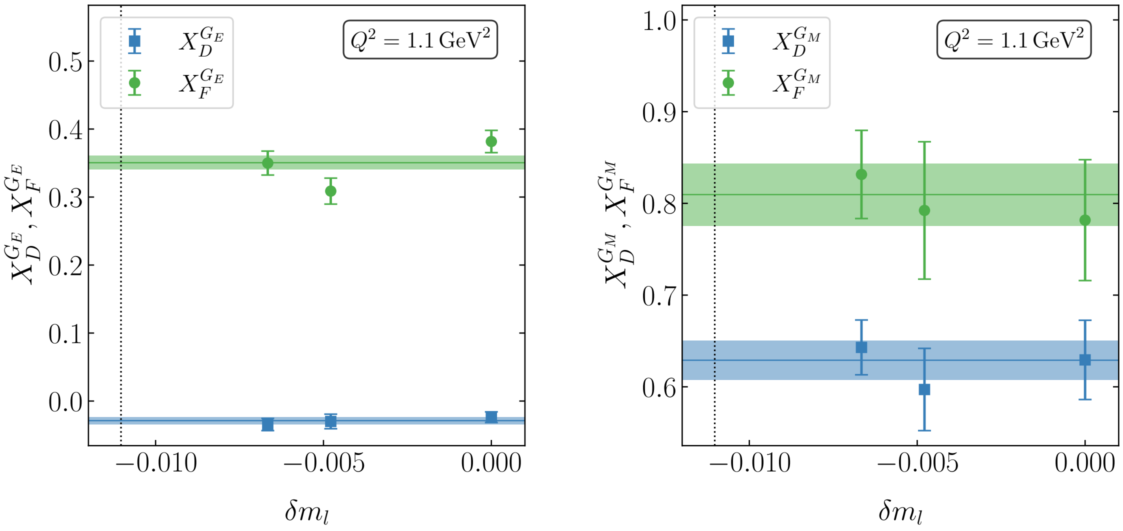

Figure D.5. The values of X_D and X_F plotted against Q^2, for the three ensembles at $\beta = 5.50$, (5-7 in table 5.2) for G_E (left) and G_M (right) at $Q^2 = 1.1\,\mathrm{GeV}^2$.

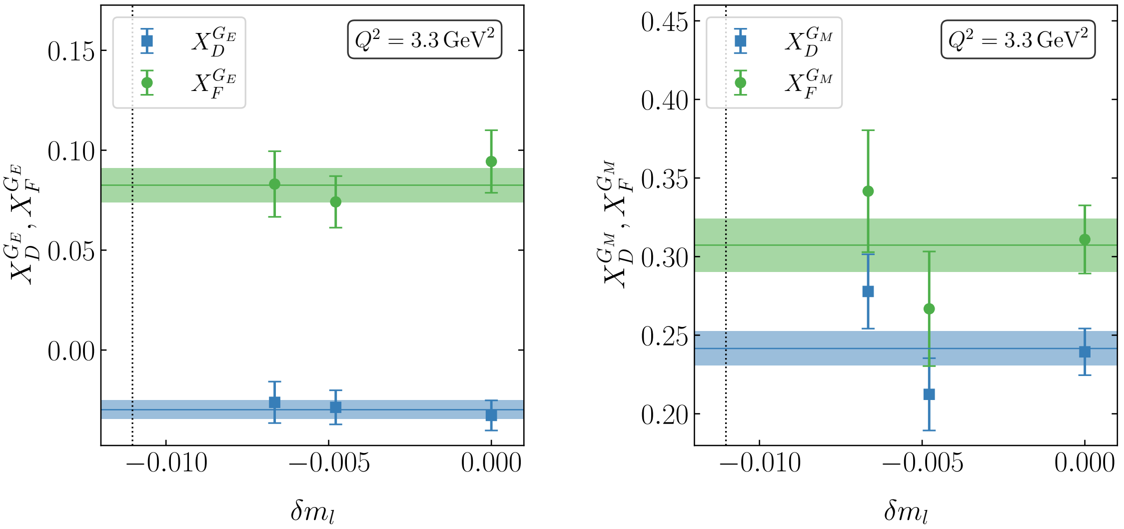

Figure D.6. The values of X_D and X_F plotted against Q^2, for the three ensembles at $\beta = 5.50$, (5-7 in table 5.2) for G_E (left) and G_M (right) at $\mathrm{Q}^2 = 3.29\,\mathrm{GeV}^2$.

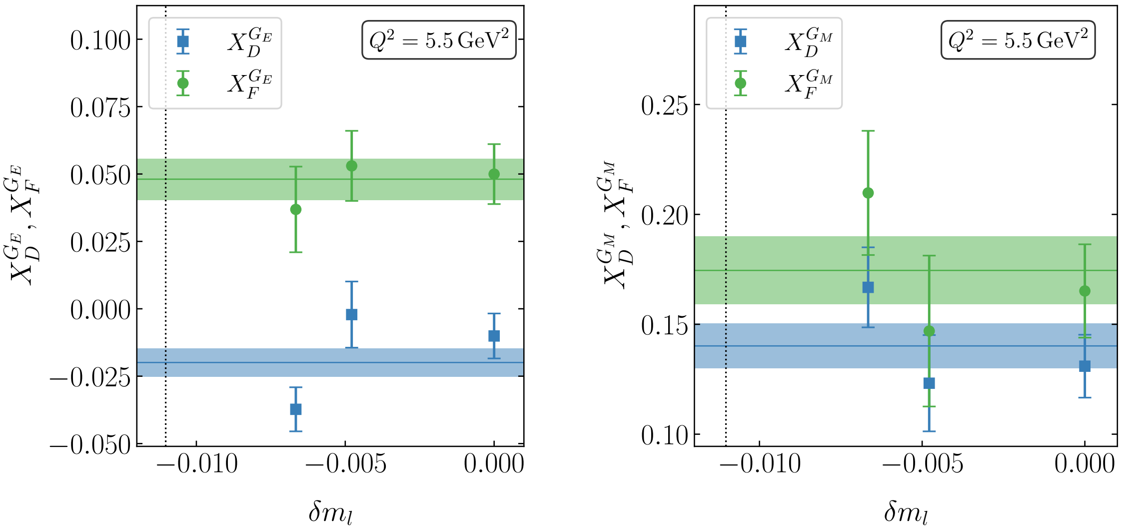

Figure D.7. The values of X_D and X_F plotted against Q^2, for the three ensembles at $\beta = 5.50$, (5-7 in table 5.2) for G_E (left) and G_M (right) at $\mathrm{Q}^2 = 5.48\,\mathrm{GeV}^2$.

D.3. $\beta = 5.65$ ensembles

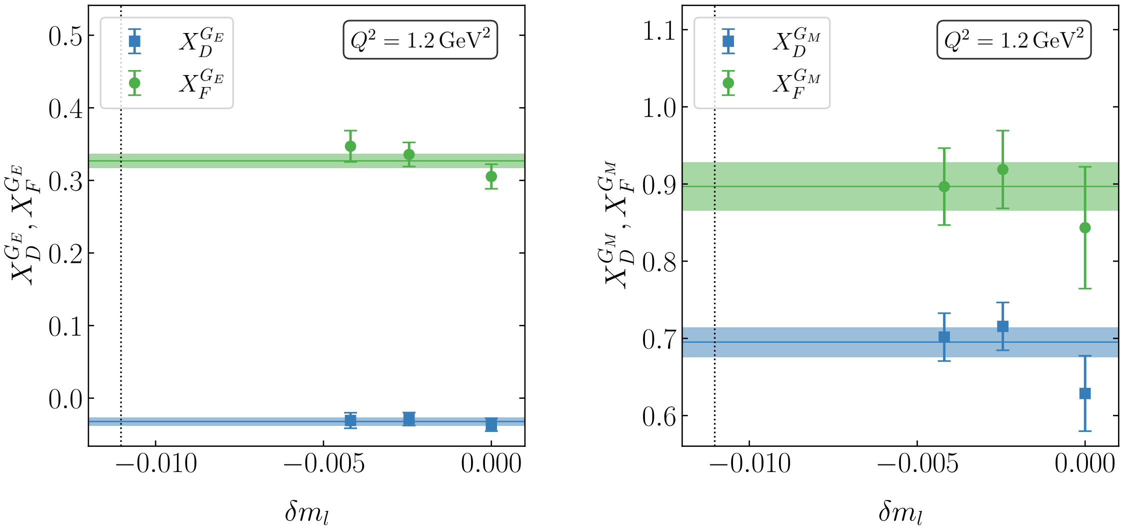

Figure D.8. The values of X_D and X_F plotted against Q^2, for the three ensembles at $\beta = 5.65$, (8-10 in table 5.2) for G_E (left) and G_M (right) at $\mathrm{Q}^2 = 1.15\,\mathrm{GeV}^2$.

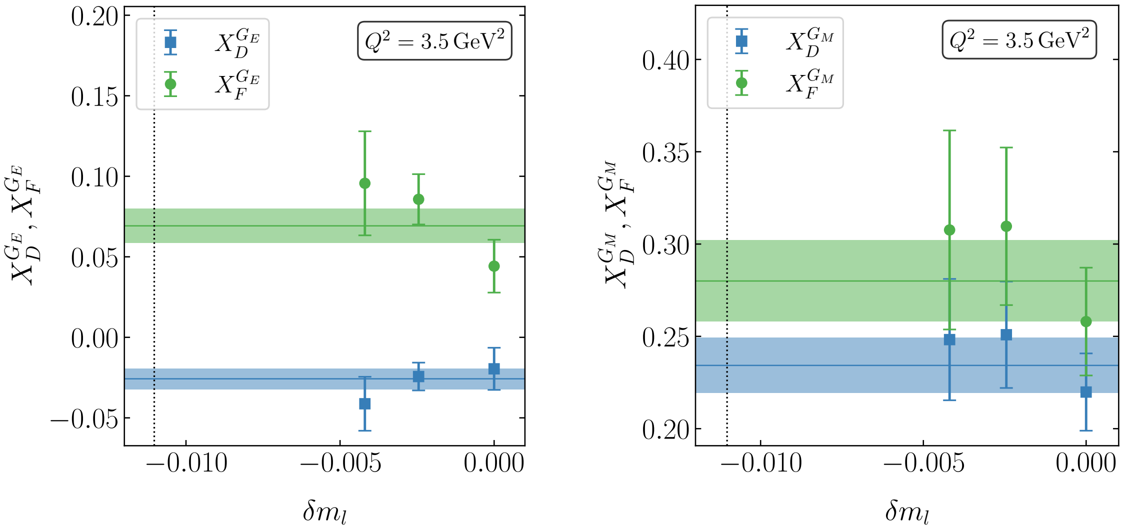

Figure D.9. The values of X_D and X_F plotted against Q^2, for the three ensembles at $\beta = 5.65$, (8-10 in table 5.2) for G_E (left) and G_M (right) at $\mathrm{Q}^2 = 3.46\,\mathrm{GeV}^2$.

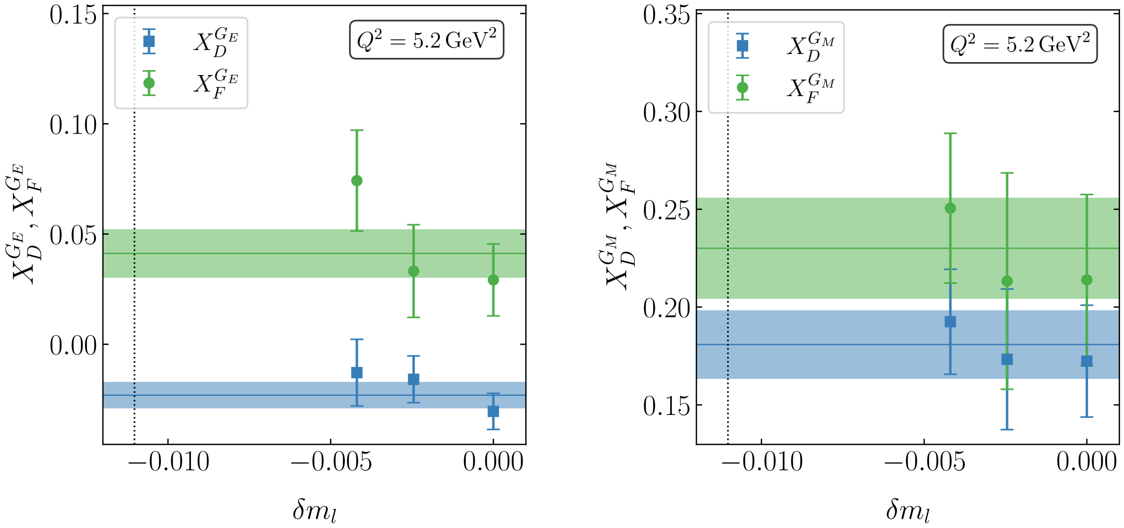

Figure D.10. The values of X_D and X_F plotted against Q^2, for the three ensembles at $\beta = 5.65$, (8-10 in table 5.2) for G_E (left) and G_M (right) at $\mathrm{Q}^2 = 5.19\,\mathrm{GeV}^2$.

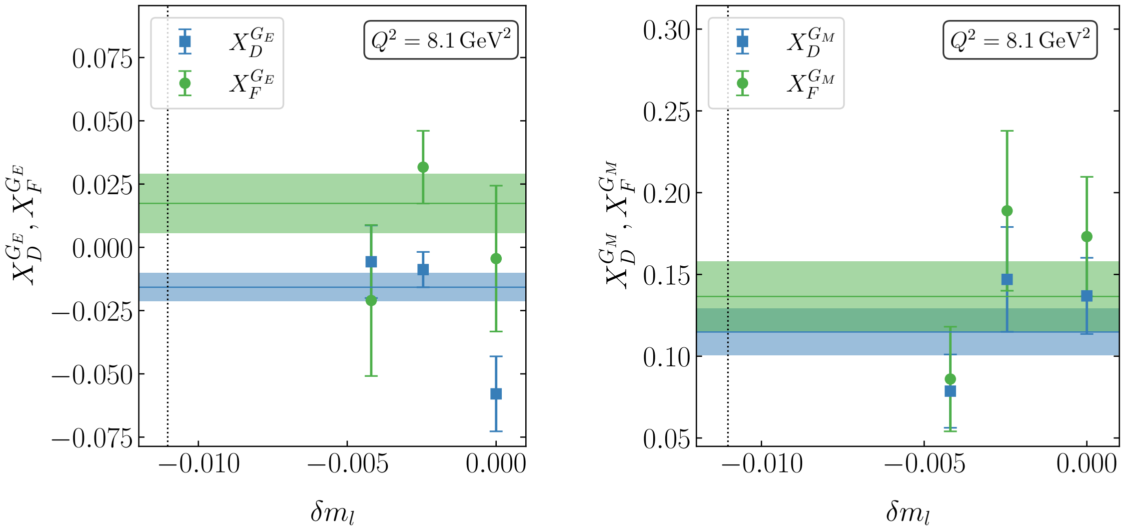

Figure D.11. The values of X_D and X_F plotted against Q^2, for the three ensembles at $\beta = 5.65$, (8-10 in table 5.2) for G_E (left) and G_M (right) at $\mathrm{Q}^2 = 8.08\,\mathrm{GeV}^2$.

D.4. $\beta = 5.80$ ensembles

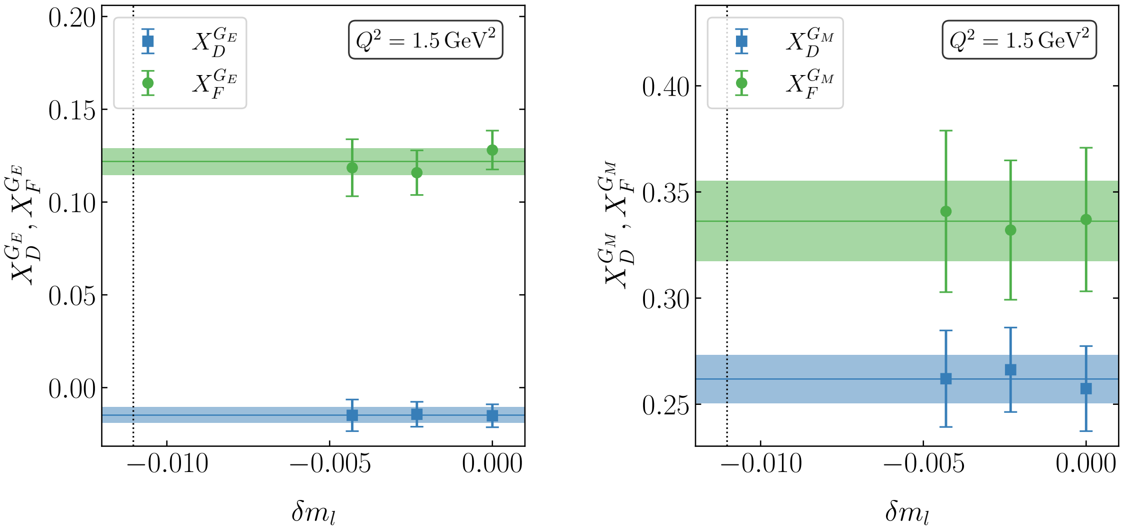

Figure D.12. The values of X_D and X_F plotted against Q^2, for the three ensembles at $\beta = 5.65$, (11-13 in table 5.2) for G_E (left) and G_M (right) at $\mathrm{Q}^2 = 1.54\,\mathrm{GeV}^2$.

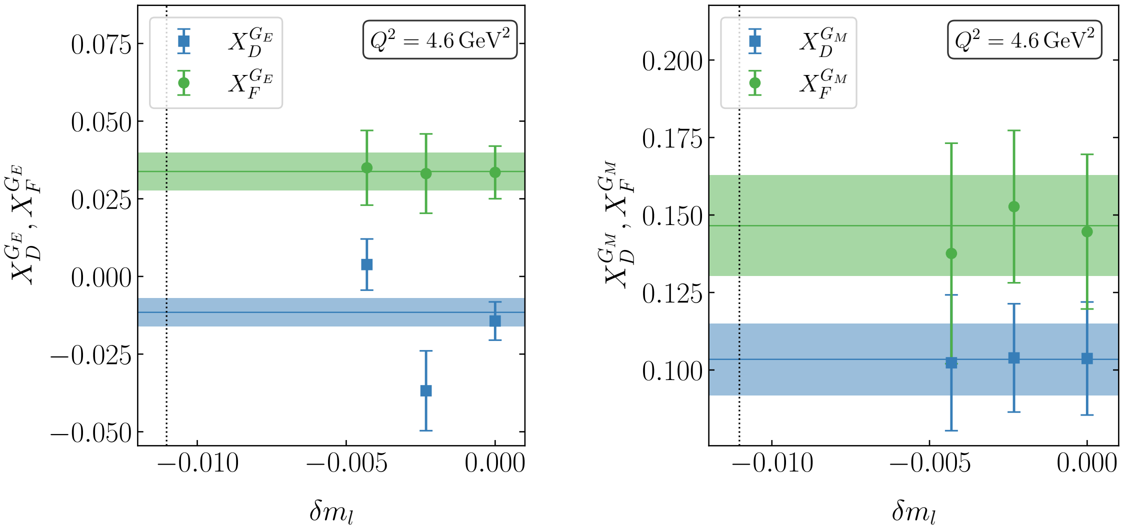

Figure D.13. The values of X_D and X_F plotted against Q^2, for the three ensembles at $\beta = 5.65$, (11-13 in table 5.2) for G_E (left) and G_M (right) at $\mathrm{Q}^2 = 4.63\,\mathrm{GeV}^2$.

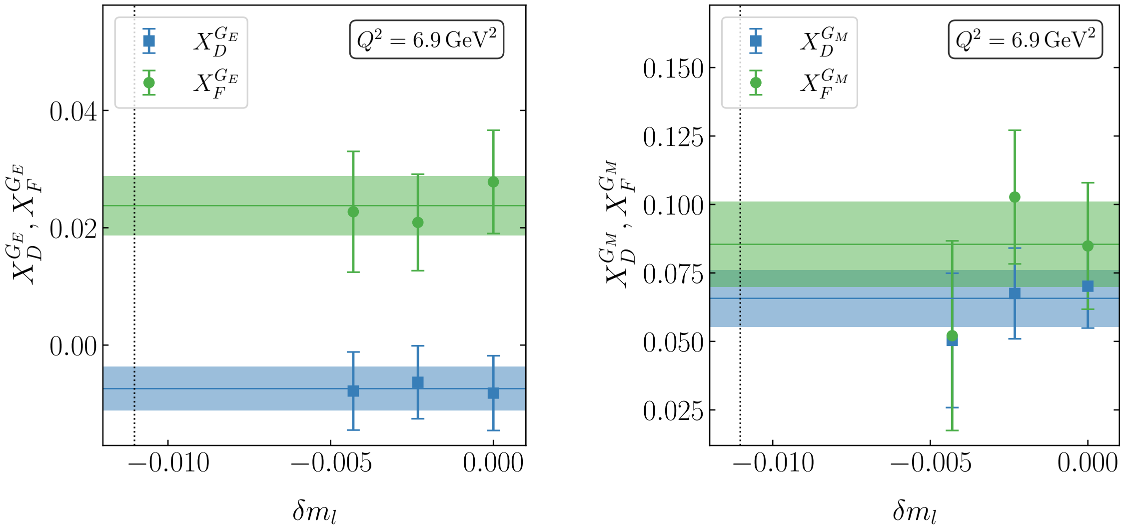

Figure D.14. The values of X_D and X_F plotted against Q^2, for the three ensembles at $\beta = 5.65$, (11-13 in table 5.2) for G_E (left) and G_M (right) at $\mathrm{Q}^2 = 6.95\,\mathrm{GeV}^2$.

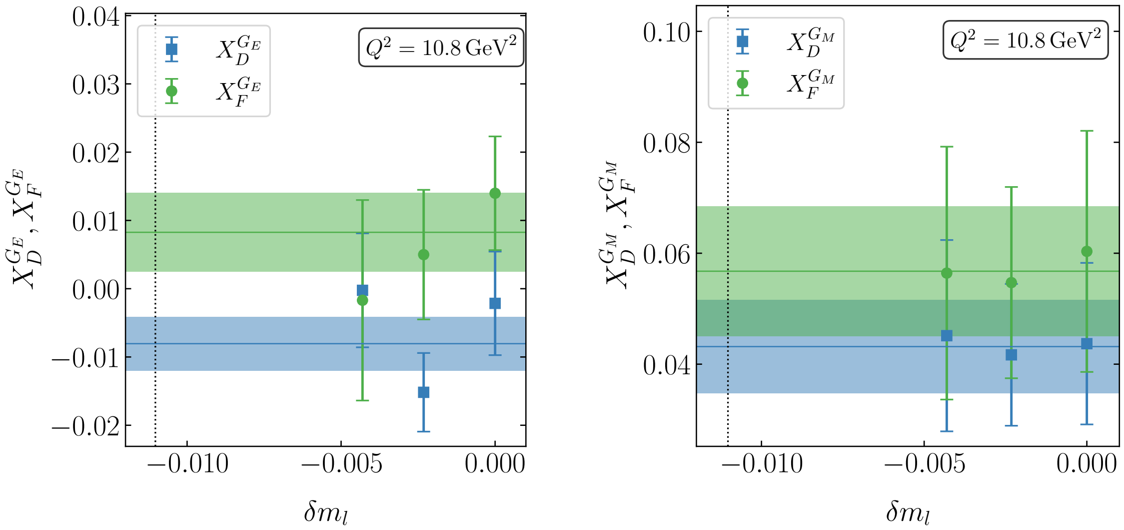

Figure D.15. The values of X_D and X_F plotted against Q^2, for the three ensembles at $\beta = 5.65$, (11-13 in table 5.2) for G_E (left) and G_M (right) at $\mathrm{Q}^2 = 10.8\,\mathrm{GeV}^2$.

Appendix E.

Global fit results

Table E.1. The fit results for momentum transfer $Q^2 = 3.13\,\mathrm{GeV}^2$

Fit	$X_D^{G_E}$	χ^2_{dof}	$X_F^{G_E}$	χ^2_{dof}	$G_{E,p}$	$\chi^2_{\mathrm{dof}}\ D_i$	$\chi^2_{\mathrm{dof}}\ F_i$
δm_l	-0.0248(29)	0.56	0.0764(48)	1.24	0.0308(91)	0.07	0.42
$a, \delta m_l$	-0.058(39)	0.54	0.102(69)	1.38	-00.01(18)	0.04	0.43
$a^2, \delta m_l$	-0.042(20)	0.53	0.090(35)	1.38	0.005(72)	0.04	0.43
δm_l^2	-0.042(20)	0.54	0.111(34)	1.26	0.087(67)	0.06	0.36
a, δm_l^2	-0.070(41)	0.53	0.139(74)	1.42	0.1(37)	0.03	0.12
a^2, δm_l^2	-0.056(26)	0.53	0.126(46)	1.42	0.08(19)	0.03	0.12
a, δm_l^2, $m_\pi L$	-0.070(41)	0.62	0.139(74)	1.66	0.1(37)	0.03	0.12
a^2, δm_l^2, $m_\pi L$	-0.056(26)	0.61	0.126(46)	1.66	0.08(19)	0.03	0.12

Fit	$X_D^{G_M}$	χ^2_{dof}	$X_F^{G_M}$	χ^2_{dof}	$G_{M,p}$	$\chi^2_{\mathrm{dof}}\ D_i$	$\chi^2_{\mathrm{dof}}\ F_i$
δm_l	0.2282(65)	2.87	0.2859(95)	1.43	0.307(18)	0.49	1.25
$a, \delta m_l$	0.430(98)	2.67	0.46(14)	1.40	0.64(37)	0.51	1.31
$a^2, \delta m_l$	0.333(50)	2.64	0.379(71)	1.38	0.47(16)	0.53	1.30
δm_l^2	0.285(45)	3.03	0.290(68)	1.61	0.40(12)	0.52	1.31
a, δm_l^2	0.52(12)	2.70	0.49(17)	1.59	0.79(41)	0.54	1.41
a^2, δm_l^2	0.414(73)	2.66	0.41(11)	1.56	0.61(20)	0.54	1.40
a, δm_l^2, $m_\pi L$	0.54(14)	3.10	0.53(20)	1.80	0.85(46)	0.54	1.41
a^2, δm_l^2, $m_\pi L$	0.416(73)	3.04	0.41(11)	1.71	0.61(21)	0.54	1.40

Table E.2. The fit results for momentum transfer $Q^2 = 4.93\,\mathrm{GeV}^2$

Fit	$X_D^{G_E}$	χ^2_{dof}	$X_F^{G_E}$	χ^2_{dof}	$G_{E,p}$	χ^2_{dof} D_i	χ^2_{dof} F_i
δm_l	-0.0195(27)	2.04	0.0436(41)	0.97	0.014(12)	0.03	0.23
$a, \delta m_l$	-0.071(26)	1.90	0.073(39)	1.00	0.14(41)	0.02	0.12
$a^2, \delta m_l$	-0.047(13)	1.88	0.058(20)	1.00	0.06(16)	0.02	0.13
δm_l^2	-0.028(16)	2.16	0.062(26)	1.00	0.11(16)	0.02	0.25
$a,\ \delta m_l^2$	-0.078(30)	2.03	0.090(46)	1.04	0.22(50)	0.02	0.12
$a^2,\ \delta m_l^2$	-0.054(21)	2.00	0.076(33)	1.04	0.15(25)	0.02	0.12
$a,\ \delta m_l^2,\ m_\pi L$	-0.077(30)	2.20	0.090(46)	1.13	0.22(50)	0.02	0.12
$a^2,\ \delta m_l^2,\ m_\pi L$	-0.053(21)	2.17	0.076(33)	1.13	0.15(25)	0.02	0.12

Fit	$X_D^{G_M}$	χ^2_{dof}	$X_F^{G_M}$	χ^2_{dof}	$G_{M,p}$	χ^2_{dof} D_i	χ^2_{dof} F_i
δm_l	0.1446(62)	1.58	0.1859(93)	1.35	0.219(17)	0.24	0.69
$a, \delta m_l$	0.347(61)	0.87	0.480(93)	0.68	0.97(37)	0.20	0.58
$a^2, \delta m_l$	0.251(32)	0.82	0.338(48)	0.66	0.55(14)	0.20	0.57
δm_l^2	0.197(38)	1.54	0.242(59)	1.37	0.33(11)	0.25	0.69
$a,\ \delta m_l^2$	0.383(69)	0.83	0.52(10)	0.68	1.13(43)	0.20	0.59
$a^2,\ \delta m_l^2$	0.290(47)	0.78	0.378(72)	0.67	0.67(20)	0.20	0.58
$a,\ \delta m_l^2,\ m_\pi L$	0.383(69)	0.90	0.52(11)	0.73	1.14(43)	0.20	0.59
$a^2,\ \delta m_l^2,\ m_\pi L$	0.290(47)	0.85	0.378(72)	0.73	0.67(20)	0.20	0.58

Table E.3. The fit results for momentum transfer $Q^2 = 7.37\,\mathrm{GeV}^2$

Fit	$X_D^{G_E}$	χ^2_{dof}	$X_F^{G_E}$	χ^2_{dof}	$G_{E,p}$	χ^2_{dof} D_i	χ^2_{dof} F_i
δm_l	-0.0146(30)	1.41	0.0298(46)	0.63	0.011(32)	0.01	0.02
$a, \delta m_l$	-00.007(21)	1.52	0.028(33)	0.68	0.04(58)	0.01	0.00
$a^2, \delta m_l$	-0.011(11)	1.52	0.028(17)	0.68	0.01(16)	0.01	0.00
δm_l^2	-0.011(21)	1.53	0.036(26)	0.68	0.02(23)	0.01	0.02
$a,\ \delta m_l^2$	-00.005(27)	1.67	0.034(40)	0.75	0.05(73)	0.01	0.00
$a^2,\ \delta m_l^2$	-00.009(22)	1.67	0.035(29)	0.75	0.03(36)	0.01	0.00
$a,\ \delta m_l^2,\ m_\pi L$	-00.005(27)	1.86	0.034(40)	0.83	0.05(73)	0.01	0.00
$a^2,\ \delta m_l^2,\ m_\pi L$	-00.009(22)	1.86	0.035(29)	0.83	0.03(36)	0.01	0.00

Fit	$X_D^{G_M}$	χ^2_{dof}	$X_F^{G_M}$	χ^2_{dof}	$G_{M,p}$	χ^2_{dof} D_i	χ^2_{dof} F_i
δm_l	0.0970(70)	0.85	0.128(10)	0.97	0.147(16)	0.35	0.69
$a, \delta m_l$	0.164(49)	0.74	0.222(71)	0.88	0.17(14)	0.36	0.73
$a^2, \delta m_l$	0.132(26)	0.73	0.176(38)	0.88	0.170(62)	0.35	0.73
δm_l^2	0.083(43)	0.92	0.121(64)	1.06	0.078(73)	0.26	0.66
$a,\ \delta m_l^2$	0.143(59)	0.77	0.199(85)	0.95	0.12(15)	0.27	0.71
$a^2,\ \delta m_l^2$	0.108(46)	0.76	0.150(68)	0.95	0.094(91)	0.27	0.71
$a,\ \delta m_l^2,\ m_\pi L$	0.143(60)	0.85	0.199(86)	1.05	0.12(15)	0.27	0.71
$a^2,\ \delta m_l^2,\ m_\pi L$	0.108(46)	0.84	0.150(67)	1.05	0.094(91)	0.27	0.71

Appendix F.

Correlation Functions

We define the baryon correlation functions as the expectation value of two baryon interpolation operators, projected onto a definite momentum value and spin-parity state.

$$C_{\lambda\Sigma\Sigma}(t) = \mathrm{tr}_D\Gamma \left\langle \tilde{B}_\Sigma(t;\vec{p})\bar{B}_\Sigma(\vec{0},0)\right\rangle_\lambda , \tag{F.1}$$

$$C_{\lambda\Sigma N}(t) = \mathrm{tr}_D\Gamma \left\langle \tilde{B}_\Sigma(t;\vec{p})\bar{B}_N(\vec{0},0)\right\rangle_\lambda , \tag{F.2}$$

$$C_{\lambda N\Sigma}(t) = \mathrm{tr}_D\Gamma \left\langle \tilde{B}_N(t;\vec{p}+\vec{q})\bar{B}_\Sigma(\vec{0},0)\right\rangle_\lambda , \tag{F.3}$$

$$C_{\lambda NN}(t) = \mathrm{tr}_D\Gamma \left\langle \tilde{B}_N(t;\vec{p}+\vec{q})\bar{B}_N(\vec{0},0)\right\rangle_\lambda , \tag{F.4}$$

The interpolating operators we define by

$$\tilde{B}_{\Sigma_\alpha}(t;\vec{p}) = \int_{\vec{x}} e^{-\vec{p}\cdot\vec{x}} B_{\Sigma_\alpha}(t;\vec{x}\,) = \sum_{\vec{x}} e^{-\vec{p}\cdot\vec{x}} \epsilon^{abc} d^a_\alpha(x) \left[d^b(x)^{T_D} C\gamma_5 s^c(x)\right] \tag{F.5}$$

$$\tilde{B}_{N_\alpha}(t;\vec{p}) = \int_{\vec{x}} e^{-\vec{p}\cdot\vec{x}} B_{N_\alpha}(t;\vec{x}\,) = \sum_{\vec{x}} e^{-\vec{p}\cdot\vec{x}} \epsilon^{abc} d^a_\alpha(x) \left[d^b(x)^{T_D} C\gamma_5 u^c(x)\right] \tag{F.6}$$

Using this, the correlation function can be written in terms of the quark propagator

$$\begin{aligned} C_{\lambda NN}(t) = \sum_{\vec{x}} & e^{-i(\vec{p}+\vec{q})\cdot\vec{x}} \epsilon_{abc}\epsilon_{a',b',c'} \\ & \langle \mathrm{tr}_D[\Gamma[G^{(dd)}(x,0)]^{aa'}]\mathrm{tr}_D[[\tilde{G}^{(uu)}(x,0)]^{bb'}[G^{(dd)}(x,0)]^{cc'}] \\ & \quad + \mathrm{tr}_D[\Gamma[G^{dd}(x,0)]^{aa'}[\tilde{G}^{(uu)}(x,0)]^{bb'}[G^{(dd)}(x,0)]^{cc'}]\rangle, \end{aligned} \tag{F.7}$$

$$\begin{aligned} C_{\lambda\Sigma\Sigma}(t) = \sum_{\vec{x}} & e^{-i\vec{p}\cdot\vec{x}} \epsilon_{abc}\epsilon_{a',b',c'} \\ & \langle \mathrm{tr}_D[\Gamma[G^{(dd)}(x,0)]^{aa'}]\mathrm{tr}_D[[\tilde{G}^{(ss)}(x,0)]^{bb'}[G^{(dd)}(x,0)]^{cc'}] \\ & \quad + \mathrm{tr}_D[\Gamma[G^{dd}(x,0)]^{aa'}[\tilde{G}^{(ss)}(x,0)]^{bb'}[G^{(dd)}(x,0)]^{cc'}]\rangle, \end{aligned} \tag{F.8}$$

$$\begin{aligned} C_{\lambda N\Sigma}(t) = \sum_{\vec{x}} & e^{-i(\vec{p}+\vec{q})\cdot\vec{x}} \epsilon_{abc}\epsilon_{a',b',c'} \\ & \langle \mathrm{tr}_D[\Gamma[G^{(dd)}(x,0)]^{aa'}]\mathrm{tr}_D[[\tilde{G}^{(us)}(x,0)]^{bb'}[G^{(dd)}(x,0)]^{cc'}] \\ & \quad + \mathrm{tr}_D[\Gamma[G^{dd}(x,0)]^{aa'}[\tilde{G}^{(us)}(x,0)]^{bb'}[G^{(dd)}(x,0)]^{cc'}]\rangle, \end{aligned} \tag{F.9}$$

$$\begin{aligned} C_{\lambda\Sigma N}(t) = \sum_{\vec{x}} & e^{-i\vec{p}\cdot\vec{x}} \epsilon_{abc}\epsilon_{a',b',c'} \\ & \langle \mathrm{tr}_D[\Gamma[G^{(dd)}(x,0)]^{aa'}]\mathrm{tr}_D[[\tilde{G}^{(su)}(x,0)]^{bb'}[G^{(dd)}(x,0)]^{cc'}] \\ & \quad + \mathrm{tr}_D[\Gamma[G^{dd}(x,0)]^{aa'}[\tilde{G}^{(su)}(x,0)]^{bb'}[G^{(dd)}(x,0)]^{cc'}]\rangle, \end{aligned} \tag{F.10}$$

Bibliography

[1] Y. Nakamura and H. Stuben, *BQCD - Berlin quantum chromodynamics program*, *PoS* **LATTICE2010** (2010) 040, [`arXiv:1011.0199`]. (document)

[2] T. R. Haar, Y. Nakamura and H. Stüben, *An update on the BQCD Hybrid Monte Carlo program*, *EPJ Web Conf.* **175** (2018) 14011, [`arXiv:1711.03836`]. (document)

[3] R. G. Edwards and B. Joó, *The chroma software system for lattice qcd*, *Nuclear Physics B - Proceedings Supplements* **140** (2005) 832 – 834. (document)

[4] K. G. Wilson, *Confinement of quarks*, *Physical Review D* **10** (oct, 1974) 2445–2459. 1, 2, 2.4

[5] M. N. Rosenbluth, *High energy elastic scattering of electrons on protons*, *Phys. Rev.* **79** (Aug, 1950) 615–619. 1

[6] V. D. Burkert, *Jefferson Lab at 12 GeV: The Science Program*, *Ann. Rev. Nucl. Part. Sci.* **68** (2018) 405–428. 1

[7] P. Achenbach et al., *The Present and Future of QCD*, `arXiv:2303.02579`. 1

[8] S. Bethke, *The 2009 World Average of alpha(s)*, *Eur. Phys. J. C* **64** (2009) 689–703, [`arXiv:0908.1135`]. 2, 2.1

[9] H. J. Rothe, *Lattice Gauge Theories : An Introduction (Fourth Edition)*, vol. 43. World Scientific Publishing Company, 2012, 10.1142/8229. 2, 2.3

[10] I. Montvay and G. Muenster, *Quantum Fields on a Lattice*, vol. 1. Cambridge University Press, 1, 1994. 2, 2.8

[11] C. Gattringer and C. B. Lang, *Quantum chromodynamics on the lattice*, vol. 788. Springer, Berlin, 2010, 10.1007/978-3-642-01850-3. 2

[12] J. Smit, *Introduction to quantum fields on a lattice: A robust mate*, vol. 1.

Cambridge University Press, 1, 2002. 2

[13] R. Gupta, *Introduction to lattice QCD: Course*, in *Les Houches Summer School in Theoretical Physics, Session 68: Probing the Standard Model of Particle Interactions*, pp. 83–219, 7, 1997. `hep-lat/9807028`. 2

[14] R. P. Feynman, *The principle of least action in quantum mechanics*. PhD thesis, Princeton U., 1942. 10.1142/9789812567635. 2.1

[15] H. B. Nielsen and M. Ninomiya, *Absence of Neutrinos on a Lattice. 1. Proof by Homotopy Theory*, *Nucl. Phys. B* **185** (1981) 20. 2.3

[16] D. Friedan, *A PROOF OF THE NIELSEN-NINOMIYA THEOREM*, *Commun. Math. Phys.* **85** (1982) 481–490. 2.3

[17] L. Susskind, *Lattice Fermions*, *Phys. Rev. D* **16** (1977) 3031–3039. 2.3

[18] J. B. Kogut and L. Susskind, *Hamiltonian Formulation of Wilson's Lattice Gauge Theories*, *Phys. Rev. D* **11** (1975) 395–408. 2.3

[19] C. van den Doel and J. Smit, *Dynamical Symmetry Breaking in Two Flavor $SU(N)$ and $SO(N)$ Lattice Gauge Theories*, *Nucl. Phys. B* **228** (1983) 122–144. 2.3

[20] K. Symanzik, *Continuum Limit and Improved Action in Lattice Theories. 1. Principles and φ^4 Theory*, *Nucl. Phys. B* **226** (1983) 187–204. 2.4

[21] B. Sheikholeslami and R. Wohlert, *Improved Continuum Limit Lattice Action for QCD with Wilson Fermions*, *Nucl. Phys. B* **259** (1985) 572. 2.4

[22] M. Luscher and P. Weisz, *On-Shell Improved Lattice Gauge Theories*, *Commun. Math. Phys.* **97** (1985) 59. 2.5

[23] S. Itoh, Y. Iwasaki, Y. Oyanagi and T. Yoshie, *Renormalization Group Improved Lattice SU(3) Gauge Action and Hadron Spectrum in Quenched QCD on a 8**3 X 16 Lattice*, *Phys. Lett. B* **148** (1984) 153–156. 2.5

[24] T. R. Haar, *Optimisations to Hybrid Monte Carlo for Lattice QCD*. PhD thesis, The University of Adelaide, 2019. 2.6

[25] R. Abbott et al., *Sampling QCD field configurations with gauge-equivariant flow models*, *PoS* **LATTICE2022** (2023) 036, [`arXiv:2208.03832`]. 2.6

[26] S. Duane, A. D. Kennedy, B. J. Pendleton and D. Roweth, *Hybrid Monte Carlo*,

Phys. Lett. B **195** (1987) 216–222. 2.6

[27] C. T. Sachrajda and G. Villadoro, *Twisted boundary conditions in lattice simulations*, *Phys. Lett. B* **609** (2005) 73–85, [`hep-lat/0411033`]. 2.7, 2.7, 6.6.3

[28] P. F. Bedaque and J.-W. Chen, *Twisted valence quarks and hadron interactions on the lattice*, *Phys. Lett. B* **616** (2005) 208–214, [`hep-lat/0412023`]. 2.7, 2.7, 6.6.3

[29] QCDSF, UKQCD collaboration, M. Gockeler et al., *Nucleon structure with partially twisted boundary conditions*, *PoS* **LATTICE2008** (2008) 138. 2.7

[30] J. M. Flynn, A. Juttner, C. T. Sachrajda, P. A. Boyle and J. M. Zanotti, *Hadronic form factors in Lattice QCD at small and vanishing momentum transfer*, *JHEP* **05** (2007) 016, [`hep-lat/0703005`]. 2.7, 6.8.2

[31] D. Guadagnoli, V. Lubicz, M. Papinutto and S. Simula, *First Lattice QCD Study of the Sigma —> n Axial and Vector Form Factors with SU(3) Breaking Corrections*, *Nucl. Phys. B* **761** (2007) 63–91, [`hep-ph/0606181`]. 2.7, 6.1

[32] F. J. Jiang and B. C. Tiburzi, *Flavor twisted boundary conditions, pion momentum, and the pion electromagnetic form-factor*, *Phys. Lett. B* **645** (2007) 314–321, [`hep-lat/0610103`]. 2.7, 6.6.3

[33] F. J. Jiang and B. C. Tiburzi, *Flavor Twisted Boundary Conditions and the Nucleon Vector Current*, *Phys. Rev. D* **78** (2008) 114505, [`arXiv:0810.1495`]. 2.7

[34] B. C. Tiburzi, *Finite Volume Effects on the Extraction of Form Factors at Zero Momentum*, *Phys. Rev. D* **90** (2014) 054508, [`arXiv:1407.4059`]. 2.7

[35] M. Creutz, *Gauge Fixing, the Transfer Matrix, and Confinement on a Lattice*, *Phys. Rev. D* **15** (1977) 1128. 2.8

[36] G. P. Lepage, *The Analysis of Algorithms for Lattice Field Theory*, in *Theoretical Advanced Study Institute in Elementary Particle Physics*, 6, 1989. 3.1.2, 3.1.2

[37] G. Parisi, *The strategy for computing the hadronic mass spectrum*, *Physics Reports* **103** (1984) 203 – 211. 3.1.2

[38] M. L. Wagman and M. J. Savage, *Statistics of baryon correlation functions in lattice QCD*, *Phys. Rev. D* **96** (2017) 114508, [`arXiv:1611.07643`]. 3.1.2

[39] S. R. Beane, W. Detmold, T. C. Luu, K. Orginos, A. Parreno, M. J. Savage et al., *High Statistics Analysis using Anisotropic Clover Lattices: (I) Single Hadron*

Correlation Functions, *Phys. Rev. D* **79** (2009) 114502, [`arXiv:0903.2990`]. 3.1.2

[40] S. R. Beane, W. Detmold, T. C. Luu, K. Orginos, A. Parreno, M. J. Savage et al., *High Statistics Analysis using Anisotropic Clover Lattices. II. Three-Baryon Systems*, *Phys. Rev. D* **80** (2009) 074501, [`arXiv:0905.0466`]. 3.1.2

[41] NPLQCD, QCDSF collaboration, S. R. Beane et al., *Charged multihadron systems in lattice QCD+QED*, *Phys. Rev. D* **103** (2021) 054504, [`arXiv:2003.12130`]. 3.1.4

[42] G. P. Lepage, *Lattice QCD for novices*, in *Strong interactions at low and intermediate energies. Proceedings, 13th Annual Hampton University Graduate Studies, HUGS'98, Newport News, USA, May 26-June 12, 1998*, pp. 49–90, 1998. `hep-lat/0506036`. 3.3

[43] P. Güttinger, *Das verhalten von atomen im magnetischen drehfeld*, *Zeitschrift für Physik* **73** (1932) 169–184. 4

[44] W. Pauli, *Principles of Wave Mechanics.* Handbuch der Physik, 1933. 4

[45] H. Hellmann, *Einführung in die Quantenchemie.* Leipzig: Franz Deuticke, 1937, https://doi.org/10.1007/978-3-662-45967-6. 4

[46] R. P. Feynman, *Forces in molecules*, *Phys. Rev.* **56** (Aug, 1939) 340–343. 4

[47] A. Agadjanov, D. Djukanovic, G. von Hippel, H. B. Meyer, K. Ottnad and H. Wittig, *The nucleon sigma terms with $N_f = 2 + 1$ O(a)-improved Wilson fermions*, `arXiv:2303.08741`. 4

[48] H. Ohki, H. Fukaya, S. Hashimoto, T. Kaneko, H. Matsufuru, J. Noaki et al., *Nucleon sigma term and strange quark content from lattice QCD with exact chiral symmetry*, *Phys. Rev. D* **78** (2008) 054502, [`arXiv:0806.4744`]. 4

[49] S. Durr et al., *Sigma term and strangeness content of octet baryons*, *Phys. Rev. D* **85** (2012) 014509, [`arXiv:1109.4265`]. 4

[50] QCDSF-UKQCD collaboration, R. Horsley, Y. Nakamura, H. Perlt, D. Pleiter, P. E. L. Rakow, G. Schierholz et al., *Hyperon sigma terms for 2+1 quark flavours*, *Phys. Rev. D* **85** (2012) 034506, [`arXiv:1110.4971`]. 4

[51] ETM collaboration, S. Dinter, V. Drach, R. Frezzotti, G. Herdoiza, K. Jansen and G. Rossi, *Sigma terms and strangeness content of the nucleon with $N_f = 2 + 1 + 1$*

twisted mass fermions, JHEP **08** (2012) 037, [arXiv:1202.1480]. 4

[52] P. E. Shanahan, A. W. Thomas and R. D. Young, *Sigma terms from an SU(3) chiral extrapolation*, Phys. Rev. D **87** (2013) 074503, [arXiv:1205.5365]. 4

[53] G. S. Bali et al., *Nucleon mass and sigma term from lattice QCD with two light fermion flavors*, Nucl. Phys. B **866** (2013) 1–25, [arXiv:1206.7034]. 4

[54] CSSM and QCDSF/UKQCD Collaborations collaboration, A. J. Chambers, R. Horsley, Y. Nakamura, H. Perlt, D. Pleiter, P. E. L. Rakow et al., *Feynman-hellmann approach to the spin structure of hadrons*, Phys. Rev. D **90** (Jul, 2014) 014510, [arXiv:1405.3019]. 4

[55] A. J. Chambers, R. Horsley, Y. Nakamura, H. Perlt, D. Pleiter, P. E. L. Rakow et al., *Applications of the Feynman-Hellmann Theorem in Hadron Structure*, PoS **LATTICE2015** (2016) 125, [arXiv:1511.07090]. 4

[56] C. Bouchard, C. C. Chang, T. Kurth, K. Orginos and A. Walker-Loud, *On the feynman-hellmann theorem in quantum field theory and the calculation of matrix elements*, Phys. Rev. D **96** (Jul, 2017) 014504, [arXiv:1612.06963]. 4, 6.1

[57] A. J. Chambers, J. Dragos, R. Horsley, Y. Nakamura, H. Perlt, D. Pleiter et al., *Electromagnetic form factors at large momenta from lattice QCD*, Physical Review D **96** (Dec., 2017) , [arXiv:1702.01513]. 4, 5.3, 5.4, 5.5

[58] C. C. "Chang and others", *A per-cent-level determination of the nucleon axial coupling from quantum chromodynamics*, Nature **558** (2018) 91–94, [arXiv:1805.12130]. 4

[59] QCDSF-UKQCD-CSSM collaboration, M. Batelaan, R. Horsley, Y. Nakamura, H. Perlt, D. Pleiter, P. E. L. Rakow et al., *Nucleon Form Factors from the Feynman-Hellmann Method in Lattice QCD*, PoS **LATTICE2021** (2022) 426, [arXiv:2202.01366]. 4

[60] R. E. Smail, R. Horsley, Y. Nakamura, H. Perlt, D. Pleiter, P. E. L. Rakow et al., *Tensor Charges and their Impact on Physics Beyond the Standard Model*, PoS **LATTICE2021** (2022) 494, [arXiv:2112.05330]. 4

[61] R. E. Smail et al., *Constraining beyond the Standard Model nucleon isovector charges*, arXiv:2304.02866. 4

[62] QCDSF, UKQCD, CSSM collaboration, R. Horsley, T. Howson, W. Kamleh,

Y. Nakamura, H. Perlt, P. E. L. Rakow et al., *Determining the glue component of the nucleon*, *PoS* **LATTICE2019** (2020) 220, [`arXiv:2001.07639`]. 4

[63] QCDSF, UKQCD, CSSM collaboration, T. L. Howson, R. Horsley, W. Kamleh, Y. Nakamura, H. Perlt, P. E. L. Rakow et al., *Directly calculating the glue component of the nucleon in lattice QCD*, *EPJ Web Conf.* **245** (2020) 06031. 4

[64] QCDSF/UKQCD collaboration, K. U. Can, *The Compton amplitude and nucleon structure functions*, *PoS* **LATTICE2022** (2023) 237, [`arXiv:2212.09197`]. 4

[65] CSSM/QCDSF/UKQCD collaboration, A. Hannaford-Gunn, R. Horsley, H. Perlt, P. Rakow, G. Schierholz, H. Stüben et al., *Generalised Parton Distributions from Lattice Feynman-Hellmann Techniques*, *PoS* **LATTICE2021** (2022) 088, [`arXiv:2202.03662`]. 4

[66] CSSM/QCDSF/UKQCD collaboration, A. Hannaford-Gunn et al., *Investigating the Compton amplitude subtraction function in lattice QCD*, *PoS* **LATTICE2021** (2022) 028, [`arXiv:2207.03040`]. 4

[67] QCDSF-UKQCD-CSSM collaboration, R. Horsley, Y. Nakamura, H. Perlt, P. E. L. Rakow, G. Schierholz, K. Somfleth et al., *Structure functions from the Compton amplitude*, *PoS* **LATTICE2019** (2020) 137, [`arXiv:2001.05366`]. 4

[68] R. Hofstadter, H. R. Fechter and J. A. McIntyre, *High-Energy Electron Scattering and Nuclear Structure Determinations*, *Phys. Rev.* **92** (1953) 978. 5.1

[69] R. Hofstadter and R. W. McAllister, *Electron Scattering From the Proton*, *Phys. Rev.* **98** (1955) 217–218. 5.1

[70] R. Hofstadter, F. Bumiller and M. R. Yearian, *Electromagnetic structure of the proton and neutron*, *Rev. Mod. Phys.* **30** (Apr, 1958) 482–497. 5.1

[71] E. E. Chambers and R. Hofstadter, *Structure of the Proton*, *Phys. Rev.* **103** (1956) 1454–1463. 5.1

[72] L. L. Foldy, *The electromagnetic properties of dirac particles*, *Phys. Rev.* **87** (Sep, 1952) 688–693. 5.1

[73] V. Punjabi et al., *Proton elastic form-factor ratios to $Q^{**}2 = 3.5\text{-}GeV^{**}2$ by polarization transfer*, *Phys. Rev. C* **71** (2005) 055202, [`nucl-ex/0501018`]. 5.1, 5.1, 5.10.3

[74] V. Punjabi, C. F. Perdrisat, M. K. Jones, E. J. Brash and C. E. Carlson, *The structure of the nucleon: Elastic electromagnetic form factors*, *The European Physical Journal A* **51** (Jul, 2015) 79. 5.1, 5.1, 5.1, 5.8.1

[75] L. Andivahis et al., *Measurements of the electric and magnetic form-factors of the proton from Q**2 = 1.75-GeV/c**2 to 8.83-GeV/c**2*, *Phys. Rev. D* **50** (1994) 5491–5517. 5.1

[76] J. Arrington, W. Melnitchouk and J. A. Tjon, *Global analysis of proton elastic form factor data with two-photon exchange corrections*, *Phys. Rev. C* **76** (2007) 035205, [`arXiv:0707.1861`]. 5.1, 5.19, 5.20, 5.21

[77] N. Cundy et al., *Non-perturbative improvement of stout-smeared three flavour clover fermions*, *Phys. Rev. D* **79** (2009) 094507, [`arXiv:0901.3302`]. 5.3

[78] W. Bietenholz et al., *Tuning the strange quark mass in lattice simulations*, *Phys. Lett. B* **690** (2010) 436–441, [`arXiv:1003.1114`]. 5.3

[79] W. Bietenholz et al., *Flavour blindness and patterns of flavour symmetry breaking in lattice simulations of up, down and strange quarks*, *Phys. Rev. D* **84** (2011) 054509, [`arXiv:1102.5300`]. 5.3, 5.7, 5.9, 5.9

[80] QCDSF-UKQCD collaboration, R. Horsley, J. Najjar, Y. Nakamura, H. Perlt, D. Pleiter, P. E. L. Rakow et al., *SU(3) flavour symmetry breaking and charmed states*, *PoS* **LATTICE2013** (2014) 249, [`arXiv:1311.5010`]. 5.3

[81] V. G. Bornyakov, R. Horsley, R. Hudspith, Y. Nakamura, H. Perlt, D. Pleiter et al., *Wilson flow and scale setting from lattice QCD*, `arXiv:1508.05916`. 5.3, 5.2, 5.7, 5.7.2

[82] J. Green, S. Meinel, M. Engelhardt, S. Krieg, J. Laeuchli, J. Negele et al., *High-precision calculation of the strange nucleon electromagnetic form factors*, *Phys. Rev. D* **92** (2015) 031501, [`arXiv:1505.01803`]. 5.3

[83] Y.-C. Jang, R. Gupta, H.-W. Lin, B. Yoon and T. Bhattacharya, *Nucleon Electromagnetic Form Factors in the Continuum Limit from 2+1+1-flavor Lattice QCD*, `arXiv:1906.07217`. 5.5

[84] PNDME collaboration, T. Bhattacharya, V. Cirigliano, S. Cohen, R. Gupta, A. Joseph, H.-W. Lin et al., *Iso-vector and Iso-scalar Tensor Charges of the Nucleon from Lattice QCD*, *Phys. Rev. D* **92** (2015) 094511, [`arXiv:1506.06411`].

5.5

[85] R. Gupta, S. Park, M. Hoferichter, E. Mereghetti, B. Yoon and T. Bhattacharya, *Pion–Nucleon Sigma Term from Lattice QCD*, *Phys. Rev. Lett.* **127** (2021) 242002, [`arXiv:2105.12095`]. 5.5

[86] J. He et al., *Detailed analysis of excited-state systematics in a lattice QCD calculation of gA*, *Phys. Rev. C* **105** (2022) 065203, [`arXiv:2104.05226`]. 5.5

[87] S. Capitani, B. Knippschild, M. Della Morte and H. Wittig, *Systematic errors in extracting nucleon properties from lattice QCD*, *PoS* **LATTICE2010** (2010) 147, [`arXiv:1011.1358`]. 5.5

[88] ALPHA collaboration, J. Bulava, M. A. Donnellan and R. Sommer, *The B*Bpi Coupling in the Static Limit*, *PoS* **LATTICE2010** (2010) 303, [`arXiv:1011.4393`]. 5.5

[89] J. Dragos, *Improved determination of hadron matrix elements using the variational method*. PhD thesis, The University of Adelaide, 2017. 5.5

[90] F. M. Stokes, W. Kamleh, D. B. Leinweber, M. S. Mahbub, B. J. Menadue and B. J. Owen, *Parity-expanded variational analysis for nonzero momentum*, *Phys. Rev.* **D92** (2015) 114506, [`arXiv:1302.4152`]. 5.5, 6.6.4

[91] J. Bickerton, R. Horsley, Y. Nakamura, H. Perlt, D. Pleiter, P. Rakow et al., *Patterns of flavor symmetry breaking in hadron matrix elements involving u , d , and s quarks*, *Phys. Rev. D* **100** (2019) 114516, [`arXiv:1909.02521`]. 5.3, 5.7, 5.10, 6.8.4

[92] J. J. Kelly, *Simple parametrization of nucleon form factors*, *Phys. Rev. C* **70** (Dec, 2004) 068202. 5.8.1, 5.8.1, 5.10.1, 5.10.2, 5.19, 5.20, 5.21

[93] P. E. Shanahan, A. W. Thomas, R. D. Young, J. M. Zanotti, R. Horsley, Y. Nakamura et al., *Electric form factors of the octet baryons from lattice QCD and chiral extrapolation*, *Phys. Rev. D* **90** (2014) 034502, [`arXiv:1403.1965`]. 5.8.1

[94] R. J. Hill and G. Paz, *Model independent extraction of the proton charge radius from electron scattering*, *Phys. Rev. D* **82** (2010) 113005, [`arXiv:1008.4619`]. 5.8.1

[95] G. Colangelo, S. Durr and C. Haefeli, *Finite volume effects for meson masses and*

decay constants, Nucl. Phys. B **721** (2005) 136–174, [`hep-lat/0503014`]. 5.9

[96] QCDSF-UKQCD collaboration, A. Ali Khan et al., *The Nucleon mass in N(f) = 2 lattice QCD: Finite size effects from chiral perturbation theory*, Nucl. Phys. B **689** (2004) 175–194, [`hep-lat/0312030`]. 5.9

[97] A. J. R. Puckett et al., *Recoil Polarization Measurements of the Proton Electromagnetic Form Factor Ratio to $Q^2 = 8.5$ GeV^2*, Phys. Rev. Lett. **104** (2010) 242301, [`arXiv:1005.3419`]. 5.10.3

[98] A. J. R. Puckett et al., *Final Analysis of Proton Form Factor Ratio Data at* $\mathbf{Q^2 = 4.0}$*, 4.8 and 5.6 GeV*$\mathbf{^2}$, Phys. Rev. C **85** (2012) 045203, [`arXiv:1102.5737`]. 5.10.3

[99] M. Kobayashi and T. Maskawa, *CP Violation in the Renormalizable Theory of Weak Interaction*, Prog. Theor. Phys. **49** (1973) 652–657. 6.1

[100] N. Cabibbo, *Unitary Symmetry and Leptonic Decays*, Phys. Rev. Lett. **10** (1963) 531–533. 6.1

[101] Particle Data Group collaboration, R. L. Workman et al., *Review of Particle Physics*, PTEP **2022** (2022) 083C01. 6.1, 6.1, 6.1

[102] FlaviaNet Working Group on Kaon Decays collaboration, M. Antonelli et al., *An Evaluation of $|V_{us}|$ and precise tests of the Standard Model from world data on leptonic and semileptonic kaon decays*, Eur. Phys. J. C **69** (2010) 399–424, [`arXiv:1005.2323`]. 6.1

[103] Flavour Lattice Averaging Group collaboration, S. Aoki et al., *FLAG Review 2019*, `arXiv:1902.08191`. 6.1

[104] S. Weinberg, *Charge symmetry of weak interactions*, Phys. Rev. **112** (1958) 1375–1379. 6.1

[105] Bristol-Geneva-Heidelberg-Orsay-Rutherford-Strasbourg collaboration, M. Bourquin et al., *Measurements of Hyperon Semileptonic Decays at the CERN Super Proton Synchrotron. 1. The $\Sigma^- \to \Lambda e^-$ Anti-neutrino Decay Mode*, Z. Phys. C **12** (1982) 307. 6.1

[106] S. Y. Hsueh et al., *A High Precision Measurement of Polarized Sigma- beta Decay*, Phys. Rev. D **38** (1988) 2056. 6.1

[107] N. Cabibbo, E. C. Swallow and R. Winston, *Semileptonic hyperon decays*, *Ann. Rev. Nucl. Part. Sci.* **53** (2003) 39–75, [`hep-ph/0307298`]. 6.1

[108] M. Ademollo and R. Gatto, *Nonrenormalization theorem for the strangeness-violating vector currents*, *Phys. Rev. Lett.* **13** (Aug, 1964) 264–266. 6.1

[109] P. G. Ratcliffe, *Hyperon beta decay and the CKM matrix*, *Czech. J. Phys.* **54** (2004) B11–B20, [`hep-ph/0402063`]. 6.1

[110] V. Mateu and A. Pich, *V(us) determination from hyperon semileptonic decays*, *JHEP* **10** (2005) 041, [`hep-ph/0509045`]. 6.1

[111] S. Sasaki and T. Yamazaki, *Lattice study of flavor SU(3) breaking in hyperon beta decay*, *Phys. Rev. D* **79** (2009) 074508, [`arXiv:0811.1406`]. 6.1

[112] S. Sasaki, *Hyperon vector form factor from 2+1 flavor lattice QCD*, *Phys. Rev. D* **86** (2012) 114502, [`arXiv:1209.6115`]. 6.1

[113] S. Sasaki, *Continuum limit of hyperon vector coupling $f_1(0)$ from 2+1 flavor domain wall QCD*, *Phys. Rev. D* **96** (2017) 074509, [`arXiv:1708.04008`]. 6.1

[114] P. E. Shanahan, A. N. Cooke, R. Horsley, Y. Nakamura, P. E. L. Rakow, G. Schierholz et al., *SU(3) breaking in hyperon transition vector form factors*, *Phys. Rev. D* **92** (2015) 074029, [`arXiv:1508.06923`]. 6.1

[115] N. Miller et al., *The hyperon spectrum from lattice QCD*, *PoS* **LATTICE2021** (2022) 448, [`arXiv:2201.01343`]. 6.1

[116] M. Batelaan, K. U. Can, R. Horsley, Y. Nakamura, P. E. L. Rakow, G. Schierholz et al., *Feynman–Hellmann approach to transition matrix elements and quasi-degenerate energy states*, `arXiv:2305.05491`. 6.1

[117] G. M. de Divitiis, R. Petronzio and N. Tantalo, *On the discretization of physical momenta in lattice QCD*, *Phys. Lett. B* **595** (2004) 408–413, [`hep-lat/0405002`]. 6.6.3

[118] J. Dragos, R. Horsley, W. Kamleh, D. B. Leinweber, Y. Nakamura, P. E. L. Rakow et al., *Nucleon matrix elements using the variational method in lattice QCD*, *Phys. Rev. D* **94** (2016) 074505, [`arXiv:1606.03195`]. 6.6.4

[119] B. J. Owen, J. Dragos, W. Kamleh, D. B. Leinweber, M. S. Mahbub, B. J. Menadue et al., *Variational approach to the calculation of g_a*, *Physics Letters B*

723 (2013) 217 – 223, [`arXiv:1212.4668`]. 6.6.4

[120] BGR [Bern-Graz-Regensburg] collaboration, G. P. Engel, C. B. Lang, M. Limmer, D. Mohler and A. Schafer, *Meson and baryon spectrum for QCD with two light dynamical quarks*, *Phys. Rev. D* **82** (2010) 034505, [`arXiv:1005.1748`]. 6.6.4

[121] R. G. Edwards, J. J. Dudek, D. G. Richards and S. J. Wallace, *Excited state baryon spectroscopy from lattice qcd*, *Phys. Rev. D* **84** (Oct, 2011) 074508. 6.6.4

[122] B. Yoon et al., *Controlling Excited-State Contamination in Nucleon Matrix Elements*, *Phys. Rev. D* **93** (2016) 114506, [`arXiv:1602.07737`]. 6.7.2